



SAKARYA ÜNİVERSİTESİ

# FEN BİLİMLERİ ENSTİTÜSÜ DERGİSİ

Sakarya University Journal of Science (SAUJS)



SAKARYA  
ÜNİVERSİTESİ

e-issn: 2147-835X

SAÜ Fen Bil Der/SAUJS

Cilt/Volume: 27

Sayı/Issue: 5

Ekim/October 2023

---

---

**Sakarya Üniversitesi Fen Bilimleri Enstitüsü Dergisi**  
**(Sakarya University Journal of Science)**  
**Cilt/Volume: 27 No/ Issue:5 Ekim/October 2023**  
**Editör Kurulu/Editorial Boards**

---

---

---

---

**Owner**

---

Hamza Al, Sakarya University (Turkey)

---

---

**Publishing Manager**

---

Hüseyin Özkan Toplan, Metallurgical and Materials Engineering, Sakarya University (Turkey)

---

---

**Editor-in-Chief**

---

Ömer Tamer, Physics, Sakarya University (Turkey)

---

---

**Associate Editors**

---

Ihsan Hakan Selvi, Information Systems Engineering, Sakarya University (Turkey)

---

---

**Editors**

---

Abderrahmane Benbrik, M'Hamed Bougara University at Boumerdes (Algeria)

Abdullah Oğuz Kızılcay, Computer Engineering, Zonguldak Bülent Ecevit University (Turkey)

Ali Cemal Benim, Faculty of Mechanical and Process Engineering, Duesseldorf University of Applied Sciences (Germany)

Ali Demir, Mathematics, Kocaeli University (Turkey)

Aligholi Niaei, Chemistry, Tabriz University (Iran)

Aslı Uçar, Faculty of Health Sciences, Nutrition and dietetics, Ankara University (Turkey)

Asude Ateş, Environmental Engineering, Sakarya University (Turkey)

Bahadır Saygı, Physic, Ege University (Turkey)

Barış Yüce, Engineering Management, Exeter University, UK

Belma Zengin Kurt, Chemistry, Bezmiâlem Vakıf University (Turkey)

Benjamin Durakovic, Department of Industrial Engineering, Bosnia International University of Sarajevo (Bosnia and Herzegovina)

Berrin Denizhan, Industrial Engineering, Sakarya University (Turkey)

Can Serkan Keskin, Chemistry, Sakarya University (Turkey)

Caner Erden, International Trade and Finance, Sakarya University of Applied Sciences (Turkey)

Ceren Tayran, Physic, Gazi University (Turkey)

Cansu Akbulut, Biology, Sakarya University (Turkey)

Ece Ümmü Deveci, Environmental Engineering, Niğde Ömer Halisdemir University (Turkey)

Edgar Perez-Esteve, Food Technology, Polytechnic University of Valencia (Spain)

Elif Ağcakoca, Civil Engineering, Sakarya Applied Science University (Turkey)

Elif Eker Kahveci, Mechanical Engineering, Sakarya University (Turkey)

Erman Aslan, Mechanical Engineering, Kocaeli University (Turkey)

Fahrettin Horasan, Computer Engineering, Kırıkkale University (Turkey)

Faruk Fırat Çalım, Civil Engineering, Alparslan Türkeş University (Turkey)

Feyza Gurbuz, Industrial Engineering, Erciyes University (Turkey)

Francesco de Paulis, Electrical and Electronics Engineering, University of L'Aquila (Italy)

Gökhan Dok, Civil Engineering, Sakarya Applied Science University (Turkey)

Grazyna S Martynkova, Nanotechnology Centre, VŠB-Technical University of Ostrava · Nanotechnology Centre (Czech Republic)

Grzegorz Jaworski, Physics, Heavy Ion Laboratory, University of Warsaw (Poland)

H. F. Nied, Department of Mechanical Engineering and Mechanics, Lehigh University (U.S.A.)

Hakan Alp, Geophysical Engineering, Cerrahpaşa University (Turkey)

Hatice Esen, Industrial Engineering, Kocaeli University (Turkey)

Hüseyin Aksoy, Biology, Sakarya University (Turkey)

Issa Al-Harty, Civil and Architectural Engineering, Sultan Qaboos University (Oman)

İbrahim Bahadır Başyığıt, Electrical and Electronics Engineering, Isparta Applied Science University (Turkey)

İsmail Hakkı Demir, Architecture, Sakarya University (Turkey)

Kamaruzzaman Sopian, Renewable Energy, Universiti Kebangsaan Malaysia (Malaysia)

Khalifa Al-Jabri, Civil and Architectural Engineering, Sultan Qaboos University (Oman)

Kevser Ovaz Akpınar, Computer Engineering, Rochester Institute of Technology of Dubai (Dubai)

Luan Thach Hoang, Mathematics, Texas Tech University (U.S.A.)

Luis A. Materon, Biology, The University of Texas Rio Grande Valley (USA)

M. Hilmi Nişancı, Electrical and Electronics Engineering, Sakarya University (Turkey)

Mahmud Tokur, Metallurgical and Materials Engineering, Sakarya University (Turkey)

Mehmet Emin Aydın, Industrial Engineering, University of Bedfordshire (UK)

Mehmet Uysal, Metallurgical and Materials Engineering, Sakarya University (Turkey)

Mesut Baran, Electrical and Computer Engineering, FREEDM Systems Center, North Carolina State University (U.S.A.)

Miraç Alaf, Metallurgical and Materials Engineering, Bilecik Şeyh Edebali University (Turkey)

Mohammad Sukri bin Mustapa, Faculty of Mechanical & Manufacturing Engineering, Universiti Tun Hussein Onn Malaysia (Malaysia)

Muhammed Fatih Adak, Computer Engineering, Sakarya University (Turkey)

Muhammed Maruf Öztürk, Computer Engineering, Süleyman Demirel University (Turkey)

Murat Güzeltepe, Mathematics, Sakarya University (Turkey)

Murat Sarduvan, Mathematics, Sakarya University (Turkey)

Murat Tuna, Chemistry, Sakarya University (Turkey)  
Mustafa Akpınar, Software Engineering, Sakarya University (Turkey)  
Mustafa Gülfen, Chemistry, Sakarya University (Turkey)  
Nahit Gencer, Chemistry, Balıkesir University (Turkey)  
Nazan Deniz Yön Ertuğ, Biology, Sakarya University (Turkey)  
Necati Olgun, Mathematics, Gaziantep University (Turkey)  
Nihan Akıncı Kenanoğlu, Biology, Çanakkale Onsekiz Mart University (Turkey)  
Oğuz Kurt, Biology, Manisa Celal Bayar University (Turkey)  
Osman Sönmez, Civil Engineering, Sakarya University (Turkey)  
Ozan Erdinç, Electrical and Electronics Engineering, Yıldız Technical University (Turkey)  
Raja Mazuir Raja Ahsan Shah, Aerospace and Automotive Engineering, Coventry University (United Kingdom)  
Rıfki Terzioğlu, Electrical and Electronics Engineering, Bolu Abant İzzet Baysal University (Turkey)  
S.C. Yao, Mechanical Engineering, Carnegie Mellon University, PA (U.S.A.)  
Sadık Kakaç, Mechanical Engineering, TOBB ETU (Turkey)  
Selma Özçağ, Mathematics, Hacettepe University (Turkey)  
Seong Jin Park, Department of Mechanical Engineering, Pohang University of Science and Technology (Korea)  
Serap Coşansu Akdemir, Food Engineering, Sakarya University (Turkey)  
Syed Nasar Abbas, Food Engineering, Curtin University (Australia)  
Şenay Çetin Doğruparmak, Environmental Engineering, Kocaeli University (Turkey)  
Tahsin Turğay, Architecture, Sakarya University (Turkey)  
Tauseef Aized, Mechanical Engineering, University of Engineering and Technology (Pakistan)  
Tuba Tatar, Civil Engineering, Sakarya University (Turkey)  
Tuğrul Çetinkaya, Metallurgical and Materials Engineering, Sakarya University (Turkey)  
Ufuk Durmaz, Mechanical Engineering, Sakarya University (Turkey)  
Urvir Singh, Electrical and Electronics Engineering, Schweitzer Engineering Laboratories: SEL Inc. (U.S.A.)

## **Guest Editors**

---

Soley Ersoy, Mathematics, Sakarya University (Turkey)

## **Managing Editor**

---

Hüseyin Yasin UZUNOK, Physics, Sakarya University (Turkey)

## **Statistical Editor**

---

Önder Gökmen YILDIZ, Mathematics, Bilecik Şeyh Edebali University (Turkey)

## **English Language Editor**

---

---

Seçkin Arı, Computer Engineering, Sakarya University (Turkey)

## **Technical Editor**

---

---

Hatice Vural, Electrical and Electronics Engineering, Amasya University (Turkey)

## **Editorial Assistant**

---

---

Ahmet Erhan Tanyeri, Sakarya University (Turkey)

Evrin Yüksel, Sakarya University (Turkey)

SAKARYA ÜNİVERSİTESİ FEN BİLİMLERİ ENSTİTÜSÜ DERGİSİ  
(SAKARYA UNIVERSITY JOURNAL OF SCIENCE)  
İÇİNDEKİLER/CONTENTS  
Cilt/Volume: 27 – No/Issue5: (EKİM/ OCTOBER-2023)

RESEARCH ARTICLES

Title	Authors	Pages
The Turkish Art of Marbling (Ebru) on Textile Fabrics: Investigation of Thickening Agent, Mordant and Fixation Temperature	Cigdem AKDUMAN, Habibe KAHVECIOGLU SARI	930-942
Post-Ultraviolet-Curing Process Effects on Low-Velocity Impact Response of 3D Printed Polylactic Acid Parts	Tarkan AKDERYA	943-955
On the Properties of $r$ -Circulant Matrices Involving Generalized Fermat Numbers	Bahar KULOĞLU, Engin ESER, Engin ÖZKAN	956-964
Production of Hydrogen Molecule from Methane Molecule Amplified with Excitation of Anti-Symmetric Modes of Vibration	Sinan ERDOGAN	965-974
Investigating the Role of Bias Correction Methods and Climate Models on Water Budget of Büyük Menderes Basin	Zülküf İbrahim ERKOL, İrem DALOĞLU ÇETİNKAYA	975-986
Classification of Forest Fires in European Countries by Clustering Analysis Techniques	Hakan SERİN, Muslu Kazım KÖREZ, Mehmet Emin TEKİN, Sinan SİREN	987-1001
Development of an Analytical Method for the Determination of Cymoxanil in Potato Flour Samples by High Performance Liquid Chromatography	Tuğçe UNUTKAN GÖSTERİŞLİ	1002-1007
Phytochemical Components, Antioxidant, Antibacterial, and Synergistic Effects of Endemic Sideritis trojana Extract in Combination with Antibiotics on Human Pathogens	Mehzat ALTUN	1008-1018
Ergonomic Risk Assessment in the Forest Products Industry	Merve YILMAZ, Muharrem ÜNVER	1019-1035
Astrophysical Parameters of the Open Cluster NGC 2509	Talar YONTAN, Seliz Koç	1036-1045
Topology Optimization of Spinal Cage Designs for Improved Stress Distribution and Bone Graft Window	Meltem ERYILDIZ	1046-1054
The Influence of Building Form Compactness on Energy Efficiency in Accommodation Structures: The Case of Türkiye	Özlem KAHRAMAN, Erdem KÖYMEN	1055-1078
Estimating Human Poses Using Deep Learning Model	Fırat MURADLI, Serap ÇAKAR, Feyza SELAMET, Gülüzar ÇİT	1079-1087

Investigation of the Usage Properties of Steel Slag as Pigment in Low-Temperature Glaze	Muhterem KOÇ, Eda TAŞÇI	1088-1096
Common Solutions to Stein Inequalities	Şerife YILMAZ, Birgül AKSOY	1097-1103
One-step and Cost-effective Conversion of Polyimide to Graphene by Utilizing a Desktop Laser	Nihan AYDEMİR	1104-1110
Short-Term Electrical Load Forecasting in Power Systems Using Deep Learning Techniques	Nihat PAMUK	1111-1121
Mulatu Numbers Which Are Concatenation of Two Fibonacci Numbers	Fatih ERDUVAN, Merve GÜNEY DUMAN	1122-1127
Enhancing Brain Tumor Detection on MRI Images Using an Innovative VGG-19 Model-Based Approach	Abdullah ŞENER, Burhan ERGEN	1128-1140
Fractal Approach to Dielectric Properties of Single Walled Carbon Nanotubes Reinforced Polymer Composites	Aykut ILGAZ, Mehmet BAYIRLI	1141-1149
Retraction: Metabolism Determination By Soft Computing Methods From Breath Molecules	Sedat METLEK, Hatice AKMAN, İsmail BAYRAKLI	1150-1158



SAKARYA ÜNİVERSİTESİ

# FEN BİLİMLERİ ENSTİTÜSÜ DERGİSİ

Sakarya University Journal of Science  
SAUJS

ISSN 1301-4048 | e-ISSN 2147-835X | Period Bimonthly | Founded: 1997 | Publisher Sakarya University |  
<http://www.saujs.sakarya.edu.tr/>

Title: The Turkish Art of Marbling (Ebru) on Textile Fabrics: Investigation of Thickening Agent, Mordant and Fixation Temperature

Authors: Cigdem AKDUMAN, Habibe KAHVECIOGLU SARI

Received: 2023-04-17 00:00:00

Accepted: 2023-06-08 00:00:00

Article Type: Research Article

Volume: 27

Issue: 5

Month: October

Year: 2023

Pages: 930-942

How to cite

Cigdem AKDUMAN, Habibe KAHVECIOGLU SARI; (2023), The Turkish Art of Marbling (Ebru) on Textile Fabrics: Investigation of Thickening Agent, Mordant and Fixation Temperature. Sakarya University Journal of Science, 27(5), 930-942, DOI: 10.16984/saufenbilder.1283596

Access link



<https://dergipark.org.tr/tr/journal/1115/issue/80257/1283596>

New submission to SAUJS

<http://dergipark.gov.tr/journal/1115/submission/start>



## The Turkish Art of Marbling (Ebru) on Textile Fabrics: Investigation of Thickening Agent, Mordant and Fixation Temperature

Cigdem AKDUMAN<sup>\*1</sup> , Habibe KAHVECIOGLU SARI<sup>1</sup> 

### Abstract

Ebru is a mysterious art and briefly described as the art of paper decoration. Turkish “Ebru” or “Marbling Art” was included in the list of world cultural heritage by UNESCO in November 2014. Today, people use marbling mainly for fabrics and papers in many ways. From a technical viewpoint, the marbling process depends on the balance of relations between the chemical character and particle size of the color pigments and their relation between the viscosity and surface tension phenomena of the marbling bath upon the surface. This study investigates the surface tension, pH and conductivity of the sizing baths and acrylic dyes, compares carrageenan and sodium alginate as thickeners for the marbling bath. Then it also explores the effect of self-fixation, fixation temperature and alum application on the fastness properties and print durability results for cotton and polyester fabric. It was seen that pattern transferring ability of carrageenan bath was better than sodium alginate bath, marbling paints have some self-crosslinking ability, alum application do not have an influence on the print durability and fastness properties, whereas, only fixation temperature of 150°C had a slight effect.

**Keywords:** Ebru, marbling, fixation temperature, marbling bath, print durability

### 1. INTRODUCTION

Ebru is briefly described as the art of paper decoration. In Ebru, a composition made with the help of paint, sprinkled with a brush on water concentrated with the help of tragacanth gum or another material [1, 2] is transferred to paper and many materials. The origin of the word Ebru comes from Persian AbRu (water face) and Ebr (cloud like) and carries the meaning of 'cloud' [1, 3-5]. Also recognized as paper marbling and is not known exactly where and when the art of marbling started. It is a mysterious art dating back to the 1100s [6]. Patterns resembling scalloped and tidal

marbling were found on glass bottles dated 1365 BC in Egypt. However, there is some information that the modern marbling known today was made in Turkestan, Samarkand in the 13th century and is thought to have spread in the 14th century to Iran, India and Anatolia [5, 6]. It is accepted that the art of marbling came from the east to the west, just like paper, using the silk road and other trade routes [1].

Turkish “Ebru” or “Marbling Art” was included in the list of world cultural heritage by UNESCO in November 2014. By this progress, the art of marbling was declared and registered as a wealthiness that Turkish

\* Corresponding author: cakduman@pau.edu.tr (C. AKDUMAN)

<sup>1</sup> Pamukkale University

E-mail: hkahveci@pau.edu.tr

ORCID: <https://orcid.org/0000-0002-6379-6697>, <https://orcid.org/0000-0003-0032-6230>



culture brought to the world cultural heritage [1]. It was used most often on the inner covers of fine books as a stylish transition between cover and content. Today, people use marbling mainly for fabrics and papers in many ways, including scarfs, ties, picture framing, wrapping paper, origami, lampshades and for decorating just about anything, tissues, boxes, woods, cans etc [3, 6].

From a technical viewpoint, the entire marbling process seems to depend on the balance of relations between the chemical character and particle size of the color pigments used and their relationship to the viscosity and surface tension phenomena of the viscous bath upon the surface [7]. In marbling, the pigment particles must be completely insoluble in water, otherwise the pigment dye or paint will mix with the aqueous solution of the bath, contaminate the bath, sink into the bath, and disappear from the surface.

A proper balance established between the viscosity of bath, hence its buoyancy power and the surface tension and the dispersion properties, results in the design of many of the beautiful patterns and color. Many thickening agents can be used to thicken water and create a gum bath (or a size) for marbling paints. Carrageenan, methyl cellulose, gum tragacanth, starch, sodium alginate and some other plant-based mucilage can be used as thickener to make size solution. Among them the most commonly used ones are, carrageenan and methyl cellulose [7, 8].

In marbling process, the pigment particles must also be surrounded by a surfactant film such as oxgall. Surfactants leads to a reduction of the interfacial tension at liquid/liquid interfaces [9]. So that thanks to the surface tension-reducing effect of the surfactant, the pigment particles are supported and finely dispersed on the bath surface, creating a floating appearance. If the surfactant does not reduce the surface tension, the pigment particles will sink to the bottom

of the bath due to their weight exceeding the buoyancy of the gum solution [7, 10].

As a surfactant, oxgall or other glycols, solutions of soaps, and some other organic substances may be used to disperse the color upon the surface of the bath, while other chemicals appear to react in the opposite manner to contract or coagulate the color into a condensed pattern. Natural oxgall, the oldest of these surfactants is obtained from animal bile. The bile of all animals contains certain organic acids containing nitrogen when these acids are chemically treated to remove sulfur and nitrogen compounds, it yields an acid known as glycocholic acid. This glycocholic, which is the main component of oxgall, is responsible for the spreading of the colors. Prior to marbling process an alum (aluminum potassium sulfate,  $KAl(SO_4)_2$ ) is used in treating the fabric and paper. When the pigment, surrounded by a film of surfactant or oxgall, is transferred to the fabric or paper, a chemical reaction occurs between the alum and the glycocholic acid. This reaction results in the formation of insoluble aluminum glycocholate salt and binds the pigment permanently to the fibers [7, 10].

In traditional marbling art, natural dyes as earth (soil) dyes and plant extract dyes are used. Soil dyes are also called earth oxide dyes. They are obtained from soils of different colors according to the minerals in the soil [11]. The main pigmenting (coloring) agents in soils are organic matter, iron, and, to a lesser extent, manganese [12]. Herbal dyes or plant extract dyes, on the other hand, are made from the roots, stems or leaves of plants that give color [11]. The modern way is to use commercial ready-to-use acrylic-based paints. They are already premixed and diluted and sold in bottles or are in the form of powder pigments which needs preparation. Today mostly water based acrylic paints consist of pigment particles dispersed in an acrylic polymer emulsion are used. In any acrylic paint there are three main components- pigment, binder and vehicle [13-14]. Pigments are milled to tiny particles and

do not dissolve in water but suspended in the paint. Pigments can be organic, inorganic, natural or synthetic. They have little or no affinity to the surface which they applied.

Acrylic paint formulation varies considerably depending on the additives, pigments, surfactants etc., that manufacturers choose to use [13]. The binder holds the pigment on the surface of the fabric or paper after the paint dried. Acrylic paints include acrylic polymer binder, which forms a film after the water evaporates. Vehicle or body carries the pigment and binder. Water is the carrier for the water-based acrylic and when combined with the binder it forms a polymer emulsion. Surfactant reduces the surface tension of the water in the acrylic emulsion thereby increasing the slickness and flow of the paint.

Although Ebru has been known for centuries, there are very few academic publications on its technical basis. Halfer's "The Progress of the Marbling Art" was the first book about technical scientific principles of marbling [10]. Then Kantrowitz and Spencer released a research bulletin named "The Process of Marbling Paper" in 1947 [7]. Some other books were mainly about patterns and methods for marbling designs. Recently, Benli et al. studied hibiscus and black carrots as alternative dyestuff sources instead of soil-based dyestuffs [4]. Begiç summarized the Marbling art, its importance as a cultural heritage and its needs [1]. Tozun and Uzunca examined and summarized the way of applying marbling to textiles, the dyestuffs, the types of fabrics, the areas of use in textiles, the color and composition characteristics, and the types of marbling on textile fabrics [5]. Xu et al., designed a real-time physical simulation for traditional marbling design, making it possible for users to create marbling patterns following the same procedure as real marbling [6].

And Karabacak investigated the effect of different types of fabric and dyes on the quality marbling of textile products. She chose cotton, rayon, polyester fabrics with

mordant and without mordant. Traditional marbling dye, liquid fabric dyes and ready to use commercially available synthetic marbling dyes were also compared. She observed that alum treated fabrics are brighter and cleaner. According to her results, in terms of ease of application, appearance, and fastness properties, ready-to-use acrylic synthetic marbling dyes are the best and followed by liquid fabric dyes and soil marbling dyes [11].

This study includes two parts. Apart from the previous studies, in the first part, the surface tension, pH and conductivity of the sizing baths and acrylic dyes were measured. Then, the use of carrageenan and sodium alginate as thickeners for the application bath and the fixation temperatures as post-treatment were compared. In the second part of the study, the effect of the mordant and self-crosslinking on the fastness properties were investigated.

Therefore, each cotton and polyester fabrics were marbled with and without alum application and allowed to wait for a week to see whether they would self-crosslink or not. These self-crosslinked fabrics were compared with 10 min fixated fabrics at temperatures of 110, 130 and 150°C for both cotton and polyester fabric. All results were compared in terms of fastness properties such as rubbing, washing and print durability.

## 2. MATERIALS AND METHODS

### 2.1. Materials

In the first part of the study cotton-1 and polyester fabrics, in the second part of the study with same polyester fabric cotton-2 were used. In the second part, 50/1 Ne cotton-2 was used, and in the conclusion it was compared with the 40/1 Ne cotton-1 fabric used in the first part. It was examined whether the increase in the surface area due to the finer yarn count had an effect on the marbling results or not. Carrageenan, fabrics and natural soft spring water and alum (aluminium potassium sulfate dodecahydrate,

( $KAl(SO_4)_2 \cdot 12H_2O$ ) were supplied locally. Fabric properties are given in Table 1. Sodium alginate was supplied from CHT Group, Turkey. Commercial acrylic paints were supplied from Pebeo.

Table 1. Fabric properties

Fabric Type	cotton-1	polyester	cotton-2
Finishing process	Bleached	Bleached	Bleached
Yarn number	Warp:40/1 Ne Weft: 40/1 Ne	Warp:90/1 Denier Weft: 90/1 Denier	Warp:50/1 Ne Weft: 50/1 Ne
Density	Warp:31 Weft:27	Warp:46 Weft:35	Warp: Weft:
Weight (g/cm <sup>2</sup> )	125	90	115

### 3. METHODS

#### 3.1. Marbling Process and After Treatments

For marbling process, first, two separate marbling baths were prepared by mixing 7 g carrageenan and 20 g sodium alginate per liter with spring water and let swell for 4 hours. Using horse hair brushes, paints were dripped on the surface of marbling baths. For spreading out the paint drops, few seconds was waited. Once the surface was covered with paint, fabric was placed on the surface of the colored bath. After few seconds, fabric was removed and line dried.

In the first part of the study, after 24 hours, marbled cotton-1 and polyester fabric were cold washed to remove the thickening bath remains and line dried. Then, just referring ironing, they were fixated shortly, for 30 seconds at 110, 130 and 150°C for cotton-1 and 100, 110 and 120°C for polyester fabric. Since polyester fabrics are more sensitive to ironing temperature, we used lower temperature for them.

In the second part of the study before the marbling process, one pair of each fabric was dipped into an alum bath for comparison. First, 15 g of alum was dissolved in warm

water (40°C), then fabrics were dipped into this bath and waited at least 20 minutes. After squeezing, they were line dried. To achieve a flat and smooth surface they were all ironed.

After marbling cotton-2 and polyester fabric were line dried and waited for a week for self-crosslinking. To evaluate the increased fixation period a piece of cotton and polyester fabric fixated for 10 minutes at 110, 130 and 150 °C and compared with non-fixated marbled fabrics. In order to investigate whether elevated temperatures further improve the fastness properties of polyester fabric, in this part, temperatures of 110, 130 and 150 °C are also used for polyester fabrics.

#### 3.2. Characterization and Fastness Tests

Viscosity of the polymer solutions was measured by using Brookfield DV-III Rheometer with the spindle type SC4-21 at 50 rpm. Surface tension measurements were carried out by a Kruss Easy Dyne Analyzer by Plate Method. Conductivity measurements were carried out using a J.P. Selecta Conductivity meter, CD-2004. All measurements were carried out at room temperature (22±2 °C), where the relative humidity was 22-40%.

Washing and rubbing fastness was carried out according to ISO 105-C06 A2S at 40°C and ISO 105-X12 as dry and wet rubbing, respectively. Print durability tests were done accordingly C15 (Marks and Spencer, Print Durability Test) at Durawash washing machine. Natural tap water was used at 50°C. 30g of automatic heavy-duty, low-lather, powder detergent containing optical brightening agent was added to the machine. Then, all specimens were tumble dried until the specimens were, dry. The degree of loss of print/marbling was assessed and each color was graded individually as no, negligible, slight, distinct, or complete.

#### 4. RESULTS AND DISCUSSION

The conductivity, surface tension and pH measurement results for spring water, marbling baths and paints were given in Table 2. Since we used spring water, its conductivity is relatively high because it contains more or less ions. Sodium alginate has almost neutral pH and show very low conductivity value but slightly higher than carrageenan bath because of the carboxylic groups.

pH of 1.5% carrageenan solutions lays between 8.0 and 11.0 [15] and in this study it was measured 8.60 which is consistent with literature. All paints have very low conductivities because they just include acrylic binder polymer emulsion, pigment, water, and surfactant, do not include ions, so they do not have a remarkable conductivity value. Their pH values were between 7.43 and 8.46, possibly related to their formulations.

The surface tension of water changes from about 72 mN/m to about 57 mN/m [16], and the spring water used in this study was 60.2 mN/m. Carrageenan bath has higher surface tension of 54.2 than sodium alginate bath of 49.0 mN/m. As the density of the liquid increases, the surface tension increases, because surface tension is a reflection of cohesive forces in a liquid [17].

When the surface tension of the liquid decreases, its wetting ability increases. Since acrylic paints have lower surface tensions and lower densities than marbling baths, they have tendency to spread out on the surface of the bath. Because of the immiscible fluids; paints and baths, paints are separated out on the bath and do not mix with each other due to their different interfacial tensions. Interfacial tension is defined as the work which must be expended to increase the size of the interface between two adjacent phases which do not mix completely with one another.

So, the reason for immiscibility is the large difference in cohesion forces between the molecules in the two liquids. If the interfacial tension strength between liquids is lower, they mix easily and emulsify at the interface, otherwise we see a sharp interface between them. Therefore, we would expect paints to spread out more on the alginate baths. Patterning would be more difficult to control, as there is less difference in surface tension between alginate bath and paints. Viscosity measurement of carrageenan bath and sodium alginate baths were 16 and 40 centiPoise (cP).

Table 2. The conductivity, surface tension and pH measurement results

	Conductivity ( $\mu\text{S}/\text{cm}$ )	Surface Tension (mN/m)	pH	Viscosity (cP)
Spring water	57.2	60.2	7.32	-
Carrageenan bath	5.86	54.2	8.60	16
Sodium alginate bath	11.78	49.0	7.61	40
Yellow	4.80	36.3	7.56	-
White	5.30	34.2	7.50	-
Brown	5.48	37.7	7.50	-
Black	6.11	38.0	7.43	-
Red	4.49	36.9	7.70	-
Green	3.60	37.5	8.19	-
Pink	5.47	35.7	7.65	-
Cyan	3.68	38.0	8.46	-
Blue	4.83	36.4	7.77	-

Color fastness to rubbing and washing results for the first part of the study is given in Table 3. Fastness to rubbing is given as dry and wet rub, fastness to washing is given as change in color and staining to cotton and lyocell. Multifiber fabric consist of six yarn type, since we observed some staining on cotton and lyocell, thus we only give staining onto cotton and lyocell. The effect of thickening agent for marbling bath and fixation temperature were compared. As mentioned, short fixation of 30 seconds was conducted to simulate the ironing effect. According to the results, for cotton fabric carrageenan bath resulted better rubbing fastness for cotton than sodium alginate bath. For polyester fabric it is not significant as cotton fabric. Wet rubbing fastness are better than cotton, because in wet rubbing fastness, there is also

removal of the fibers from the printed surface of the fabric, however in case of synthetic filament polyester yarns, it is not possible to remove fibers from the structure.

Table 3. Color Fastness to Rubbing and Washing Results of Cotton-1 and Polyester in Part I

Fabric	Medium (Thickening agent)	Fixation Temp. °C	Fastness to Rubbing ISO 105-X12		Fastness to Washing ISO 105-C06/A2S		
			Dry	Wet	Change in Color	Staining	
						Cotton	Lyocell
Cotton-1	Carrageenan	110	4	2-3	4-5	4-5	4-5
		130	4	2-3	4-5	4-5	4-5
		150	4	2-3	4-5	4-5	4-5
	Sodium Alginate	110	2	1-2	4-5	4-5	4-5
		130	2	1-2	4-5	4-5	4-5
		150	2	1-2	4-5	4-5	4-5
Polyester	Carrageenan	100	2	3	4-5	4-5	4-5
		110	1-2	3	4-5	4-5	4-5
		120	1-2	3	4-5	4-5	4-5
	Sodium Alginate	100	2	3-4	4-5	4-5	4-5
		110	2	3-4	4-5	4-5	4-5
		120	2	3-4	4-5	4-5	4-5

When washing fastness were compared, both cotton and polyester fabrics show good results for both carrageenan and sodium alginate baths. It was also seen that fixation temperature has not an effect on the washing and rubbing results. In washing fastness, each color should be assessed for change in color. But only in red color there was a significant color change therefore we just assessed general color change of all marbling and assessed as 4-5.

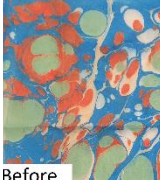



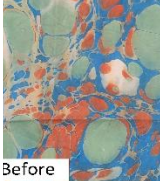

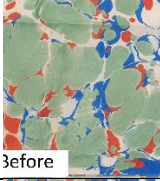

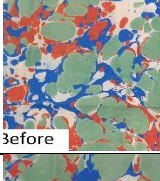
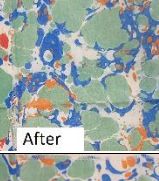
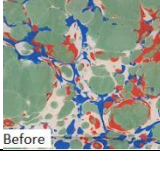
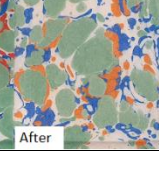
Print durability results for the Part I are given in Table 4 and Table 5 for cotton-1 and polyester, respectively. Marbling designs on the surface of the bath depend on the how much and where drops are dripped. So, it is not possible to achieve exactly same design for each sample. For instance, when dropped paints are more or less than the other one, the color depth could be slightly different. It was seen that green paint spread out more than blue and red paints, because of higher surface tension of 37.5 mN/m than blue and red paints.

It was more significant for sodium alginate bath. Since sodium alginate bath's surface tension was lower than carrageenan bath,

spreading of the green color was larger in sodium alginate bath. It pushed red and blue paint and green color became dominant. For all specimens, blue and green paint preserved their color tone however red color lost its tone and turned to orange, most probably because of the pigment dye it consists of. Therefore, apart from other colors, red color change was evaluated with grey scale and scored 1 to 5, and together with the color change, print loss was commented in the same column.

According to the Table 4, for cotton-1 carrageenan bath resulted in better print durability than sodium alginate bath, while increase of the fixation temperature had no significant effect. While better durability was expected with increasing fixation temperature, worse results were also seen in some cases. Just for 150°C, slight improvements were achieved. Since all samples were individually marbled, generally clearer patterns were obtained for the first marbling samples, the later ones slightly blurred because of the contamination of the sizing bath. And these blurred marblings showed worse print durability than clearer ones.

Table 4. Print durability results of cotton-1 in Part I

Marbling Bath (Thickening agent)	Fixation Temp°C	Cotton-1				
		Print Durability			Before	After
		Blue	Red Color Change/ Print Loss	Green		
Carrageenan	110	Slight	3/ Negligible	Negligible		
	130	Slight	2-3/Slight	Negligible		
	150	Slight	3/Slight	Slight		
Sodium Alginate	110	Slight	2-3/Slight	Slight		
	130	Slight	3/Slight	Slight		
	150	Distinct	2-3/Distinct	Distinct		

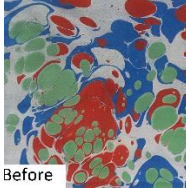
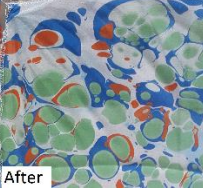
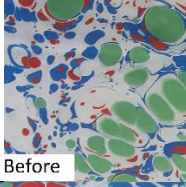

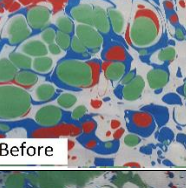
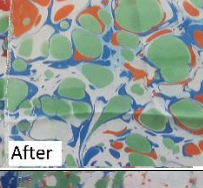
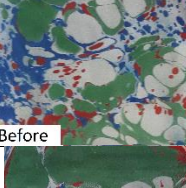
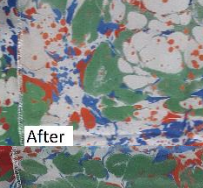
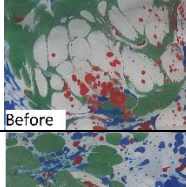
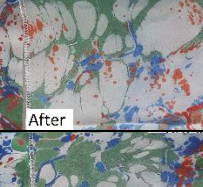
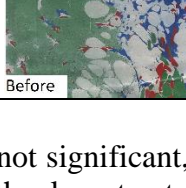
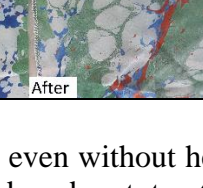
When cotton-1 and polyester marbling was compared, it was seen that acrylic paints showed better patterns and print durability on polyester fabric especially in carrageenan bath. It might be related to the better adhesion forces between polyester and binder than cotton and binder, due to binder formulation. Because some copolymers that binders contain for “internal” crosslinking can be useful for prints on hydrophobic materials [18] and here marbling gave better results for polyester than cotton fabric. Another possible explanation is that polyester fabric has thinner

yarns than cotton-1 fabrics, and due to texturized yarn structure, it has rougher surface than cotton. Thus, absorbed patterns are clearer and might be better hold onto the polyester fabric.

According to the Table 5, carrageenan bath pattern transferring ability was better than sodium alginate bath, and again this was resulted in better durability. According to the viscosity measurement sodium alginate bath has slightly higher viscosity and this may alter

the absorption of the patterns which may also result the poorer durability.

Table 5. Print durability results of polyester in Part I

Marbling Bath (Thickening agent)	Fixation Temp°C	Polyester			Print Durability	
		Blue	Red Color Change/ Print Loss	Green	Before	After
Carrageenan	100	Negligible	3/ Negligible	Negligible		
	110	Negligible	3/ Negligible	Negligible		
	130	Negligible	3-4/ Negligible	Negligible		
Sodium Alginate	100	Slight	3/Slight	Distinct		
	110	Slight	3-4/ Slight	Slight		
	130	Slight	3-4/ Slight	Distinct		

In the second part of the study, we would like to see whether these commercial ready to use acrylic marbling paints have self-crosslinking ability and, do alum application influences the print durability. In Table 6. rubbing fastness and washing fastness of both cotton-2 and polyester fabrics are given together. It is seen that for cotton samples, there is slight tendency of better rubbing and washing fastness with the increasing of fixation temperature to the 150°C. For polyester

fabric, it is not significant, even without heat fixation both alum treated and not treated polyester fabric show good dry rubbing results than almost all other heat fixated polyester fabrics and heat fixation does not cause any notable difference. When we compare the washing test results, again there is no significant tendency of decreasing or increasing, just for 150°C of heat fixation slightly increased the staining results.



Table 6. Color fastness to rubbing and washing results of cotton-2 and polyester in Part II

Cotton-2							
Process Conditions	Fixation Temperature °C	Fastness to Rubbing ISO 105-X12		Fastness to Washing ISO 105-C06/A2S			
		Dry	Wet	Change in color		Staining	
				Red	Yellow	Cotton	Lyocell
Without Mordant	None	4-5	2-3	3	4-5	4	3-4
	110	4	2-3	3-4	4-5	4	4
	130	4-5	3	3	4-5	3-4	4
	150	4-5	3-4	3	4-5	4	4
With Mordant	None	4	2-3	3-4	4-5	3-4	3-4
	110	4	3	3	4-5	4	4
	130	3-4	3	3-4	4-5	4	4
	150	4	3	3	4-5	4	4
Polyester							
Process Conditions	Fixation Temperature °C	Fastness to Rubbing ISO 105-X12		Fastness to Washing ISO 105-C06/A2S			
		Dry	Wet	Change in color		Staining	
				Red	Yellow	Cotton	Lyocell
Without Mordant	None	4	2-3	3-4	4-5	3-4	3-4
	110	3-4	3	3-4	4-5	3-4	3-4
	130	4	3	3-4	4-5	3-4	4
	150	3-4	2-3	3-4	4-5	4-5	4-5
With Mordant	None	4	2-3	3-4	4-5	3-4	3-4
	110	3-4	2-3	3-4	4-5	4	3-4
	130	3-4	2-3	3-4	4-5	4	4
	150	3-4	3	3-4	4-5	4-5	4-5

Print durability results of cotton-2 and polyester fabrics for the second part of the study are given in Table 7 and Table 8. Images before and after print durability test are also inserted to the tables. Both tables include three fixation temperature as 110, 130 and 150°C for 10 min, longer than which has been carried out in the Part I and “none” for without fixation for both cotton-2 and polyester fabric. As we observed in Part I, red color loses its red tone after all condition. Therefore, its color change was evaluated with grey scale and scored 1 to 5, but together with the color change, print loss was commented in the same column as we have done in Part I. From the Table 7, for cotton-2, in contrary to alum treatment, fixation temperature has some effect on the print durability results.

It was also seen that, marbled samples that were not heat fixated, showed fair durability if they were let to stay few days without washing. Acrylic paints that are also used in painting art, attach to the surface of the canvas





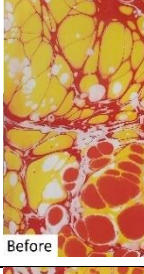
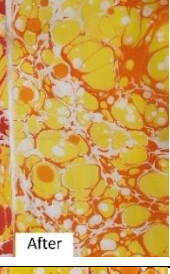

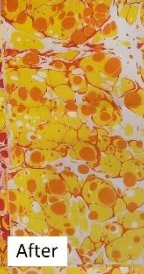
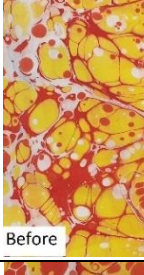



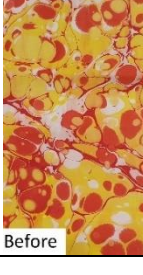

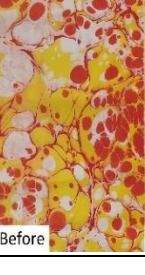

permanently with self-fixation. Also, it is known that for some heat sensitive fabrics, low heat fixation binders could be used in textile printing applications. Herewith it is supposed that ready to use marbling paints include a low fixation binder and if waited enough without washing, self-crosslinking occurs and strong bonds are formed, fair to good print durability results can be achieved.

In case of mordant application, no significant difference could be seen in durability results between alum treated and not treated marblings. Because these ready to use paints include their own binder system and surfactant. As mentioned in the introduction part, in traditional marbling, natural earth dyes and some natural root and herbal dyes were used and in order to spread these pigment dyes, natural ox-gall was employed. These dyes did not include a binder system which can bind the pigment to the paper or fabric. For this reason, alum treatment was necessary to provide durable patterns to water. During the chemical reaction between

the alum and the glycocholic acid, insoluble aluminum glycocholate salt is formed which binds the pigment to the paper or fabric. However, today's easy marbling paints already contain binders and surfactants. Thus,

alum treatment is not necessary for the bonding, as we have shown in our print durability results as well as the rubbing and the washing fastness results.



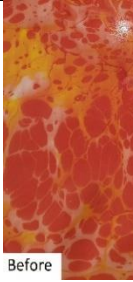



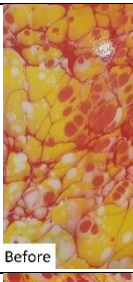



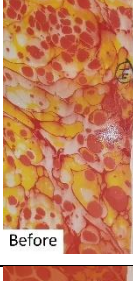





Table 7. Print durability results of cotton-2 in Part II

Cotton-2								
Print Durability								
Fixation Temp°C	Yellow	Red Color Change/ Print Loss	Without Potassium alum		Yellow	Red Color Change/ Print Loss	With Potassium alum	
None	Negligible	3/ Negligible			Negligible	3/ Negligible		
110	Negligible	3-4/ Negligible			Negligible	3-4/ Negligible		
130	Negligible	3-4/ Negligible			Negligible	3-4/ Negligible		
150	Negligible	4/ Negligible			Negligible	4/ Negligible		

All similar results were seen in Table 8 for polyester marblings. Very slight improvement was only observed for the fixation at 150°C. Again, alum treatment had no effect and not necessary. When we compare Part I and Part II, cotton fabrics had different yarn counts and cotton-1 yarns were

thicker than cotton-2. Like chiffon polyester marbling, due to the increased surface area of finer yarns, pigments and binders were better adhered to the fabric surface and resulted in good marbling and durability.

Table 8. Print durability results of polyester in Part II

Polyester								
Print Durability								
Fixation Temp. °C	Yellow	Red Color Change/ Print Loss	Without Potassium alum		Yellow	Red Color Change/ Print Loss	With Potassium alum	
None	Negligible	2-3/ Slight			Negligible	3/ Slight		
110	Negligible	3-4/ Negligible			Negligible	3-4/ Negligible		
130	Negligible	3-4/ Negligible			Negligible	3-4/ Negligible		
150	Negligible	3-4/ Negligible			Negligible	3-4/ Negligible		

## 5. CONCLUSION

The entire marbling process depends on the balance of relations between the chemical character and particle size of the color pigments and their relationship to the viscosity and surface tension phenomena of the viscous bath upon the surface. Although Ebru Art/marbling has been known for centuries, today easy marbling paints are quite different than traditional marbling dyes. Because of the immiscible fluids with different surface tensions; marbling paints are

separated out on the baths and do not mix with each other. In this study, it was seen that, carrageenan bath has higher surface tension of 54.2 than sodium alginate bath of 49.0 mN/m. Therefore, paints were spread out more upon the surface of alginate bath than carrageenan bath which was not ideal to control the patterns. On the other hand, day after washing good washing fastness were obtained. However especially for cotton-1 wet rubbing fastness resulted 2-3 for carrageenan bath and 1-2 for sodium alginate bath. It was also seen that pattern transferring ability of carrageenan

bath was better than sodium alginate bath. In case of short fixations, only for 150°C, slight improvements were achieved. In the second part of the study, it was shown that easy marbling paints have self-crosslinking ability and, alum application do not influence the print durability. Because these easy, ready to use marbling dyes include a binder system possibly with a low temperature fixating agent. When they are let to dry for few days without washing, they show good print durability results. Only slight improvements were observed for the fixation temperature of 150°C while alum treatment seemed unnecessary. Different fabric finishes and fabric construction would be the subjects of further studies about marbling onto textile fabrics.

#### ***Funding***

The authors have not received any financial support for the research, authorship, or publication of this study.

#### ***Authors' Contribution***

The authors contributed equally to the study.

#### ***The Declaration of Conflict of Interest/ Common Interest***

No conflict of interest or common interest has been declared by the authors.

#### ***The Declaration of Ethics Committee Approval***

This study does not require ethics committee permission or any special permission.

#### ***The Declaration of Research and Publication Ethics***

The authors of the paper declare that they comply with the scientific, ethical and quotation rules of SAUJS in all processes of the paper and that they do not make any falsification on the data collected. In addition, they declare that Sakarya University Journal of Science and its editorial board have no responsibility for any ethical violations that may be encountered, and that this study has not been evaluated in any academic

publication environment other than Sakarya University Journal of Science.

### **REFERENCES**

- [1] H. N. Begiç, "Unesco Dünya Kültürel Miras Listesinde Yer Alan Geleneksel Türk Ebru Sanatı'nda Yeni Yorumlar," Selçuk Üniversitesi Türkiyat Araştırmaları Dergisi, vol. 1, no. 37, pp. 587-605, 2015.
- [2] Jacquard Products, Marbling Color, April 11, 2023. [Online]. Available: <https://www.jacquardproducts.com/marbling-color>.
- [3] O. Goktas, H. Toker, "Effects of the traditional Turkish art of marbling (Ebru) techniques on the adhesion, hardness, and gloss of some finishing varnishes". Forest Products Journal, vol. 60, no. 7-8, pp. 648-653, 2010.
- [4] H., Benli, İ., Bahtiyari, M. Yılmaz, "Geleneksel Türk Ebru Sanatında Doğal Boyarmaddelerin Kullanılabilirliği", Akdeniz Sanat, vol. 5, no. 10, pp. 21-22, 2012.
- [5] H. Tozun, G. Uzunca, "Ebru Sanatının Tekstilde Kullanımı. İnönü Üniversitesi Sanat ve Tasarım Dergisi", vol. 5, no.12, pp.93-99, 2015.
- [6] J. Xu, X. Mao, X. Jin, Nondissipative marbling. IEEE Computer Graphics and Applications, vol. 28, no. 2, pp.35-43, 2008.
- [7] M. S., Kantrowitz, E. W. Spencer, "The Process of Marbling Paper (No. 1)". USA, US Government Printing Office, 1947, pp.1-10.
- [8] Dharmatrading, April 11, 2023 [Online]. Available: <https://www.dharmatrading.com/techniques/marbling/marbling-history.html?Inav=techniques.html>,

- [9] P. Schmiedel, W. V. Rybinski, "Applied Theory of Surfactants" in "Chemistry and Technology of Surfactants". Oxford, England: Blackwell Publishing Ltd, 2006, pp. 46-88.
- [10] J. Halfer, "The Progress of the Marbling Art: From Technical Scientific Principles." New York, USA, LH Kinder, 1893, pp.1-89.
- [11] C. Ş. Karabacak, "Farklı tip kumaş ve boya kullanımının ebru tekstil ürünlerinin kalitesine etkisi" M.S. Dissertation, Dept. Textile Design, Fine Arts Institute, Gazi University, Turkey 2018.
- [12] P. R., Owens, E. M. Rutledge, "Morphology" in "Encyclopedia of Soils in the Environment" Daniel Hillel (Ed), Academic Press. 2005, pp 511-520,
- [13] A., Iscen, N. C., Forero-Martinez, O., Valsson, K. Kremer, "Acrylic paints: An atomistic view of polymer structure and effects of environmental pollutants". The Journal of Physical Chemistry B, vol. 125, no. 38, pp.10854-10865, 2021.
- [14] Liquitex, What is acrylic paint? April 11. 2023 [Online]. Available: <https://www.liquitex.com/row/knowledge/what-is-acrylic-paint/>.
- [15] Agargel, What Is Carrageenan?, April 11. 2023 [Online]. Available: <https://agargel.com.br/en/carrageenan/#tipos>.
- [16] S. D., Lubetkin, M. Akhtar, "The variation of surface tension and contact angle under applied pressure of dissolved gases, and the effects of these changes on the rate of bubble nucleation". Journal of Colloid and Interface Science, vol. 180, no. 1, pp.43-60, 1996.
- [17] B., Kronberg, K. Holmberg, B., Lindman, "Surface and Interfacial Tension" in "Surface Chemistry of Surfactants and Polymers". John Wiley & Sons, 2014, pp. 231-249.
- [18] A. K. R. Choudhury, "Direct, Discharge and Resist Styles of Printing" in "Principles of Textile Printing" CRC Press, 2023, pp.147-200.



SAKARYA ÜNİVERSİTESİ

# FEN BİLİMLERİ ENSTİTÜSÜ DERGİSİ

Sakarya University Journal of Science  
SAUJS

ISSN 1301-4048 | e-ISSN 2147-835X | Period Bimonthly | Founded: 1997 | Publisher Sakarya University |  
<http://www.saujs.sakarya.edu.tr/>

Title: Post-Ultraviolet-Curing Process Effects on Low-Velocity Impact Response of 3D Printed Polylactic Acid Parts

Authors: Tarkan AKDERYA

Received: 2023-04-09 00:00:00

Accepted: 2023-06-13 00:00:00

Article Type: Research Article

Volume: 27

Issue: 5

Month: October

Year: 2023

Pages: 943-955

How to cite

Tarkan AKDERYA; (2023), Post-Ultraviolet-Curing Process Effects on Low-Velocity Impact Response of 3D Printed Polylactic Acid Parts. Sakarya University Journal of Science, 27(5), 943-955, DOI: 10.16984/saufenbilder.1279767

Access link

<https://dergipark.org.tr/tr/journal/1115/issue/80257/1279767>

New submission to SAUJS

<http://dergipark.gov.tr/journal/1115/submission/start>

## Post-Ultraviolet-Curing Process Effects on Low-Velocity Impact Response of 3D Printed Polylactic Acid Parts

Tarkan AKDERYA \*<sup>1</sup> 

### Abstract

In this study, polylactic acid (PLA) parts produced with the 3D fused deposition modelling (FDM) technique were cured with ultraviolet irradiation (post-UV-curing) after production, and the low-velocity impact behaviour of the parts was experimentally investigated. Accordingly, PLA parts were subjected to post-UV-curing at 15-, 30-, 45-, and 60-minute periods. The impact behaviour of the specimens produced with production parameters of 200 °C printing temperature, 0.2 mm layer thickness, 50 mm/s printing speed, 100% infill rate, and 45° raster angle was compared with the raw specimens after the post-UV-curing process was applied. As a result of the impact tests, peak force, peak displacement, peak energy, and puncture energy values were obtained from the force-displacement graphs. It has been revealed that the post-UV-curing implementation increases the peak force values of PLA specimens and decreases the displacement values compared to the raw specimens. All specimens' impact behaviour improves with the post-UV-curing process; however, a decreasing trend is entered after 30 min.

**Keywords:** FDM, UV irradiation, polylactic acid, impact response, 3D printing

### 1. INTRODUCTION

Additive manufacturing (AM) technology can be characterised as blending consumables such as resin or filament by fusion or solidification. It is based on forming the design layer by layer using three-dimensional (3D) computer-aided design (CAD) modelling. AM performs manufacturing operations by using 3D computer data containing the object's geometric details or using Standard Tessellation Language (STL) files. AM is preferred for manufacturing small-volume specimens with high design complexity and parts often requiring design orientation. It is a production method in which

parts can be produced by overcoming the limitations of traditional production methods.

In addition, controllable production parameters and active interaction with material properties are also considered among its essential advantages compared to traditional production methods. AM technologies and methods find various application areas, such as automotive, medical, and aerospace, and are increasing in terms of market share. However, it has disadvantages such as geometric accuracy and extended production time [1, 2].

There are many AM methods according to how the layers are placed, the working

\* Corresponding author: [tarkan.akderya@bakircay.edu.tr](mailto:tarkan.akderya@bakircay.edu.tr) (T. AKDERYA)

<sup>1</sup> İzmir Bakırçay University

ORCID: <https://orcid.org/0000-0001-6459-386X>



principle, and the materials used to obtain the part. There are AM methods such as Selective Laser Melting (SLM), Selective Laser Sintering (SLS), and fused deposition modelling (FDM), which work on the principle of melting the consumable material or bringing it to a softer form in order to obtain layers. AM production techniques are also based on curing liquid consumables under certain conditions, such as stereolithography (SLA) [3-5]. In FDM technology, the polymer preferred as a consumable is liquefied and extruded in a semi-molten form via a nozzle into the path obtained from CAD data [6-8]. The part whose design is completed with CAD software is loaded into the slicing software as an STL file and divided into cross sections by determining the production parameters. G-codes are obtained by specifying geometric and manufacturing parameters using the slicing software interface [9, 10]. Introducing the G-codes to the printer system pushes the selected filament towards the heated liquefier and extrudes with a nozzle in semi-melt form. The semi-molten filament is deposited on the path determined as G-code by the slicer software. Within this scope, all paths in a layer specified in the G-code file continue by completing the layer and moving to the next one [11-13].

PLA is relatively economical, biodegradable, has a low melting temperature, does not cause toxic gas emissions, and is environmentally compatible as an amorphous thermoplastic frequently used in the FDM technique [14]. Even though PLA has good mechanical properties, its fields of application are limited owing to its low thermal resistance. Due to its biocompatibility, it is used in various practical application areas, from plastic containers to medical implants [15]. In the biomedical field, it can be injected into the human body with minimal inflammation in applications such as bone fixation devices, drug delivery systems, ureteral and vascular stents, and scaffolds [16-18].

The fibre-to-fibre bond strength and void density of the parts are affected by FDM

printing parameters such as infill rate [19], raster layout [20], layer thickness [21], and printing speed [22]. For this reason, studies are carried out to predict FDM polymeric objects' mechanical response and success and determine which factors affect how much. In some studies, models have been used to predict the effects of printing parameters on the mechanical behaviours of PLA specimens [23-26]. The specimens fabricated by the FDM process are considered composite laminates and analysed using classical lamination theory, limited to linear elastic analysis [15, 27].

When the literature is reviewed, there are studies on how the behaviours of parts fabricated with the FDM technique are affected by the printing parameters, such as production temperature [28, 29], layer thickness [30, 31], production speed [32, 33], and filling rate [34, 35]. Very few studies examine the effects of post-production processes on the characteristics of these parts. Despite the superior properties of PLA, the problems of being unable to be completely stacked or cured due to the material-stacking process of the production with the FDM technique can prevent PLA from being produced with the desired mechanical properties. The UV light wavelength irradiation process is applied in order to reduce the unevenness of bonding success caused by stacking problems between layers, to eliminate the problems of non-uniform curing due to the formation of different cooling zones in part, and to interfere with the material characteristics with a post-production process [36]. In addition, it is known that one of the various surface modification techniques used to modify the characteristic properties of polymer surfaces, such as wettability, antistatic, antimicrobial or dye adsorption, is UV treatment [37].

Studies examining the effects of post-UV-curing, one of the post-production processes, on the mechanical behaviours of the parts fabricated with the FDM technique are relatively new [36, 38]. In the study conducted



by Akderya [38], the 405 nm post-UV-curing process was applied to the PLA parts at different exposure times of 15, 30, 45 and 60 minutes, and then how the flexural and absorption behaviours were affected by the post-UV-curing application was investigated. In this study, the effects of post-UV-curing treatment on the impact behaviour of PLA specimens produced by the FDM technique were investigated. Additionally, the interaction of specimen surface morphology with post-UV-curing was evaluated by SEM analysis.

## 2. MATERIAL AND METHOD

CAD data of the low-velocity impact specimens designed by Solidworks software were converted to an STL file and transferred to Ultimaker Cura slicing software to obtain G-code. The recommended printing parameters of 1.75 mm diameter white PLA filaments supplied by Ultrafuse (BASF 3D, The Netherlands) are as follows: Nozzle temperature between 190-230 °C, bed temperature between 50-70 °C, nozzle diameter of 0.4 mm and above, print speed between 40-80 mm/sec. Creality CR-05 Pro H (Creality 3D Technology Co., Ltd., China) was chosen as the FDM printer, and Esun eBox (Esun Industrial Co., Ltd.) was used throughout the production process at 40 °C to remove moisture from the PLA filaments and preheat. The post-UV-curing application, which is defined as the post-production process of the finished specimens, was carried out using the Anycubic wash and cure 2.0 device (Anycubic Technology Co., Ltd., China).

The nozzle temperature was chosen as 200 °C, nozzle diameter as 0.4 mm, bed temperature as 60 °C, and production speed as 50 mm/sec, taking into account the recommended production parameters of the filament supplier and the printing parameters used in scientific studies. All printing parameters are given in Figure 1. Specimens produced at 200 °C were subjected to post-UV-curing process at intervals of 15 minutes for 60 minutes.

Schematically, the FDM production process and production parameters are given in Figure 2.

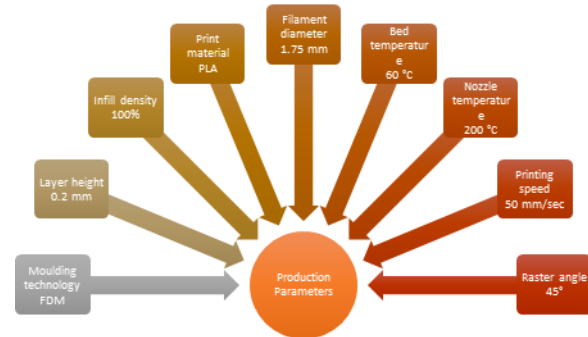


Figure 1 Used printing parameters

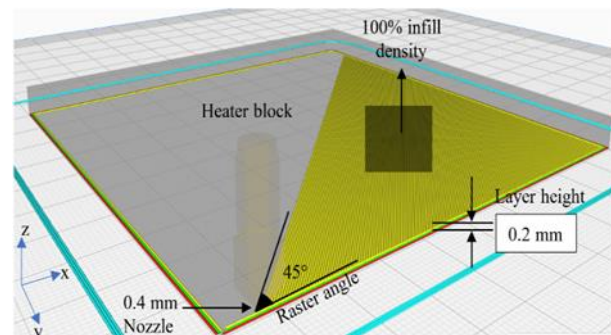


Figure 2 Schematic view of the low-velocity impact specimen's printing parameters

The process of curing PLA parts, whose production is completed with determined FDM parameters, at adjustable durations in a device that performs UV irradiation is described as post-UV-curing. This process is accomplished by applying continuous UV irradiation (405 nm) to the PLA specimen, which is positioned vertically in the middle of a turning platform, by the UV LED panel. The UV-blocking top cover prevents UV irradiation from contacting the naked eye, and the reflector ensures that UV light reaches every part of the specimen equally. The parts of the UV-curing machine are presented in Figure 3.

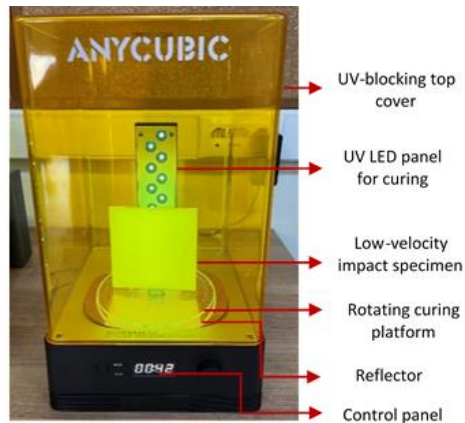


Figure 3 Parts of UV-curing machine

## 2.3. Characterisation

### 2.3.1 Low-velocity impact test

Post-UV-cured and untreated PLA parts were subjected to 20 J impact tests according to ISO 6603 standard [39] using the Instron Ceast (Instron Mechanical Testing Systems Co., Ltd., USA) low-velocity impact test device. Five specimens were tested for each parameter. Impact testing was performed using a 20 mm diameter hemispherical hardened steel impactor. Impact loading on all specimens was performed using a constant energy level of 20 J and was calibrated by adjusting the impactor height to reach the desired energy level. The impact process was adjusted, so the impactor's speed was 2.70 m/s. Equipped with load and displacement transducers, the impactor provides force/displacement graphs by performing the impact operation.

The specimens whose dimensions are given in Figure 4(a) were fixed by placing them on a support with a 76.2 mm inside diameter shown in Figure 4(b). Tests were conducted such that a hemispherical hardened steel impactor with a mass of 5.50 kg would strike through the centre of the specimens. The specimen impacted from its centre is given in Figure 4(c). Impact test parameters are given in Table 1.

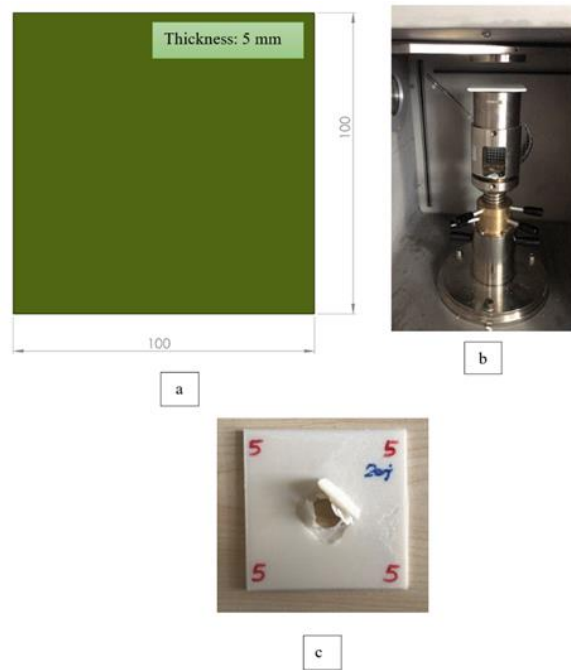


Figure 4 (a) CAD-model of the impact specimen according to ISO 6603 (Dimensions are given in millimetres.), (b) Instron Ceast 9350 impact test machine, and (c) an impacted specimen

Table 1 Impact test parameters

Impact Test Parameters	Unit	Value
Impact energy	J	20
Impact velocity	m/s	2.70
Falling height	mm	371
Additional mass	kg	5.50

This study used force-displacement data from impact tests to reveal the impact response of non-cured (raw) and post-UV-cured specimens. The force-displacement data obtained by the complete puncture of the impact test specimens were used to obtain the absorbed energy levels. Absorbed energy is the transferred energy to the specimen by the impactor upon impact. The absorbed energy was found by integrating the force-displacement graph, while the peak energy was found by integrating the part up to the peak force value in the force-displacement graph. Displacement refers to the distance travelled by the impacted surface of the specimen after the impact loading.

### 2.3.2 Morphological properties

The surface morphology of post-UV-cured and untreated PLA specimens was determined using SEM analysis in accordance with ASTM E986 [40] standard. Micrographs of PLA specimens coated with 5 nm vanadium under vacuum using an ION COATER COXEM device (COXEM Co., Ltd. Korea) before SEM analysis were obtained with Field Emission Scanning Electron Microscope Carl Zeiss 300VP device (Carl Zeiss Co., Ltd., Germany) with 15 kV acceleration voltage.

### 3. RESULTS AND DISCUSSION

The study was conducted to reveal the influence of the post-UV-curing post-production process on the impact behaviour of PLA parts obtained by the FDM process. The force-displacement graphs obtained from the impact tests of the raw and post-UV-cured PLA parts at exposure times of 15, 30, 45, and 60 minutes are given in Figures 5-9, respectively. Characteristically, peak force, peak displacement, peak energy, and puncture energy values obtained for all PLA specimens from force-displacement graphs are given in Figures 10-13, respectively, with their standard deviation values.

If it is mentioned about the determination of characteristic data, the area under the force/displacement graph gives the total energy. Peak energy indicates the shaded area up to the peak force value on this graph. Peak force gives the highest force value that can be read on this graph, while peak displacement expresses the displacement value corresponding to the peak force.

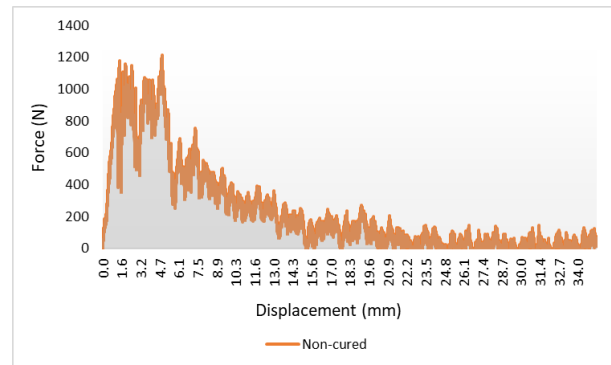


Figure 5 Force – Displacement graphs of non-cured PLA specimens

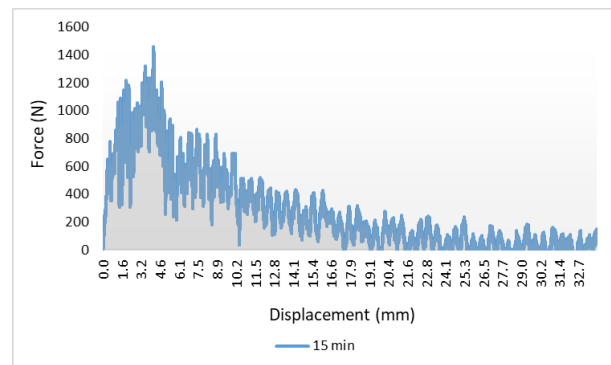


Figure 6 Force – Displacement graph of 15 min-cured PLA specimens

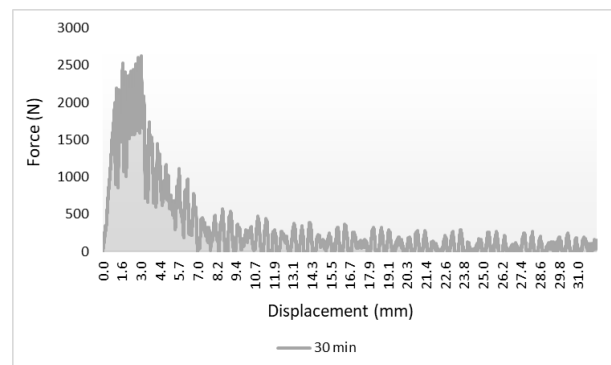


Figure 7 Force – Displacement graph of 30 min-cured PLA specimens

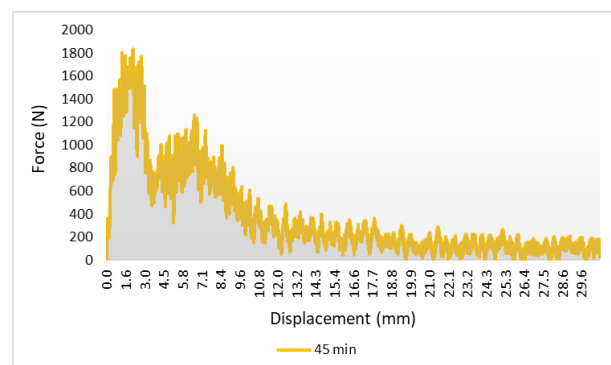


Figure 8 Force – Displacement graph of 45 min-cured PLA specimens

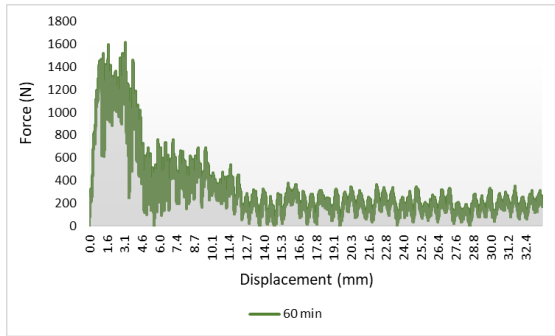


Figure 9 Force – Displacement graph of 60 min-cured PLA specimens

The peak force-duration values of the raw specimens are compared with that of the post-UV-cured specimens in Figure 10. The peak force values of all post-UV-cured ones were higher than the non-cured ones but entered a downward trend after 30 minutes. The highest peak force is observed in PLA specimens exposed to post-UV-curing for 30 min. The peak force value of the 30 min post-UV-cured specimen is 116.35% higher than that of the raw specimens, 80% higher than that of the 15 min post-UV-cured ones, 51.44% higher than that of the 45 min post-UV-cured ones, and 62.45% higher than that of the 60 min post-UV-cured ones.

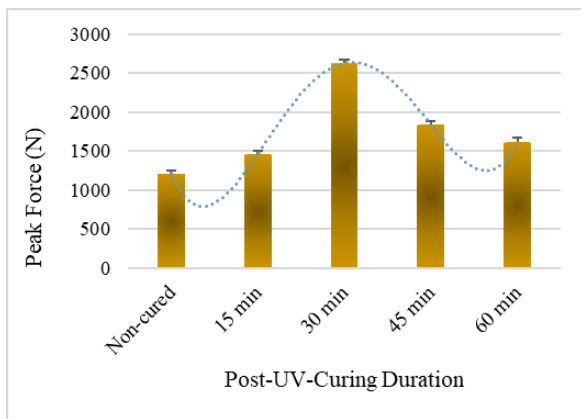


Figure 10 Peak Force – Post-UV-Curing Duration graph of PLA specimens

Considering the peak displacement values (Figure 11), all post-UV-cured specimens have lower values than the raw specimens. The lowest value is 2.14 mm in the specimens exposed to post-UV-curing for 45 minutes. The peak displacement value of the 30 min post-UV-cured specimens with the highest peak force is 36.44% lower than that of the

raw specimens. Compared to the non-cured ones, post-UV-cured ones have higher peak force and lower peak displacement. Post-UV-curing implementation increases the stiffness of the specimens, resulting in the specimens being punctured at a higher force and a lower displacement value [41, 42].

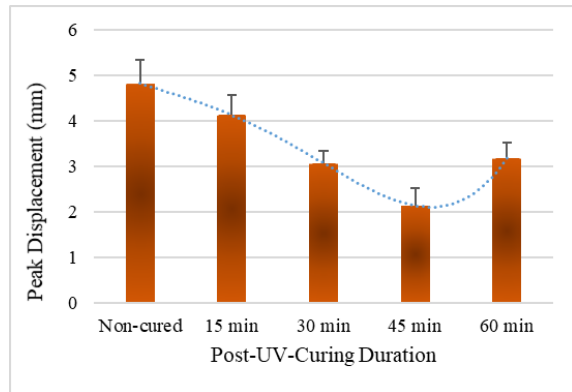


Figure 11 Peak Displacement – Post-UV-Curing Duration graph of PLA specimens

The peak energy graph, which expresses the energy required up to the highest peak force value recorded during the impact tests of the raw and post-UV-cured specimens, is given in Figure 12. When the peak energy values are examined, the specimen cured for 30 minutes has the highest value with 4.76 J, and all other cured specimens have lower values than the raw specimens. It is found that the specimens subjected to post-UV-curing for 30 minutes are 26.93% higher than the raw ones, 47.37% higher than the 15-min post-UV-cured ones, 85.94% higher than the 45-min post-UV-cured ones, and 41.67% higher than the 60-min post-UV-cured ones.

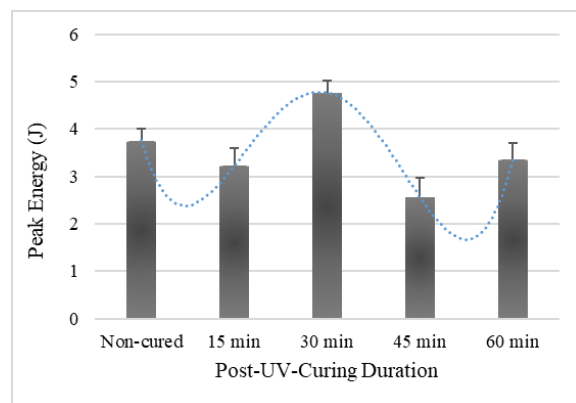


Figure 12 Peak Energy – Post-UV-Curing Duration graph of PLA specimens

During the low-velocity impact tests, the puncture energies required by the impactor to completely pierce the specimen are given in Figure 13. Puncture energy refers to the sum of the energy spent by the impactor during its movement from the moment it contacts the specimen to it exits the lower surface of the specimen. Accordingly, similar to the peak force graph, the highest puncture energy value belongs to the 30-min post-UV-cured specimens. The 30-min post-UV-cured specimen with a puncture energy value of 5.26 J is 24.35% higher than the raw specimen with a puncture energy value of 4.23 J.

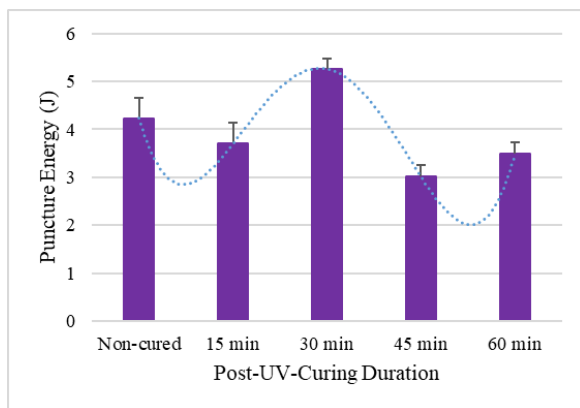


Figure 13 Puncture Energy – Post-UV-Curing Duration graph of PLA specimens

In the study of Hsueh et al. [36], the post-UV-curing process with a wavelength of 425 nm was applied for 60 minutes to PLA parts produced with the FDM technique. The findings of this study are consistent with the study conducted by Hsueh et al. [36], and the 60-min post-UV-curing process causes a decrease in the mechanical properties of PLA parts. In the study by Akderya [38], the effects of the post-UV-curing process applied between 15-60 minutes on the flexural and absorptive properties of PLA parts were investigated. In accordance with this study, it is seen that the mechanical properties of the specimens applied 30-min post-UV-curing have the highest value.

After UV irradiation, alterations in the impact behaviours of the specimens are observed, and 30 minutes post-UV-cured specimens have the highest peak force and peak energy values. The increase in the impact properties of the

material is not continuous with the increase of the post-UV-curing exposure time. The impact properties decrease after a specific exposure time (30 minutes). This is due to the photo-oxidative degradation phenomenon that occurs after a certain exposure time of the post-UV-curing process applied to PLA impact specimens. The photo-oxidative degradation process is the most effective phenomenon that can cause degradation in the structure of polymeric substrates under certain ambient conditions by exposure to UV irradiation [43, 44]. The degradation mechanism due to the phenomenon's nature has caused the molecular chains to begin to break [45, 46]. The shorter chain structure resulting from the photo-oxidative degradation process starts after a certain period, depending on the duration, nature, and other parameters of the modifying agent, in this case, UV irradiation. The photo-oxidative degradation process leads to the deterioration of the physicochemical properties of the polymers after this period [47-49]. As a result of the emergence of the photo-oxidative degradation process with the effect of UV-irradiation, an irregular, uneven, and variable adhesion success has emerged between the printing fibres. The biodegradable structure of PLA is triggered by the emergence of the photo-oxidative degradation process, and the phenomenon adversely affects the adhesion success of printing fibres that form the material structure [38, 50]. In addition, the specimens exposed to the post-UV-curing process for 30 minutes have the highest peak force and energy values. It can be said that the reason for this is that the post-UV curing process applied at certain critical times forms a stronger adhesion between the printing fibres, especially starting from the outermost surfaces of the specimens [36, 38].

The printing fibre diameters of the raw, 30- and 60-min post-UV-cured specimens were measured and given in Figure 14. Accordingly, printing fibre diameters of the raw and 60 min post-UV-cured ones, which

are significant on the outermost surface, are more extensive than that of the 30 min post-UV-cured specimen. The post-UV-curing process has caused the diameter of the printing fibres to decrease. The molecular chains on the outermost surface of the material have been rearranged to be tighter by applying the post-UV-curing process. Therefore, a new order is formed to shorten the distance between the molecular chains [36, 51]. Modifying inert polymer surfaces is achieved by increasing the surface energy by photo-oxidised polar groups by applying UV irradiation. In this way, it can be said that the bonding ability of the fibres to the layer surfaces increases thanks to the increased surface energy [52, 53]. When the diameter of the printing fibres of the 30-min post-UV-cured specimens, which have the highest impact resistance, is examined, it is seen that the diameter of the printing fibres has the smallest value compared to the raw and 60-minute post-UV-cured ones in accordance with Figure 14. With the application of 30-min post-UV-curing, the ability of the printing fibres to adhere to surfaces increases, and the diameter of the fibres that adhere better to the surface becomes smaller. Accordingly, printing fibres that adhere better to the surface due to the increase in surface energy cause a more rigid material surface to be formed, and it is seen that displacement values decrease due to the increased stiffness value.

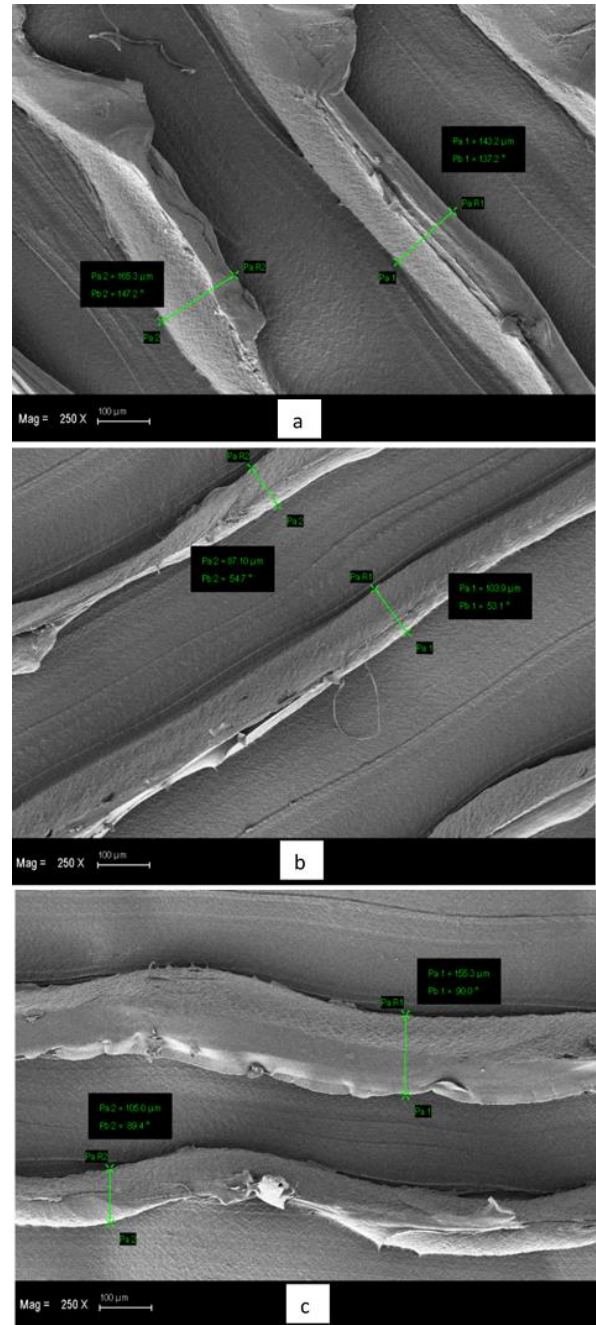


Figure 14 Diameters for the print fibres of (a) raw, (b) 30 min, and (c) 60 min post-UV-cured specimens

#### 4. CONCLUSION

This experimental study investigated the effect of the post-UV-curing process applied at different durations on the impact behaviour of PLA specimens. Accordingly, the findings are itemised below.

- When the peak force values of the post-UV-cured specimens are compared with

the raw specimens, it is found that post-UV-curing increases the peak force value of PLA specimens for all exposure times.

- It is observed that the post-UV-cured specimens have lower peak displacement values compared to the raw specimens.
- The surface energy increased by post-UV-curing application causes the fibres to develop better adhesion to the surface, and it has been revealed that the highest peak energy values are in the specimens with 30-min post-UV-cured ones.
- When the puncture energy values, which are defined as the energy value required from the first contact of the impactor on the top surface of the specimen until it pierces the bottom layer, are examined, it is seen that the 30-min post-UV-cured ones have the highest value.
- Post-UV-curing application to PLA specimens at different durations increases the impact strength and stiffness values. The impact strength ability of the specimens increases when the peak force values are taken into account, and the stiffness values increase when the peak displacement values are taken into account. It has been revealed that the stiffness value, which is described as the resistance of specimens against deformation in response to the applied force, increases.

#### ***Funding***

The author received no financial support for the research, authorship, and/or publication of this paper.

#### ***The Declaration of Conflict of Interest/ Common Interest***

No conflict of interest or common interest has been declared by the author.

#### ***The Declaration of Ethics Committee Approval***

The author declares that this document does not require an ethics committee approval or any special permission.

#### ***The Declaration of Research and Publication Ethics***

The author of the paper declares that he complies with the scientific, ethical, and quotation rules of SAUJS in all processes of the paper and that he does not make any falsification on the data collected. In addition, he declares that Sakarya University Journal of Science and its editorial board have no responsibility for any ethical violations that may be encountered and that this study has not been evaluated in any academic publication environment other than Sakarya University Journal of Science.

## **REFERENCES**

- [1] S. E. Zeltmann, N. Gupta, N. G. Tsoutsos, M. Maniatakos, J. Rajendran, R. Karri, "Manufacturing and Security Challenges in 3D Printing," *The Journal of The Minerals, Metals & Materials Society*, vol. 68, no. 7, pp. 1872-1881, 2016.
- [2] I. Gibson, D. W. Rosen, B. Stucker, *Additive manufacturing technologies: Rapid prototyping to direct digital manufacturing: Second Edition*. Springer Inc., 2010.
- [3] N. Hopkinson, P. Dickens, "Analysis of rapid manufacturing - Using layer manufacturing processes for production," *Proceedings of the Institution of Mechanical Engineers, Part C: Journal of Mechanical Engineering Science*, vol. 217, no. 1, pp. 31-39, 2003.
- [4] R. Hague, I. Campbell, P. Dickens, "Implications on design of rapid manufacturing," *Proceedings of the Institution of Mechanical Engineers, Part C: Journal of Mechanical*

- Engineering Science, vol. 217, no. 1, pp. 25-30, 2003.
- [5] H. Bikas, P. Stavropoulos, G. Chryssolouris, "Additive manufacturing methods and modeling approaches: A critical review," *The International Journal of Advanced Manufacturing Technology*, vol. 83, pp. 389-405, 2016.
- [6] D. Hodzic, A. Pandzic, "Influence of carbon fibers on mechanical properties of materials in fdm technology," in *Annals of DAAAM and Proceedings of the International DAAAM Symposium*, Vienna, Austria, 2019, pp. 334-342.
- [7] T. Yao, K. Zhang, Z. Deng, J. Ye, "A novel generalised stress invariant-based strength model for inter-layer failure of FFF 3D printing PLA material," *Materials & Design*, vol. 193, 2020.
- [8] K. S. Boparai, R. Singh, H. Singh, "Development of rapid tooling using fused deposition modeling: A review," *Rapid Prototyping Journal*, vol. 22, no. 2, pp. 281-299, 2016.
- [9] D. Hodzic, A. Pandzic, I. Hajro, P. Tasic, "Strain rate influence on mechanical characteristics of FDM 3D printed materials," in *Annals of DAAAM and Proceedings of the International DAAAM Symposium*, Vienna, Austria, 2020, pp. 168-175.
- [10] R. B. Kristiawan, F. Imaduddin, D. Ariawan, Ubaidillah, Z. Arifin, "A review on the fused deposition modeling (FDM) 3D printing: Filament processing, materials, and printing parameters," *Open Engineering*, vol. 11, no. 1., pp. 639-649, 2021.
- [11] J. Edgar, S. Tint, "Additive Manufacturing Technologies: 3D Printing, Rapid Prototyping, and Direct Digital Manufacturing," *Johnson Matthey Technology Review*, vol. 59, no. 3, pp. 193-198, 2015.
- [12] A. Gebhardt, *Understanding Additive Manufacturing*. Carl Hanser Verlag GmbH & Co., 2011.
- [13] A. R. Zekavat, A. Jansson, J. Larsson, L. Pejryd, "Investigating the effect of fabrication temperature on mechanical properties of fused deposition modeling parts using X-ray computed tomography," *The International Journal of Advanced Manufacturing Technology*, vol. 100, pp. 287-296, 2019.
- [14] L. T. Sin, B. S. Tuen, "Overview of Biodegradable Polymers and Polylactic acid," in *Polylactic Acid*, Second Edition, Ed. L. T. Sin, William Andrew Publishing, 2019, pp. 1-52.
- [15] O. Volgin, I. Shishkovsky, "Material modelling of FDM printed PLA part," *Engineering Solid Mechanics*, vol. 9, no. 2, pp. 153-160, 2021.
- [16] R. P. Pawar, S. U. Tekale, S. U. Shisodia, J. T. Totre, A. J. Domb, "Biomedical applications of polylactic acid," *Recent Patents on Regenerative Medicine*, vol. 4, no. 1, pp. 40-51, 2014.
- [17] E. M. Elmowafy, M. Tiboni, M. E. Soliman, "Biocompatibility, biodegradation and biomedical applications of polylactic acid/poly(lactic-co-glycolic acid) micro and nanoparticles," *Journal of Pharmaceutical Investigation*, vol. 49, no. 4., pp. 347-380, 2019.
- [18] F. S. Senatov, K. V. Niaza, M. Y. Zadorozhnyy, A. V. Maksimkin, S. D. Kaloshkin, Y. Z. Estrin, "Mechanical properties and shape memory effect of 3D-printed PLA-based porous scaffolds," *Journal of the Mechanical*



- Behavior of Biomedical Materials, vol. 57, pp. 139-148, 2016.
- [19] J. Villacres, D. Nobes, C. Ayranci, "Additive manufacturing of shape memory polymers: effects of print orientation and infill percentage on mechanical properties," *Rapid Prototyping Journal*, vol. 24, no. 4, pp. 744-751, 2018.
- [20] J. Kiendl, C. Gao, "Controlling toughness and strength of FDM 3D-printed PLA components through the raster layout," *Composites Part B: Engineering*, vol. 180, 2020.
- [21] L. Fontana, P. Minetola, L. Iuliano, S. Rifuggiato, M. S. Khandpur, V. Stiuso, "An investigation of the influence of 3d printing parameters on the tensile strength of PLA material," *Materials Today Proceedings*, vol. 57, no. 2, pp. 657-663, 2022.
- [22] A. A. Ansari, M. Kamil, "Effect of print speed and extrusion temperature on properties of 3D printed PLA using fused deposition modeling process," *Materials Today Proceedings*, vol. 45, no. 6, pp. 5462-5468, 2021.
- [23] S. R. Rajpurohit, H. K. Dave, K. P. Rajurkar, "Prediction of tensile strength of fused deposition modeling (FDM) printed PLA using classic laminate theory," *Engineering Solid Mechanics*, vol. 10, no. 1, pp. 13-24, 2022.
- [24] T. Yao, Z. Deng, K. Zhang, S. Li, "A method to predict the ultimate tensile strength of 3D printing polylactic acid (PLA) materials with different printing orientations," *Composites Part B: Engineering*, vol. 163, pp. 393-402, 2019.
- [25] Y. Zhao, Y. Chen, Y. Zhou, "Novel mechanical models of tensile strength and elastic property of FDM AM PLA materials: Experimental and theoretical analyses," *Materials & Design*, vol. 181, 2019.
- [26] T. Akderya, U. Özmen, B. O. Baba, "A micromechanical approach to elastic modulus of long-term aged chicken feather fibre/polylactic acid biocomposites," *International Journal of Materials Research*, vol. 113, no. 9, pp. 759-775, 2022.
- [27] M. Somireddy, A. Czekanski, C. V. Singh, "Development of constitutive material model of 3D printed structure via FDM," *Materials Today Communications*, vol. 15, pp. 143-152, 2018.
- [28] J. B. Soares, J. Finamor, F. P. Silva, L. Roldo, L. H. Cândido, "Analysis of the influence of polylactic acid (PLA) colour on FDM 3D printing temperature and part finishing," *Rapid Prototyping Journal*, vol. 24, no. 8, pp. 1305-1316, 2018.
- [29] S. Wang, Y. Ma, Z. Deng, S. Zhang, J. Cai, "Effects of fused deposition modeling process parameters on tensile, dynamic mechanical properties of 3D printed polylactic acid materials," *Polymer Testing*, vol. 86, 2020.
- [30] E. Carlier, "Investigation of the parameters used in fused deposition modeling of polylactic acid to optimise 3D printing sessions," *International Journal of Pharmaceutics*, vol. 565, pp. 367-377, 2019.
- [31] M. Algarni, S. Ghazali, "Comparative study of the sensitivity of pla, abs, peek, and petg's mechanical properties to fdm printing process parameters," *Crystals*, vol. 11, no. 8, pp. 1-21, 2021.
- [32] Ł. Miazio, "Impact of Print Speed on Strength of Samples Printed in FDM Technology," *Agricultural*

- Engineering, vol. 23, no. 2, pp. 33-38, 2019.
- [33] R. Hashemi Sanatgar, C. Campagne, V. Nierstrasz, "Investigation of the adhesion properties of direct 3D printing of polymers and nanocomposites on textiles: Effect of FDM printing process parameters," *Applied Surface Science*, vol. 403, pp. 551-563, 2017.
- [34] Z. Yu, "Study on Effects of FDM 3D Printing Parameters on Mechanical Properties of Polylactic Acid," in *IOP Conference Series: Materials Science and Engineering*, 2019, vol. 688, no. 3, pp. 1-5.
- [35] J. Maszybrocka, M. Dworak, G. Nowakowska, P. Osak, B. Łosiewicz, "The Influence of the Gradient Infill of PLA Samples Produced with the FDM Technique on Their Mechanical Properties," *Materials (Basel)*, vol. 15, no. 4, 2022.
- [36] M. H. Hsueh, "Effects of printing temperature and filling percentage on the mechanical behavior of fused deposition molding technology components for 3d printing," *Polymers (Basel)*, vol. 13, no. 17, 2021.
- [37] G. H. Koo, J. Jang, "Surface Modification of Polylactic acid by UV/Ozone Irradiation," *Fibers and Polymers*, vol. 9, no. 6, pp. 674-678.
- [38] T. Akderya, "Effects of Post-UV-Curing on the Flexural and Absorptive Behaviour of FDM-3D-Printed Polylactic acid Parts," *Polymers (Basel)*, vol. 15, no. 2, 2023.
- [39] International standard organisation, "ISO 6603, Determination of puncture impact behaviour of rigid plastics," 61010-1 © Iec2001, vol. 2014, 2014.
- [40] ASTM, "ASTM E986-04 Standard Practice for Scanning Electron Microscope Beam Size Characterization," ASTM Copyright., vol. 03. 1997.
- [41] B. O. Baba, "Curved sandwich composites with layer-wise graded cores under impact loads," *Composite Structures*, vol. 159, pp. 1-11, 2017.
- [42] M. V. Podzorova, Y. V. Tertyshnaya, P. V. Pantyukhov, A. A. Popov, S. G. Nikolaeva, "Influence of ultraviolet on polylactide degradation," in *AIP Conference Proceedings*, 2017, vol. 1909.
- [43] L. Zaidi, M. Kaci, S. Bruzaud, A. Bourmaud, Y. Grohens, "Effect of natural weather on the structure and properties of polylactide/Cloisite 30B nanocomposites," *Polymer Degradation and Stability*, vol. 95, no. 9, pp. 1751-1758, 2010.
- [44] T. O. Kumanayaka, R. Parthasarathy, M. Jollands, "Accelerating effect of montmorillonite on oxidative degradation of polyethylene nanocomposites," *Polymer Degradation and Stability*, vol. 95, no. 4, pp. 672-676, 2010.
- [45] C. Kaynak, A. R. Erdogan, "Mechanical and thermal properties of polylactide/talc microcomposites: Before and after accelerated weathering," *Polymers and Advanced Technologies*, vol. 27, no. 6, pp. 812-822, 2016.
- [46] A. Copinet, C. Bertrand, S. Govindin, V. Coma, Y. Couturier, "Effects of ultraviolet light (315 nm), temperature and relative humidity on the degradation of polylactic acid plastic films," *Chemosphere*, vol. 55, no. 5, pp. 763-773, 2004.
- [47] E. Olewnik-Kruszkowska, "Effect of UV irradiation on thermal properties of

- nanocomposites based on polylactide," *Journal of Thermal Analysis and Calorimetry*, vol. 119, no. 1, pp. 219-228, 2015.
- [48] S. Bocchini, K. Fukushima, A. Di Blasio, A. Fina, A. Frache, F. Geobaldo, "Polylactic acid and polylactic acid-based nanocomposite photooxidation," *Biomacromolecules*, vol. 11, no. 11, pp. 2919-2926, 2010.
- [49] L. Botta, N. T. Dintcheva, F. P. La Mantia, "The role of organoclay and matrix type in photo-oxidation of polyolefin/clay nanocomposite films," *Polymer Degradation and Stability*, vol. 94, no. 4, pp. 712-718, 2009.
- [50] M. V. Podzorova, Y. V. Tertyshnaya, D. M. Ziborov, M. Poletto, "Damage of polymer blends polylactide-polyethylene under the effect of ultraviolet irradiation," in *AIP Conference Proceedings*, 2020, vol. 2310.
- [51] J. L. Liu, R. Xia, "A unified analysis of a micro-beam, droplet and CNT ring adhered on a substrate: Calculation of variation with movable boundaries," *Acta Mechanica Sinica*, vol. 29, no. 1, pp. 62-72, 2013.
- [52] J. Jang, "Textile Finishing Technology Using Ultraviolet Curing," *Fiber Technology Industry*, vol. 7, pp. 303-321, 2001.
- [53] K. Bazaka, J. Ahmad, M. Oelgemöller, A. Uddin, M. V. Jacob, "Photostability of plasma polymerised  $\gamma$ -terpinene thin films for encapsulation of OPV," *Scientific Reports*, vol. 7, 45599, 2017.



SAKARYA ÜNİVERSİTESİ

# FEN BİLİMLERİ ENSTİTÜSÜ DERGİSİ

Sakarya University Journal of Science  
SAUJS

ISSN 1301-4048 | e-ISSN 2147-835X | Period Bimonthly | Founded: 1997 | Publisher Sakarya University |  
<http://www.saujs.sakarya.edu.tr/>

Title: On the Properties of  $r$ -Circulant Matrices Involving Generalized Fermat Numbers

Authors: Bahar KULOĞLU, Engin ESER, Engin ÖZKAN

Received: 2023-04-10 00:00:00

Accepted: 2023-06-13 00:00:00

Article Type: Research Article

Volume: 27

Issue: 5

Month: October

Year: 2023

Pages: 956-964

How to cite

Bahar KULOĞLU, Engin ESER, Engin ÖZKAN; (2023), On the Properties of  $r$ -Circulant Matrices Involving Generalized Fermat Numbers. Sakarya University Journal of Science, 27(5), 956-964, DOI: 10.16984/sofenbilder.1280572

Access link

<https://dergipark.org.tr/tr/journal/1115/issue/80257/1280572>

New submission to SAUJS

<http://dergipark.gov.tr/journal/1115/submission/start>

## On the Properties of $r$ -Circulant Matrices Involving Generalized Fermat Numbers

Bahar KULOĞLU<sup>\*1</sup>, Engin ESER<sup>2</sup>, Engin ÖZKAN<sup>3</sup>

### Abstract

$r$ -circulant matrices have applied in numerical computation, signal processing, coding theory, etc. In this study, our main goal is to investigate the  $r$ -circulant matrices of generalized Fermat numbers which are shown by  $GR_{a,b,n} = a^{2^n} + b^{2^n}$ . We obtain the eigenvalues, determinants, sum identity of matrices. Also we find upper and lower bounds for the spectral norms of generalized Fermat  $r$ -circulant matrices. Beside these, we present  $GR_{a,b,r}^*$  matrix in the form of the Hadamard product of two matrices as  $GR_{a,b,r}^* = A \cdot B$ . In addition, we get the right and skew-right circulant matrices for  $r = 1$  and  $r = -1$ . Finally, we examine their different norms (Spectral and Euclidean) and limits for matrix norms.

**Keywords:** Fermat number, generalized Fermat numbers, norm (spectral and Euclidean), eigenvalues, circulant matrices

### 1. INTRODUCTION

Special numbers were created by grouping prime numbers within themselves. The best known of these are Pierre de Fermat and Marin Mersenne. Fermat numbers included pseudoprimes. First, Fermat conjectured that all numbers produced by  $2^k + 1$  ( $k$  is a nonnegative integer) are prime numbers ( $k$  must be the power of 2).

It can be easily seen that the first 5 numbers are prime, but when it comes to the 6th number there is a problem. Later, Euler

proved that this number has factors. So, it was a composite number. Fermat had made a calculation error. Now an open question: Are there any other numbers like this? Mersenne numbers in the form  $2^k - 1$  were studied in antiquity because of their connection with perfect numbers. Euclid-Euler theorem gives this connection.

Later, Francois Proth studied Fermat numbers. Proth gave a generalized version of Fermat numbers in the form  $k2^n + 1$  where  $2^n > k$  for  $n, k \in \mathbb{Z}^+$  and  $k$  is an odd number. The Proth numbers are also known

\*Corresponding author: bahar\_kuloglu@hotmail.com (B. KULOĞLU)

<sup>1</sup>Hatuniye Hatuniye Vocational and Technical Anatolian High School, Ministry of Education, Mardin, Türkiye

<sup>2</sup>Graduate School of Natural and Applied Sciences, Erzincan Binali Yıldırım University, Erzincan, Türkiye

<sup>3</sup>Department of Mathematics, Faculty of Arts and Sciences, Erzincan Binali Yıldırım University, Erzincan, Türkiye

E-mail: engineser1978@gmail.com, eozkan@erzincan.edu.tr

ORCID: <https://orcid.org/0000-0001-7624-8270>, <https://orcid.org/0000-0001-5965-4162>, <https://orcid.org/0000-0002-4188-7248>



as  $k$ -Fermat numbers [1]. From this, it can be easily seen that the general forms of Proth numbers without any restrictions are  $k$ -Fermat numbers. The first terms of these numbers are as follows:

3, 5, 13, 17, 41, 97, 113, 193, 241, 257, 353, 449, 577, 641, 673, 769, 929, 1153, 1217, 1409, 1601, 2113, 2689, 2753, 3137, 3329, 3457, 4481, 4993, 6529, 7297, 7681, 7937, 9473, 9601, 9857

(Proth numbers are referenced in the On-Line Encyclopedia of Integer Sequences in OEIS as: A080076 [2])

Generalized Fermat numbers [3], denoted by  $\{GR_{a,b,n}\}$  is defined by

$$GR_{a,b,n} = a^{2^n} + b^{2^n}, \tag{1}$$

where  $a$  and  $b$  are any relatively prime integers,  $a > b > 0, a \geq 2, n \geq 0$ . The first terms of these numbers as follow:

$n$	0	1	2	3	...
$GR_{a,b,n}$	$a + b$	$a^2 + b^2$	$a^4 + b^4$	$a^8 + b^8$	...

These matrices are shown by  $C_r$ . Their inverse, conjugate, transposes, sums, and multiplications have been calculated in [4].

The algebraic properties of these matrices have been investigated in [5, 6]. For any  $r$  complex number except zero, we can define those matrices. We can analyze its eigenvalues, Euclidean norm, spectral norm, determinants and inverse.  $C_r$  is determined by its first-row element and  $r$ . Given  $r = +1$  and  $r = -1$  in recurrence relation, we obtain its eigenvalues and determinant for right and skew right circulant matrices.

Circulant matrices and  $r$ -circulant matrices including such as Fibonacci, Pell, Pell-Lucas numbers have been great interest. In several studies, eigenvalues, determinants, norms, bounds and inverses for these matrices are

found. For instance, Bueno [7] presented eigenvalues and the determinant of the right circulant matrices with Pell numbers and Pell-Lucas numbers.

Solak [8] presented norms for circulant matrices including Fermant and Mersenne numbers. S.-Q., Shen et al. [9, 10] presented the bounds for  $r$ -circulant matrices with Fibonacci and Lucas numbers and also presented the spectral norms with  $k$ -Fibonacci and  $k$ -Lucas numbers. Zheng et al. [11] showed the exact inverse of circulant matrices with Fermat and Mersenne numbers. Bozkurt [12] solved the determinants of these matrices using matrix decomposition. Kumari et al. studied on the properties of the  $r$ -circulant matrices involving Mersenne and Fermat numbers [13].

Marin has also discussed examples of concrete usage areas of studies similar to those in [14, 15]. Pucanovic et al. by taking the  $r$ -circulant matrix and Chebyshev polynomials as the subject, handled the inputs of the  $r$ -circulant matrices by constructing them from Chebyshev polynomials [16]. In this paper, we study  $r$ -circulant matrices with generalized Fermat numbers.

**Lemma 1.1** [17, 18] Let  $X = (x_{ij})$  be a matrix.

The Frobenius or Euclidean norm of  $X$  is defined as

$$\|X\|_{E=F} = \sqrt{\sum_{i=1}^a \sum_{j=1}^b |x_{ij}|^2}.$$

The column norm of  $X$  is defined as

$$\|X\|_1 = \max_{1 \leq j \leq n} \sum_{i=1}^n |x_{ij}|.$$

The row norm of  $X$  is defined as

$$\|X\|_\infty = \max_{1 \leq j \leq m} \sum_{i=1}^n |x_{ij}|.$$

The spectral norm of a matrix  $X$  defined as

$$\|X\|_2 = \sqrt{\gamma(X^*X)} = \mu_{max}(X).$$

where  $\gamma(X^*X)$  denote the eigenvalues of  $(X^*X)$  and  $X^*$  is the conjugate transpose of  $X$  and  $\mu_{max}(X)$  is the largest singular value of  $X$ .

Matrix  $X$  has the relationship between the norm values given below:

$$\frac{1}{\sqrt{n}} \|X\|_F \leq \|X\|_2 \leq \|X\|_F \tag{2}$$

**Lemma 1.2** [13] For  $A = [a_{ij}] \in \mathbb{M}_{m,n}(\mathbb{C})$ ,  $B = [b_{ij}] \in \mathbb{M}_{m,n}(\mathbb{C})$ , If  $C$  is the Hadamard product of  $A$  and  $B$ , then we get

$$\|C\|_2 \leq m(A)n(B) \tag{3}$$

where  $m(A) = \max_{1 \leq i \leq m} \sqrt{\sum_{j=1}^n |a_{ij}|^2}$  and  $n(B) = \max_{1 \leq j \leq n} \sqrt{\sum_{i=1}^m |b_{ij}|^2}$ .

**Definition 1.3** [19] For  $r \in \mathbb{C} - \{0\}$ , a matrix  $C_r$  is said to be  $r$ -circulant matrix if it is of the form and it is denoted by  $C_r = Circ(r; \vec{c})$ , where  $\vec{c} = (c_0, c_1, \dots, c_{n-1})$  is the first row vector. For  $r = 1$  and  $r = -1$ , we get the right and skew-right circulant matrices, respectively

$$C = \begin{bmatrix} c_0 & c_1 & c_2 & \dots & c_{n-2} & c_{n-1} \\ rc_{n-1} & c_0 & c_1 & \dots & c_{n-3} & c_{n-2} \\ \vdots & \vdots & \vdots & \ddots & \vdots & \vdots \\ rc_2 & rc_3 & rc_4 & \dots & c_0 & c_1 \\ rc_1 & rc_2 & rc_3 & \dots & rc_{n1} & c_0 \end{bmatrix}$$

**Lemma 1.4** [19] Let  $C_r$  be  $r$ -circulant matrices then its eigenvalues

$$\mu_i = \sum_{j=0}^{n-1} c_j (pw^{-i})^j, \quad i = 0, 1, 2, \dots, n-1$$

where  $w$  is the  $n$ th root of unity and  $p$  is the  $n$ th root of  $r$ .

**Lemma 1.5** [13] The Euclidean norm of  $r$ -circulant matrix  $C_r$  is given by

$$\|C_r\|_E = \sqrt{\sum_{j=0}^{n-1} |c_j|^2 [n - j(1 - |r|^2)]} \tag{4}$$

**Lemma 1.6** [7] For any  $a$  and  $b$ , we get

$$\prod_{i=0}^{n-1} (a - bp_i w_{-i}) = a^n - rb^n \tag{5}$$

where  $w$  is the  $n$ -th root of unity and  $p$  is the  $n$ -th root of  $r$ .

**Lemma 1.7** [20] Determinant of the circulant matrix  $C_n$  is

$$|C_n| = \prod_{i=0}^{n-1} \left( \sum_{j=0}^{n-1} c_j (t_l^j) \right)$$

where the entry  $\{i, j\}$  is equal to the entry  $\{i + l, j + l\}$  for  $l = 1, 2, \dots$ ,  $t_l = e^{\frac{2\pi l}{n}}$  are the  $n$ -th roots of unity and  $p_i$  are  $n$ th root of  $r$ . Using above lemmas, we can calculate the eigenvalues, the determinant, Euclidean norms, bounds for spectral norms of  $r$ -circulant matrices involving generalized Fermat numbers with arithmetic indices. We present many new identities for generalized Fermat numbers. In addition,  $r$ -circulant studies for Fermat and  $k$ -Fermat are handled in the most general format depending on the numbers  $a, b$  and  $n$  on these number sequences.

## 2. GENERALIZED FERMAT $r$ -CIRCULANT MATRIX

Let  $u$  and  $v$  be non-negative integers and  $r \in \mathbb{C} - \{0\}$  and show the Generalized Fermat  $r$ -circulant matrices with  $GR_{a,b,r}$ .

**Definition 2.1** Generalized Fermat  $r$ -circulant matrix is defined as  $GR_{a,b,r} = Circ(a, b, r; \vec{c})$  where first row vector is

$$\vec{c} = (GR_{a,b,u}, GR_{a,b,u+v}, GR_{a,b,u+2v}, \dots, GR_{a,b,u+(n-1)v})$$

ie., matrix of the form:

$$GR_{a,b,r} = \begin{bmatrix} GR_{a,b,u} & GR_{a,b,u+v} & \dots & GR_{a,b,u+(n-1)v} \\ rGR_{a,b,u+(n-1)v} & GR_{a,b,u} & \dots & GR_{a,b,u+(n-2)v} \\ \vdots & \vdots & \ddots & \vdots \\ rGR_{a,b,u+2v} & rGR_{a,b,u+3v} & \dots & GR_{a,b,u+v} \\ rGR_{a,b,u+v} & rGR_{a,b,u+2v} & \dots & GR_{a,b,u} \end{bmatrix}$$

Let's show eigenvalues of  $GR_{a,b,r}$  with  $\lambda_i(GR_{a,b,r})$ .

**Theorem 2.2** The eigenvalues of the generalized Fermat  $r$ -circulant matrix  $GR_{a,b,r}$  are as follows.

$$\lambda_i(GR_{a,b,r}) = \sum_{j=0}^{n-1} (a^{2^{u+jv}} + b^{2^{u+jv}}) (pw^{-i})^j$$

**Proof.** If we substitute  $a^{2^{u+jv}} + b^{2^{u+jv}}$  for  $c_j$  in Lemma 1.4, the proof ends.

**Corollary 2.3**

$$\sum_{j=0}^{n-1} (a^{2^{u+jv}} + b^{2^{u+jv}}) (pw^{-i})^j = \sum_{j=0}^{n-1} \sqrt[n]{r^j(1)^{-ji}} \left( (a^{2^u})^{(2^v)^j} + (b^{2^u})^{(2^v)^j} \right)$$

**Proof.** Since  $w$  is the  $n$ -th root of unity and  $p$  is the  $n$ -th root of  $r$ , we get  $(pw^{-i})^n = p^n(w^{-i})^n = r$ .

$$\begin{aligned} \sum_{j=0}^{n-1} (a^{2^{u+jv}} + b^{2^{u+jv}}) (pw^{-i})^j &= \left( (a^{2^u})^{(2^v)^0} + (b^{2^u})^{(2^v)^0} \right) \\ &+ pw^{-i} \left( (a^{2^u})^{(2^v)} + (b^{2^u})^{(2^v)} \right) \\ &+ (b^{2^u})^{(2^v)} \\ &+ (pw^{-i})^2 \left( (a^{2^u})^{(2^v)^2} + (b^{2^u})^{(2^v)^2} \right) + \dots \end{aligned}$$

$$\begin{aligned} &+ (pw^{-i})^{n-2} \left( (a^{2^u})^{(2^v)^{n-2}} + (b^{2^u})^{(2^v)^{n-2}} \right) \\ &+ (pw^{-i})^{n-1} \left( (a^{2^u})^{(2^v)^{n-1}} + (b^{2^u})^{(2^v)^{n-1}} \right) \\ &= \sqrt[n]{r^0(1)^0} \left( (a^{2^u})^{(2^v)^0} + (b^{2^u})^{(2^v)^0} \right) \\ &+ \sqrt[n]{r(1)^{-i}} \left( (a^{2^u})^{(2^v)} + (b^{2^u})^{(2^v)} \right) \\ &+ \sqrt[n]{r^2(1)^{-2i}} \left( (a^{2^u})^{(2^v)^2} + (b^{2^u})^{(2^v)^2} \right) + \dots \\ &+ \sqrt[n]{r^{n-2}(1)^{-(n-2)i}} \left( (a^{2^u})^{(2^v)^{n-2}} + (b^{2^u})^{(2^v)^{n-2}} \right) \\ &+ \sqrt[n]{r^{n-1}(1)^{-(n-1)i}} \left( (a^{2^u})^{(2^v)^{n-1}} + (b^{2^u})^{(2^v)^{n-1}} \right) \\ &= \sum_{j=0}^{n-1} \sqrt[n]{r^j(1)^{-ji}} \left( (a^{2^u})^{(2^v)^j} + (b^{2^u})^{(2^v)^j} \right). \end{aligned}$$

If we simplify the operations for convenience, we obtain the following equation.

$$\begin{aligned} &= (a^{2^u} + b^{2^u}) + pw^{-i} \left( (a^{2^u})^{(2^v)} + (b^{2^u})^{(2^v)} \right) \\ &+ (pw^{-i})^2 \left( (a^{2^u})^{(2^v)^2} + (b^{2^u})^{(2^v)^2} \right) + \dots \\ &+ \frac{rw^{2i}}{p^2} \left( (a^{2^u})^{(2^v)^{n-2}} + (b^{2^u})^{(2^v)^{n-2}} \right) \\ &+ \frac{rw^i}{p} \left( (a^{2^u})^{(2^v)^{n-1}} + (b^{2^u})^{(2^v)^{n-1}} \right). \end{aligned}$$

**Corollary 2.4** For  $r = 1$  and  $r = -1$ , we get eigenvalues for the generalized Fermat right circulant and skew-right circulant matrices respectively, so that

$$\begin{aligned} \lambda_i(GR_{a,b,1}) &= (a^{2^u} + b^{2^u}) \\ &+ pw^{-i} \left( (a^{2^u})^{(2^v)} + (b^{2^u})^{(2^v)} \right) \\ &+ (pw^{-i})^2 \left( (a^{2^u})^{(2^v)^2} + (b^{2^u})^{(2^v)^2} \right) + \dots \\ &+ \frac{w^{2i}}{p^2} \left( (a^{2^u})^{(2^v)^{n-2}} + (b^{2^u})^{(2^v)^{n-2}} \right) \end{aligned}$$



$$\begin{aligned}
 & + \frac{w^i}{p} \left( (a^{2^u})^{(2^v)^{n-1}} + (b^{2^u})^{(2^v)^{n-1}} \right) \\
 \lambda_i(GR_{a,b,-1}) & = (a^{2^u} + b^{2^u}) \\
 & + pw^{-i} \left( (a^{2^u})^{(2^v)} + (b^{2^u})^{(2^v)} \right) \\
 & + (pw^{-i})^2 \left( (a^{2^u})^{(2^v)^2} + ((b^{2^u})^{2^v})^2 + \dots \right) \\
 & - \frac{w^{2i}}{\xi^2} \left( (a^{2^u})^{(2^v)^{n-2}} + (b^{2^u})^{(2^v)^{n-2}} \right) \\
 & - \frac{w^i}{\xi} \left( (a^{2^u})^{(2^v)^{n-1}} + (b^{2^u})^{(2^v)^{n-1}} \right)
 \end{aligned}$$

where  $\xi$  is the  $n$ -th root of  $-1$ .

**Theorem 2.5** For a positive integer  $n$ , we have

$$\begin{aligned}
 & \sum_{i=0}^{n-1} (a^{2^u} + b^{2^u}) \\
 & + pw^{-i} \left( (a^{2^u})^{(2^v)} + (b^{2^u})^{(2^v)} \right) \\
 & + (pw^{-i})^2 \left( (a^{2^u})^{(2^v)^2} + (b^{2^u})^{(2^v)^2} \right) + \dots \\
 & + \frac{rw^{2i}}{p^2} \left( (a^{2^u})^{(2^v)^{n-2}} + (b^{2^u})^{(2^v)^{n-2}} \right) \\
 & + \frac{rw^i}{p} \left( (a^{2^u})^{(2^v)^{n-1}} + (b^{2^u})^{(2^v)^{n-1}} \right) \\
 & = n(a^{2^u} + b^{2^u}).
 \end{aligned}$$

**Proof.** To get the desired result, we need to know that the trace of any given square matrix is equal to the sum of the eigenvalues of that matrix. In that case

$$\begin{aligned}
 & \sum_{i=0}^{n-1} \lambda_i(GR_{a,b,r}) = \\
 & \sum_{i=0}^{n-1} (a^{2^u} + b^{2^u}) \\
 & + pw^{-i} \left( (a^{2^u})^{(2^v)} + (b^{2^u})^{(2^v)} \right) \\
 & + (pw^{-i})^2 \left( (a^{2^u})^{(2^v)^2} + (b^{2^u})^{(2^v)^2} \right) + \dots \\
 & + \frac{rw^{2i}}{p^2} \left( (a^{2^u})^{(2^v)^{n-2}} + (b^{2^u})^{(2^v)^{n-2}} \right) \\
 & + \frac{rw^i}{p} \left( (a^{2^u})^{(2^v)^{n-1}} + (b^{2^u})^{(2^v)^{n-1}} \right)
 \end{aligned}$$

according to the expression given above,

$$\begin{aligned}
 \sum_{i=0}^{n-1} \lambda_i(GR_{a,b,r}) & = n \cdot GR_{a,b,u} \\
 & = n(a^{2^u} + b^{2^u}).
 \end{aligned}$$

### The Sum Identity

On setting  $i = 0, r = 1$  and  $p = 1$  in eigenvalues for generalized Fermat numbers, the following identity is verified for these numbers.

$$\begin{aligned}
 & \sum_{j=0}^{n-1} GR_{a,b,u+jv} \\
 & = (a^{2^u} + b^{2^u}) + \left( (a^{2^u})^{(2^v)} + (b^{2^u})^{(2^v)} \right) \\
 & + \left( (a^{2^u})^{(2^v)^2} + (b^{2^u})^{(2^v)^2} \right)^2 + \dots \\
 & + \left( (a^{2^u})^{(2^v)^{n-2}} + (b^{2^u})^{(2^v)^{n-2}} \right) \\
 & + \left( (a^{2^u})^{(2^v)^{n-1}} + (b^{2^u})^{(2^v)^{n-1}} \right)
 \end{aligned}$$

### 3. NORM OF GENERALIZED FERMAT $r$ -CIRCULANT MATRICES

When we take  $u = 0$  and  $v = 1$ , we get

$$GR_{a,b,r}^* = \begin{bmatrix} GR_{a,b,0} & GR_{a,b,1} & \dots & GR_{a,b,n-1} \\ rGR_{a,b,n-1} & GR_{a,b,0} & \dots & GR_{a,b,n-2} \\ \vdots & \vdots & \ddots & \vdots \\ rGR_{a,b,2} & rGR_{a,b,3} & \dots & GR_{a,b,1} \\ rGR_{a,b,1} & rGR_{a,b,2} & \dots & GR_{a,b,0} \end{bmatrix},$$

with the help of the lemma given below, the sum of the squares of the generalized Fermat numbers will be used to obtain the norms of different matrices.

**Lemma 3.1** The finite sum of squares of the generalized Fermat numbers is given by

$$\sum_{j=0}^{n-1} (GR_{a,b,j})^2 = \sum_{i=0}^{n-1} (a^{2^i} + b^{2^i})^2$$

**Proof.**

$$\begin{aligned} \sum_{j=0}^{n-1} (GR_{a,b,j})^2 &= \sum_{j=0}^{n-1} a^{2j} + 2(ab)^{2j} + b^{2j} \\ &= a^{2^1} + a^{2^2} + \dots + a^{2^n} \\ &\quad + 2((ab)^1 + (ab)^2 + \dots \\ &\quad + (ab)^n) + b^{2^1} + b^{2^2} + \dots \\ &\quad + b^{2^n} \\ &= \sum_{i=0}^{n-1} (a^{2^i} + b^{2^i})^2 \end{aligned}$$

**Theorem 3.2** The Euclidean norm for the generalized Fermat  $r$ -circulant matrices is given by

$$\|GR_{a,b,r}^*\|_E = \sum_{j=0}^{n-1} (GR_{a,b,j+1} + 2(ab)^{2j}) [n - j(1 - |r|^2)]$$

**Proof.** By equation (4) we get

$$\|GR_{a,b,r}^*\|_E^2 = \sum_{j=0}^{n-1} (GR_{a,b,j+1} + 2(ab)^{2j})^2 [n - j(1 - |r|^2)]^2$$

$$\begin{aligned} &\sqrt{\sum_{i=0}^{n-1} (a^{2^i} + b^{2^i})^2} \leq \|GR_{a,b,r}^*\|_2 \\ &\leq \sqrt{a + b + |r|^2 \left( \sum_{i=0}^{n-1} (a^{2^i} + b^{2^i})^2 \right)} \cdot \sqrt{\sum_{i=0}^{n-1} (a^{2^i} + b^{2^i})^2} \end{aligned}$$

and for  $|r| < 1$

$$\begin{aligned} |r| \sqrt{\sum_{i=0}^{n-1} (a^{2^i} + b^{2^i})^2} &\leq \|GR_{a,b,r}^*\|_2 \leq \\ &\sqrt{n \sum_{i=0}^{n-1} (a^{2^i} + b^{2^i})^2}. \end{aligned}$$

**Proof.** By Eq (4), the Euclidean norm is given as

$$\|GR_{a,b,r}^*\|_E^2 = \sum_{j=0}^{n-1} (GR_{a,b,j})^2 [n - j(1 - |r|^2)]$$

**State1.**

If  $|r| \geq 1$ , then from Lemma 3.1 we get

**Theorem 3.3** The bound for the spectral norm of the generalized Fermat  $r$ -circulant matrices is: for  $|r| \geq 1$

$$\frac{\|GR_{a,b,r}^*\|_E}{\sqrt{n}} \geq \sqrt{\sum_{i=0}^{n-1} (a^{2^i} + b^{2^i})^2}$$

and from Eq. (1.2) we get

$$\|GR_{a,b,r}^*\|_2 \geq \sqrt{\sum_{i=0}^{n-1} (a^{2^i} + b^{2^i})^2}$$

Now to obtain the upper bound for the spectral norm, we write  $GR_{a,b,r}^*$  in the form of the Hadamard product of two matrices.

$$A = \begin{bmatrix} GR_{a,b,0} & 1 & \dots & 1 & 1 \\ rGR_{a,b,n-1} & GR_{a,b,0} & \dots & 1 & 1 \\ \vdots & \vdots & \ddots & \vdots & \vdots \\ rGR_{a,b,2} & rGR_{a,b,3} & \dots & GR_{a,b,0} & 1 \\ rGR_{a,b,1} & rGR_{a,b,2} & \dots & rGR_{a,b,n-1} & GR_{a,b,0} \end{bmatrix}$$

and

$$B = \begin{bmatrix} 1 & GR_{a,b,1} & \dots & GR_{a,b,n-2} & GR_{a,b,n-1} \\ 1 & 1 & \dots & GR_{a,b,n-3} & GR_{a,b,n-2} \\ \vdots & \vdots & \ddots & \vdots & \vdots \\ 1 & 1 & \dots & 1 & GR_{a,b,1} \\ 1 & 1 & \dots & 1 & 1 \end{bmatrix}$$

then clearly  $GR_{a,b,r}^* = A \circ B$ , where  $\circ$  denotes the Hadamard product. Now,

$$\begin{aligned}
 u(A) &= \max_{1 \leq i \leq n} \sqrt{\sum_{j=1}^n |a_{ij}|^2} \\
 &= \sqrt{(GR_{a,b,0})^2 + |r|^2 \sum_{j=1}^{n-1} (GR_{a,b,j})^2} \\
 &= \sqrt{a + b + |r|^2 \sum_{i=0}^{n-1} (a^{2^i} + b^{2^i})^2} \\
 &\leq \sqrt{\sum_{i=0}^{n-1} (a^{2^i} + b^{2^i})^2} \leq \|GR_{a,b,r}^*\|_2 \\
 &\leq \sqrt{a + b + |r|^2 \sum_{i=0}^{n-1} (a^{2^i} + b^{2^i})^2} \cdot \sqrt{\sum_{i=0}^{n-1} (a^{2^i} + b^{2^i})^2}.
 \end{aligned}$$

**State 2.** If  $|r| < 1$ , then from Eq. (4) and Lemma 3.1 we get

$$\begin{aligned}
 \|GR_{a,b,r}^*\|_E^2 &\geq \sum_{j=0}^{n-1} (n-j)|r|^2 |GR_{a,b,j}|^2 \\
 &\quad + |r|^2 \sum_{j=0}^{n-1} j |GR_{a,b,j}|^2 \\
 &= n|r|^2 \left( \sum_{i=0}^{n-1} (a^{2^i} + b^{2^i})^2 \right)
 \end{aligned}$$

and

$$\begin{aligned}
 v(B) &= \max_{1 \leq j \leq n} \sqrt{\sum_{i=1}^n |b_{ij}|^2} \\
 &= \sqrt{1 + \sum_{j=1}^{n-1} (GR_{a,b,j})^2} \\
 &= \sqrt{1 + \sum_{i=0}^{n-1} (a^{2^i} + b^{2^i})^2}.
 \end{aligned}$$

Thus, by Lemma 1.2, we get

$$\begin{aligned}
 \|GR_{a,b,r}^*\|_2 &\leq u(A)v(B) = \\
 &\sqrt{a + b + |r|^2 \sum_{i=0}^{n-1} (a^{2^i} + b^{2^i})^2} \cdot \\
 &\sqrt{\sum_{i=0}^{n-1} (a^{2^i} + b^{2^i})^2} \\
 \frac{\|GR_{a,b,r}^*\|_E}{\sqrt{n}} &\geq |r| \sqrt{\sum_{i=0}^{n-1} (a^{2^i} + b^{2^i})^2}
 \end{aligned}$$

and from Eq. (2) we get

$$\|GR_{a,b,r}^*\|_2 \geq |r| \sqrt{\sum_{i=0}^{n-1} (a^{2^i} + b^{2^i})^2}.$$

We calculate the upper bound for the spectral norm of  $GR_{a,b,r}^*$ .

Let

$$\begin{aligned}
 N &= \begin{bmatrix} GR_{a,b,0} & GR_{a,b,1} & \dots & GR_{a,b,n-2} & GR_{a,b,n-1} \\ GR_{a,b,n-1} & GR_{a,b,0} & \dots & \dots & GR_{a,b,n-2} \\ \vdots & \vdots & \ddots & \vdots & \vdots \\ GR_{a,b,2} & GR_{a,b,3} & \dots & \dots & GR_{a,b,1} \\ GR_{a,b,1} & GR_{a,b,2} & \dots & \dots & GR_{a,b,0} \end{bmatrix} \\
 &= \begin{bmatrix} GR_{a,b,0} & GR_{a,b,1} & \dots & GR_{a,b,n-2} & GR_{a,b,n-1} \\ GR_{a,b,n-1} & GR_{a,b,0} & \dots & \dots & GR_{a,b,n-2} \\ \vdots & \vdots & \ddots & \vdots & \vdots \\ GR_{a,b,2} & GR_{a,b,3} & \dots & \dots & GR_{a,b,1} \\ GR_{a,b,1} & GR_{a,b,2} & \dots & \dots & GR_{a,b,0} \end{bmatrix}
 \end{aligned}$$

hence, we have

$$M = \begin{bmatrix} 1 & 1 & 1 & \dots & 1 & 1 \\ r & 1 & 1 & \dots & 1 & 1 \\ \vdots & \vdots & \vdots & \ddots & \vdots & \vdots \\ r & r & r & \dots & r & 1 \\ r & r & r & \dots & r & 1 \end{bmatrix}$$

then clearly  $GR_{a,b,r}^* = M \circ N$ , where  $\circ$  denotes the Hadamard product. So,

$$s_1(M) = \max_{1 \leq i \leq n} \sqrt{\sum_{j=1}^n |m_{ij}|^2} = \sqrt{n}$$

$$t_1(N) = \max_{1 \leq j \leq n} \sqrt{\sum_{i=1}^n |n_{ij}|^2}$$

$$= \sqrt{\sum_{j=1}^n GR_{a,b,j}^2} = \sqrt{\sum_{i=0}^{n-1} (a^{2^i} + b^{2^i})^2}$$

hence, by Lemma 1.2, we have

$$\|GR_{a,b,r}^*\|_2 \leq s_1(M)t_1(N)$$

$$= \sqrt{n \sum_{i=0}^{n-1} (a^{2^i} + b^{2^i})^2}$$

thus

$$|r| \sqrt{\sum_{i=0}^{n-1} (a^{2^i} + b^{2^i})^2} \leq \|GR_{a,b,r}^*\|_2$$

$$\leq \sqrt{n \left( \sum_{i=0}^{n-1} (a^{2^i} + b^{2^i})^2 \right)}$$

as desired.

#### 4. CONCLUSION

Based on the generalized Fermat numbers with similar recurrences, which have been studied less, the  $r$ -circulant matrices of these sequences were created. Euclidean, row and spectral norms, which are eigenvalues, determinants, and some special norm values, are discussed depending on this matrix. In addition, the lower and upper bounds of these matrices for the spectral norm were examined in closed form. In addition, right circulant and skew-right circulant matrices are examined for 1 and -1 values of  $r$  depending on eigenvalues. Finally, some interesting results and sum properties are given.

#### Funding

The author (s) has no received any financial support for the research, authorship or publication of this study.

#### Authors' Contribution

The authors contributed equally to the study.

#### The Declaration of Conflict of Interest/ Common Interest

No conflict of interest or common interest has been declared by the authors.

#### The Declaration of Ethics Committee Approval

This study does not require ethics committee permission or any special permission.

#### The Declaration of Research and Publication Ethics

The authors of the paper declare that they comply with the scientific, ethical and quotation rules of SAUJS in all processes of the paper and that they do not make any falsification on the data collected. In addition, they declare that Sakarya University Journal of Science and its editorial board have no responsibility for any ethical violations that may be encountered, and that this study has not been evaluated in any academic publication environment other than Sakarya University Journal of Science.

#### REFERENCES

- [1] W. Weisstein, Eric, "Proth Number", mathworld.wolfram.com, 2019.
- [2] N. J. A. Sloane, "A Handbook of Integer Sequences", Academic Press, New York, <https://oeis.org>, 1973.
- [3] Generalized Fermat numbers, OEIS. Generalized Fermat numbers - OeisWiki, 2022.
- [4] B. Fischer and J. Modersitzki, "Fast inversion of matrices arising in image processing", Number Algorithms vol. 22 no.1, pp.1-11, 1999.

- [5] S. Georgiou and C. Kravvaritis, New good quasi-cyclic codes over  $GF(3)$ , *International Journal of Algebra* vol.1, no.1, pp.11-24, 2007.
- [6] I. Kra and S. R. Simanca, On circulant matrices, *Notices AMS* vol.59, no.3, pp.368-377, 2012.
- [7] A. C. F. Bueno, “On the Eigenvalues and the Determinant of the Right Circulant Matrices with Pell and Pell–Lucas Numbers”, *International Journal of Mathematics and Scientific Computing*, vol.4, no.1, pp.19-20, 2014.
- [8] S. Solak, “On the norms of circulant matrices with the Fibonacci and Lucas numbers”, *Applied Mathematics and Computation*, vol.160, no.1, pp.125-132, 2005.
- [9] S. Shen, J. Cen, “On the bounds for the norms of  $r$ -circulant matrices with the Fibonacci and Lucas numbers”, *Applied Mathematics and Computation*, vol.216, no.10, pp. 2891-2897, 2010.
- [10] S. Q. Shen, J. M. Cen, “On the spectral norms of  $r$ -circulant matrices with the  $k$ -Fibonacci and  $k$ -Lucas numbers”, *International Journal of Contemporary Mathematical Sciences*, vol. 5, no. 12, pp. 569-578, 2010.
- [11] Y. Zheng, S. Shon, “Exact inverse matrices of Fermat and Mersenne circulant matrix”, In *Abstract and Applied Analysis*, Hindawi, 2015.
- [12] D. Bozkurt, T. Y. Tam, “Determinants and inverses of circulant matrices with Jacobsthal and Jacobsthal–Lucas numbers”, *Applied Mathematics and Computation*, vol.219, no. 2, pp.544-551, 2012.
- [13] M. Kumaria, K. Prasada, J. Tantib, and E. Özkan, “On the properties of  $r$ -circulant matrices involving Mersenne and Fermat numbers”, *International Journal of Nonlinear Analysis and Applications*, vol.1, no.11, 2023.
- [14] M. Marin, “Generalized solutions in elasticity of micropolar bodies with voids”, *Revista de la Academia Canaria de Ciencias*, vol.8, no.1, pp. 101-106, 1996
- [15] M. Marin, “Contributions on uniqueness in thermoelastodynamics on bodies with voids”, *Ciencias matemáticas (Havana)*, vol.16, no.2, pp.101-109, 1998.
- [16] Z. Pucanovic, and M. Pesovic “Chebyshev polynomials and  $r$ -circulant matrices”, *Applied Mathematics and Computation*, vol.437, no.127521, 2023.
- [17] J. M. Blackledge, “Vector and Matrix norm”, *Digital Signal Processing*, pp.208-236, 2006.
- [18] Simon Foucart, <http://www.math.drexel.edu/foucart/TeachingFiles/F12/M504Lect6.pdf>
- [19] R. E. Cline, R. J. Plemmons, and G. Worm, “Generalized inverses of certain Toeplitz matrices”, *Linear Algebra and its Application* vol.8, no.1, pp.25-33, 1974.
- [20] K. Irwin, R. Santiago, Simanca, “On circulant matrices”, <://www.math.colombia.edu/ums/pdf/cir-not5.pdf>



SAKARYA ÜNİVERSİTESİ

# FEN BİLİMLERİ ENSTİTÜSÜ DERGİSİ

Sakarya University Journal of Science  
SAUJS

ISSN 1301-4048 | e-ISSN 2147-835X | Period Bimonthly | Founded: 1997 | Publisher Sakarya University |  
<http://www.saujs.sakarya.edu.tr/>

Title: Production of Hydrogen Molecule from Methane Molecule Amplified with Excitation of Anti-Symmetric Modes of Vibration

Authors: Sinan ERDOGAN

Received: 2022-12-28 00:00:00

Accepted: 16.06.2023

Article Type: Research Article

Volume: 27

Issue: 5

Month: October

Year: 2023

Pages: 965-974

How to cite

Sinan ERDOGAN; (2023), Production of Hydrogen Molecule from Methane Molecule Amplified with Excitation of Anti-Symmetric Modes of Vibration. Sakarya University Journal of Science, 27(5), 965-974, DOI: 10.16984/saufenbilder.1225856

Access link

<https://dergipark.org.tr/tr/journal/1115/issue/80257/1225856>

New submission to SAUJS

<http://dergipark.gov.tr/journal/1115/submission/start>

## Production of Hydrogen Molecule from Methane Molecule Amplified with Excitation of Anti-Symmetric Modes of Vibration

Sinan ERDOGAN \*<sup>1</sup> 

### Abstract

Some factors, such as pressure and temperature, affect the rate of chemical reactions. In addition, the activation energy barrier must be overcome for the reaction to be initiated. It can be preferred to overcome this barrier by using catalysts and preheating. The catalyst ensures that it obtains the energy to react quickly by transferring it to the reactants. Similarly, the translational, vibrational, and rotational energy levels of reactants can be increased by preheating. According to the kinetic molecular theory of gases, preheating increases the kinetic energies of the gases and the speed of their collision, so the reaction takes place faster. This study theoretically investigates possible reactions of methane that can occur with the effect of only vibrational energy levels. The vibrational excitation of the molecules affects the reaction rates, and the activation barrier is overcome with lower energies. Using laser-based techniques makes the excitation of well-defined vibrational modes possible. This study investigated inelastic collisions of a methane molecule with well-characterized energy levels in infrared spectroscopy with some gases and the vibrational energy transfers that occur in these collisions. The methane molecule is the simplest form of a molecular structure consisting of more than three atoms of hydrogen atoms, which play an essential role in combustion chemistry. It shows that C—H stretch excitation increases the reaction rate of methane (CH<sub>4</sub>) molecules.

**Keywords:** Methane, molecular vibration, energy transfer, vibrational spectroscopy

### 1. INTRODUCTION

The importance of hydrogen is increasing day by day with the development of new technologies. The widespread use of hydrogen-powered vehicles, especially in transportation, is crucial for accelerating the global energy transformation. In this energy conversion process, studies on clean hydrogen production, storage of hydrogen, and getting maximum efficiency from hydrogen have gained momentum.

It has become the primary goal to produce energy without burning and creating harmful emissions. Even though almost all the hydrogen production is provided from fossil fuels, studies on clean hydrogen production have increased in recent years [1-3].

Traditional hydrogen production methods from fossil fuels, such as (1) steam reforming of natural gas, (2) partial oxidation of methane, and (3) coal gasification, are prominent. Other methods are (4) biomass gasification and (5) electrolysis methods [1].

\* Corresponding author: [sinanerdogan@sakarya.edu.tr](mailto:sinanerdogan@sakarya.edu.tr) (S.ERDOGAN)

<sup>1</sup> Sakarya University

ORCID: <https://orcid.org/0000-0001-8844-0761>



Recent research has focused on enhancing hydrogen production by the direct thermocatalytic decomposition of methane to form elemental carbon and hydrogen as an attractive alternative to the conventional steam reforming process [4]. Thermodynamically, the reaction of  $\text{CH}_4(\text{g}) \rightarrow \text{C} + 2\text{H}_2(\text{g})$  can occur from  $543^\circ\text{C}$ , but kinetically, the reaction becomes dominant from  $800^\circ\text{C}$  without any catalyst [5]. Methane decomposition is a moderately endothermic reaction. Due to the strong C–H bonds, non-catalytic thermal cracking of methane requires temperatures higher than  $1200^\circ\text{C}$  to obtain a reasonable yield experimentally [4].

The use of solar radiation as a heating source to achieve high temperatures has been studied in recent studies. Hirsch and Steinfeld [6] investigated using concentrated solar radiation as the source of high-temperature process heat. They determined that the conversion of methane was 67% at  $1327^\circ\text{C}$  and 1 atm. Dahl et al. [7] obtained that the conversion of methane was 90% at  $1860^\circ\text{C}$  using concentrated solar energy as a heating source.

Maag et al. [8] calculated methane conversion and hydrogen yield exceeding 95% at  $1027\text{--}1327^\circ\text{C}$  with solar energy.

In a study, hydrogen was produced through a thermal decomposition reaction by injecting methane gas into a molten slag obtained in the metal industry. The decomposition reaction sequence is expressed as  $\text{CH}_4(\text{g}) \rightarrow \text{CH}_3(\text{radical}) \rightarrow \text{CH}_2(\text{radical}) \rightarrow \text{CH}(\text{radical}) \rightarrow \text{C}$  (soot) [5].

Using a catalyst can significantly reduce the reaction's temperature [4]. Traditionally, methane decomposition has been catalyzed by nickel, copper, iron, and some noble metals [9].

In a study using a Ni-based catalyst at a temperature of  $700^\circ\text{C}$ , it was calculated that the concentration of  $\text{H}_2$  was around 80%, corresponding to a methane conversion close

to the theoretical equilibrium value [10]. On the contrary, Fe catalysts can decompose methane at a temperature range of  $700\text{--}1000^\circ\text{C}$  [11]. Methane conversion was not as high when methane decomposition was performed below  $600^\circ\text{C}$ .

As seen in the studies, hydrogen can be produced from methane at high temperatures. However, developments in quantum mechanics in recent years have revealed that some chemical reactions can be carried out without reaching high temperatures.

The chemical industry has discovered in recent years that chemical reaction rates or efficiency have been increased by ultrasound-assisted technologies [12]. In addition, studies on the effect of microwave-assisted reactions on mass and heat transfer have risen in recent years [13]. These exciting developments make it necessary to examine chemical reactions from the perspective of quantum mechanics.

From this perspective, researchers study molecular motions. The different types of molecular motion are translation, rotation, vibration, and electronic motion. The translation motion occurs from the center-of-mass motions of molecules. The electron configuration of the system defines an electronic state, and each electronic state corresponds to one of the molecule's energy levels. Electronic motion defines transitions between different electronic states. The vibrational transitions occur between different vibrational levels of the same electronic state. Rotational transitions occur mainly between rotational levels of the same vibrational state. The number of independent ways a molecule of gas can move is called the degree of freedom [14].

Some related research in molecular motions is as follows. Huarte-Larrañaga and Manthe [15] investigated the reaction between methane molecule and hydrogen atom regarding quantum mechanics. Palma et al. [16] studied the rate constants of the  $\text{CH}_4+\text{H}$



reaction and investigated the transition of the vibrational energies of the reacting CH<sub>4</sub> molecule to the CH<sub>3</sub> molecule during the reaction. Camden et al. [17] investigated the effects of C—H stretching excitation of CH<sub>4</sub> molecule on the reaction with hydrogen. Simpson et al. [18] investigated the reaction mechanism of atomic chlorine with vibrationally excited CH<sub>4</sub> and CHD<sub>3</sub> molecules. Bourcin et al. [19] investigated the rotational relaxation and vibrational energy transfer processes that occur in inelastic collisions of methane with H<sub>2</sub> and He at -80°C and 23°C. Corchado et al. [20] discussed the reaction of CH<sub>4</sub> and H atom in terms of energy surface area to obtain a hydrogen molecule. Another study presented the investigation of rovibrational transitions of methyl radicals (CH<sub>3</sub>, CD<sub>3</sub>) by infrared spectroscopy [21].

This study discusses preparing suitable conditions for reactions with electromagnetic (EM) waves by considering molecules' vibrational excitation energy levels. In addition, the behavior of the fundamental ( $v_3=0\rightarrow 1$ ) and overtone ( $v_3=0\rightarrow 2$ ) levels of the CH<sub>4</sub> molecule under vibrational stimulation was investigated. In addition, inelastic collisions of a vibrationally excited CH<sub>4</sub> molecule with hydrogen with specific kinetic energy were aimed, and the breaking of chemical bonds and the formation of new bonds as a result of this collision were discussed.

## 2. THEORY AND METHOD

In this section, the basic information for the theoretical design of the study is given. Especially the vibration modes of methane, the kinetic theory, the theory of inelastic collision, and the chemical reactions formed the infrastructure of this study.

### 2.1. Vibration Spectroscopy and Vibration Modes of Methane

The molecule or the atoms that make up the molecule are continually motion. These are the translational motion of the molecule,

rotational motion around an axis, periodic changes in the length of a chemical bond, or vibrational movements that cause periodic changes in the angles between the atoms that make up the molecule [14]. Differences in translational, rotational, and vibrational energy levels indicate that molecules differ in their energies. These differences reveal the molecule's absorption, emission and reflection properties by molecular spectroscopy techniques. EM waves that cause vibration and rotational movements of the molecule are located in the infrared region of the electromagnetic spectrum and are examined by infrared spectroscopy [22]. The molecule is stimulated to an upper or two higher vibrational levels and raises its energy level by absorbing the energy of EM waves. The electric field of EM waves acts on the molecule and further strengthens one of the molecular motions [19].

It is easy to determine the vibrational modes of diatomic or triatomic molecules and the energies they absorb. However, making these calculations for polyatomic molecules becomes problematic depending on the atomic number. Methane gas, the smallest molecule containing more than three atoms, has been investigated within the scope of this study. With the increase in the number of atoms, many vibrational centers are formed, and there are various interactions between these centers. All effects must be taken into account in the calculations. The vibrations between atoms can be collected in two classes. These are stretching and bending vibrations. Stretching vibrations occur when the distance between two atoms constantly changes along the bond axis of the atoms. It has two sub-modes as symmetrical and asymmetrical stress. Bending vibrations result from changing the angle between two bonds and have four modes; scissoring, rocking, wagging, and twisting modes [23].

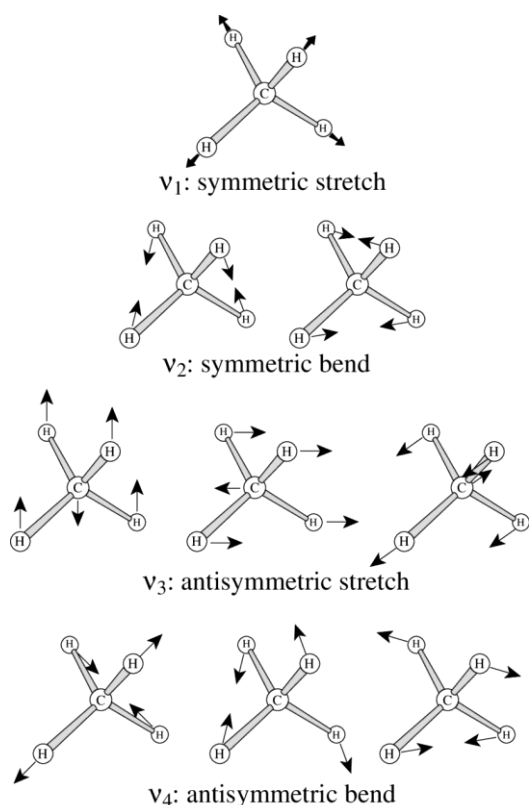


Figure 1 Vibration modes of methane [24]

The degree of freedom of a molecule with  $N$  atoms is  $3N$ , and the total degree of freedom of the  $\text{CH}_4$  molecule is 15. These modes belong to translational movements, three modes to rotation, and the remaining nine modes belong to vibrational motions. The vibrational modes of the  $\text{CH}_4$  molecule are shown in Fig.1.

The vibrational modes of the methane molecule are called  $v_1$ ,  $v_2$ ,  $v_3$ , and  $v_4$ . The  $v_3$  and  $v_4$  vibration modes have three different energy levels, while the  $v_2$  vibration mode has two different energy levels. The energy levels of these vibrational modes are  $2917 \text{ cm}^{-1}$  (in terms of energy, its value is  $34.90 \text{ kJ/mol}$ ;  $0.36 \text{ eV}$ ) for  $v_1$ ,  $1533 \text{ cm}^{-1}$  ( $18.34 \text{ kJ/mol}$ ;  $0.19 \text{ eV}$ ) for  $v_2$ ,  $3019 \text{ cm}^{-1}$  ( $36.12 \text{ kJ/mol}$ ;  $0.37 \text{ eV}$ ) for  $v_3$ , and  $1311 \text{ cm}^{-1}$  ( $15.68 \text{ kJ/mol}$ ;  $0.16 \text{ eV}$ ) for  $v_4$ , respectively [17].

## 2.2. Kinetic Theory and Chemical Reactions

The energies of molecules change especially with movements such as translation, rotation,

and vibration. As the energy levels of molecules excited by vibration rise to higher levels, the molecule's energy significantly increases. Gaseous molecules freely collide with each other and can transfer their energy to other molecules. Suppose the total energies of the two vibrationally excited molecules are equal to the energy required for a molecule to rotate. In that case, the collision occurs in an inelastic manner, and the motion modes of the molecules can change with the energy transfer [25]. If the molecules collide with collision energy below the energy level required for the molecules to absorb, they will bounce off each other by making elastic collisions. With inelastic collisions, the potential energies of the molecules can turn into kinetic energy, or their kinetic energies can turn into potential energy. According to the kinetic theory, molecules with increased kinetic energies tend to collide more with other molecules. When molecules collide inflexibly, the kinetic energy of the molecules can be used to stretch, bend, and eventually break bonds that lead to chemical reactions [19]. Thus, chemically, atoms or smaller groups of molecules in the molecule begin to separate.

There is a specific energy required for molecules to break existing bonds during a chemical reaction [26]. As it is known, the minimum energy requirement that must be met for a chemical reaction to take place is called activation energy [27]. The elementary reaction of the decomposition of  $\text{CH}_4$  to  $\text{CH}_3$  is  $\text{CH}_4(\text{g}) \rightarrow \text{CH}_3 + \text{H}$  which activation energy is  $264\text{-}430 \text{ kJ/mol}$  [5]. For chemical reactions to begin, the activation energy barrier must be overcome, and molecules or atoms must collide with the correct orientation. If the molecules move too slowly with too little kinetic energy or collide in the wrong direction, they do not react and bounce off each other in an elastic collision. However, some methods are being developed to increase the collision numbers of molecules. In this method, the direction of the molecules is adjusted according to the permanent dipole moment under an electric or magnetic field. Thus the reaction rate can be increased by

providing more precisely oriented collisions [28] Therewithal, reactions can be initiated with lower activation energy by lowering the energy barrier by using a catalyst [29]. The activation energy of  $\text{CH}_4(\text{g}) + \text{H} \rightarrow \text{CH}_3(\text{g}) + \text{H}_2(\text{g})$  reaction with radical hydrogen is 45-60 kJ/mol [5].

Consequently, molecules with an energy above the low energy barrier will tend to react. This effect will increase the reaction rate. With another method that has been tried in recent years, the vibrational energy levels of molecules are stimulated using EM waves, and the molecule rapidly reacts by transferring its energy to another molecule during collisions. These methods pull down the activation energy barrier, allowing more molecules to react even at low temperatures [30-32].

Hydrogen separation from methane gas has recently been a suitable prototype for the theoretical study of bimolecular reactions due to its relatively small size, and its chemical reaction is as follows.



There are several theoretical and experimental studies in the literature that deal with the collision reactions of the X atom, such as Cl, O, or H [18, 19].

### 3. THEORETICAL DESIGN OF HYDROGEN PRODUCTION FROM AN EXCITED METHANE

The accelerated H atoms are produced by the UV photolysis of HBr, and the antisymmetric stretching fundamental or overtone of methane is prepared by direct infrared absorption.

Accelerated hydrogen atoms are obtained by photolysis by sending EM radiation with a 200-230 nm wavelength in the ultraviolet (UV) region onto the hydrogen bromide (HBr) molecule [17]. Thus, the H atom will acquire translational kinetic energy.

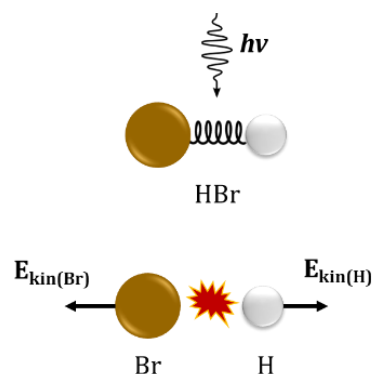


Figure 2 Dissociation of the HBr molecule

The atoms move away from each other at certain speeds by sending an EM beam located in the UV region to the HBr molecule. Thus, the HBr molecule dissociates into H and Br atoms as shown in Fig. 2 [33]. The balance of energy changes due to bond dissociation of the HBr molecule by the laser beam is shown in Eq.2 [34].

$$h\nu + E_{int(HBr)} = D_0 + E_{kin(Br)} + E_{kin(H)} \quad (2)$$

The dissociation energy of the Br molecule is  $D_0=3.75$  eV [35]. The internal energy of the HBr ( $E_{int(HBr)}$ ) molecule is negligible at 25°C [34]. In this case, the energy of the EM radiation will be spent for the two atoms to gain kinetic energy and scatter in opposite directions. The kinetic energies they gain will be proportional to their masses ( $E_{kin}=mV^2/2$ ). In this case, the kinetic energy that hydrogen will gain will be  $E_{kin(H)}=2.27$  eV if the incoming photon is a laser beam with a wavelength of approximately 205 nm, while  $E_{kin(H)}=1.63$  eV in the case of a laser beam with a wavelength of approximately 230 nm.

The parametric conversion of Nd:YAG (Neodymium-doped Yttrium Aluminum Garnet) laser radiation ( $\lambda = 1.064 \mu\text{m}$ ) in nonlinear crystals is a promising means of generating tunable radiation. KTP (KTiOPO<sub>4</sub>-Potassium Titanyl Phosphate) can be used as a nonlinear optical crystal with excellent nonlinear, electrooptical, and acousto-optic properties. It was shown that the KTP crystal had attractive potentialities for a highly efficient parametric light

generator tunable in the eye-safe region of the spectrum since this crystal possesses appropriate tuning characteristics in the IR and visible regions (0.3-4.5  $\mu\text{m}$ ). In addition, a nonlinear  $\beta\text{-BaB}_2\text{O}_4$  (BBO-Beta-Barium Borate) crystal can also be used for this purpose [36]. The schematic diagram for the Nd:YAG is shown in Fig.3.

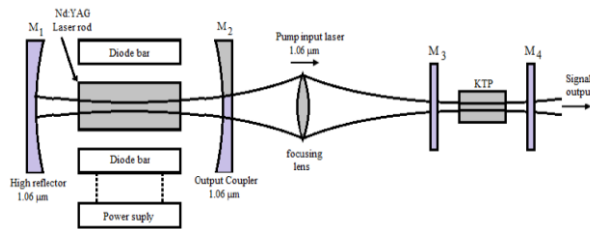
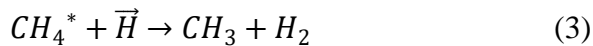


Figure 3 Schematic diagram for the Nd:YAG eye safe laser system [37]

The proposed initial reaction is the inelastic collision of the excited  $\text{CH}_4$  molecule with the accelerated hydrogen shown in Eq.3.



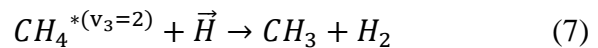
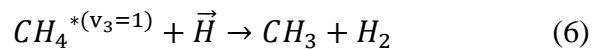
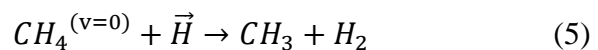
In this reaction,  $\vec{H}$  represents the accelerated hydrogen atom with a specific kinetic energy.  $\text{CH}_4^*$  indicates an excited methane gas. The excitation will be performed on  $\nu_3$  vibration mode. As a result of the absorption of asymmetric stretching modes in methane by electromagnetic radiation at wavelengths of 1.7  $\mu\text{m}$  and 3.3  $\mu\text{m}$  in the infrared region, the vibration mode is excited to  $\nu_3=2$  and  $\nu_3=1$  energy levels, respectively.

The change in the total energy of the reaction in Eq.3 is the sum of the impact energy of hydrogen on methane and the vibrational energy increased by excitation (Eq.4).

$$\Delta E_{tot} = \Delta E_{coll} + \Delta E_{vib} \quad (4)$$

The collision energy was determined as 1.63 eV and 2.27 eV, and it was calculated that 0.37 eV should be given to increase the vibration energy level to the first level and 0.74 eV to increase the energy level to the second level with the stimulation of the  $\nu_3$  anti-symmetric stress mode.

The sum of the collision energy of 1.63 eV and the energy given by stimulating the C—H bond anti-symmetric stretching mode to the first level ( $\nu_3=1$ ) becomes 2.00 eV. The sum of the same collision energy and the excitation energy to the second vibrational level ( $\nu_3=2$ ) of the C—H bond is 2.37 eV. In case of higher collision energy (2.27 eV) accelerated hydrogen collides with  $\text{CH}_4$ , the changes in total energies according to the excitation levels are 2.64 eV for  $\nu_3=1$  and 3.01 eV for  $\nu_3=2$ , and the related reactions are given in Eq.5-7.

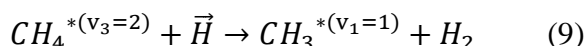
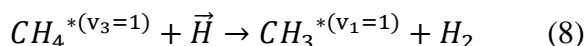


The possible reactions as a result of the processes are as follows. According to reaction (5),  $\text{CH}_4$ , whose vibrational level is in the ground state, collides with accelerated hydrogen. This way, hydrogen can be separated from the methane and combined with the other hydrogen. In addition, the  $\text{CH}_3$  molecule can also exit the reaction in the ground state. According to reaction (6), methane excited to the  $\nu_3=1$  vibration mode can collide with accelerated hydrogen. The combined energies of both reactants can make the reaction occur. As a result,  $\text{CH}_3$  molecule and  $\text{H}_2$  molecule can be formed in fundamental vibrational mode. In reaction (7), methane excited to  $\nu_3=2$  vibrational mode collides with accelerated hydrogen. As a result of this reaction, the  $\text{CH}_3$  molecule and  $\text{H}_2$  molecule will be formed in the ground state.

The energy level of the  $\nu_1$  vibrational mode of the  $\text{CH}_3$  molecule is  $3004 \text{ cm}^{-1}$ ,  $\nu_2=606 \text{ cm}^{-1}$ ,  $\nu_3=3161 \text{ cm}^{-1}$  and  $\nu_4=1400 \text{ cm}^{-1}$  [17]. The energy level of the  $\nu_1=1$  vibrational mode of the  $\text{CH}_3$  molecule is  $3004 \text{ cm}^{-1}$ , which is very close to the energy level of the  $\nu_3$  vibrational mode of methane ( $3019 \text{ cm}^{-1}$ ). For this reason, it seems possible that a methyl molecule

whose  $v_1$  vibration mode is excited by an inelastic collision can also be formed.

In addition, during the collision during the reaction, the energy of the  $v_3$  anti-symmetric stretching mode of the methane can be transferred to the methyl formed so that the  $v_1$  symmetrical stretching mode of the methyl molecule remains in an excited state. Eq.8-9 show the reactions for these probabilities.



According to the reaction (8), the accelerated hydrogen collides with the methane excited to the  $v_3=1$  vibration mode. In this way, one hydrogen can be separated from the methane and combined with the other hydrogen. In addition, the  $CH_3$  molecule can also exit the reaction by being excited to the  $v_1=1$  vibrational mode. Another alternative reaction (9) is that methane excited to  $v_3=2$  vibrational mode reacts with accelerated hydrogen to form  $CH_3$  excited to  $v_1=1$  vibrational mode, and  $H_2$ .

#### 4. DISCUSSION AND CONCLUSION

$CH_4$  contains four powerful localized C—H bonds, and the bond energy of H— $CH_3$  was determined to be 439.3 kJ/mol under standard conditions [38]. There are conventional methods to break this H— $CH_3$  bond, but these can take place at very high temperatures or overvoltages. Although the steam reforming method is the cheapest hydrogen production method, it is formed by reacting water vapor between 700 and 1000 °C and natural gas with a nickel catalyst. The most basic by-products of this reaction are CO,  $CO_2$  and other greenhouse gases. In electrolysis, another prominent method, overvoltages in the system increase the cost of this method. Although this method takes place at low temperatures, the cost is high. In these methods, the energy levels of the molecules increase and when the energy level exceeds the activation energy, the reaction takes place.

The  $v_3$  vibrational mode is excited to the first energy level by giving 0.37 eV energy to the methane molecule at a wave number of 3019  $cm^{-1}$ . In the same way, 0.74 eV energy must be given at a frequency of the same wave number to overtone the  $v_3$  vibration mode. This study discusses the initiation or acceleration of reactions with lower activation energies because of inelastic collisions of a vibrationally excited  $CH_4$  molecule with hydrogen with a specific kinetic energy. In addition, the breaking of chemical bonds resulting from the collision and the formation of new bonds were evaluated theoretically.

Since the  $v_3$  vibrational mode energy of the  $CH_4$  molecule and the  $v_1$  vibrational mode energies for the methyl group ( $CH_3$ ) are very similar, the scattering dynamics as a result of the reaction may cause a similar result to be produced.

As a result, research for the development of simplified models of molecules containing more than four atoms is presented in this study. Theoretical studies have revealed that C—H stretch excitation increases the reaction rate of hydrogen and methane to  $CH_4$ .

It is thought that these reactions may be sufficient to initiate chain reactions. It has been shown that as a result of the reaction of the  $v_3$  vibrational excited  $CH_4$  molecule with hydrogen, the  $v_1$  vibrational mode excited  $CH_3$  molecule can be formed. It is understood that with the excitation of the  $CH_3$  molecule, the reaction of hydrogen abstraction from this molecule can be accelerated and facilitated.

In addition, it has been demonstrated that asymmetric stretching modes in methane can be achieved by absorption with electromagnetic radiation at wavelengths of 1.7  $\mu m$  and 3.3  $\mu m$  in the infrared region. The energy of 0.37 eV (36.12 kJ/mol) or 0.74 eV (72.24 kJ/mol) is required to generate electromagnetic radiation in this IR region. When the proposed method is validated experimentally, solar energy can achieve UV

photolysis naturally. In conventional methods, 439.3 kJ/mol needs to break the H-CH<sub>3</sub> bond. This value is tried to be lowered with the help of various catalysts. It is also envisaged that these reactions will be carried out at lower temperatures. In these respects, this method has many advantages.

In future studies, hydrogen abstraction reactions from CH<sub>3</sub>, CH<sub>2</sub> and CH molecules can be examined similarly and all possible reactions can be determined. Also, reaction rates and equilibrium constants for all reactions can be determined.

#### ***Funding***

The author received no financial support for the research, authorship, and/or publication of this paper.

#### ***The Declaration of Conflict of Interest/ Common Interest***

No conflict of interest or common interest has been declared by the author.

#### ***The Declaration of Ethics Committee Approval***

The author declares that this document does not require an ethics committee approval or any special permission.

#### ***The Declaration of Research and Publication Ethics***

The authors of the paper declare that they comply with the scientific, ethical and quotation rules of SAUJS in all processes of the paper and that they do not make any falsification on the data collected. In addition, they declare that Sakarya University Journal of Science and its editorial board have no responsibility for any ethical violations that may be encountered, and that this study has not been evaluated in any academic publication environment other than Sakarya University Journal of Science.

## **REFERENCES**

- [1] M. Kayfeci, A. Keçebaş, M. Bayat, "Chapter 3 - Hydrogen production," Solar hydrogen production, Elsevier, 2019, p. 45-83.
- [2] A. J. Esswein, D. G. Nocera, "Hydrogen production by molecular photocatalysis," Chemical Reviews, vol. 107, no.10, pp. 4022-47, 2007.
- [3] J. D. Holladay, J. Hu, D. L. King, Y. Wang, "An overview of hydrogen production technologies," Catalysis Today, vol. 139, no. 4, pp. 244-60, 2009.
- [4] H. F. Abbas, W. W. Daud, "Hydrogen production by methane decomposition: a review," International Journal of Hydrogen Energy, vol. 35, no. 3, pp. 1160-90, 2010.
- [5] Y. Kashiwaya, M. Watanabe, "Kinetic analysis of the decomposition reaction of CH<sub>4</sub> injecting into molten slag," ISIJ International, vol. 52, no. 8, pp. 1394-403, 2012.
- [6] D. Hirsch, A. Steinfeld, "Solar hydrogen production by thermal decomposition of natural gas using a vortex-flow reactor," International Journal of Hydrogen Energy, vol. 29, no. 1, pp. 47-55, 2004.
- [7] J. K. Dahl, K. J. Buechler, A.W. Weimer, A. Lewandowski, C. Bingham, "Solar-thermal dissociation of methane in a fluid-wall aerosol flow reactor," International Journal of Hydrogen Energy, vol. 29, no. 7, pp. 725-36, 2004.
- [8] G. Maag, G. Zanganeh, A. Steinfeld, "Solar thermal cracking of methane in a particle-flow reactor for the co-production of hydrogen and carbon," International Journal of Hydrogen

- Energy, vol. 34, no. 18, pp. 7676-85, 2009.
- [9] D. P. Serrano, J. A. Botas, J. L. G. Fierro, R. Guil-López, P. Pizarro, G. Gómez, "Hydrogen production by methane decomposition: origin of the catalytic activity of carbon materials," *Fuel*, vol. 89, no. 6, pp. 1241-8, 2010.
- [10] I. Suelves, M. Lázaro, R. Moliner, B. Corbella, J. Palacios, "Hydrogen production by thermo catalytic decomposition of methane on Ni-based catalysts: influence of operating conditions on catalyst deactivation and carbon characteristics," *International Journal of Hydrogen Energy*, vol. 30, no. 15, pp. 1555-67, 2005.
- [11] S. Takenaka, M. Serizawa, K. Otsuka, "Formation of filamentous carbons over supported Fe catalysts through methane decomposition," *Journal of Catalysis*, vol. 222, no. 2, pp.520-31, 2004.
- [12] A. A. Kiss, R. Geertman, M. Wierschem, M. Skiborowski, B. Gielen, J. Jordens, J. J. John, T. V. Gerven, "Ultrasound-assisted emerging technologies for chemical processes," *Journal of Chemical Technology & Biotechnology*, vol.93, no. 5, pp. 1219-27, 2018.
- [13] M. Nuechter, U. Mueller, B. Ondruschka, A. Tied, W. Lautenschlaeger, "Microwave-assisted chemical reactions," *Chemical Engineering & Technology*, vol. 26, no. 12, pp. 1207-16, 2003.
- [14] P. Atkins, J. Paula, *Physical Chemistry*. Oxford University Press, 2014.
- [15] F. Huarte-Larrañaga, U. Manthe, "Quantum dynamics of the  $\text{CH}_4+\text{H}\rightarrow\text{CH}_3+\text{H}_2$  reaction: full-dimensional and reduced dimensionality rate constant calculations," *The Journal of Physical Chemistry A*, vol. 105, no. 12, pp. 2522-9, 2001.
- [16] J. Palma, J. Echave, D. C. Clary, "Rate constants for the  $\text{CH}_4+\text{H}\rightarrow\text{CH}_3+\text{H}_2$  reaction calculated with a generalized reduced-dimensionality method," *The Journal of Physical Chemistry A*, vol. 106, no. 36, pp. 8256-60, 2002.
- [17] J. P. Camden, H. A. Bechtel, D. J. A. Brown, R. N. Zare, "Effects of C–H stretch excitation on the  $\text{H}+\text{CH}_4$  reaction," *The Journal of chemical physics*, vol. 123, no. 13, 134301, 2005.
- [18] W. R. Simpson, T. P. Rakitzis, S. A. Kandel, A. J. Orr-Ewing, R. N. Zare, "Reaction of Cl with vibrationally excited  $\text{CH}_4$  and  $\text{CHD}_3$ : State-to-state differential cross sections and steric effects for the HCl product," *The Journal of Chemical Physics*, vol. 103, no. 17, pp. 7313-35, 1995.
- [19] F. Menard-Bourcin, C. Boursier, L. Doyennette, J. Menard, "Rotational and vibrational relaxation of methane excited to  $2\nu_3$  in  $\text{CH}_4/\text{H}_2$  and  $\text{CH}_4/\text{He}$  mixtures at 296 and 193 K from double-resonance measurements," *The Journal of Physical Chemistry A*, vol. 109, no. 14, pp. 3111-9, 2005.
- [20] J. C. Corchado, J. L. Bravo, J. Espinosa-Garcia, "The hydrogen abstraction reaction  $\text{H}+\text{CH}_4$ . I. New analytical potential energy surface based on fitting to ab initio calculations," *The Journal of Chemical Physics*, vol. 130, no.18, pp. 184314, 2009.
- [21] H. Hoshina, M. Fushitani, T. Momose, "Infrared spectroscopy of rovibrational transitions of methyl radicals ( $\text{CH}_3$ ,  $\text{CD}_3$ ) in solid parahydrogen," *Journal of Molecular Spectroscopy*, vol. 268, no.1-2, pp. 164-72, 2011.

- [22] D. A. McQuarrie, J. D. Simon, *Physical Chemistry: A Molecular Approach*, University Science Books Sausalito, CA, 1997.
- [23] F. Kumsar, "Investigation of the rotation-vibration energies of diatomic and polyatomic molecules by approximation method," Hitit University, 2015.
- [24] P. Maroni, "Bond-and mode-specific reactivity of methane on Ni (100)," Pisa University, EPFL, 2005.
- [25] W. Kauzmann, *Kinetic Theory of Gases*, Courier Corporation, 2012.
- [26] R. Sanderson, *Chemical Bonds and Bonds Energy*, Elsevier, 2012.
- [27] C. K. Law, *Combustion Physics*, Cambridge University Press, 2010.
- [28] M. Brouard, D. H. Parker, S. Y. Van de Meerakker, "Taming molecular collisions using electric and magnetic fields," *Chemical Society Reviews*, vol. 43, no. 21, pp. 7279-94, 2014.
- [29] A. Laganà, G. A. Parker, *Chemical Reactions: Basic Theory and Computing*, Springer, 2018.
- [30] A. Domínguez, B. Fidalgo, Y. Fernández, J. Pis, J. Menéndez, "Microwave-assisted catalytic decomposition of methane over activated carbon for CO<sub>2</sub>-free hydrogen production," *International Journal of Hydrogen Energy*, vol. 32, no. 18, pp. 4792-9, 2007.
- [31] Y. Y. Tanashev, V. I. Fedoseev, Y. I. Aristov, V. V. Pushkarev, L.B. Avdeeva, V. I. Zaikovskii, V. N. Parmon, "Methane processing under microwave radiation: Recent findings and problems," *Catalysis Today*, vol. 42, no. 3, pp. 333-6, 1998.
- [32] W. H. Chen, H. J. Liou, C. I. Hung, "A numerical approach of interaction of methane thermocatalytic decomposition and microwave irradiation," *International Journal of Hydrogen Energy*, vol. 38, no. 30, pp. 13260-71, 2013.
- [33] A. G. Smolin, O. S. Vasyutinskii, G. G. Balint-Kurti, A. Brown, "Photodissociation of HBr. 1. Electronic structure, photodissociation dynamics, and vector correlation coefficients," *The Journal of Physical Chemistry A*, vol. 110, no.16, pp.5371-8, 2006.
- [34] N. H. Nahler, R. Baumfalk, U. Buck, H. Vach, P. Slavíček, P. Jungwirth, "Photodissociation of HBr in and on Ar n clusters: the role of the position of the molecule," *Physical Chemistry Chemical Physics*, vol. 5, no. 16, pp. 3394-401, 2003.
- [35] P. M. Regan, S. R. Langford, A. J. Orr-Ewing, M. N. Ashfold. "The ultraviolet photodissociation dynamics of hydrogen bromide," *The Journal of Chemical Physics*, vol. 110, no. 1, pp. 281-8, 1999.
- [36] V. Belyi, N. Kondratyuk, A. Shagov, A. Mashchenko, "Parametric amplification of light in a BBO crystal with pumping by YAG: Nd laser radiation," *Journal of Applied Spectroscopy*, vol. 67, pp. 364-8, 2000.
- [37] K. Semwal, S. Bhatt, "Tuning of wavelengths for producing eye safe laser using second order nonlinear processes," *International Journal of Optics and Applications*, vol. 2, no. 3, pp. 20-8, 2012.
- [38] Y. R. Luo, *Comprehensive Handbook of Chemical Bond Energies*, CRC Press, 2007.





SAKARYA ÜNİVERSİTESİ

# FEN BİLİMLERİ ENSTİTÜSÜ DERGİSİ

Sakarya University Journal of Science  
SAUJS

ISSN 1301-4048 | e-ISSN 2147-835X | Period Bimonthly | Founded: 1997 | Publisher Sakarya University |  
<http://www.saujs.sakarya.edu.tr/>

Title: Investigating the Role of Bias Correction Methods and Climate Models on Water Budget of Büyük Menderes Basin

Authors: Zülküf İbrahim ERKOL, İrem DALOĞLU ÇETİNKAYA

Received: 2022-06-02 00:00:00

Accepted: 19.06.2023

Article Type: Research Article

Volume: 27

Issue: 5

Month: October

Year: 2023

Pages: 975-986

How to cite

Zülküf İbrahim ERKOL, İrem DALOĞLU ÇETİNKAYA; (2023), Investigating the Role of Bias Correction Methods and Climate Models on Water Budget of Büyük Menderes Basin. Sakarya University Journal of Science, 27(5), 975-986, DOI: 10.16984/saufenbilder.1125240

Access link

<https://dergipark.org.tr/tr/journal/1115/issue/80257/1125240>

New submission to SAUJS

<http://dergipark.gov.tr/journal/1115/submission/start>

## Investigating the Role of Bias Correction Methods and Climate Models on Water Budget of Büyük Menderes Basin

Zülküf İbrahim ERKOL<sup>1</sup> , İrem DALOĞLU ÇETİNKAYA<sup>1\*</sup> 

### Abstract

Büyük Menderes Basin is one of the largest basins in Turkey, with almost half of the basin area utilized for agricultural purposes. The amount of water allocated to the agricultural areas in the basin corresponds to 80% of water use in the watershed. Hence, the impact of climate change on the water supply in the Büyük Menderes Basin will be significant for the basin. In this study, we model the effects of climate change on the water budget (water supply and demand balance) of the Büyük Menderes Basin using the Water and Evaluation and Planning (WEAP) tool. Future precipitation, temperature, and evaporation data for the basin are attained from outputs of the HadGEM2-ES global circulation model (GCM), along with CNRM-CM5.1 and GFDL-ESM2M regional circulation models (RCM) for RCP 4.5 and RCP 8.5 scenarios. Subsequently, the study applies different statistical bias correction methods (Linear Scaling (LS), Distribution Mapping (DM), Local Precipitation Scaling (PLIS), and Power Transformation of Precipitation (PTP) for raw outputs of GCMs and RCMs and analyzes the changes in outcomes of projected climate data and the impact of changes on the hydrology of the basin using the WEAP model. For this analysis, calibrated and validated WEAP model for the 12 reservoirs of Büyük Menderes Basin is used to understand the impact of different bias correction methods on reservoir levels.

**Keywords:** Büyük Menderes Basin, climate models, WEAP, bias correction methods, water budget

### 1. INTRODUCTION

Due to climate change, extreme events like floods, droughts, and heat waves have increased. Therefore, modeling these impacts on surface water become more vital as we observe the ecosystem impacts of climate change more vividly. The success in modeling the climate change impacts also depends on the reliability of climate change projection

data. For climate projection data, Global Circulation Models (GCMs) and Regional Circulation Models (RCMs) are used to quantitatively assess changes in climate conditions [1].

The resolution of GCMs varies from 12 km to 100 km, and they are at global or regional scales [2]. The coarse resolutions of GCMs do not match the fine-scale resolution of the

\* Corresponding author: irem.daloglu@boun.edu.tr (İ DALOĞLU ÇETİNKAYA)

<sup>1</sup> Boğaziçi University, Institute of Environmental Sciences, Istanbul, Türkiye

E-mail: ibrahim.erkol@boun.edu.tr

ORCID: <https://orcid.org/0000-0002-9456-4610>, <https://orcid.org/0000-0002-9923-9032>



hydrological models, which are built at the basin scale [3-4]. To overcome this challenge, RCMs with higher spatial resolution have been developed. The resolution of RCMs rises proportionately with increasing computational power. Currently, RCMs with 5 km resolution are more in use. However, datasets with this highest resolution are not available for regions such as the Middle East and North Africa (MENA) [5-8]. Therefore, for studying climate change impacts at finer scales, such as at the watershed scale, it is necessary to perform downscaling methods to produce local-scale, bias-corrected, and finer-resolution climate datasets based on the outputs of GCMs and RCMs [9].

Aside from the relatively coarse resolution of GCMs and RCMs, the constraints of climate models, such as simplification of real-world physics (as an inevitable feature of all models), incomplete knowledge of the Earth's climate system, and impact of model bias on climate assessments make downscaling indispensable for climate change impact studies [10]. In this study we use outputs of HadGEM2-ES (GCM), along with CNRM-CM5.1 and GFDL-ESM2M (RCMs). HadGEM2-ES is developed by the UK Met Office and combines an atmosphere-ocean-land-sea ice model, providing a comprehensive understanding of the climate system. CNRM-CM5.1 is a model developed by France's National Centre for Meteorological Research (CNRM) that simulates the interactions between the atmosphere, oceans, land surface, and sea ice. GFDL-ESM2M, developed by the Geophysical Fluid Dynamics Laboratory (GFDL) in the United States, is renowned for its ability to capture complex climate processes, making it a valuable tool in climate change studies.

In terms of climate scenarios, our models considered two climate projections, namely RCP 4.5 and RCP 8.5. These scenarios are developed by the Intergovernmental Panel on Climate Change (IPCC) to explore

potential future trajectories of greenhouse gas emissions and their impact on the Earth's climate. RCP 4.5 addresses a more safe discharge pathway, expecting that global greenhouse gas emissions peak around the year 2040 and afterward decline. The implementation of significant mitigation measures and a shift toward cleaner energy sources are assumed in this scenario. RCP 8.5, on the other hand, is a high-emission pathway whose greenhouse gas emissions will continue to rise throughout the 21st century, causing significant effects on climate change. This situation expects a future with restricted climate policies and heavy dependence on fossil fuels. Higher temperatures, rising sea levels, and widespread disruptions to ecosystems are all depicted in RCP 8.5 as future climate conditions become more severe.

Two methods of downscaling for bias correction (BC) purposes are statistical and dynamic downscaling [11]. For both methods, the goal is to transform or map outputs of the future simulated models into the observation domain, with the help of utilizing the relationship between the observations and the model value for the base/historical period [12].

Given the importance of the operation of downscaling in climate change impact studies, this study focuses on the effects of downscaling methods on the water budget of BMB under different climate scenarios and models. At this point, Water and Evaluation and Planning (WEAP) is advantageous because the WEAP model comprehensively takes into account both the water supplies (inflows) computed through watershed-scale hydrologic processes along with water demands (outflows) coming from various water users and environmental requirements. The watershed and the physical network of reservoirs govern the hydrological modeling process. In doing so, WEAP calculates the water budget at the watershed scale and is widely used to assess the impacts of climate change on water resources at the watershed

scale [13-15]. In addition, WEAP can operate on watersheds of large geographic scales and spatially scattered water demand sites [16]. Considering that BMB occupies an area of around 25,000 km<sup>2</sup> and that there are scattered demand sites across the basin, WEAP is a suitable hydrological modeling tool [17].

## 2. STUDY AREA

Büyük Menderes Basin is the 8th largest basin in Turkey and occupies an area of about 25,000 km<sup>2</sup> [17]. The drainage area of BMB corresponds to approximately 3% of the country [18]. The Büyük Menderes River originates near the Dinar district of Afyon and flows into the Aegean Sea, flowing through Uşak, Denizli, and Aydın (Figure 1). While almost half of the basin area is currently utilized for agricultural purposes, the amount of water allocated to the agricultural areas in the basin corresponds to 80% of the water use in the basin [19]. During 1975 and 2009, the average summer temperature in the basin was around 23-26 °C, and the average winter temperature was around 5-7 °C. During the

same period, the annual precipitation rate was approximately 600 mm. Both temperature and precipitation rates are relatively higher in Aydın and Muğla compared to Uşak and Denizli, situated upstream of the basin [20]. The cities Aydın, Denizli, Muğla, and Uşak located inside BMB consist of around 90% of the total basin area [18]. Among the cities occupying most of BMB, Aydın, Denizli, and Muğla accommodate the major reservoirs in the watershed. There are currently 12 reservoirs in the basin whose storage capacities, initial storage values, and size of irrigation areas are given in Table 1 [21].

## 3. METHOD

### 3.1. WEAP

WEAP is a physical modeling tool for estimating the water budget of watersheds under changing hydrological conditions and policy scenarios [22]. WEAP simulates the water budget of the watershed by incorporating both climatic conditions and water use behaviors [23-24].

Table 1 Capacities and establishment years of reservoirs in BMB, Source: Adapted from [21]

	Reservoir Capacity (million m <sup>3</sup> )	Initial Storage at the year of establishment (million m <sup>3</sup> )	Planned Irrigation Area (ha)	Establishment Year
Kemer	419,17	123.847	58.930	1958
Yaylakavak	31,42	3.294	3.348	1997
Topçam	97,74	25.986	4.983	1985
Çine	350,00	221.814	22.358	2010
Karacasu	17,2	9.342	2.814	2012
İkizdere	194,96	83.131	3.625	2009
Adıgüzel	1.076,00	477.526	78.060	1990
Işıklı	237,8	72.335	50.486	1953
Gökpınar	27,72	12.219	5.824	2002
Cindere	84,27	59.249	78.060	2008
Tavas	65,00	51.135	3.304	2010
Bayır	7,17	1.919	1.050	2008
Total	2.608,45	1.141.197	312.842	

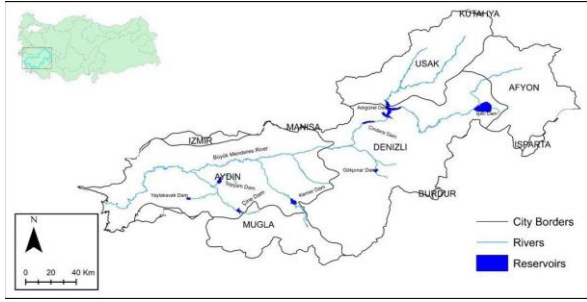


Figure 1 Map of BMB with water supplies and city borders, Source: Adapted from [21]

As a water budget model tool, WEAP requires datasets of water supply and demand for the area of interest. With these datasets, WEAP creates a water account that consists of water supply from different resources (i.e. aquifers, groundwater resources, and reservoirs) and water demand of various agents/users such as industry, municipalities, households, and agricultural production [25]. An advantage of WEAP is to rank the priority level of each demand node [22], giving the modelers the flexibility to predetermine a rule that dictates meeting a particular demand (i.e., household water need) over other water demand types. In doing so, WEAP allows its users to represent the study areas' characteristics and enables them to create a wide range of scenarios where users can test the impacts of various priority-driven policies in the watershed of interest. Once the basin's water budget is calibrated and validated, these models are also used for forecasting purposes [22].

### 3.2. Downscaling Methods

Downscaling aims to transform or map outputs of the future simulated model into the observation domain with the help of utilizing the relationship between the observations and the model value for the base/historical period [26]. Dynamic downscaling (DD) reanalyzes the outputs of GCMs or RCMs to produce localized climate datasets through models, such as Limited Area Models [27]. Carrying out dynamical downscaling involves interactions between different elements of climate systems, such as precipitation and temperature. Therefore, it is computationally intensive and time demanding [28].

Statistical downscaling is a method of establishing statistical relationships between historical and current large-scale atmospheric and local climate variables. Subsequently, future climate variables that GCMs/RCMs project are used to forecast future local climate data [29]. In the literature, the prevalently utilized SD methods are quantile mapping (QM), delta change/correction (DC) approach, statistical downscaling method (SDSM), linear scaling (LS), distribution mapping (DM), local intensity scaling (LOCI), and power transformation of precipitation (PTP) [30-34]. This study will compare the performances of LS, PTP, LOCI, and DM methods in terms of their improvements in climate projection data.

Linear Scaling (LS) is a statistical method to match the mean of downscaled data with the observed data [35] and has been used in various climate change impact studies [36-39]. Using the differences between the observed and simulated data obtained directly from GCMs and RCMs, LS operates with monthly downscaling values. Precipitation is corrected with a multiplier term and temperature with an additive term on a monthly basis. In Equations 1 and 2,  $P_{down,m,d}$  and  $T_{down,m,d}$  represent corrected precipitation and temperature values respectively on the  $d^{th}$  day of the  $m^{th}$  month. Besides,  $P_{raw,m}$  and  $T_{raw,m}$  denote raw simulated precipitation and temperature values sequentially on the month's  $d^{th}$ . Lastly,  $\mu()$  indicates the expectation function. For instance,  $\mu(T_{obs,m})$  represents the mean value of observed temperature at month  $m$  [40].

$$P_{down,m,d} = P_{raw,m} * \mu(P_{obs,m}) / \mu(P_{raw,m}) \quad (1)$$

$$T_{down,m,d} = T_{raw,m} + \mu(T_{obs,m}) - \mu(T_{raw,m}) \quad (2)$$

Power transformation of precipitation (PTP) can be carried through several software packages available in the literature, such as CMhyd and Powertransformation v2.0 [41-43]. The main advantage of this method is that, unlike LS (correcting the biases solely in the mean), PTP also corrects the coefficient of variation defined as the ratio between sample

standard deviation and sample mean [44]. The algorithm through which PTP carries out the correction operations is based on a non-linear transformation. In Equation 3, the power "b" is predicted monthly with a 90-day window centered on the interval with a root-finding algorithm. Consequently,  $P^b$  is multiplied by the coefficient obtained by dividing the monthly mean observed precipitation by the monthly mean powered projected precipitation [45].

$$P^* = a * P^b \quad (3)$$

The Local Intensity Scaling (LOCI) Method for Precipitation amends frequencies and intensities of wet days and thus improves the raw data with drizzle days [46]. This method validates the precipitation intensity threshold ( $P_{thres,m}$ ) for each month. This way, it is assured that the number of days exceeding a threshold for the simulation model matches the wet-day frequency of the observation data. Consequently, a scaling factor ( $S_m$ ) is computed, so that the mean of the corrected rainfall equals the mean of the observed rainfall (Equations 4 and 5) [40].

$$S_m = \frac{\mu(P_{obs,m,d} | P_{obs,m,d} > 0)}{\mu(P_{raw,m,d} | P_{raw,m,d} > P_{thres,m})} \quad (4)$$

$$P_{cor,m,d} = \begin{cases} 0 & \text{if } P_{raw,m,d} < P_{thres,m} \\ P_{raw,m,d} & \text{if } P_{raw,m,d} \geq P_{thres,m} \\ P_{raw,m,d} * S_m & \text{otherwise} \end{cases} \quad (5)$$

Lastly, distribution mapping (DM) is another widely utilized downscaling method for processing projected climate change data [44] to align the distribution function of observation data with the raw data [45]. DM matches the standard deviation, mean, and quantiles of both datasets, raw/unprocessed, and observation [40]. For precipitation, a gamma distribution with parameter  $\alpha$  and scale parameter  $\beta$  is used (Equation 6).

$$f(x | \alpha, \beta) = x^{\alpha-1} * \frac{1}{\beta^\alpha} * e^{-x/\beta} ; \quad x \geq 0, \alpha, \beta > 0 \quad (6)$$

Consequently, the threshold for a wet day in the LOCI method comes into play before applying DM so that the effects of the days with little precipitation (drizzle effects) are minimized. After applying the threshold used for the LOCI method, the corrected precipitation values are removed from the drizzle effect (Equation 7). In the formulation,  $F_\gamma$  and  $F_\gamma^{-1}$  represent Gamma cumulative distribution functions and their inverse, respectively [29].

$$P_{cor,m,d} = F_\gamma^{-1} (F_\gamma (P_{LOCI,m,d} | \alpha_{LOCI,m}, \beta_{LOCI,m}) | \alpha_{obs,m}, \beta_{obs,m}) \quad (7)$$

For water budget calculations, the WEAP model requires climate (temperature and precipitation) data at the local scale. The downscaling methods provide local-scale, bias-corrected, and finer resolution climate datasets based on the outputs of GCMs and RCMs.

This study uses the precipitation dataset obtained from the Turkish State Meteorological Service. The study area covers three cities in BMB, namely Aydın, Denizli, and Muğla (Table 2). The future climate data are spatially averaged for each city within given coordinates (Table 2)

Table 2 Meteorological stations for data collection in the historical/observed period and the coordinates for future climate data

City	Station Code	Turkish State Meteorological Service Station Coordinates	Coordinates for GCM and RCM climate data
Aydın	17234	37.84 N, 27.83 E	27.28-28.6E, 37.5-38N
Denizli	17237	37.76 N, 29.09 E	28.6-29.9E, 37.15-38.3N
Muğla	17292	37.2 N, 28.36 E	27.6-28.7E, 37-37.5N

## 4. RESULTS

The climatic parameters such as temperature, precipitation, and evapotranspiration are significant determinants of the water budget at

the watershed scale. Understanding the impacts of climate change on the water budget requires precise prediction of these parameters. Hence different downscaling methods and their particular effects on climatic variables need to be studied. In doing so, we use the already calibrated and validated WEAP model developed for the Büyük Menderes Basin and its 12 reservoirs [21]. The existing model has satisfactory model evaluation and can be used to understand the impacts of future climate change projections for RCP 4.5 and RCP 8.5 scenarios of various GCM (HADGEM2-ES) and RCMs (CNRM-CM5.1 and GFDL-ESM2M). Our study reports future precipitation values for the cities that lie within the Büyük Menderes Basin (Aydın, Denizli, Muğla, Uşak) using different downscaling methods. As a representative case, in Figures 2-5 we demonstrate future precipitation values for Aydın using DM downscaling method for the CNRM-CM5.1 model (RCP 4.5 scenario) dataset. The Appendix section demonstrates the precipitation data of Aydın and Denizli downscaled using the downscaling methods for 3 GCM/RCM and for two scenarios (RCP 4.5 and RCP 8.5).

For this analysis, the impacts of different downscaling methods using different GCMs and RCMs outputs are measured by investigating the changes in reservoir volumes. In the BMB, 12 reservoirs have different storage capacities and average annual total volumes (Table 1). The average of 12 reservoirs' total volume in BMB from 2005 to 2018 was 1.49 billion cubic meters per year with annual fluctuations. Figure 6 shows the historical change in the overall reservoir storage volume in BMB for 2005 to 2018 [21].

**CNRM Monthly Precipitation Corrected by DM for Aydın in RCP4.5**

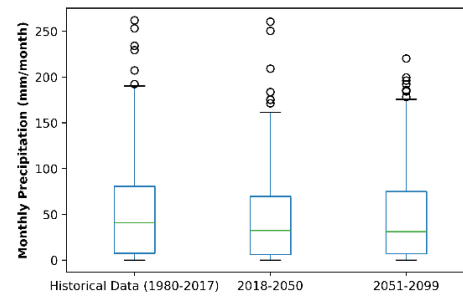


Figure 2 Average precipitation change by 2100 in Aydın with CNRM data under RCP4.5 scenario, using DM correction method

**CNRM Monthly Precipitation Corrected by LS for Aydın in RCP4.5**

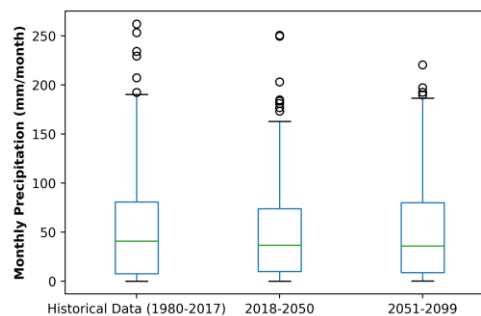


Figure 3 Average precipitation change by 2100 in Aydın with CNRM data under RCP4.5 scenario, using LS correction method

**CNRM Monthly Precipitation Corrected by PLIS for Aydın in RCP4.5**

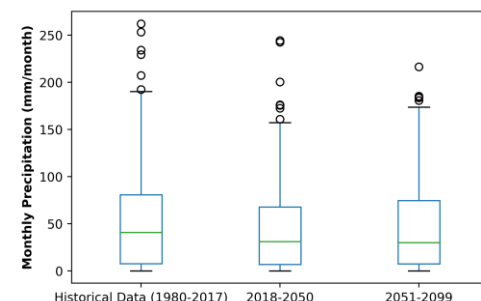


Figure 4 Average precipitation change by 2100 in Aydın with CNRM data under RCP4.5 scenario, using PLIS correction method

For the simulation period of 2019-2099 with all three circulation models, the WEAP model takes downscaled and bias corrected precipitation data from GCM (HADGEM2-ES) and RCMs (CNRM-CM5.1 and GFDL-ESM2M) as input and projects changes in the total amount of water in the reservoirs (compared to the historical total average).

CNRM Monthly Precipitation Corrected by PTP for Aydın in RCP4.5

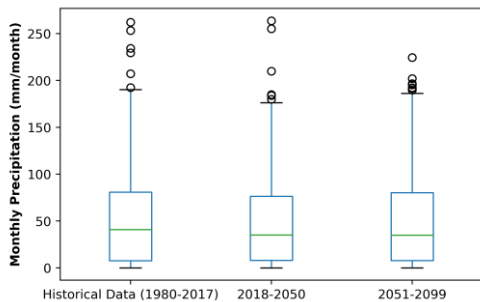


Figure 5 Average precipitation change by 2100 in Aydın with CNRM data under RCP4.5 scenario, using PTP correction method

The most significant reduction among the three models is observed with the HADGEM2-ES model dataset. Under the RCP4.5 and RCP 8.5 scenarios, the results with the HADGEM2-ES indicate a 6%-7% decrease from the historical average when downscaled with DM method.

Table 3 Average changes in total reservoir volume when different downscaling methods were applied to GCM and RCM models under RCP4.5 scenario

	DM RCP4. 5	LS RCP4. 5	PLIS RCP4. 5	PTP RCP4. 5
CNRM- CM5.1	-5.43%	-5.22%	-5.80%	-5.05%
GFDL- ESM2M	-5.17%	-4.57%	-5.43%	-4.54%
HADGEM 2-ES	-6.83%	-3.34%	-5.36%	-3.45%

However, different statistical downscaling methods yield highly different results, especially for the HADGEM2-ES model. The results obtained with HADGEM2-ES show that, under the RCP4.5 scenario, a reduction of 3% and 7% - with respect to average baseline volume is observed during the simulation period range depending on the downscaling method applied. The downscaled CNRM-CM5.1 dataset demonstrate a 5% lower reservoir water volume than the historical average volume rates. Additionally, for CNRM-CM5.1 and GFDL-ESM2M datasets, different bias methods does not indicate significant differences. Under the RCP4.5 scenario, the total reservoir volume

decrease around 5% with all downscaling methods (Table 3).

Table 4 Average changes in total reservoir volume when different downscaling methods were applied to GCM and RCM models under RCP8.5 scenario

	DM RCP8. 5	LS RCP8. 5	PLIS RCP8. 5	PTP RCP8. 5
CNRM- CM5.1	-5.06%	-4.80%	-5.10%	-4.86%
GFDL- ESM2M	-6.51%	-5.48%	-6.09%	-5.71%
HADGEM 2-ES	-6.95%	-4.09%	-5.87%	-4.19%

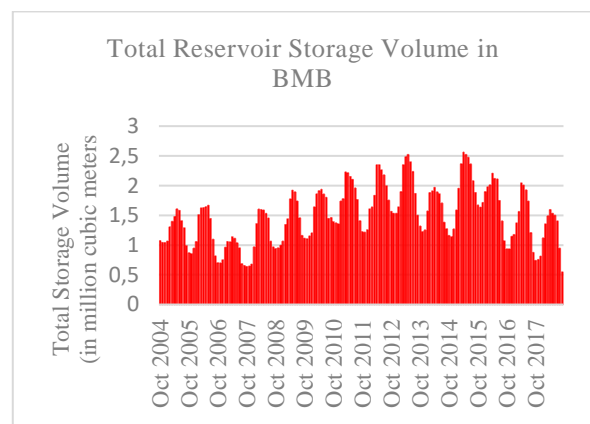


Figure 6 Total reservoir storage volume during 2005-2018 observation period, Source: Adapted from [21]

Similarly, under the RCP8.5 scenario, the results indicate an approximately 6% decline for all downscaling methods (Table 4). In other words, the RCM-based (CNRM-CM5.1 and GFDL-ESM2M) results are not significantly impacted by the choice of downscaling methods. However, for GCM-based (HADGEM2-ES) results, the choice of downscaling methods significantly impact the total reservoir volume (Tables 3 and 4).

Taylor diagrams in the Appendix section (Figures 45 and 46) demonstrate the improvement rates by applying different downscaling methods for GCM/RCMs. These figures demonstrate that the downscaling method is evidently influential in the outputs of HADGEM2-ES. While the Pearson coefficient between the raw data of the HADGEM2-ES model and the observed



historical precipitation data was 0.1, the value of this coefficient increases to almost 0.5 with the application of different bias correction methods. The most remarkable improvement for the Pearson coefficient is with the Power Transformation of Precipitation (PTP) method. However, the outputs of the CNRM-CM5.1 along with GFDL-ESM2M models are not influenced by the statistical bias correction processes as much as the outputs of HADGEM2-ES. Pearson coefficients of both models are approximately 0.4 with raw (not processed) RCM outputs and increase to 0.50 – 0.55 in the post-correction period.

## 5. CONCLUSION

Climate change has been threatening the existing freshwater resources, complicating the management issues and requiring adaptation measures to be devised. Increased frequency of extreme events (floods, droughts) augments the need for precise future projections. However, one of the most critical factors influential in the reliability and robustness of a model is the accuracy of climate change projection data. Compared to the scale of climate change impact studies on freshwater systems, the resolution of climate change data are still relatively coarser despite advancements in the last decades. Therefore, downscaling climate change data is vital in determining the success of modeling studies. This study reveals the impact of the downscaling method chosen on simulation results. The outputs of projection data are from GCM HADGEM2-ES, along with RCMs CNRM-CM5.1 and GFDL-ESM2M. Besides, this study investigates DM, LS, PLIS, and PTP as downscaling methods and shows that the downscaling method has an impact on the outputs of HADGEM2-ES dataset the most. Outputs of HADGEM2-ES indicate significant differences depending on the different downscaling methods. Under the RCP4.5 and RCP8.5 scenarios, average reservoir volume during the simulation period show a difference between 3% and 7% with respect to the average observed volume.

On the other hand, the results obtained with outputs of CNRM-CM5.1 and GFDL-ESM2M indicate a 5% lower reservoir water volume compared to the historical average volume rates. For the RCM models (CNRM-CM5.1 and GFDL-ESM2M), the downscaling methods are less influential.

### *Acknowledgments*

The authors would like to Onur Cem Yoloğlu and Kamil Çöllü for their support in processing climate data.

### *Funding*

The authors have not received any financial support for the research, authorship or publication of this study.

### *Authors' Contribution*

The authors' contribution is as follows: ZIE: Methodology, Validation, Visualization, Writing, and IDC: Conceptualisation, Methodology, Writing, Supervision

### *The Declaration of Conflict of Interest/ Common Interest*

No conflict of interest or common interest has been declared by the authors.

### *The Declaration of Ethics Committee Approval*

This study does not require ethics committee permission or any special permission.

### *The Declaration of Research and Publication Ethics*

The authors of the paper declare that they comply with the scientific, ethical and quotation rules of SAUJS in all processes of the paper and that they do not make any falsification on the data collected. In addition, they declare that Sakarya University Journal of Science and its editorial board have no responsibility for any ethical violations that may be encountered, and that this study has not been evaluated in any academic publication environment other than Sakarya University Journal of Science.

## REFERENCES

- [1] S. Hagemann, C. Chen, J. O. Haerter, J. Heinke, D. Gerten, C. Piani, "Impact of a statistical bias correction on the projected hydrological changes obtained from three gcms and two hydrology models," *Journal of Hydrometeorology*, vol. 12, no. 4, pp. 556–578, 2011.
- [2] H. Chen, C.-Y. Xu, S. Guo, "Comparison and evaluation of multiple GCMS, statistical downscaling and hydrological models in the study of climate change impacts on runoff," *Journal of Hydrology*, vol. 434-435, pp. 36–45, 2012.
- [3] T. Olsson, M. Kämäräinen, D. Santos, T. Seitola, H. Tuomenvirta, R. Haavisto, W. Lavado-Casimiro, "Downscaling climate projections for the Peruvian coastal Chancay-Huaral Basin to support river discharge modeling with Weap," *Journal of Hydrology: Regional Studies*, vol. 13, pp. 26–42, 2017.
- [4] S. Yuan, S. M. Quiring, M. M. Kalcic, A. M. Apostel, G. R. Evenson, H. A. Kujawa, "Optimizing Climate Model Selection for Hydrological Modeling: A case study in the Maumee River basin using the Swat," *Journal of Hydrology*, vol. 588, pp. 1–14, 2020.
- [5] F. Driouech, K. ElRhaz, W. Moufouma-Okia, K. Arjald, S. Balhane, "Assessing future changes of climate extreme events in the Cordex-MENA region using regional climate Model Aladin-Climate," *Earth Systems and Environment*, vol. 4, no. 3, pp. 477–492, 2020.
- [6] M. Rummukainen, "Added value in regional climate modeling," *WIREs Climate Change*, vol. 7, no. 1, pp. 145–159, 2015.
- [7] B. Rockel, "The Regional Downscaling Approach: A brief history and recent advances," *Current Climate Change Reports*, vol. 1, no. 1, pp. 22–29, 2015.
- [8] S. Shamshirband, A. Mosavi, Narjes Nabipour, K.-wing Chau, "Application of ERA5 and MENA simulations to predict offshore wind energy potential," arXiv, 2020.
- [9] R. L. Wilby, T. M. Wigley, D. Conway, P. D. Jones, B. C. Hewitson, J. Main, D. S. Wilks, "Statistical downscaling of General Circulation Model Output: A comparison of methods," *Water Resources Research*, vol. 34, no. 11, pp. 2995–3008, 1998.
- [10] F. Dierickx, "Copernicus Climate Change Programme: User Learning Service content," Bookdown, 28-Apr-2019. [Online]. Available: <https://bookdown.org/floriandierickx/bookdown-demo/>. [Accessed: 28-May-2022].
- [11] H. J. Fowler, S. Blenkinsop, C. Tebaldi, "Linking climate change modelling to impacts studies: Recent advances in downscaling techniques for hydrological modelling," *International Journal of Climatology*, vol. 27, no. 12, pp. 1547–1578, 2007.
- [12] T. Lee, V. P. Singh, "Statistical downscaling for hydrological and environmental applications," in *Statistical downscaling for Hydrological and environmental applications*, Boca Raton, FL, US: CRC Press, Taylor & Francis Group, 2019, pp. 39–50.
- [13] S. Agarwal, J. P. Patil, V. C. Goyal, A. Singh, "Assessment of water supply–demand using water evaluation and planning (WEAP) model for Ur River watershed, Madhya Pradesh, India," *Journal of The Institution of Engineers*

- (India): Series A, vol. 100, no. 1, pp. 21–32, 2018.
- [14] H. Ayt Ougougdal, M. Yacoubi Khebiza, M. Messouli, A. Lachir, "Assessment of future water demand and supply under IPCC climate change and socio-economic scenarios, using a combination of models in Ourika watershed, High Atlas, Morocco," *Water*, vol. 12, no. 6, pp. 1–18, 2020.
- [15] B. Höllermann, S. Giertz, B. Diekkrüger, "Benin 2025—balancing future water availability and demand using the WEAP 'water evaluation and planning' system," *Water Resources Management*, vol. 24, no. 13, pp. 3591–3613, 2010.
- [16] J. Gao, P. Christensen, W. Li, "Application of the WEAP model in Strategic Environmental Assessment: Experiences from a case study in an arid/semi-arid area in China," *Journal of Environmental Management*, vol. 198, pp. 363–371, 2017.
- [17] DSİ, "Toprak ve Su Kaynakları," Devlet Su İşleri Genel Müdürlüğü, 2010. [Online]. Available: <http://www.dsi.gov.tr/topraksu.htm>. [Accessed: 28-May-2022].
- [18] T.C. Çevre ve Şehircilik Bakanlığı Çevre Yönetimi Genel Müdürlüğü. (2016). Büyük Menderes Havzası Kirlilik Önleme Eylem Planı. Ankara.
- [19] Büke, A., Gültekin, M., Aksoy, M., Dıvrak, A., Göcek, B. B., Berke, Ç., Çeşmeci, H., 2013. Büyük Menderes Havza Atlası.
- [20] TÜBİTAK, "Büyük Menderes Havzası Eylem Plan Raporu," Tarım ve Orman Bakanlığı Su Yönetimi Genel Müdürlüğü, 2010. [Online]. Available: <https://www.tarimorman.gov.tr/SYGM>. [Accessed: 28-May-2022].
- [21] Z. İ. Erkol, "Modelling the Impacts of Climate Change on Water Supply and Demand Balance of Büyük Menderes Basin," thesis, 2020.
- [22] D. Yates, J. Sieber, D. Purkey, A. Huber-Lee, "Weap21—a demand-, priority-, and preference-driven water planning model," *Water International*, vol. 30, no. 4, pp. 487–500, 2005.
- [23] L. Yang, M. Hao, Q. Cao, K. Liu, L. Xiao, L. Pei, X. Wu, "Quantitative impact and research on Water Supply Management and demand in Beijing under the WEAP model," *IOP Conference Series: Earth and Environmental Science*, vol. 514, no. 2, 2020.
- [24] J. Sieber, D. Purkey, WEAP-Water Evaluation and Planning System: User Guide for WEAP. Stockholm Environment Institute-US Center, Somerville, 2015
- [25] R. A. Pielke, "Examples of mesoscale models," *International Geophysics*, pp. 427–500, 2013.
- [26] Z. Xu, Y. Han, Z. Yang, "Dynamical downscaling of regional climate: A review of methods and limitations," *Science China Earth Sciences*, vol. 62, no. 2, pp. 365–375, 2018.
- [27] S. Trzaska, E. Schnarr, "A Review of Downscaling Methods for Climate Change Projections," Ciesin, 2014. [Online]. Available: [http://www.ciesin.org/documents/Downscaling\\_CLEARED\\_000.pdf](http://www.ciesin.org/documents/Downscaling_CLEARED_000.pdf). [Accessed: 28-May-2022].
- [28] M. A. Faiz, D. Liu, Q. Fu, M. Li, F. Baig, A. A. Tahir, M. I. Khan, T. Li, S. Cui, "Performance evaluation of hydrological models using ensemble of general circulation models in the northeastern China," *Journal of*

- Hydrology, vol. 565, pp. 599–613, 2018.
- [29] M. Luo, T. Liu, F. Meng, Y. Duan, A. Frankl, A. Bao, P. De Maeyer, "Comparing bias correction methods used in downscaling precipitation and temperature from regional climate models: A case study from the Kaidu River basin in western China," *water*, vol. 10, no. 8, p. 1046, 2018.
- [30] M. Mendez, B. Maathuis, D. Hein-Griggs, L.-F. Alvarado-Gamboa, "Performance evaluation of bias correction methods for climate change monthly precipitation projections over Costa Rica," *water*, vol. 12, no. 2, pp. 1–34, 2020.
- [31] M. Sharma, P. Coulibaly, Y. Dibike, "Assessing the need for downscaling RCM data for Hydrologic Impact Study," *Journal of Hydrologic Engineering*, vol. 16, no. 6, pp. 534–539, 2011.
- [32] M. Shrestha, S. C. Acharya, P. K. Shrestha, "Bias correction of climate models for hydrological modelling - are simple methods still useful?," *Meteorological Applications*, vol. 24, no. 3, pp. 531–539, 2017.
- [33] A. H. Azman, N. N. Tukimat, M. A. Malek, "Analysis of linear scaling method in downscaling precipitation and temperature," *Water Resources Management*, vol. 36, no. 1, pp. 171–179, 2021.
- [34] A. Casanueva, S. Herrera, J. Fernández, J. M. Gutiérrez, "Towards a fair comparison of statistical and dynamical downscaling in the framework of the euro-CORDEX initiative," *Climatic Change*, vol. 137, no. 3-4, pp. 411–426, 2016.
- [35] R. Mahmood, S. Jia, N. Tripathi, S. Shrestha, "Precipitation extended linear scaling method for correcting GCM precipitation and its evaluation and implication in the transboundary jhelum river basin," *Atmosphere*, vol. 9, no. 5, pp. 1–15, 2018.
- [36] M. Nasser, G. Schoups, M. Taheri, "A spatiotemporal framework to calibrate high-resolution global monthly precipitation products: An application to the Urmia Lake Watershed in Iran," *International Journal of Climatology*, vol. 42, no. 4, pp. 2169–2194, 2021.
- [37] G. H. Fang, J. Yang, Y. N. Chen, C. Zammit, "Comparing bias correction methods in downscaling meteorological variables for a hydrologic impact study in an arid area in China," *Hydrology and Earth System Sciences*, vol. 19, no. 6, pp. 2547–2559, 2015.
- [38] AgriMetsoft, "AgriMetSoft," Agricultural and meteorological software. [Online]. Available: <https://agrimetsoft.com/Default>. [Accessed: 28-May-2022].
- [39] H. Rathjens, K. Bieger, R. Srinivasan, I. Chaubey, J. G. Arnold, "CMhyd User Manual," Soil & Water Assessment Tool, 2016. [Online]. Available: [https://swat.tamu.edu/media/115265/bias\\_cor\\_man.pdf](https://swat.tamu.edu/media/115265/bias_cor_man.pdf). [Accessed: 28-May-2022].
- [40] Fang, G. H., Yang, J., Chen, Y. N., & Zammit, C.. Comparing bias correction methods in Downscaling meteorological variables for a hydrologic impact study in an arid area in China. *Hydrology and Earth System Sciences*, 19(6), 2547-2559, 2015.
- [41] R. Leander, T. A. Buishand, "Resampling of regional climate model output for the simulation of Extreme

- River flows," *Journal of Hydrology*, vol. 332, no. 3-4, pp. 487–496, 2007.
- [42] W. Terink, R. T. Hurkmans, P. J. Torfs, R. Uijlenhoet, "Evaluation of a bias correction method applied to downscaled precipitation and temperature reanalysis data for the Rhine Basin," *Hydrology and Earth System Sciences*, vol. 14, no. 4, pp. 687–703, 2010.
- [43] J. Schmidli, C. Frei, P. L. Vidale, "Downscaling from GCM precipitation: A benchmark for dynamical and statistical downscaling methods," *International Journal of Climatology*, vol. 26, no. 5, pp. 679–689, 2006.
- [44] X. Yuan, "An experimental seasonal hydrological forecasting system over the Yellow River basin – part 2: The added value from climate forecast models," *Hydrology and Earth System Sciences*, vol. 20, no. 6, pp. 2453–2466, 2016.
- [45] T. Zhao, J. C. Bennett, Q. J. Wang, A. Schepen, A. W. Wood, D. E. Robertson, M.-H. Ramos, "How suitable is quantile mapping for postprocessing GCM precipitation forecasts?," *Journal of Climate*, vol. 30, no. 9, pp. 3185–3196, 2017.



SAKARYA ÜNİVERSİTESİ

# FEN BİLİMLERİ ENSTİTÜSÜ DERGİSİ

Sakarya University Journal of Science  
SAUJS

ISSN 1301-4048 | e-ISSN 2147-835X | Period Bimonthly | Founded: 1997 | Publisher Sakarya University |  
<http://www.saujs.sakarya.edu.tr/>

Title: Classification of Forest Fires in European Countries by Clustering Analysis  
Techniques

Authors: Hakan SERİN, Muslu Kazım KÖREZ, Mehmet Emin TEKİN, Sinan SİREN

Received: 2023-04-26 00:00:00

Accepted: 2023-06-21 00:00:00

Article Type: Research Article

Volume: 27

Issue: 5

Month: October

Year: 2023

Pages: 987-1001

How to cite

Hakan SERİN, Muslu Kazım KÖREZ, Mehmet Emin TEKİN, Sinan SİREN; (2023),  
Classification of Forest Fires in European Countries by Clustering Analysis  
Techniques. Sakarya University Journal of Science, 27(5), 987-1001, DOI:  
10.16984/saufenbilder.1288073

Access link

<https://dergipark.org.tr/tr/journal/1115/issue/80257/1288073>

New submission to SAUJS

<http://dergipark.gov.tr/journal/1115/submission/start>

## Classification of Forest Fires in European Countries by Clustering Analysis Techniques

Hakan SERİN\*<sup>1</sup>, Muslu Kazım KÖREZ<sup>2</sup>, Mehmet Emin TEKİN<sup>1</sup>, Sinan SİREN<sup>3</sup>

### Abstract

The biggest threat to the forests, which are natural habitats in European countries, as they are in the whole world, is forest fires. The aim of this study is to group the 38 European countries which have completely accessible fire indexes between the years 2008 to 2022; with respect to their similarities in fire regimes; and to compare the obtained groups with respect to their fire indexes. The clustering technique, which is a data mining method, was used while making these comparisons since it would be more objective and realistic to group and evaluate the countries according to their similarities. In the K-Means technique 2 clusters, and in the Ward's method 3 clusters were obtained. In the K-Means technique, significant statistical differences were found between the 2 clusters in terms of all fire indexes ( $p < 0.05$ ). In the Ward's method, statistically significant differences were found between the clusters in terms of the number of fires, total area burned (ha) and woodland ( $p < 0.05$ ). In the result of the studies, the fire regimes in Turkey, Bosnia and Herzegovina, Ukraine, Italy, Spain, and Portugal resulted higher than the other countries in both clustering algorithms. Since many factors were taken into consideration in the study, countries heavily associated with fires such as Greece and France were separated from those with high fire regimes. It is recommended to conduct modelling studies with data mining algorithms by taking different fire indexes into account in order to increase the reliability of the results.

**Keywords:** Data mining method, ward method, k-means, cluster analysis, forest fire

### 1. INTRODUCTION

Forests play an active role in protecting the balance of nature, contributing to the country's economy, increasing biodiversity, and combating global warming. Fires are the largest factor affecting forest presence in the

world. When forest fires cannot be brought under control they can cause serious damage to bio-habitats, as well as vegetation; and cause the forest ecosystem to deteriorate [1, 2]. Although forest fires are a problem everywhere in the world, they may differ from region to region [3]. European countries have

\* Corresponding author: hakan.461995@gmail.com (H. SERİN)

<sup>1</sup> Selcuk University, Faculty of Veterinary Medicine, Department of Biostatistics, Konya, Türkiye

<sup>2</sup> Selcuk University, Faculty of Medicine, Department of Biostatistics, Konya, Türkiye

<sup>3</sup> Selcuk University, Faculty of Veterinary Medicine, Department of Physiology, Konya, Türkiye

E-mail: mkkorez@gmail.com, mtekin@selcuk.edu.tr, sinan.siren1996@gmail.com

ORCID: <https://orcid.org/0000-0002-1290-4547>, <https://orcid.org/0000-0001-9524-6115>, <https://orcid.org/0000-0002-3449-9984>, <https://orcid.org/0000-0003-2182-5047>



developed forest management programs in order to protect the existence of forests covering 110 million hectares (ha), and the biodiversity in them. However, 500.000 hectares of land are affected by forest fires in Europe every year [4, 5]. Although forest fires that only destroy a small area are beneficial for the renewal of nature, the negative effects are much worse when the fires spread over larger areas. Global warming, which has increased in recent years, and the resulting climate changes are altering forest fire regimes. The increase in dry vegetation in forests due to increased drought can be given as an example of this situation. All these reasons force countries to develop effective fire management strategies in the fight against forest fires [6].

The fires in forest areas not only cause economic damage to countries but also destroy the benefits of nature to human health.

Fires cause adverse reactions in some properties of the soil, both damaging the vegetation and also increasing the risks of natural disasters such as erosion and landslides. As a result of all these, the living spaces of the local people residing in the region are damaged, causing people to leave the region and thus change the social structure [7, 8].

Average amount of burning area and the average number of fires in the countries between 2010 and 2019 is given in Table 1. When Table 1 is examined, it is seen that Mediterranean countries are mostly in the top 5 among 26 European countries when the 10-year average amount of burned area and the number of fires is taken into account. The climate of the region, its vegetation, human-induced causes (arson, neglect), and tourism are conspicuous among the main reasons for this situation.

Table 1 Average amount of burning area and the average number of fires in the countries between 2010 and 2019 [9]

Ranking	Country	Burning Annual Average Amount of Area (ha)	Ranking	Country	Annual Average Number of Fires
1	Portugal	134307.6	1	Portugal	16800
2	Spain	94513.8	2	Spain	11859.9
3	Italy	63907.2	3	Poland	7188.2
4	Greece	24220.3	4	Italy	5419.6
5	France	12163.3	5	Sweden	4521.3
6	Croatia	11241.2	6	France	3907.4
7	Turkey	7332.1	7	Turkey	2477.3
8	Bulgaria	5266.4	8	Ukraine	1626.3
9	Hungary	4742.4	9	Czech Republic	1275.1
10	Sweden	4700	10	Finland	1260
11	North Macedonia	4473.5	11	Hungary	1218.3
12	Ukraine	3369.1	12	Greece	949.8
13	Poland	3027	13	Germany	864.7
14	Romania	1830.5	14	Latvia	580.5
15	Cyprus	1578.8	15	Bulgaria	470.8
16	Norway	1067.5	16	Romania	297.4
17	Germany	758.8	17	Slovakia	234.5



Table 1 Average amount of burning area and the average number of fires in the countries between 2010 and 2019 (Continue)

Ranking	Country	Burning Annual Average Amount of Area (ha)	Ranking	Country	Annual Average Number of Fires
18	Latvia	612.1	18	Austria	213.9
19	Finland	523.4	19	Norway	209.6
20	Slovakia	427.3	20	North Macedonia	209
21	Czech Republic	347.1	21	Croatia	199.4
22	Slovenia	270.5	22	Holland	181.8
23	Lithuania	117.5	23	Lithuania	152
24	Holland	112.1	24	Cyprus	102.7
25	Switzerland	107.6	25	Switzerland	98.4
26	Austria	66.5	26	Slovenia	83.1

There are 2 main factors in the emergence of forest fires in the world. These are lightning strikes (1%) and human-caused factors (99%). Human-caused fires occur intentionally or because of negligence. More than 95% of fires in Europe are a result from human-caused factors [5, 10]. The climate and vegetation in the region play a decisive role in the damage caused by forest fires. In regions with Mediterranean-type climates drought and high temperatures cause fires to be more common [11, 12].

Factors such as the migration of people from rural settlements and the limited use of low-yielding forest areas in Mediterranean coastal countries cause an increase in the density of highly flammable vegetation in forests. Therefore, when all these factors are combined with the heat waves in the summer months and human-induced causes, even an ineffectual fire factor can cause the burning of vast areas [13, 14]. It is expected that climate change will significantly increase the number of fires and the amount of burned forest areas; because of increasing drought, heat waves, and strong winds; especially in European countries with a coast to the Mediterranean Sea. In addition, the decrease in the rural population and the change in the demographics of the regions with the increase in tourism-oriented compositions are also important factors in the incrementation of forest fires [15, 16]. The number of fires in Turkey in 2021 according to their causes are given in Figure 1. In Figure 1, when we look at the number of fires that occurred in 2021 in

Turkey, with respect to their reason for starting; it is seen that approximately 40% of the fires are caused by humans. However, this rate can be much higher when fires with unknown causes are considered.

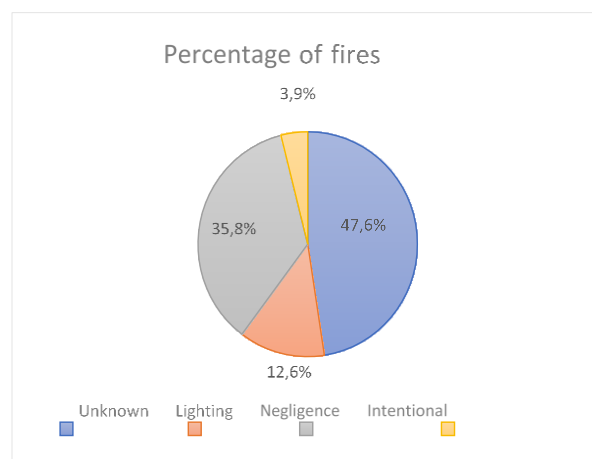


Figure 1 Number of fires in Turkey in 2021 according to their causes [17]

The classification or clustering of forest fires plays an important role for countries to take a measure against fire. There are many studies that use of clustering and classification algorithms to predict and discriminate of forest fires. Junior et al. classify the fire risk situation in summer and winter months with meteorological fire indicators of 310 regions in the European Nomenclature of territorial units for statistics (NUTS) 3 region with K-means, Fuzzy K-means and Gaussian mixture models. More accurate predictions are obtained with Gaussian mixture models in summer, and K-means method in winter [18]. Cortez and Morais estimate the amount of

burnt area using Multiple Regression (MR), Decision Trees (DT), Neural Networks (NN), Support Vector Machines (SVM) and Random Forests (RF) algorithms in spatial and temporal fire indicators show that the algorithms are predicted small fires more accurately than large fires and the best performance is obtained with the SVM method [19].

Li et al. develop an algorithm for automatic identification of fire smoke with artificial neural networks using high resolution radiometer images. Thus, they determine that possible forest fires can be put out much faster before the severity of the fire increases [20]. Han et al. estimate the forest fire hazardous area with the likelihood ratio and conditional probability methods. According to the results of FHR (Forest Fire Hazard Rate) and PRC (Prediction Rate Curve), more accurate predictions are obtained with the likelihood ratio method than the conditional probability method [21]. Shidik and Mustofa used Fuzzy C-Means and Back-Propagation Neural Network methods to classify burned forest areas and obtained 97.5% correct classification rate [22].

Rosadi and Andriyani compare the performances of Decision Trees (DT), Support Vector Machines (SVM), Fuzzy c-means and Adaptive Boosting (AdaBoost) algorithms using the variables of burned forest area, number of fires and their ratio to area. The most accurate classification performance is obtained from AdaBoost and the lowest is obtained from SVM algorithm [23]. Sinha et al. use a semi-supervised rule-based classification model to classify fires according to their severity and obtain a model accuracy of 96% [24]. Tutmez et al. cluster the number of forest fires and the amount of burnt area in Antalya using the K-Mod clustering method [25]. Yin et al. classify the fire incidence in forest, grassland, cropland and bare land areas in the Central Asia region using the K-Means method [26].

In this study, it aims to group European countries according to their fire regimes using data mining methods and to compare the obtained groups by considering fire factors. The study is a preliminary information for the researchers who search the literature on forest fire. In addition, it is an example for the classification of forest fires with machine learning and a guide for future studies. When the literature is analysed, the performances of machine learning algorithms on forest fires are generally compared. However, it is seen that the contribution of the obtained results to the application area is limited. In this study, not only the algorithm classification but also the intersection and differentiation aspects of the classifications made by these algorithms in an applied field with the literature are discussed and a different perspective is brought to the field.

## 2. MATERIALS AND METHODS

### 2.1. Study Area

In the study, data covering the years 2008-2022 are used. In order to group European countries according to the degree of exposure to forest fires, clustering analysis is performed by using the number of fires, total area burned (ha), woodland (km<sup>2</sup>) and burnt area by fire.

Table 2 Fire indicators and units used in the study

Fire Indexes	Unit
Number of fires	Number
Total area burned	Hectare
Woodland	km <sup>2</sup>
Burnt area by fire	Hectare

While selecting the variables used in the study, variables directly related to forest fire are selected in order to make an objective and accurate classification (Table 2). In addition, machine learning studies on forest fires are analysed and taken into consideration for variable selection [27, 28]. Data are obtained from the "Current Statistics Portal" of the EFFIS (European Forest Fire Information System) database [29]. The sample of the study consists of 38 European countries, 27 of

which are members of the European Union and 11 of which are not. These are Austria, Belgium, Bulgaria, Croatia, Cyprus, Czech Republic, Denmark, Estonia, Finland, France, Germany, Greece, Hungary, Ireland, Italy, Latvia, Lithuania, Luxembourg, Malta, Netherlands, Poland, Portugal, Romania, Slovakia, Slovenia, Spain, and Sweden which are members of the European Union. The countries that are not members of the European Union are Albania, Andorra, Bosnia and Herzegovina, Macedonia, Montenegro, Norway, Serbia, Switzerland, Turkey, Ukraine, and the United Kingdom.

## 2.2. Statistical Analysis

All statistical analyses are performed with R statistical language (version 4.2.1; The R Foundation for Statistical Computing, Vienna, Austria; <https://www.r-project.org>). K-Means technique and Ward's method for the hierarchical clustering method are used in the study. The Elbow method is used to determine the optimum number of clusters in K-Means technique. In this study, the most widely used Euclidean distance is used to determine the distance matrix [30]. In the clustering technique, data on forest fire indexes are standardized and included in the analysis.

In order to apply the K-Means technique used in the study, the data should be of continuous type. In this method, units are classified by taking into account their distance to the cluster mean. K-Means technique gives consistent results in large data masses. However, the disadvantage of this method is that it is sensitive to outliers and the number of clusters is determined by the researcher. In Ward technique, the other technique used in the study, the number of clusters is decided by looking at the dendrogram graph. Ward technique is more statistical than other techniques since it performs variance-based merging. The disadvantage of this technique is that if the researcher is inexperienced, he may misinterpret the dendrogram graph and determine the number of clusters differently.

Shapiro–Wilk test and Q-Q plots graphs are used to assess the normality of the data in the groups obtained in the result of the cluster analysis. Mann–Whitney U test and Kruskal–Wallis test followed by Dunn's post-hoc test with Bonferroni correction are run to determine whether there is a statistically significant difference in the number of fires, total area burned, woodland and burnt area by fire between clustering. A  $p$ -value less than 0.05 is considered statistically significant.

## 2.3. Clustering Methods

Data mining is an important process that allows the discovery of hidden knowledge from large amounts of data. Clustering analysis is an important data mining method that allows dividing a data set with a mixed structure into homogeneous subgroups by reducing the size. In today's technology, clustering analysis is often used in databases as an unsupervised learning method for the analysis of large sized data [30, 31]. There is no predetermined classification process in this analysis method. The aim of clustering techniques is to separate homogeneous clusters within clusters and heterogeneous clusters between clusters.

When determining the number of clusters in clustering methods, a number of clusters can be suggested by the researcher by considering the theoretical structure in the K-Means technique or methods for determining the optimum number of clusters can be used. In hierarchical clustering analysis, on the other hand, the distance matrix between the objects is calculated and the objects that are similar are combined to form clusters, the number of clusters is not predetermined [31, 32]. The sum of the squared values of distance from the centre of the cluster to which each data is assigned according to its distance from the cluster centre is taken, and obtaining a cluster composition in which the sum of squares within the cluster are minimum is attempted [30, 33]. Clustering techniques are depend on creating homogeneous groups using distance

matrices. Distance matrices such as Euclidean, Manhattan, and Minkowski are used for the distance between observations in the clustering process. The most widely used of these is the Euclidean distance. The formula for calculating the Euclidean distance is given in the equation below [34].

$$d_{Euclidian}(x, y) = \sqrt{\sum_{i=1}^n (x_i - y_i)^2} \quad (1)$$

Ward's method is the most commonly used hierarchical technique. This method differs from other techniques as clusters are joined based on variances. It is a method based on merging clusters whose sum of error squares is minimum [31, 32].

In hierarchical clustering methods; the number of clusters can be decided by examining the dendrogram graph of the distance between clusters, or it can be determined as the optimum number of clusters by examining the breakpoint of the graph obtained by dividing the in-group variance by the intergroup variance. In addition, another method proposed by Lewis and Thomas is to determine it according to the total variance and according to the contribution of the added set to the variance [30]. The determined clusters should have the ability to explain 80% of the variance and the added cluster should have a contribution of at

least 5% to the total variance [30, 35]. However, all clustering methods, there is no definite criterion for determining the number of clusters, so it can be undecided. Therefore, some formulas have been developed for calculating the number of clusters. The most used one is " $k = \sqrt{n/2}$ " [36, 37].

### 3. RESULTS AND DISCUSSION

#### 3.1. Results of K-Means Cluster Analysis with Fire Indexes of European Countries

In the study, fire indexes are examined with the K- Means clustering technique. In order to determine the optimal number of clusters; information about the countries such as their location, climate, vegetation coverage, and fire statistics are taken into account. In addition, the number of clusters is decided by using the methods of determining the optimal number of clusters. The results are obtained in the R statistical program; and "dplyr", "stats", "cluster", "clusterR", and "ggplot2" packages are used.

The optimal number of clusters is determined by using mathematical measurement methods (Elbow and Silhouettes techniques) [34, 38]. In Figure 2, the results of the Elbow and Silhouettes techniques are given.

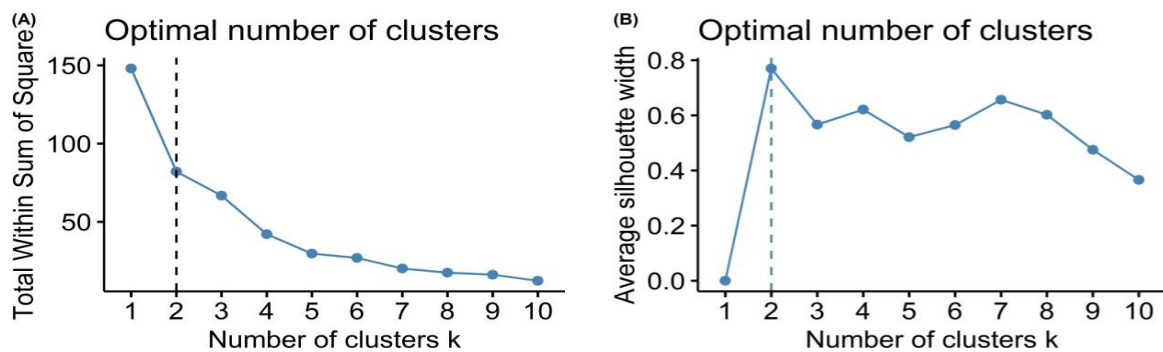


Figure 2 Determination of the optimal number of clusters using the Elbow (A) and Silhouette (B) methods

The number of clusters is determined as 2 since the total value of the squares within the cluster in the elbow graph gradually decreases after two and considering the peak of the

silhouette width in the silhouette graph. The number of observations in the clusters is 32 and 6, respectively, and the cluster compositions are shown in Figure 3. In Figure 3, after the

clustering analysis, the cluster centres and the findings of the two clusters are given in two dimensions. According to these results, it is seen that the majority of European countries, including all Northern European countries,

are in the first cluster. The countries of Turkey, Ukraine, Italy, Spain, Portugal, and Bosnia and Herzegovina are in the second cluster. The results comparing the fire indexes of the two clusters are given in Table 3.

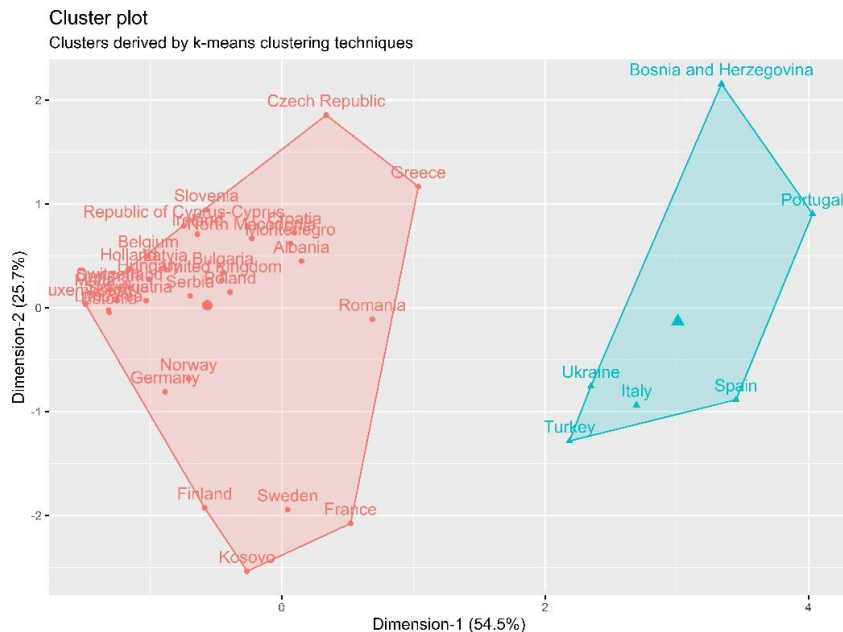


Figure 3 Clusters obtained by fitting K-Means clustering based on fire indexes

Table 3 Comparison of clusters by fire indexes

Fire Indexes	Cluster 1 (n=32)	Cluster 2 (n=6)	p-value
Number of fires	75 (9.25 – 545)	3149.5 (1893.50 – 3675.50)	<.001
Total area burned (Ha)	11436 (1365.75 – 113737.25)	981322.5 (746628.25 – 1333282.50)	<.001
Woodland (km <sup>2</sup> )	23983 (7584 – 62107.5)	105868 (30264.75 – 192330.25)	.045
Burnt area by fire (Ha)	195.5 (122.5 – 290.75)	383.5 (203.50 – 576.25)	.029

*p*-values are calculated by Mann-Whitney U test.

Data are presented as median with interquartile range (25th percentile – 75th percentile).

*p*< .05 is considered statistically significant.

As a result of the Mann-Whitney U test performed on fire indexes which are divided into two clusters, a significant difference is found between the two clusters in terms of all indexes (Figure 4). The results obtained in Table 2 support that the two cluster compositions are completely divided from each other.

When the number of fires, total area burned, woodland and burnt area by fire in Turkey, Ukraine, Italy, Spain, Portugal, and Bosnia and Herzegovina countries in Cluster 2 are examined, it is found that these numbers are significantly higher than other European countries.

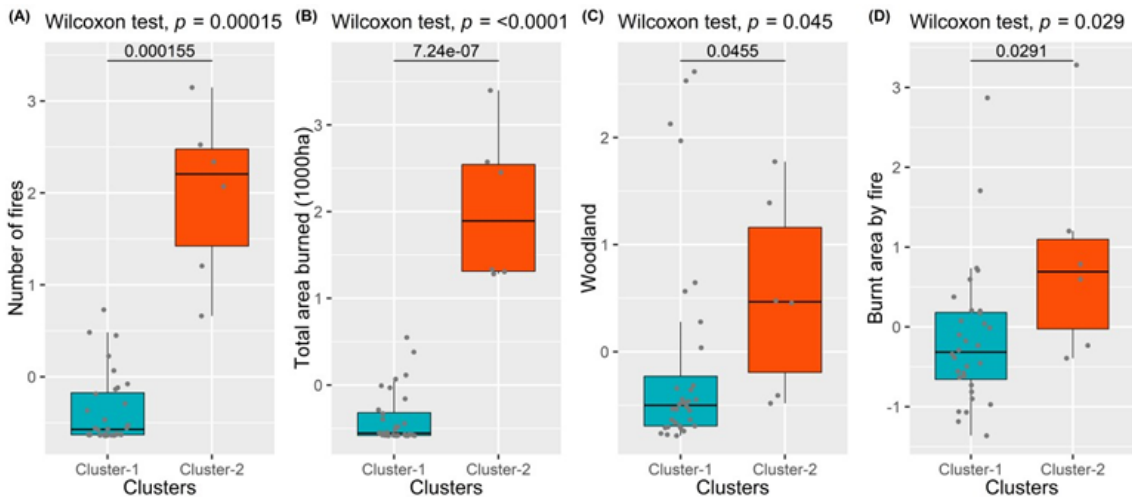


Figure 4 Comparison of the clusters in terms of the number of fires (A), total area burned (B), woodland (C) and burnt area by fire (D). Data are presented as standardized values.

### 3.2. Results of Hierarchical Cluster Analysis with Forest Fire Indexes of European Countries

In addition to the K-Means clustering technique, Hierarchical clustering techniques are also applied to the forest fire indexes are discussed in the study, and the results are evaluated. In hierarchical clustering techniques, the number of clusters is decided by evaluating the dendrogram graph [31]. Cluster compositions are obtained through the R program language, and the packages "dendextend", "purr", "gridExtra", "ggpubr", "factoextra", "hclust", "dplyr", and "tidyverse" are used.

In this study, hierarchical clustering techniques called linkage and variance techniques are used. Among the linkage

methods, "single connection", "average connection", and "complete connection" techniques are used; while Ward's method are used in the variance technique. In order to choose the most fitting method, the agglomeration coefficient of each technique is examined and obtained as 0.76 for single connection, 0.82 for average connection, 0.88 for full connection, and 0.93 for the Ward's method. Since the closer the agglomeration coefficient is to 1 the stronger the cluster composition will be, the analysis is continued using the Ward's method. The dendrogram graph obtained by Ward's method is given Figure 5. Ward's method is preferred also because it gives more accurate results in studies that try to minimize in-cluster variability, and where there are small sample size [30, 37].

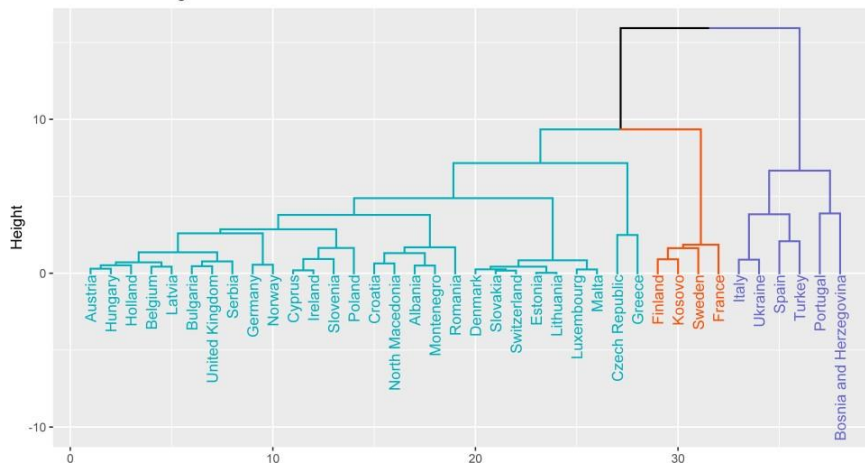


Figure 5 Ward dendrogram of fire indexes

When Figure 5 is examined, it shows that it is ideal to divide the countries included in the study into 3 clusters. When these clusters are examined, it is seen that the first cluster consists of 28 countries, the second cluster consists of 4 countries, and the third cluster consists of 6 countries. The clusters are

compared with the Kruskal-Wallis H test in order to better analyze the forest fire indexes of the determined clusters and to examine the heterogeneity between clusters with other statistical methods. The results are given in Table 4 and Figure 6.

Table 4 Comparison of clusters by fire indexes

Fire Indexes	Cluster 1 (n=28)	Cluster 2 (n=4)	Cluster 3 (n=6)	p-value*
Number of fires	44.5 (7.25 – 545) <sup>b</sup>	214 (48 – 980) <sup>ab</sup>	3149.5 (1893.5 – 3675.5) <sup>a</sup>	<.001
Total area burned (Ha)	8967.5 (1257.25 – 113737.25) <sup>b</sup>	41074.5 (12666.75 – 174710.25) <sup>ab</sup>	981322.5 (746628.25 – 1333282.5) <sup>a</sup>	<.001
Woodland (km <sup>2</sup> )	21223 (7540 – 36250) <sup>b</sup>	263685 (236650 – 286182.5) <sup>a</sup>	105868 (30264.75 – 192330.25) <sup>a</sup>	<.001
Burnt area by fire (Ha)	205.5 (106.75 – 290.75) <sup>a</sup>	164.5 (138.75 – 289.25) <sup>a</sup>	383.5 (203.5 – 576.25) <sup>a</sup>	.085

p-values are calculated by Kruskal-Wallis test.

Different small superscript letters in each row denote that statistically significant difference in post-hoc analysis Data are presented as median with interquartile range (25<sup>th</sup> percentile – 75<sup>th</sup> percentile).

p< .05 is considered statistically significant.

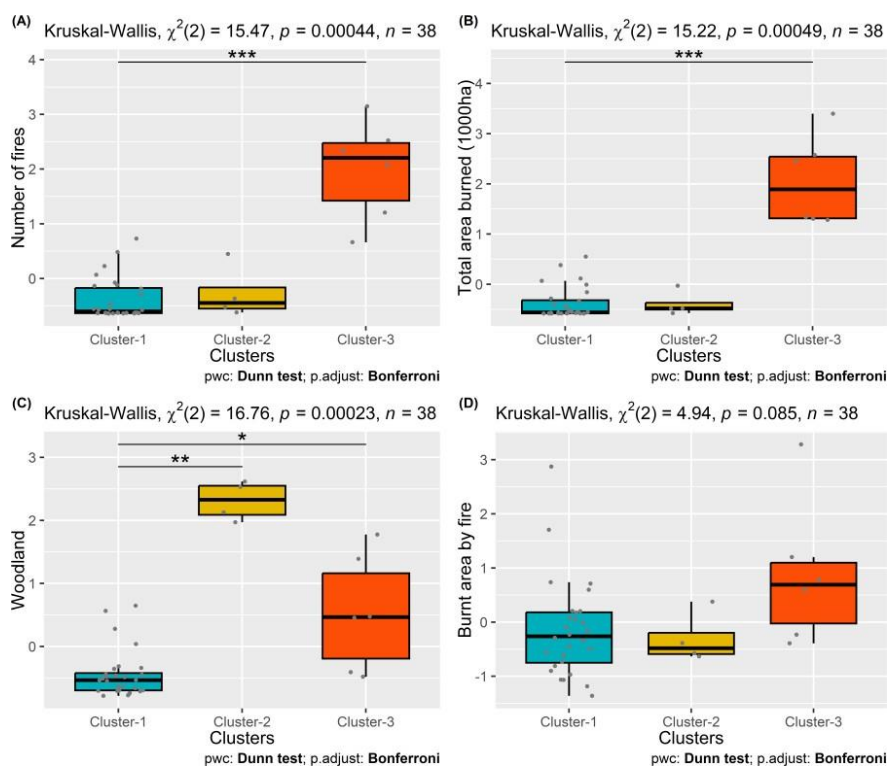


Figure 6 Comparison of the clusters in terms of the number of fires (A), total area burned (B), woodland (C) and burnt area by fire (D). Data are presented as standardized values.

Considering to the comparison of clusters according to the fire indexes using Kruskal-Wallis test, there is a statistically significant difference in the number of fires ( $\chi^2=15.47$ ,  $p<.001$ ), total area burned ( $\chi^2=15.47$ ,  $p<.001$ ) and woodland ( $\chi^2=15.47$ ,  $p<.001$ ) between clusters. Dunn post-hoc test reveal that the number of fires (3149.5 [IQR, 1893.5

– 3675.5] vs. 44.5 [IQR, 7.25 – 545], adj. p-value<.001) and total area burned (981322.5 [IQR, 746628.25 – 1333282.5] vs. 8967.5 [IQR, 1257.25 – 113737.25], adj. p-value<.001) in Cluster-3 countries are significantly higher than that in Cluster-1 countries. In addition to, Woodland in Cluster- 2 (263685 [IQR, 236650 –

286182.5]) countries are significantly larger compared to Cluster-1 (21223 [IQR, 7540 – 36250], adj.  $p$ -value<.001) and Cluster-3 (105868 [IQR, 30264.75 – 192330.25], adj.  $p$ -value=.012) countries (Figure 6). When the two clusters that formed in the result of the K-Means cluster analysis are examined, Turkey, Bosnia and Herzegovina, Ukraine, Italy, Spain, and Portugal are in the same cluster; while the remaining European countries form the other cluster. As a result of the hierarchical clustering analysis performed with the Ward's method, the countries are divided into 3 clusters. Finland, Kosovo, Sweden, and France formed a cluster; and Turkey, Bosnia and Herzegovina, Ukraine, Italy, Spain, and Portugal formed a separate cluster. The remaining European countries constitute the third cluster.

In various studies on forest fires in European countries Various in studies on forest fires in European Countries [5, 11, 14-16, 39, 40] it is reported that forest fires are concentrated in France, Portugal, Spain, Greece, and Italy in the Mediterranean region. When the results are interpreted in the light of the literature, it is seen that this situation is caused by reasons such as climate, vegetation, arson, neglect, and tourism in Mediterranean countries (Turkey, Italy, Spain, Portugal, France) [5, 14]. Bosnia and Herzegovina has a climate structure with different climate types, including the Mediterranean climate. In addition, seasonal factors such as precipitation regime and temperature increase are shown to play an important triggering role in fires [41]. In the two clusters structure preferred in the K-Means clustering method in this study, Spain, Portugal and Italy are in the first cluster, while Greece and France are in the second cluster, although they differ from other European countries. In the cluster composition obtained by the Ward's method; Spain, Portugal, and Italy are in the same cluster; France is clustered together with

Finland, Kosovo, and Sweden; and Greece is in the same cluster with the other European countries. Therefore, although there are some differences, it is seen that the results are compatible with the literature. When the literature is examined [9, 42], it is seen that the fire regime in countries such as Finland, Sweden, Turkey, and Ukraine differs from other European countries. These studies support the findings obtained as a result of cluster analysis. In both the K-Means and Ward's methods, the country of Bosnia and Herzegovina is in the same cluster with countries such as Spain, Portugal, and Italy; while countries of Finland and Kosovo are in the same group with France in the Ward's method. In addition, the most surprising result of the study is that Greece is included in the group dominated by low-fire regimes, which includes the majority of European countries in both clustering techniques (Figure 3, Figure 5). The general thought is that this difference occurs due to the many factors that are examined together in clustering analysis.

#### 4. CONCLUSIONS

Forest fires pose a serious problem for European countries as they do all over the world [5]. In this study, the similarities and differences between European countries in terms of forest fire indexes are examined in light of it being an ongoing and interesting subject. In the study, clustering analysis, which is a data mining method, was carried out to segment 38 European countries, whose data are fully accessible, according to their forest fire indexes. In the cluster analysis carried out for this purpose, the clusters formed by the countries are examined and the countries are classified according to their fire regimes in terms of the factors included in the analysis. Then, the clusters are compared according to their fire indexes and the results are evaluated.



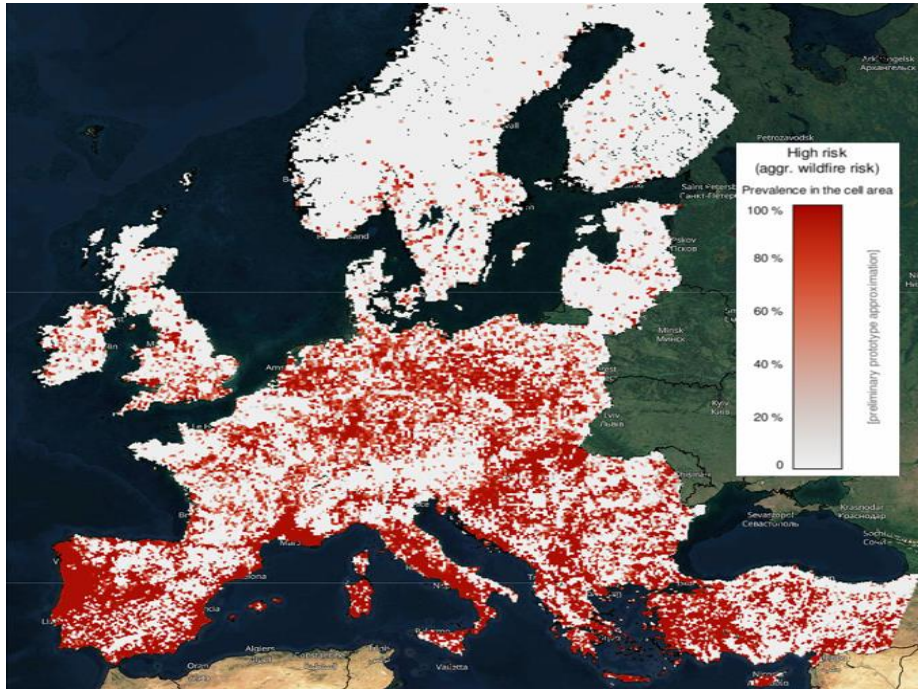


Figure 7 EFFIS Forest Fire Risk Map for European countries [18]

In this study, unlike similar studies in the literature, the results obtained from the classification algorithms are tried to be interpreted both in terms of theoretical results and in the field of forest fires. In this respect, the study constitutes a good example of the application of machine learning results to an applied science. It also serves as a preliminary information for future research in this field and guides the researcher in the process of research design. Since the study compares different clustering techniques, it gives the researcher the opportunity to interpret the classification principle of these techniques.

The study also gives the researcher an idea about how effective European countries are in fire planning. Countries in the same region should take into account the fire planning of countries that are in the same risk group but suffer less damage from forest fires when developing fire management strategies. For example, although Italy and Croatia have similar vegetation cover, Italy is in Cluster-3 with high fire regime while Croatia is in Cluster-1 with low fire regime. Therefore,

Italy's fire management plans and penal sanctions are insufficient to prevent forest fires.

When Figure 7 is examined, the findings obtained as a result of the study coincide with the European fire map by EFFIS. The study is carried out by taking into account only the countries included in the EFFIS database; and the countries whose data cannot be accessed are excluded from the scope of the study. Unexpected results may occur, since cluster analysis makes an objective evaluation by considering many factors rather than a subjective point of view. The scope of the study can be expanded by increasing the number of countries and the fire indexes used, and different clustering methods can be used for estimation. In addition, it is foreseen that modeling studies can be carried out using data mining algorithms and estimation variables.

#### ***Funding***

The author (s) has no received any financial support for the research, authorship or publication of this study.

#### ***Authors' Contribution***

The authors contributed equally to the study.

***The Declaration of Conflict of Interest/ Common Interest***

No conflict of interest or common interest has been declared by the authors

***The Declaration of Ethics Committee Approval***

This study does not require ethics committee permission or any special permission.

***The Declaration of Research and Publication Ethics***

The authors of the paper declare that they comply with the scientific, ethical and quotation rules of SAUJS in all processes of the paper and that they do not make any falsification on the data collected. In addition, they declare that Sakarya University Journal of Science and its editorial board have no responsibility for any ethical violations that may be encountered, and that this study has not been evaluated in any academic publication environment other than Sakarya University Journal of Science.

**REFERENCES**

- [1] E. A. Johnson, K. Miyanishi, "Forest fires: behavior and ecological effects". Elsevier, Amsterdam, 2001.
- [2] E. Gutiérrez, S. Lozano, "Avoidable damage assessment of forest fires in European countries: an efficient frontier approach," *European journal of forest research*, vol. 132, no. 1, pp. 9-21, 2013.
- [3] J. G. Pausas, "Changes in fire and climate in the eastern Iberian Peninsula (Mediterranean basin)", *Journal of Climatic change*, vol. 63, no. 3, pp. 337-350, 2004.
- [4] F. Europe, F. Unece, "State of Europe's forests 2015," presented at the Ministerial Conference on the Protection of Forests in Europe, 04.11.2015, 2015.
- [5] N. Khabarov, A. Krasovskii, M. Obersteiner, R. Swart, "Forest fires and adaptation options in Europe," *Journal of Regional Environmental Change*, vol. 16, no. 1, pp. 21-30, 2016.
- [6] M. Grünig, R. Seidl, C. Senf, "Increasing aridity causes larger and more severe forest fires across Europe," *Journal of Global Change Biology*, Dec 14 2022.
- [7] A. Hamit, K. Ali, C. Huseyin, "The structure and importance of fire suppressing organizations in Turkey," *Journal of Scientific Research and Essays*, vol. 5, no. 5, pp. 456-460, 2010.
- [8] Z. G. Yılmaz, "Yaşar Kemal ve Orman Yangınları," *Ekoeleştiri Çevre ve Edebiyat*. Phoenix Yayınevi, Ankara, pp. 129-169, 2012.
- [9] C. Şahan, K. İsmail, "Türkiye ve Avrupa Ülkeleri Orman Yangınlarının Bazı Değişkenler Açısından Değerlendirilmesi," *Ordu Üniversitesi Sosyal Bilimler Enstitüsü Sosyal Bilimler Araştırmaları Dergisi*, vol. 12, no. 1, pp. 1-14, 2022.
- [10] A. Küçükosmanoğlu, "Ülkemizde orman yangınları ve yangın sezonları," *Journal of the Faculty of Forestry Istanbul University*, vol. 44, no. 1-2, pp. 121-128, 1994.
- [11] A. Dimitrakopoulos, C. Gogi, G. Stamatelos, I. Mitsopoulos, "Statistical Analysis of the Fire Environment of Large Forest Fires (> 1000 ha) in Greece," *Polish Journal of Environmental Studies*, vol. 20, pp. 327-332, 01/01 2011.
- [12] O. Kahraman, O. Esin, G. Çamalan, "İzmir-Tırazlı orman yangınının uydu ve model verileri ile analizi," *Ulusal Çevre Bilimleri Araştırma Dergisi*, vol. 4, no. 1, pp. 1-12, 2021.

- [13] F. Moreira, O. Viedma, M. Arianoutsou, T. Curt, N. Koutsias, "Landscape-wildfire interactions in southern Europe: implications for landscape management," *Journal of environmental management*, vol. 92, no. 10, pp. 2389-2402, 2011.
- [14] J. San Miguel Ayanz, J. M. Moreno, A. Camia, "Analysis of large fires in European Mediterranean landscapes: Lessons learned and perspectives," *Journal of Forest Ecology and Management*, vol. 294, pp. 11-22, 2013.
- [15] J. San Miguel Ayanz, M. Rodrigues, S. Oliveira, C. Pacheco, F. Moreira, "Land cover change and fire regime in the European Mediterranean region," in *Journal of Post-fire management and restoration of southern European forests*: Springer, 2012, pp. 21-43.
- [16] F. Rego, E. Rigolot, P. Fernandes, C. Montiel, J. Silva, "Towards integrated fire management. European Forest Institute Policy Brief 4," (Joensuu, Finland), 2010.
- [17] T. C. T. v. O. B. O. G. M. "Ormancılık İstatistikleri "(accessed 26.12.2022, 2022).
- [18] J. S. Júnior, J. R. Paulo, J. Mendes, D. Alves, L. M. Ribeiro, C. Viegas, "Automatic forest fire danger rating calibration: Exploring clustering techniques for regionally customizable fire danger classification," *Expert Systems with Applications*, vol. 193, p. 116380, 2022.
- [19] P. Cortez, A. d. J. R. Morais, "A data mining approach to predict forest fires using meteorological data," Department of Information Systems R&D Algoritmi Centre, University of Minho, 2007.
- [20] Z. Li, Y. Kaufman, C. Ichoku, R. Fraser, A. Trishchenko, L. Giglio, J. Jin, X. Yu, "A review of AVHRR-based active fire detection algorithms: Principles, limitations, and recommendations," *Global and regional vegetation fire monitoring from space, planning and coordinated international effort*, pp. 199-225, 2001.
- [21] J. G. Han, K. H. Ryu, K. H. Chi, Y. K. Yeon, "Statistics based predictive geo-spatial data mining: Forest fire hazardous area mapping application," in *Web Technologies and Applications: 5th Asia-Pacific Web Conference, APWeb 2003, Xian, China, April 23-25, 2003 Proceedings 5, 2003*: Springer, pp. 370-381.
- [22] G. F. Shidik, K. Mustofa, "Predicting size of forest fire using hybrid model," in *Information and Communication Technology: Second IFIP TC5/8 International Conference, ICT-EurAsia 2014, Bali, Indonesia, April 14-17, 2014. Proceedings 2, 2014*: Springer, pp. 316-327.
- [23] D. Rosadi, W. Andriyani, "Prediction of forest fire using ensemble method," in *Journal of Physics: Conference Series*, 2021, vol. 1918, no. 4: IOP Publishing, p. 042043.
- [24] D. Sinha, R. Kumari, S. Tripathi, "Semisupervised classification based clustering approach in WSN for forest fire detection," *Wireless Personal Communications*, vol. 109, pp. 2561-2605, 2019.
- [25] B. Tutmez, M. G. Ozdogan, A. Boran, "Mapping forest fires by nonparametric clustering analysis," *Journal of forestry research*, vol. 29, pp. 177-185, 2018.
- [26] H. Yin, J. Guli, L. Jiang, T. Yu, J. Umuhoza, X. Li, "Monitoring fire regimes and assessing their driving

- factors in Central Asia," *Journal of Arid Land*, vol. 13, pp. 500-515, 2021.
- [27] J. Li, Y. Shan, S. Yin, M. Wang, L. Sun, D. Wang, "Nonparametric multivariate analysis of variance for affecting factors on the extent of forest fire damage in Jilin Province, China," *Journal of Forestry Research*, vol. 30, pp. 2185-2197, 2019.
- [28] L. Iliadis, M. Vangeloudh, S. Spartalis, "An intelligent system employing an enhanced fuzzy c-means clustering model: Application in the case of forest fires," *Computers and Electronics in Agriculture*, vol. 70, no. 2, pp. 276-284, 2010.
- [29] E. F. F. I. S. EFFIS. "EFFIS Statistics Portal." (accessed 10.11.2022, 2022).
- [30] Y. K. Akın, "Veri madenciliğinde kümeleme algoritmaları ve kümeleme analizi," *Marmara Üniversitesi / Sosyal Bilimler Enstitüsü / Ekonometri Ana Bilim Dalı, Marmara Üniversitesi / Sosyal Bilimler Enstitüsü / Ekonometri Ana Bilim Dalı, Turkey, 2008.*
- [31] B. Altunkaynak, "Veri madenciliği yöntemleri ve R uygulamaları". Seçkin Yayıncılık, Ankara, 2019.
- [32] F. Murtagh, P. Legendre, "Ward's hierarchical agglomerative clustering method: which algorithms implement Ward's criterion?," *Journal of classification*, vol. 31, no. 3, pp. 274-295, 2014.
- [33] H. Ehsan, D. A. Hamed, S. Jamal, "Application of data mining techniques in stock markets: A survey," *Journal of Economics and International Finance*, vol. 2, no. 7, pp. 109-118, 2010.
- [34] A. Kassambara, "Practical guide to cluster analysis in R: Unsupervised machine learning". STHDA, 2017.
- [35] F. J. M. Ruíz, "Strategic group analysis in strategic marketing: an application to Spanish savings banks", *Marketing Intelligence & Planning*, vol. 6, pp. 257-270, 1998.
- [36] C. Alpar, *Uygulamalı çok değişkenli istatistiksel yöntemler*. Detay Yayıncılık, Ankara, 2017.
- [37] C. Sungur, "Sağlık göstergelerine göre Ekonomik Kalkınma ve İşbirliği Örgütü ülkelerinin kümeleme analizi," *SGD-Sosyal Güvenlik Dergisi*, vol. 6, no. 1, pp. 197-224, 2016.
- [38] Ö. F. Rençber, "Veri madenciliğinde kullanılan kümeleme algoritmalarının karşılaştırılması üzerine bir inceleme," *Düzce Üniversitesi Bilim ve Teknoloji Dergisi*, vol. 7, no. 3, pp. 1671-1685, 2019.
- [39] P. Barbosa, A. Camia, J. Kucera, G. Liberta, I. Palumbo, "Assessment of forest fire impacts and emissions in the European Union based on the European Forest Fire Information System," *Journal of Developments in Environmental Science*, vol. 8, pp. 197-208, 2008.
- [40] P. Mateus, P. M. Fernandes, "Forest fires in Portugal: dynamics, causes and policies," *Journal of Forest context and policies in Portugal*: Springer, 2014, pp. 97-115.
- [41] B. Drašković, B. Miletic, M. Gatalj, S. Stjepanović, "Climate changes and fires in Bosnia and Herzegovina," in *XI International Scientific Agriculture Symposium ,AGROSYM, Republic of Srpska, Bosnia and Herzegovina, October 2020*, pp. 694-702.
- [42] F. Tedim, G. Xanthopoulos, V. Leone, "Forest fires in Europe: Facts and

challenges," in *Wildfire hazards, risks and disasters*: Elsevier, 2015, pp. 77-99.



SAKARYA ÜNİVERSİTESİ

# FEN BİLİMLERİ ENSTİTÜSÜ DERGİSİ

Sakarya University Journal of Science  
SAUJS

ISSN 1301-4048 | e-ISSN 2147-835X | Period Bimonthly | Founded: 1997 | Publisher Sakarya University |  
<http://www.saujs.sakarya.edu.tr/>

Title: Development of an Analytical Method for the Determination of Cymoxanil in Potato Flour Samples by High Performance Liquid Chromatography

Authors: Tuğçe UNUTKAN GÖSTERİŞLİ

Received: 2023-03-15 00:00:00

Accepted: 2023-07-03 00:00:00

Article Type: Research Article

Volume: 27

Issue: 5

Month: October

Year: 2023

Pages: 1002-1007

How to cite

Tuğçe UNUTKAN GÖSTERİŞLİ; (2023), Development of an Analytical Method for the Determination of Cymoxanil in Potato Flour Samples by High Performance Liquid Chromatography. Sakarya University Journal of Science, 27(5), 1002-1007, DOI: 10.16984/saufenbilder.1265507

Access link

<https://dergipark.org.tr/tr/journal/1115/issue/80257/1265507>

New submission to SAUJS

<http://dergipark.gov.tr/journal/1115/submission/start>

## Development of an Analytical Method for the Determination of Cymoxanil in Potato Flour Samples by High Performance Liquid Chromatography

Tuğçe UNUTKAN GÖSTERİŞLİ \*<sup>1,2</sup> 

### Abstract

In this study, a high performance liquid chromatography-ultraviolet detection method was introduced for the detection of cymoxanil. The experimental parameters of the procedure were thoroughly evaluated. Cymoxanil was eluted by ammonium formate buffer (50.0 mM, pH 4.0):acetonitrile (55:45 v/v) as mobile phase. Under the optimal conditions, the limits of detection and quantification (LOD and LOQ) were found as 7.4 – 24.8  $\mu\text{g kg}^{-1}$ , which allows trace determination of pesticides in food samples. Proposed method was then implemented for the determination of selected fungicide in potato flour samples with acceptable % recoveries in the range of 81.4–112.9%, while the values of relative standard deviation (RSD) were below 10% showing a satisfactory applicability for cymoxanil in such complex real samples matrix.

**Keywords:** Cymoxanil, potato flour, high performance liquid chromatography, fungicide

### 1. INTRODUCTION

Pesticides are defined as toxic chemical compounds for living organisms because of their environmental persistence and bioaccumulation [1]. Agricultural pesticide residues are one of the critical environmental contaminants that adversely impact the human health and food safety [2, 3]. Among diverse groups of foods, fruits and vegetables are known to contain more pesticide residues that contaminate water, air, and soil with their high toxicity as a result of agricultural activities [1]. Accordingly, pesticides, even at trace concentrations, are harmful to both the environment and human health, including cancer, asthma, diabetes, parkinson's disease,

cognitive effects, and unknown diseases [4-6].

Cymoxanil was introduced in 1977 as an agrochemical fungicide to control related pathogens in fruit, vegetables, and plants. In practice, it is mainly used to treat seeds and protect crops from fungus attacks [7, 8]. However, long-term consumption of cymoxanil can have adverse effects on the liver, body immunity and gastrointestinal system and can even cause cancer [9]. The limit in order to reduce risks regarding the high consumption of cymoxanil residues in drinking water was determined to be 0.38 ppm [10]. Taking these into account, it is urgent to develop a sensitive analytical

\* Corresponding author: tugceunutkan@gmail.com (T. UNUTKAN GÖSTERİŞLİ)

<sup>1</sup> Yıldız Technical University, Science and Technology Application and Research Center, 34349 İstanbul, Türkiye

<sup>2</sup> Yıldız Technical University, Department of Chemical Engineering, 34349 İstanbul, Türkiye

ORCID: <https://orcid.org/0000-0002-1143-4192>



method for the determination of cymoxanil residues in food products for public health.

There are various analytical methods for assessing cymoxanil, such as high-performance liquid chromatography (HPLC) [11], liquid chromatography tandem mass spectrometry (LC-MS/MS) [12], gas chromatography (GC) [13], and voltammetry [14]. However, some methods have some limitations, including high costs, complicated sample pretreatments such as derivatization steps for GC, and high requirements for skilled technicians. In addition, HPLC could provide accurate and reliable determination results for cymoxanil [15, 16]. Considering the limitations of GC methods, there has been an increasing demand for immediate, simple, and effective methods to monitor the presence of cymoxanil in food samples.

In this study, a sensitive and suitable method for the determination of cymoxanil was established in potato flour samples. Several parameters affecting chromatographic elution were investigated to obtain the best experimental results.

## 2. MATERIALS AND METHODS

### 2.1. Instrumentation and Chromatographic Conditions

A Shimadzu LC-20AT HPLC system, consisted of a delivery pump, SPD-20A UV-Vis detector and a SIL-20A HT autosampler was used in the experiment. A Phenomenex-Aqua C18 column (250×4.6 mm i.d., 5µm particle size) was used for chromatographic separation at ambient temperature. The isocratic mobile phase consisted of ammonium formate buffer (50.0 mM, pH 4.0) and acetonitrile in the ratio of 55:45 (v/v), at a constant flow rate of 1.2 mL min<sup>-1</sup> with 30 µL injection volume and UV detection at 254 nm. The pH measurements were performed with a Hanna HI 2211 pH/Orp meter. The overall analysis time was 7.0 min.

### 2.2. Reagents and Chemicals

The standards for the analyzed fungicide, cymoxanil was supplied from Dr. Ehrenstorfer GmbH (Augsburg, Germany). All substances were analytical grade. Acetonitrile, formic acid, ammonium hydroxide (25%) were supplied from Merck, Germany. Deionized water was supplied from the Elga PureLab Flex 3 Ultrapure, London, UK. Cymoxanil calibration and working solutions were gravimetrically prepared by appropriate dilution of stock solutions with acetonitrile to obtain different concentrations and stored at +4 °C in a refrigerator until use.

### 2.3. Sample Preparations

Potato flour sample was purchased from a local market in İstanbul, Türkiye. Firstly, each potato flour sample was thoroughly mixed and homogenized.

An aliquot (10 g) of potato flour samples was weighed inside a 50 mL-flask and filled up to a final volume with acetonitrile. The solution was vigorously mixed in an ultrasound bath for 30 min. Acetonitrile extract was passed through a 0.45 µm syringe filter to prevent any blockage that may occur in the analytical column and spiked at 50 µg L<sup>-1</sup>-5.0 mg L<sup>-1</sup> within the linear calibration range. Finally, matrix-matched standard solutions were placed into 2.0 mL vials prior to chromatographic analysis.

## 3. RESULTS AND DISCUSSION

### 3.1. Chromatographic Separation of Cymoxanil

In this study, primarily instrumental parameters such as column, mobile phase composition, and flow rate were optimized to determine optimum chromatographic conditions and symmetric/sharp peaks.

Several commercially obtained chromatographic columns, including a Zorbax C18 column (250 mm, 4.6 mm, 5 µm), Zorbax C8 column (250 mm, 4.6 mm, 5 µm) and a Phenomenex-Aqua C18 column (250



mm, 4.6 mm, 5  $\mu\text{m}$ ) were initially tested to obtain a well-separated signal with good shape. The eluted peak belonging to cymoxanil was more tailed in the first two columns compared to the Phenomenex-Aqua column. The most efficient and satisfactory separation for cymoxanil was achieved with the Phenomenex-Aqua C18 column using an ammonium formate buffer (50.0 mM) adjusted to pH 4.0 with ammonia and acetonitrile in a ratio of 55:45 v/v mobile phase. The most appropriate flow rate for the mobile phase was 1.2 mL min<sup>-1</sup>. Upon using these parameters, the retention time of cymoxanil was 4.85 min.

### 3.2. Analytical Figures of Merit

The performance of the developed method, such as the linear range (LR), correlation coefficient ( $R^2$ ), limit of detection, and quantification (LOD and LOQ) was evaluated under the optimum conditions stated in Table 1. The calibration plot was established by plotting the peak areas against changing concentrations of cymoxanil in the range of 26.1  $\mu\text{g kg}^{-1}$  – 50.1 mg kg<sup>-1</sup>. The prepared chromatographic method takes 7.0 min with a 4.85 min retention time and exhibits an excellent level of linearity ( $R^2 = 1.000$ ) in the linear concentration range, good separation (Figure 1) and very low LOD and LOQ values where preconcentration is not required. The LOQ was designated by determining the lowest concentration of cymoxanil that could be measured. The LOD (3xStd Dev/Slope) was 7.4  $\mu\text{g kg}^{-1}$  (mass based) and the LOQ (10xStd Dev/Slope) was 24.8  $\mu\text{g kg}^{-1}$  as shown in Table 2. The repeatability of retention time was also satisfactory.

Table 1 Optimum parameters of HPLC-UV system

Column	Phenomenex-Aqua C18 (250 mm, 4.6 mm, 5 $\mu\text{m}$ )
Mobile Phase	Ammonium formate buffer (50.0 mM, pH 4.0) and acetonitrile (55:45, v/v)
Flow Rate	1.2 mL min <sup>-1</sup>
Injection Volume	30 $\mu\text{L}$
Wavelength	254 nm

Table 2 Analytical performance values for HPLC-UV system

Method	HPLC-UV
LOD, $\mu\text{g kg}^{-1}$	7.4
LOQ, $\mu\text{g kg}^{-1}$	24.8
LR	26.1 $\mu\text{g kg}^{-1}$ – 50.1 mg kg <sup>-1</sup>
$R^2$	1.0000

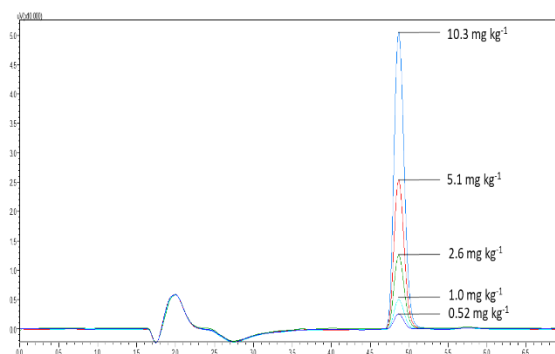


Figure 1 Overlay chromatograms of 0.52, 1.0, 2.6, 5.1 and 10.3 mg kg<sup>-1</sup> standard solutions of cymoxanil

### 3.3. Recovery Studies

Two brands of potato flour were used to evaluate the performance of the method with real samples. Blank analysis indicated that they were free of the target analyte or didn't contain detectable amounts of the analyte. The method accuracy was checked with two spiked potato flour samples in the linear concentration range of 0.10-2.50 mg kg<sup>-1</sup> with the results shown in Table 3. The matrix matching strategy was used to quantify cymoxanil in the spiked samples. Although the analyte had a different retention time in

the potato flour samples because of the diversity and complexity of the food samples matrix than the standard, both samples represented similar chromatographic behavior with each concentration point.

Matrix matching calibration, where all standards were prepared in the extract of another potato flour sample, was used. Hence, no problem was observed. There was no chromatographic interference from the matrix on the cymoxanil signal. Recovery values using the developed method were in the range of 81.4–112.9%. Chromatograms of 2.50 mg kg<sup>-1</sup> potato flour samples are shown in Figure 2.

Table 3 Percent recovery results in the HPLC-UV system

Samples	Spiked concentration, mg L <sup>-1</sup>	Recovery% ± Std Dev, %
Potato Flour-Brand A	0.10	81.4 ± 2.7
	0.20	98.9 ± 6.5
	0.50	93.1 ± 1.8
	1.00	96.5 ± 1.8
	2.50	96.9 ± 0.5
Potato Flour-Brand B	0.10	98.7 ± 1.9
	0.20	112.9 ± 2.5
	0.50	104.9 ± 3.6
	1.00	102.7 ± 0.9
	2.50	104.4 ± 0.3

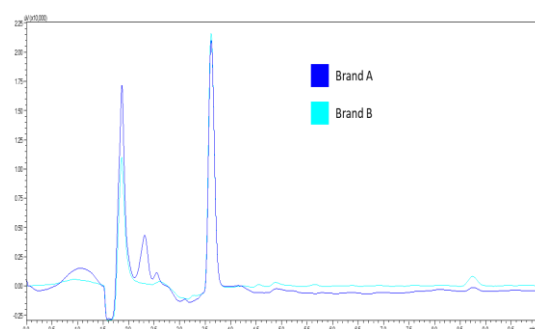


Figure 2 Overlay chromatograms of 2.5 mg kg<sup>-1</sup> standard solutions of spiked potato flour samples

#### 4. CONCLUSION

The present work has been undertaken to develop a suitable and sensitive method for

the quantification of cymoxanil in potato flour samples. To achieve the best performance of the method, the effects of various experimental parameters were investigated. The mobile phase composition was optimized focusing on the efficient chromatographic separation and short analysis time period. The retention time value of cymoxanil was 4.85 min with a 7.0 min total run time. Therefore, the developed HPLC method was successfully performed to potato flour samples for recovery studies. The developed method showed remarkable features involving wide linear range, low LOD/LOQ values, and acceptable precision and satisfactory recovery results. As a result, the proposed method is rapid, and easy applicable to analyze cymoxanil in food samples.

#### Funding

The author did not receive any financial support for the research, authorship, or publication of this study.

#### Authors' Contribution

The author contributed solely to the study.

#### The Declaration of Conflict of Interest/ Common Interest

No conflict of interest or common interest has been declared by the author.

#### The Declaration of Ethics Committee Approval

This study does not require ethics committee permission or any special permission.

#### The Declaration of Research and Publication Ethics

The authors of the paper declare that they comply with the scientific, ethical and quotation rules of SAUJS in all processes of the paper and that they do not make any falsification on the data collected. In addition, they declare that Sakarya University Journal of Science and its editorial board have no responsibility for any ethical violations that may be encountered, and that this study has not been evaluated in any academic

publication environment other than Sakarya University Journal of Science.

## REFERENCES

- [1] F. M. Al-Nasir, A. G. Jiries, G. J. Al-Rabadi, M. H. Alu'datt, C. C. Tranchant, S. A. Al-Dalain, N. Alrabadi, O. Y. Madanat, R. S. Al-Dmour, "Determination of pesticide residues in selected citrus fruits and vegetables cultivated in the Jordan Valley" *LWT*, vol. 123, pp. 109005, 2020.
- [2] A. Abbasalizadeh, S. M. Sorouraddin, M. A. Farajzadeh, M. Nemati, M. R. A. Mogoddam, "Dispersive solid phase extraction of several pesticides from fruit juices using a hydrophobic metal organic framework prior to HPLC-MS/MS determination" *Journal of Food Composition and Analysis*, vol. 114, pp. 104788, 2022.
- [3] H. Serbest, "Determination of Resmethrin in Corn Silk Matrix by Gas Chromatography-Flame Ionization Detector (GC-FID)" *Sakarya University Journal of Science*, vol. 26(5), pp. 1022-1028, 2022.
- [4] S. Amini, M. Amiri, H. Ebrahimzadeh, S. Seidi, S. H. kandeh, "Synthesis of magnetic Cu/CuFe<sub>2</sub>O<sub>4</sub>@ MIL-88A (Fe) nanocomposite and application to dispersive solid-phase extraction of chlorpyrifos and phosalone in water and food samples" *Journal of Food Composition and Analysis*, vol. 104, pp. 104128, 2021.
- [5] R.C. Gilden, K. Huffling, B. Sattler, "Pesticides and health risks" *Journal of Obstetric, Gynecologic & Neonatal Nursing*, vol. 39(1), pp. 103-110, 2010.
- [6] K. -H. Kim, E. Kabir, S. A. Jahan, "Exposure to pesticides and the associated human health effects" *Science of the total environment*, vol. 575, pp. 525-535, 2017.
- [7] V. Feigenbrugel, S. Le Calvé, P. Mirabel, "Molar absorptivities of 2, 4-D, cymoxanil, fenpropidin, isoproturon and pyrimethanil in aqueous solution in the near-UV" *Spectrochimica Acta Part A: Molecular and Biomolecular Spectroscopy*, vol. 63(1), pp. 103-110, 2006.
- [8] J. -Y. Yoon, J. E. Kim, H. J. Song, K. B. Oh, J. W. Jo, Y. -H. Yang, S. H. Lee, G. Kang, H. J. Kim, Y. -K. Choi, "Assessment of adsorptive behaviors and properties of grape pomace-derived biochar as adsorbent for removal of cymoxanil pesticide" *Environmental Technology & Innovation*, vol. 21, pp. 101242, 2021.
- [9] X. Jiang, H. Jin, Y. Sun, R. Gui, "Colorimetric and fluorometric dual-channel ratiometric determination of fungicide cymoxanil based on analyte-induced aggregation of silver nanoparticles and dually emitting carbon dots" *Microchimica Acta*, vol. 186, pp. 1-12, 2019.
- [10] H. Mercan, R. Inam, "Determination of Cymoxanil Fungicide in Commercial Formulation and Natural Water by Square-wave Stripping Voltammetry" *CLEAN–Soil, Air, Water*, vol. 38(5-6), pp. 558-564, 2010.
- [11] P. Fidente, C. D. Giovanni, S. Seccia, P. Morrica, "Determination of cymoxanil in drinking water and soil using high-performance liquid chromatography" *Biomedical Chromatography*, vol. 19(10), pp. 766-770, 2005.
- [12] A. S. TP, K. Banerjee, M. Jadhav, R. Girame, S. Utture, S. Hingmire, D.

- Oulkar, "Residue dissipation and processing factor for dimethomorph, famoxadone and cymoxanil during raisin preparation" *Food chemistry*, vol. 170, pp. 180-185, 2015.
- [13] M. J. Hengel, T. Shibamoto, "Development of a gas chromatographic method for fungicide cymoxanil analysis in dried hops" *Journal of agricultural and food chemistry*, vol. 49(2), pp. 570-573, 2001.
- [14] D. Baval, J. Zima, J. Barek, H. Dejmkova, "Voltammetric determination of cymoxanil and famoxadone at different types of carbon electrodes" *Electroanalysis*, vol. 28(5), pp. 1029-1034, 2016.
- [15] K. Dost, M. Öksüz, M. Cittan, B. Mutlu, B. Tural, "Determination of boscalid, pyraclostrobin and trifloxystrobin in dried grape and apricot by HPLC/UV method" *Journal of Food Composition and Analysis*, vol. 115, pp. 104926, 2023.
- [16] R. R. Pasupuleti, Z. -F. Wang, W. -J. Ya, C. -A. Kuo, Y. -Y Chao, Y. -L. Huang, "Extraction and detection of chlorophenols in water samples using deep eutectic solvent-based dispersive liquid-liquid microextraction coupled with HPLC-UV" *Microchemical Journal*, vol. 182, pp. 107843, 2022.



SAKARYA ÜNİVERSİTESİ

# FEN BİLİMLERİ ENSTİTÜSÜ DERGİSİ

Sakarya University Journal of Science  
SAUJS

ISSN 1301-4048 | e-ISSN 2147-835X | Period Bimonthly | Founded: 1997 | Publisher Sakarya University |  
<http://www.saujs.sakarya.edu.tr/>

Title: Phytochemical Components, Antioxidant, Antibacterial, and Synergistic Effects of Endemic *Sideritis trojana* Extract in Combination with Antibiotics on Human Pathogens

Authors: Mehzat ALTUN

Received: 2023-03-08 00:00:00

Accepted: 2023-07-06 00:00:00

Article Type: Research Article

Volume: 27

Issue: 5

Month: October

Year: 2023

Pages: 1008-1018

How to cite

Mehzat ALTUN; (2023), Phytochemical Components, Antioxidant, Antibacterial, and Synergistic Effects of Endemic *Sideritis trojana* Extract in Combination with Antibiotics on Human Pathogens. Sakarya University Journal of Science, 27(5), 1008-1018, DOI: 10.16984/saufenbilder.1261904

Access link

<https://dergipark.org.tr/tr/journal/1115/issue/80257/1261904>

New submission to SAUJS

<http://dergipark.gov.tr/journal/1115/submission/start>

## Phytochemical Components, Antioxidant, Antibacterial, and Synergistic Effects of Endemic *Sideritis trojana* Extract in Combination with Antibiotics on Human Pathogens

Mehzat ALTUN<sup>1\*</sup> 

### Abstract

In recent years, dramatically rising multidrug-resistant bacteria (MDR) and side effects of antibiotics lead ethnopharmacology to discover novel antimicrobials derived from plants for bacterial infections. Traditionally, decoction or infusion of the species of *Sideritis* has been used for the treatment of diseases such as cough, stomach, gastrointestinal, and kidney disorders. In this study, we aimed to investigate the antioxidant and antibacterial activity of the ethanolic extract of *Sideritis trojana* (*S.trojana*) and its synergistic potential with antibiotics against human pathogens. Gas chromatography-mass spectrometry (GC-MS), Folin- Ciocalteu, 1-diphenyl-2-picrylhydrazyl radical (DPPH), disc diffusion, and minimum inhibitory concentration (MIC) assays were used for identifying phytochemicals, total phenolic content (TPC), antioxidant, and antibacterial activity of ethanolic extract of *S.trojana* alone and binary combination with selected antibiotics against Gram-positive and Gram-negative bacterial strains, respectively. Furthermore, the combined effects of the extract with classical antibiotics were evaluated by measuring the inhibition zone diameter (IZD). The *S.trojana* extract showed moderate antibacterial activity with the MIC ranging between 15.625 to 500 µg/mL against human pathogens and the synergistic effect was detected in a dual combination of extract and antibiotics. The extract exhibited high antioxidant activity with a low IC<sub>50</sub> value (0.138±0.010 mg/mL). The TPC value was 47.95±0.24 (mg GAE/g extract). After measurements of cytotoxicity were performed, *S.trojana* can be used alone or combined with antibiotics as an alternative therapy to eliminate pathogens and can be preferred as an antioxidant agent in the pharmaceutical industry.

**Keywords:** *S.trojana*, antioxidant capacity, antibacterial activity, synergism

### 1. INTRODUCTION

Antibiotics play an important role in the prevention and treatment of bacterial diseases.

Nowadays, the excessive and inappropriate consumption of antibiotics, coupled with the lack of new effective antibiotics, and resistance mechanism developed by bacteria leads to treatment failures [1-3]. Antibiotic-resistant bacteria are reported by the World

<sup>1</sup> \* Corresponding author: mehzataaltun@comu.edu.tr (M. ALTUN)

Canakkale Onsekiz Mart University, Vocational School of Health Services, Türkiye

ORCID: <https://orcid.org/0000-0001-7363-5056>



Health Organization (WHO) as a major global health issue due to increased morbidity, mortality, and healthcare costs [4, 5].

Difficulty to eliminate bacteria has led to research on natural antibacterial agents like extracts of plants with pharmacological activity. Among plants, the *Lamiaceae* family contains natural therapeutically bioactive compounds and has been used in traditional medicine since ancient times [6]. The extract of the genus *Sideritis* (belonging to *Lamiaceae*) includes 46 species in the flora of Turkey and 25 of them are endemic. *S.trojana* is used as an herbal tea for the treatment of colds and is endemic to Kazdagları (Ida Mountains) [7, 8].

Aerial parts of the *Sideritis* plant extracts are used in traditional medicine as an anti-inflammatory, antioxidant, and antimicrobial agent due to their variety content of secondary metabolites such as essential oils, flavonoids, iridoids, sterols, and terpenes [9]. Plant extracts combined with antibiotics may act synergistically and enhance their therapeutic effects against bacteria [10].

The objective of this study was to determine the phytochemical components, TPC, antioxidant, and antimicrobial activity of ethanolic extract of *S.trojana* alone and combined with classical antibiotics against 9 bacterial strains.

## 2. MATERIALS and METHODS

### 2.1. Plant Material

Aerial parts of *S.trojana* were collected from Kazdagları (Bayramic, Canakkale) in the Marmara Region of Turkey on August 2021. The plant was identified by Canakkale Onsekiz Mart University, Herbarium of the Department of Biology, and the voucher specimen was 002865. The plants were dried at 37°C in an oven.

### 2.2. Preparation of Ethanolic Extract

Aerial parts (stems, leaves, and flowers) of the *S.trojana* (20 gr) were milled into powder using an electric blender and extracted with 70% ethanol (250 mL) using a Soxhlet extractor for 6 h. Then, the filtrate was evaporated at 45°C by a vacuum evaporator. The crude extract was weighed and stored at 4°C in a dark until bioassays.

### 2.3. Gas Chromatography-mass Spectrometry

The chemical composition of *S.trojana* ethanolic extract was determined by GC-MS using Shimadzu GCMS QP 2010 ULTRA (USA) containing an RXI-5MS capillary column (30 m; 0.25 mm; 0.25  $\mu$ m). Helium was used as a carrier gas (1.0 mL/min). The split ratio was 1:30. The injector temperature was set at 250°C. The initial oven temperature was set at 50°C for 5 min. Then it was programmed to increase from 50 to 270°C at the rate of 5°C/min and held at 270°C for 5 min. The achieved chromatographic mass spectra of the peaks were identified by comparison of their mass spectra with Wiley 9 (Wiley, New York, NY, USA) and NIST 11 (National Institute of Standards and Technology) (Gaithersburg, MD, USA) libraries.

### 2.4. Total Phenolic Content and Antioxidant Activity of the Ethanolic Extract

The Folin-Ciocalteu assay determines the total phenolic content by reacting phenolic compounds with the Folin-Ciocalteu reagent, resulting in the formation of a measurable blue complex detected spectrophotometrically. This method was used to determine the TPC of the ethanolic extract of *S.trojana*. The antioxidant activity of the extract was performed using a DPPH assay. Briefly, 0.0024 g DPPH was dissolved in 100 mL ethanol (0.6 mmol/L). 250  $\mu$ L plant extract was added to 2.5 mL DPPH solution.

Gallic acid was used as a standard solution. Then, their antioxidant capacity was measured at 517 nm spectrophotometrically, and half maximal inhibitory concentration (IC<sub>50</sub>) values were calculated [11].

## 2.5. Antibacterial Activity Assays

### 2.5.1. Bacterial Strains and Culture Condition

The strains were obtained from American Type Culture Collection (ATCC). Ethanolic extract of *S.trojana* was tested for antibacterial activity against *Proteus vulgaris* ATCC 13315, *Escherichia coli* ATCC 25922, *Staphylococcus epidermidis* ATCC 12228, *Staphylococcus aureus* ATCC 25923, *Streptococcus pyogenes* ATCC 19615, *Bacillus subtilis* ATCC 6633, *Enterococcus faecalis* ATCC 29212, *Pseudomonas aeruginosa* ATCC 10145, and *Streptococcus agalactiae* ATCC 12386. All strains were stored at -20°C in Brain Heart Infusion broth (BHI) (Biokar, France) with 20% glycerol (Sigma Aldrich).

### 2.5.2. Agar Disk Diffusion Assay

The antimicrobial activity of the extract of *S.trojana* was determined by using the disc diffusion method [12]. The strains were refreshed in BHI at 37°C for 24h. The bacterial suspension was adjusted to a concentration of  $1.5 \times 10^6$  CFU/mL, and then, spread on Brain Heart Agar (BHA) (Biokar, France) plates. The crude extract was resuspended in 2.5% dimethyl sulfoxide (DMSO) and filtered through a 0.45 µm syringe filter. 2 mg/mL of 20 µL of extract-DMSO was impregnated to the 6 mm diameter paper discs under aseptic condition and incubated at room temperature for 20 minutes. After incubation at 37°C for 20 h, the inhibition zone diameters (IZDs) were measured. Gentamicin, ampicillin, and vancomycin were used as positive controls. DMSO (solvent) was used as a negative control.

### 2.5.3. Synergistic Activity of Ethanolic Extract of the Aerial Parts of *S.Trojana* in Combination with Selected Antibiotics

Gentamicin (for Gr negative strains), ampicillin (for Gr positive strains), and vancomycin (for *S.aureus*, and *S.epidermidis*) antibiotics were used in combination with aerial parts of the extract to evaluate the synergistic antimicrobial activity using double disc diffusion assay. 100 µL of each inoculum ( $1.5 \times 10^6$  CFU/mL) was spread on BHA plates. 10 µL of extract (at a concentration of 2 mg/mL) was added to antibiotic discs placed on the surface of the BHA plates. Followed by incubation at 37°C for 20 h, IZDs were measured in mm. To detect the combined effect between antimicrobials interpreted following the formula:

Growth inhibitory indices (GIIs): IZD in combination/IZD of the extract + IZD of antibiotic

If the result was GIIs > 0.5, 0.5, and < 0.5, the interaction was considered synergistic, additive, and antagonistic, respectively [13].

### 2.5.4. Determination of Minimum Inhibitory Concentration

The MIC of the extract was determined by microdilution broth using 96 well plates. Briefly, 100 µL of extract (2 mg/mL) was dissolved in 2.5% DMSO, then serially diluted in 100 µL of BHI in wells. Concentrations of ethanolic extract of *S.trojana* ranged from 1000 to 3.91 µg/mL. Each bacterial inoculum (20 µL) was added to all wells except sterility control [14]. Then, incubated at 37°C for 20 h, 10 µL of 0.2 mg/mL growth indicator (iodonitrotetrazolium chloride dye, Sigma-Aldrich) was added to each well to determine MIC. 5 µL of inoculum from negative wells was transferred on BHA and incubated at the same condition. The extract concentration, in which bacteria did not grow, was defined as MBC [15].



### 2.5.5. Statistical Analysis

Statistical analysis was performed using SPSS 19 version. One-way ANOVA and post hoc Tukey test were used to compare data (\* $p < 0.05$ ).

## 3. RESULTS

### 3.1. Phytochemical Analysis of *S.trojana* Extract

Ethanollic extract of *S.trojana* was prepared by Soxhlet extractor. The GC-MS chromatogram of the extract is shown in Figure 1 and a total of 67 compounds were identified and shown in Table 1. Hydrocarbons 20.28% (Tridecane, tetradecane, dodecane, and trimethyl-tetrahydronaphthalene), sesquiterpenes 10.38% (caryophyllene oxide,  $\beta$ -caryophyllene, germacrene-D, bibisabolol oxide, cyclogermacrene, and farnesene),

monoterpenes 8.31% (carvacrol, eugenol, geranyl- $\alpha$ -terpinene, 1,8-cineole, linalool, and myrtenol), maltol 3.68%, and sesquiterpenoids 3.14% ( $\alpha$ -bisabolol, and  $\beta$ -bisabolene) were the main components of the extract and responsible for its biological properties.

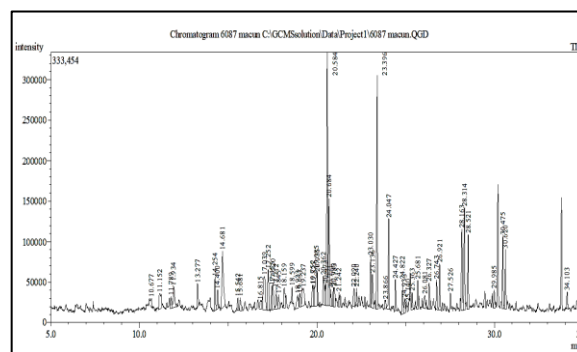


Figure 1 GC-MS chromatogram files of the aerial parts of the *S.trojana* extract with the Retention times (Rt)

Table 1 Composition (%) of ethanolic extract of *S.trojana* aerial parts

Peak	Rt	Area (%)	Components	Classification
1	1.445	1.75	Formic acid	Carboxylic acid
2	1.515	0.48	Propanal, 2-methyl-	Aldehyde.
3	1.694	2.76	Acetic acid (CAS)	Carboxylic acid
4	3.620	0.52	2,3-Butanediol (CAS)	Diol
5	4.704	2.57	Dimethylsulfoxonium formylmethylide	Ylide
6	10.677	0.52	Hexanoic acid (CAS)	Carboxylic acid
7	11.152	1.38	3-Hydroxy-4-pyrone	Pyrone
8	11.789	0.52	1,8-Cineole	Monoterpene oxide
9	11.934	1.19	Benzyl alcohol	Aromatic alcohol
10	13.277	0.82	Capryl alcohol	Fatty alcohol
11	14.254	1.25	Linalool	Terpene alcohol
12	14.400	0.75	Pelargonaldehyde	Aldehyde
13	14.681	3.68	Maltol	Pyrone
14	15.542	0.50	Bicyclo[3.1.1]heptan-3-ol, 6,6-dimethyl-2-methylene-, [1S-(1.alpha.,3.alpha.,5.alpha.)]-	Bicyclic alcohol
15	15.681	0.69	2,3-Dihydro-3,5-dihydroxy-6-methyl-4H-pyran-4-one	Pyranone
16	16.815	0.66	Geranyl butyrate	Ester
17	17.039	3.00	Undecanoic acid, ethyl ester (CAS)	Ester
18	17.252	2.08	3-Cyclohexene-1-methanol, .alpha.,.alpha.,4-trimethyl-, (S)- (CAS)	Cyclohexene alcohol
19	17.455	0.91	Myrtenol	Terpene alcohol
20	17.520	1.32	Butane, 1,1'-[methylenebis(oxy)]bis[3-methyl-	Bisether
21	17.712	0.83	Decanal (CAS)	Aldehyde
22	17.845	0.72	Bicyclo[3.1.1]hept-3-en-2-one, 4,6,6-trimethyl-, (1S)-	Bicyclic ketone

Table 1 Composition (%) of ethanolic extract of *S.trojana* aerial parts (Continue)

Peak	Rt	Area (%)	Components	Classification
23	18.159	1.11	Ethanol, 2-phenoxy- (CAS)	Ether
24	18.599	0.46	1H-Pyrrole-2,5-dione, 3-ethyl-4-methyl- (CAS)	Pyrrolidinedione
25	18.923	0.90	Benzeneacetic acid, ethyl ester (CAS)	Ester
26	19.037	0.53	3-Octanol (CAS)	Alcohol
27	19.237	1.60	Geranyl phenylacetate	Ester
28	19.752	1.10	Benzaldehyde, 4-propyl-	Aldehyde
29	19.825	1.02	cis-Pinonic acid	Carboxylic acid.
30	19.985	2.42	Dodecane, 4-methyl-	Alkane
31	20.035	0.72	Nonanoic acid (CAS)	Carboxylic acid
32	20.362	1.61	Propan-2-ol, 1-(3,4-dimethoxyphenyl)-2-methyl-	Alcohol
33	20.473	0.78	2-Propanol, 1-[2-(2-methoxy-1-methylethoxy)-1-methylethoxy]- (CAS)	Alcohol
34	20.584	9.16	Tridecane	Alkane
35	20.684	4.34	Carvacrol	Monoterpene phenol
36	20.771	0.58	Formamide, N,N-dibutyl-	Amide
37	20.930	0.83	Tri(1,2-propyleneglycol), monomethyl ether	Glycol ether
38	20.983	0.64	Guaiacol <4-vinyl->	Phenolic compound
39	21.242	0.56	Cyclohexane, 1,1,4,4-tetramethyl-2,6-bis(methylene)-	Substituted cycloalkane
40	22.090	0.87	trimethyl-tetrahydronaphthalene	Polycyclic hydrocarbon
41	22.240	0.48	Eugenol	Phenolic compound
42	23.030	1.47	2-Buten-1-one, 1-(2,6,6-trimethyl-1,3-cyclohexadien-1-yl)-, (E)-	Enone
43	23.136	1.48	trans-Z-.alpha.-Bisabolene epoxide	Sesquiterpene
44	23.396	7.83	Tetradecane (CAS)	Alkane
45	23.866	0.47	6,8-Nonadien-2-one, 6-methyl-5-(1-methylethylidene)-	Unsaturated ketone
46	24.047	3.00	Trans-β-Caryophyllene	Sesquiterpene
47	24.427	0.91	op[e]azulen-7-ol, decahydro-1,1,7-trimethyl-4-methylene-, [1a.alpha.,4a.alpha.,7.beta.,7a.beta.,	Tricyclic sesquiterpene alcohol
48	24.822	1.20	Diisopropyl adipate	Ester
49	24.933	0.73	Farnesene <(E)-, beta->	Sesquiterpene
50	25.140	0.45	Methyl-(2-hydroxy-3-ethoxy-benzyl)ether	Ether
51	25.363	0.62	Lauryl alcohol	Fatty alcohol
52	25.681	1.08	Germacrene-D	Sesquiterpene hydrocarbon
53	26.081	0.84	Bicyclogermacrene	Sesquiterpene hydrocarbon
54	26.327	1.00	beta.-Bisabolene	Sesquiterpene hydrocarbon.
55	26.744	0.93	Naphthalene, 1,2,3,5,6,8a-hexahydro-4,7-dimethyl-1-(1-methylethyl)-, (1S-cis)-	Bicyclic hydrocarbon
56	26.921	1.48	2(4H)-Benzofuranone, 5,6,7,7a-tetrahydro-4,4,7a-trimethyl-, (R)-	Benzofuranone derivative
57	27.526	0.45	Caryophyllene oxide	Sesquiterpene oxide
58	28.163	3.20	op[e]azulen-7-ol, decahydro-1,1,7-trimethyl-4-methylene	Opazulenoid alcohol
59	28.315	3.54	Caryophyllene oxide	Sesquiterpene oxide
60	28.521	2.43	Pentanoic acid, 2,2,4-trimethyl-3-carboxyisopropyl, isobutyl ester	Ester
61	29.985	0.74	Bisabolol oxide B <alpha->	Sesquiterpene oxide

Table 1 Composition (%) of ethanolic extract of *S.trojana* aerial parts (Continue)

Peak	Rt	Area (%)	Components	Classification
62	30.475	2.34	2H)-Naphthalenone, octahydro-4a,8a-dimethyl-7-(1-methylethyl)-, [4aR-(4a.alpha.,7.beta.,8a.alpha.	Octahydro-naphthalenone
63	30.620	2.14	Alpha-Bisabolol	Sesquiterpene alcohol
64	34.103	0.57	2-Pentadecanone, 6,10,14-trimethyl-	Ketone.
65	36.455	0.81	geranyl-.alpha.-terpinene	Terpene
66	37.125	1.03	18-Norabietane	Triterpene hydrocarbon
67	37.867	0.66	4b,8-Dimethyl-2-isopropylphenanthrene, 4b,5,6,7,8,8a,9,10-octahydro-	Phenanthrene derivative
		100		

Rt: Retention time

### 3.2. Antioxidant Properties of *S.trojana* Extract

The extract yields, TPC, and IC<sub>50</sub> values for the extract are given in Table 2. According to the DPPH assay, the extract showed a strong radical scavenging effect with a low IC<sub>50</sub> value of 0.138±0.010 mg/mL.

Table 2 Extract yield, and antioxidant capacity of *S.trojana* extract

The yield of extract (%)	TPC (mg GAE/g extract)	DPPH (IC <sub>50</sub> mg/mL)
23%	47.95±0.24	0.138±0.010

### 3.3. Antibacterial Activity

The endemic plant extract was tested for its inhibitory activity alone and in combination with antibiotics on Gram-positive (*S.epidermidis*, *S.aureus*, *S.pyogenes*, *B.subtilis*, *E.faecalis*, and *S.agalactiae*) and Gram-negative (*P.aeruginosa*, *E.coli*, and *P.vulgaris*) bacterial strains using disc diffusion assay. The IZDs and MIC/MBC results were given in Table 3. The extract showed excellent antibacterial activity on strains (p< 0.05) except *P.aeruginosa* (p: 0.910) compared to antibiotics. The synergistic effect of the ethanolic extract of *S.trojana* was detected in combination with antibiotics against all strains except *P.aeruginosa*. The highest antibacterial effect of *S.trojana* extract against *B.subtilis*, and *P.aeruginosa* with a MIC value of 15.625 µg/mL.

## 4. DISCUSSION

Medicinal plants like *Sideritis* species and their active components have been used as antioxidant, antibacterial, anti-inflammatory, and antifungal alternative agents in pharmacology [16-20]. In a study conducted by Tunalier et al., the extract yields (%) of 27 *Sideritis* species were found between 15.8 to 31.2% as same as our result (23%) [21]. In this study, hydrocarbons and the group of terpene which is responsible for its antioxidant and antimicrobial properties were detected in the *S.trojana* extract. Many studies have reported that common components of *Sideritis* species were monoterpenoids, monoterpenes, diterpenes, hydrocarbon, oxygenated monoterpene, and sesquiterpenoids [22, 23]. The differences in the compositions of the ethanolic extract are due to the climatic and experimental conditions, parts of the plant, the solvent type, and components that may affect its pharmacological activity [9, 24].

The antioxidant activity of *Sideritis* taxa [25-27], the TPC value of the methanolic extract of *Sideritis perfoliata* L. (41.64±0.99 mg GAEs/g extract) [28], and the ethanolic extract of *Salvia officinalis* (*Lamiaceae* family; 43.55 mg GAE/g) [29] was previously reported were consistent with our data. Different TPC and DPPH results of *Sideritis raeseri* ssp. *attica* [30] and *Sideritis cypria* [31] extracts were observed. The differences between results may be due to the extraction

method, species type, climate, and geographical location [32].

The experimental results of this study showed the MIC/MBC values ranged from 15.625 to 500 µg/mL. González-burgos et al. reported that the *Sideritis* spp. extracts exhibited strong antibacterial activity with MIC values ranging from 0.03 to 0.38 mg/mL against *B.subtilis*, *E.coli*, and *P.aeruginosa* [9]. The extract of *S.italica* showed antibacterial activity against *P.aeruginosa*, *P.mirabilis*, *S.typhi*, and *P.vulgaris* [33]. In a study conducted by Askun et al., antibacterial activity was detected the methanolic extract of *S.leptoclada* with a MIC of 640 µg/mL against *Enterobacter aerogenes* and *Salmonella typhimurium* [34]. The extract of *S.perfoliata* exhibited an antibacterial effect on *Cutibacterium acnes* [35]; *Streptococcus mutans* and *Prevotella intermedia* (Lall) with MIC values of 500 µg/mL, 6.25 mg/mL, and 3.125 mg/mL, respectively [14]. Moreover, the methanolic extract of *S.inca* represented an antibacterial effect against Gram-positive and Gram-negative bacteria with MICs ranging

from 2.60 to 20.863 mg/mL [36]. The antibacterial properties of the ethanolic extract of *S.trojana* are attributed to the presence of terpenes, some flavonoids, iridoids, sterols, and essential oils [8, 10, 37, 38].

In this study, synergistic interactions between *S.trojana* extract and commercial antibiotics on *P.vulgaris*, *E.coli*, *S.epidermidis*, *S.aureus*, *S.pyogenes*, *B.subtilis*, *E.faecalis*, and *S.agalactiae* were detected. These findings are in accordance with the results of the study conducted by Abullais et al., the ethanolic *P.granatum*, *Commiphora molmol*, and *Azadirachta indica* extracts in combination with amoxicillin, tetracycline, metronidazole, and azithromycin antibiotics showed a synergistic inhibitory effect on periodontopathic bacteria [10]. Another study reported that the ethanolic extract of *Ocimum sanctum* Linn. (*Lamiaceae*) showed synergistic activity in combination with chloramphenicol and trimethoprim against *Salmonella typhi* isolates [39].

Table 3 Antibacterial activity of *S.trojana* ethanolic extract alone and in combination with antibiotics used for the treatment of bacterial infections

Bacteria	Antibiotics	IZD Extract (mm)	IZD Antibiotics (mm)	IZD Antibiotics+ Extract (mm)	Outcome	p value	MIC (µg/mL)	MBC (µg/mL)
<i>S.epidermidis</i> ATCC 12228	VA	25.50 ±1.290	18.5 ±0.577	22.50 ±0.577	0.511 S		62.5	125
<i>S.aureus</i> ATCC 25923	VA	22.25 ±1.258	24.50 ±0.577	27.50 ±0.577	0.588 S		31.25	62.5
<i>S.pyogenes</i> ATCC 19615	AMP	12.00 ±0.816	10.50 ±0.577	17.25 ±0.50	0.766 S	p< 0.05	500	Growth
<i>B.subtilis</i> ATCC 6633	AMP	23.25 ±2.50	11.25 ±0.957	25.25 ±0.50	0.644 S		15.625	62.5
<i>E.faecalis</i> ATCC 29212	AMP	15.00 ±0.816	14.75 ±0.50	15.75 ±1.50	0.529 S		250	Growth
<i>S.agalactiae</i> ATCC 12386	AMP	21.00 ±0.816	18.25 ±1.258	27.25 ±0.25	0.694 S		62.5	500
<i>E.coli</i> ATCC 25922	GEN	26.25 ±0.957	18.75 ±1.50	22.75 ±0.957	0.505 S		62.5	250
<i>P.vulgaris</i> ATCC 13315	GEN	22.25 ±0.957	18.75 ±1.258	26.00 ±0.816	0.634 S		31.25	125
<i>P.aeruginosa</i> ATCC 10145	GEN	29.25 ±0.957	20.50 ±0.577	20.75 ±0.957	0.417 A	p:0.910	15.625	62.5

\*p < 0.05 = significant difference; S: Synergism, Ad: Additive, A: Antagonism. VA: Vancomycin, AMP: Ampicillin, GEN: Gentamycin

## 5. CONCLUSION

The ethanolic extract of aerial parts of *S.trojana* showed strong antioxidant activity and exhibited antibacterial activity both alone and combined with antibiotics against 8 human pathogens. The extract has a huge potential to develop new antibiotic formulations for the treatment of bacterial diseases. The combined use of antibiotics and plant extract can increase the antibacterial effect on resistant bacteria and may decrease their costs and side effects.

However, *in vitro* and *in vivo* toxicity assays and clinical trials are required for its use in therapy.

### **Funding**

The author has not received any financial support for the research, authorship, or publication of this study.

### **Authors' Contribution**

Laboratory studies, statistical analysis, writing article were performed by MA.

### **The Declaration of Conflict of Interest/ Common Interest**

No conflict of interest.

### **The Declaration of Ethics Committee Approval**

This study does not require ethics committee permission or any special permission.

### **The Declaration of Research and Publication Ethics**

The authors of the paper declare that they comply with the scientific, ethical and quotation rules of SAUJS in all processes of the paper and that they do not make any falsification on the data collected. In addition, they declare that Sakarya University Journal of Science and its editorial board have no responsibility for any ethical violations that may be encountered, and that this study has not been evaluated in any academic publication environment other than Sakarya University Journal of Science.

## REFERENCES

- [1] T. Pulingam, T. Parumasivam, A. M. Gazzali, A. M. Sulaiman, J. Y. Chee, M. Lakshmanan, C. F. Chin, K. Sudesh, "Antimicrobial resistance: Prevalence, economic burden, mechanisms of resistance and strategies to overcome", *European Journal of Pharmaceutical Sciences*, vol 170, pp. 106103, 2022.
- [2] S. B. Zaman, M. A. Hussain, R. Nye, V. Mehta, K. T. Mamun, N. Hossain, "A Review on Antibiotic Resistance: Alarm Bells are Ringing", *Cureus*, vol. 9, pp. 1403, 2017.
- [3] J. M. Munita, C. A. Arias, "Mechanisms of Antibiotic Resistance", *Microbiology Spectrum*, vol.4,10.1128/microbiolspec.VMBF-0016-2015, 2016.
- [4] M. Huemer, S. Mairpady Shambat, S. D. Brugger, A. S. Zinkernagel, "Antibiotic resistance and persistence- Implications for human health and treatment perspectives", *European Molecular Biology Organization Reports*, vol. 21, pp. 51034, 2020.
- [5] M. E. de Kraker, A. J. Stewardson, S. Harbarth, "Will 10 Million People Die a Year due to Antimicrobial Resistance by 2050?", *Public Library of Science Medicine*, vol. 13, e1002184, 2016.
- [6] E. Zvezdina, J. Dayronas, I. Bochkareva, I. Zilfikarov, E. Y. Babaeva, E. Ferubko, Z. Guseynova, F. Serebryanaya, S. Kaibova, T. Ibragimov, "Members of the family *Lamiaceae* Lindl. as sources of medicinal plant raw materials to obtain neurotropic drugs", *Pharmacy & Pharmacology*, vol. 8, pp. 4-28, 2020.
- [7] M. Temel, R. Kara, R. Müdüroğlu, L. Akkaya, "Antibacterial Activity of Turkish Endemic *Sideritis akmanii*

- (*Lamiaceae*)”, *Global Journal for Research Analysis*, vol. 3, pp. 83-84, 2012.
- [8] G. Topcu, A. C. Goren, T. Kilic, Y. K. Yildiz, G. Tumen, “Diterpenes from *Sideritis trojana*”, *Natural Product Letters*, vol. 16, pp. 33–37, 2002.
- [9] E. González-Burgos, M. E. Carretero, M. P. Gómez-Serranillos, “*Sideritis* spp.: Uses, chemical composition, and pharmacological activities - A review”, *Journal of Ethnopharmacology*, vol. 135, pp. 209-225, 2011.
- [10] S. Abullais Saquib, A. Abdullah, N. Qahtani, I. Ahmad, S. Arora, S. Mohammed Asif, M. Ahmed Javali, N. Nisar, “Synergistic antibacterial activity of herbal extracts with antibiotics on bacteria responsible for periodontitis”, *The Journal of Infection in Developing Countries*, vol. 15, pp. 1685-1693, 2021.
- [11] B. Y. Kardas, M. E. Diken, H. Bayhan, M. Acar, S. Dogan, “Cytoprotective, antimutagenic/anti recombinogenic and antibacterial properties of *Lallemantia iberica* extracts”, *Journal of the Science of Food and Agriculture*, 2022.
- [12] P. A. Wayne, “Materials and Methods Clinical and Laboratory Standards Institute (CLSI)”, *Performance Standards for Antimicrobial Disk Susceptibility Testing*, 28th ed. M100S, CLSI, USA, vol. 38, 2018.
- [13] S. Mandal, M. D. Mandal, N. K. Pal, K. Saha, “Synergistic anti-*Staphylococcus aureus* activity of amoxicillin in combination with *Emblica officinalis* and *Nymphae odorata* extracts”, *Asian Pacific Journal of Tropical Medicine*, vol. 3, pp. 711-714, 2010.
- [14] N. Lall, A. Chrysargyris, I. Lambrechts, B. Fibrich, A. Blom Van Staden, D. Twilley, M. N. de Canha, C. B. Oosthuizen, D. Bodiba, N. Tzortzakis, “*Sideritis perfoliata* (subsp. *perfoliata*) Nutritive Value and Its Potential Medicinal Properties”, *Antioxidants*, vol. 8, pp. 521, 2019.
- [15] A. Bouyahya, N. Dakka, A. Talbaoui, A. Et-Touys, H. El-Boury, J. Abrini, Y. Bakri, “Correlation between phenological changes, chemical composition, and biological activities of the essential oil from Moroccan endemic Oregano (*Origanum compactum* Benth)”, *Industrial Crops and Products*, vol. 108, pp. 729-737, 2017.
- [16] I. Jeremic, S. Petricevic, V. Tadic, D. Petrovic, J. Tosic, Z. Stanojevic, M. Petronijevic, S. Vidicevic, V. Trajkovic, A. Isakovic, “Effects of *Sideritis scardica* extract on glucose tolerance, triglyceride levels and markers of oxidative stress in ovariectomized rats”, *Planta Medica*, vol. 85, pp. 465–472, 2019.
- [17] O. Sagdic, A. Aksoy, G. Ozkan, L. Ekici, S. Albayrak, “Biological activities of the extracts of two endemic *Sideritis* species in Turkey”, *Innovative Food Science & Emerging Technologies*, vol. 9, pp. 80–84, 2008.
- [18] A. Ugur, O. Varol, O. Ceylan, “Antibacterial Activity of *Sideritis curvidens* and *Sideritis lanata* from Turkey”, *Pharmaceutical Biology*, vol. 43, pp. 47–52, 2005.
- [19] M. T. Charami, D. Lazari, A. Karioti, H. Skaltsa, D. Hadjipavlou-Litina, C. Souleles, “Antioxidant and antiinflammatory activities of *Sideritis perfoliata* subsp. *perfoliata* (*Lamiaceae*)”, *Phytotherapy Research*, vol. 22, pp. 450–454, 2008.

- [20] T. M. Karpinski, "Essential oils of *Lamiaceae* family plants as antifungals", *Biomolecules*, vol. 10, pp. 103, 2020.
- [21] Z. Tunalier, M. Kosar, N. Ozturk, K. H. C. Baser, H. Duman, N. Kirimer, "Antioxidant Properties and Phenolic Composition of *Sideritis* Species", *Chemistry of Natural Compounds*, vol. 40, pp. 206-210, 2004.
- [22] A. Koutsaviti, I. Bazos, M. Milenkovi'c, M. Pavlovi'c-Drobac, O. Tzakou, "Antimicrobial activity and essential oil composition of five *Sideritis* taxa of Empedoclia and Hesiodia sect. from Greece", *Records of Natural Products*, vol. 7, pp. 6-14, 2013.
- [23] N. Kirimer, N. Tabanca, T. Ozek, G. Tumen, K. H. Baser, "Essential oils of annual *Sideritis* species growing in Turkey", *Pharmaceutical Biology*, vol. 38, pp. 106-111, 2000.
- [24] A. B. Trendafilova, M. N. Todorova, L. N. Evstatieva, D. V. Antonova, "Variability in the Essential-Oil Composition of *Sideritis scardica* Griseb. from Native Bulgarian Populations", *Chemistry and Biodiversity*, vol. 10, pp. 484-492, 2013.
- [25] M. Kara, H. Sahin, H. Turumtay, S. Dinc, A. Gumuscu, "The phenolic composition and antioxidant activity of tea with different parts of *Sideritis* condensate at different steeping conditions", *Journal of Food and Nutrition Research*, vol. 2, pp. 258-262, 2014.
- [26] A. Gokbulut, A. N. Yazgan, H. Duman, B. S. Yilmaz, "Evaluation of the antioxidant potential and Chlorogenic acid contents of three endemic *Sideritis* taxa from Turkey", *Fabad Journal of Pharmaceutical Sciences*, vol. 42, pp. 81-86, 2017.
- [27] Z. O. Sagir, S. Carikci, T. Kilic, A. C. Goren, "Metabolic profile and biological activity of *Sideritis brevibracteata* PH Davis endemic to Turkey", *International Journal of Food Properties*, vol. 20, pp. 2994-3005, 2017.
- [28] C. Sarikurkcü, M. Locatelli, A. Mocan, G. Zengin, B. Kirkan, "Phenolic Profile and Bioactivities of *Sideritis perfoliata* L.: The Plant, Its Most Active Extract, and Its Broad Biological Properties", *Frontiers in Pharmacology*, vol. 10, pp. 1642, 2020.
- [29] R. Ariduru, G. Arabaci, "Determination of antioxidant activities in fresh liver (*salvia officinalis*) plant", *Sakarya University Journal of Science*, vol. 17, pp. 241-246, 2013.
- [30] D. Stagos, N. Portesis, C. Spanou, D. Mossialos, N. Aligiannis, E. Chaita, C. Panagoulis, E. Reri, L. Skaltsounis, A. M. Tsatsakis, D. Kouretas, "Correlation of total polyphenolic content with antioxidant and antibacterial activity of 24 extracts from Greek domestic *Lamiaceae* species", *Food and Chemical Toxicology*, vol. 50, pp. 4115-4124, 2012.
- [31] K. Lytra, E. M. Tomou, A. Chrysargyris, M. D. Christofi, P. Miltiadous, N. Tzortzakis, H. Skaltsa, "Bio-Guided Investigation of *Sideritis cypria* Methanol Extract Driven by in Vitro Antioxidant and Cytotoxic Assays", *Chemistry and Biodiversity*, vol. 18, pp. 2000966, 2021.
- [32] C. Dincer, I. Tontul, I. B. Cam, K. S. Ozdemir, A. Topuz, H. Ş. Nadeem, R. S. Gokturk, "Phenolic composition and antioxidant activity of *Salvia tomentosa*

- Miller: Effects of cultivation, harvesting year, and storage”, Turkish Journal of Agriculture and Forestry, vol. 37, pp. 561–567, 2013.
- [33] A. Basile, F. Senatore, R. Gargano, S. Sorbo, M. Del Pezzo, A. Lavitola, A. Ritieni, M. Bruno, D. Spatuzzi, D. Rigano, M. L. Vuotto, “Antibacterial and antioxidant activities in *Sideritis italica* (Miller) Greuter et Burdet essential oils”, Journal of Ethnopharmacology, vol. 107, pp. 240–248, 2006.
- [34] T. Askun, G. Tumen, F. Satil, M. Ates, “Characterization of the phenolic composition and antimicrobial activities of Turkish medicinal plants”, Pharmaceutical Biology, vol. 47, pp. 563–571, 2009.
- [35] A. P. S. A. Da Silva, L. C. Nascimento Da Silva, C. S. Martins Da Fonseca, J. M. de Araújo, M. T. dos Santos Correia, M. da Silva Cavalcanti, V. L. de Menezes Lima, “Antimicrobial activity and phytochemical analysis of organic extracts from *Cleome spinosa* Jacq”, Frontiers in Microbiology, vol. 7, pp. 1–10, 2016.
- [36] A. Bouymajane, F. R. Filali, Y. O. El Majdoub, M. Ouadik, R. Abdelilah, E. Cavò, N. Miceli, M. F. Taviano, L. Mondello, F. Cacciola, “Phenolic Compounds, Antioxidant and Antibacterial Activities of Extracts from Aerial Parts of *Thymus zygis* subsp. *gracilis*, *Mentha suaveolens* and *Sideritis incana* from Morocco”, Chemistry and Biodiversity, vol. 19, pp. 202101018, 2022.
- [37] N. Kirimer, B. Demirci, G. Işcan, K. H. C. Başer, H. Duman, “Composition of the essential oils of two *Sideritis* species from Turkey and antimicrobial activity”, Chemistry of Natural Compounds, vol. 44, pp. 121-123, 2008.
- [38] H. Kırmızıbekmez, E. Ariburnu, M. Masullo, M. Festa, A. Capasso, E. Yeşilada, S. Piacente, “Iridoid, phenylethanoid and flavonoid glycosides from *Sideritis trojana*”, Fitoterapia, vol. 83, pp. 130-136, 2012.
- [39] S. Mandal, M. D. Mandal, N. K. Pal, “Enhancing chloramphenicol and trimethoprim in vitro activity by *Ocimum sanctum* Linn. (*Lamiaceae*) leaf extract against *Salmonella enterica* serovar Typhi”, Asian Pacific Journal of Tropical Medicine, vol. 5, pp. 220-224, 2012.





SAKARYA ÜNİVERSİTESİ

# FEN BİLİMLERİ ENSTİTÜSÜ DERGİSİ

Sakarya University Journal of Science  
SAUJS

ISSN 1301-4048 | e-ISSN 2147-835X | Period Bimonthly | Founded: 1997 | Publisher Sakarya University |  
<http://www.saujs.sakarya.edu.tr/>

Title: Ergonomic Risk Assessment in the Forest Products Industry

Authors: Merve YILMAZ, Muharrem ÜNVER

Received: 14.03.2023

Accepted: 2023-07-07 00:00:00

Article Type: Research Article

Volume: 27

Issue: 5

Month: October

Year: 2023

Pages: 1019-1035

How to cite

Merve YILMAZ, Muharrem ÜNVER; (2023), Ergonomic Risk Assessment in the Forest Products Industry. Sakarya University Journal of Science, 27(5), 1019-1035, DOI: 10.16984/saufenbilder.1265076

Access link

<https://dergipark.org.tr/tr/journal/1115/issue/80257/1265076>

New submission to SAUJS

<http://dergipark.gov.tr/journal/1115/submission/start>

## Ergonomic Risk Assessment in the Forest Products Industry

Merve YILMAZ\*<sup>1</sup> , Muharrem ÜNVER<sup>1</sup> 

### Abstract

With the advancement of technology, the pressure on personnel in corporate operations has been reduced and productivity has increased. However, many industries continue to profit from labor. MSD can develop as a result of poor working conditions and repetitive movements. This research was carried out in a forest products enterprise with two facilities in Western Black Sea Region. The company produces construction timber using Fir and Pine as the base material. First, the demographic information of the field workers was obtained, then the musculoskeletal diseases of the local parts of the body were examined by using the Cornell (CMDQ) questionnaire. In the second step, REBA analysis was performed independently for the workstations determined in the company. According to the CMDQ study, employees reported the most strain on the lower back, back, and right wrist. It was determined that the most discomfort was in the lumbar region (35.90%). Again, according to the pain felt, it was seen that the most obstacles to work were caused by the waist, right upper leg and back. Scores overlap according to the common body regions evaluated in the Cornell and REBA analysis.

**Keywords:** Ergonomic risk assessment, cornell questionnaire, reba method, ergonomics, musculoskeletal system disorders

### 1. INTRODUCTION

Ergonomics science encompasses all efforts aimed at making people's living abilities more comfortable. Providing a work organization that aligns with the physiological characteristics of employees and improving ergonomic working conditions translates to increased productivity and profitability for employers. The goal of ergonomics is not solely to prevent occupational diseases and accidents. It also contributes to increased motivation and job performance through the improvement of working conditions.

Ergonomics aims to optimize individuals' lifestyles for their own well-being [1].

As a result of continuous repetitive movements and ergonomically unfavorable body postures in the work environment, musculoskeletal disorders have become inevitable. Ergonomic risk factors that contribute to these disorders can be categorized into three main headings: work-related, personal, and environmental factors. Daily activities such as bending, squeezing, reaching, grasping, straightening, and even prolonged static positions can create

\* Corresponding author: merveylmzzz78@mail.com (M. YILMAZ)

<sup>1</sup> Karabuk University, Engineering Faculty, Department of Industrial Engineering, 78100, Karabuk, Türkiye  
E-mail: muharremunver@karabuk.edu.tr

ORCID: <https://orcid.org/0000-0001-9879-351X>, <https://orcid.org/0000-0001-7587-6849>



ergonomic risks in the workplace. Factors contributing to the hazardous nature of these activities include high force requirements, rapid and repetitive movements, prolonged static postures, and insufficient time between movements.

Despite the development of technology reducing the physical workload of individuals in the workplace, musculoskeletal disorders maintain their significance among employee health problems. These physical risk factors in the work environment also have implications for employees' psychology. Situations such as lack of rest breaks or minimal breaks, temporal risk factors resulting from overtime, or reluctance towards work can be considered psychosocial risk factors. Personal risk factors include factors such as aging, smoking and alcohol consumption, weight, and medical history. Environmental risk factors can be created by conditions such as noise, slippery floor surfaces, and poor lighting in the workplace [2].

The forest products industry is a sector based on the processing and shaping of raw materials obtained from forests. The diversity of processing the natural form of wood before manufacturing the products can vary. This diversity can be divided into two main groups. The first group of activities involves the direct use of raw timber obtained from forests. This includes activities such as timber production, plywood manufacturing, packaging, veneering, plywood, paper industry, particleboard, and more. The second group of activities involves the use and processing of the products obtained from the first group as semi-finished goods. In this group, products such as parquet, carpentry, wooden prefabricated elements, toys, matches, musical instruments, etc., are produced.

Within the scope of this study, a timber production factory in the first group of activities is discussed. As in any industry, the installation and equipment used in the forest products industry contribute to improving

production quality but also pose risks of accidents or occupational diseases [3]. Equipment such as saws, milling and turning machines, raw material sizing machines, equipment used to reduce surface defects, rotating/moving parts, sharp and hazardous components or dust during the supply and processing of wood, can create hazardous work environments [4]. Additionally, improperly positioned conveyor belts can lead to risks such as excessive bending, twisting, or falling from heights for workers. Such situations can result in accidents, decreased worker performance, and long-term health issues.

Efforts are made to minimize factors that cause musculoskeletal disorders in employees through ergonomic risk assessment methods. These methods can be categorized into three classes: questionnaire, systematic, and direct measurement methods [5]. Questionnaire methods are cost-effective and easy to implement, but in production environments where ergonomic risks are considered high, it is recommended to use systematic or direct measurement methods. Ergonomic risk assessment methods can work individually or in combination based on the workplace activities, workplace requirements, number of employees, time required for work, and body parts exposed to ergonomic risks. In this study, a combination of observation-based methods such as REBA analysis and questionnaire methods such as CMDQ survey was used. Risk assessment targeting employees was conducted through the survey, and the production was analyzed ergonomically from both perspectives by conducting observation-based risk assessment using the REBA method.

The workplace conditions and working styles of employees in a timber production factory, which is one of the labor-intensive establishments, were thoroughly evaluated. The aim of this study was to determine the level of exposure to ergonomic risks such as posture, body mechanics, and repetitive movements for employees, and to identify

measures to reduce these risks. Based on the applied methods within the scope of the study, it was observed that ergonomic adjustments should be made as soon as possible, and various recommendations were provided to the relevant departments of the company. It was observed that the holistic approach taken by using both systematic and questionnaire methods yielded more reliable results in the research scope.

The ongoing section of the study includes a literature review, a section describing the company and the production process, a methodology section detailing the methods used, an implementation section discussing the application of the study, and a findings and recommendations section.

## 2. LITERATURE REVIEW

Ünver and Kaya (2015) conducted a study evaluating the postures of 70 female workers employed in the reforestation operations at Trabzon-of Forest Nursery using the Rapid Entire Body Assessment (REBA) method to determine their risk levels. The REBA results indicated an ergonomic risk level of 7, signifying a moderate level of risk. It was suggested that measures should be taken regarding occupational health and safety and ergonomic arrangements in the workplace for workers identified to be at moderate risk[6].

Gönen et al. (2017) aimed to prevent workforce losses in a transformer manufacturing assembly line by using the Computerized Moving Diagram Quest (CMDQ), REBA, and Ovako Working Posture Analysis System (OWAS) methods. The study revealed that the most at-risk body parts were the back, waist, feet, and neck. To minimize these risks and enhance work efficiency under ergonomic conditions, an adjustable assembly table was recommended [7]. Nam et al. (2017) investigated the manual cleaning of residues such as gunpowder and mud from the barrel after firing heavy weapons like tanks and cannons in the armed forces.

The REBA analysis indicated an urgent need for action, calling for preventive measures. The OWAS analysis also yielded similar results. It was recommended to use automated barrel cleaning tools to reduce these high ergonomic risks, resulting in REBA and OWAS scores being reduced to the second level. Nagaraj and Jeyepaul conducted a study in a textile industry establishment, assessing ergonomic risks related to poor posture among sewing machine operators. They employed the CMDQ questionnaire and REBA analysis. The study found a mismatch between the operators' body dimensions and the machine. Furthermore, prolonged standing resulted in discomfort in the lower back region. Recommendations included adjusting the height of workstations within the company, incorporating breaks and exercises to ensure continuity[8]. Yalçın and Ayvaz (2018) conducted an ergonomic risk assessment for workers operating on four different workstations in a wheel production factory. The study identified the workstations with the highest strain based on the production process and determined the physical strains using the REBA and Quick Exposure Check (QUEC) methods. Recommendations were provided to reduce risks for two workstations with high REBA and QUEC scores. The implemented improvements aimed to minimize risks[9].

Gündüz and İde (2021) examined musculoskeletal system disorders and fatigue levels among students engaging in online education during the pandemic. The Checklist Individual Strength (CIS) and CMDQ questionnaire were used to analyze fatigue levels. Results showed that 84.1% of the students felt fatigued. According to the Cornell scale, the most commonly reported discomfort was in the lower back (18.25%), followed by the neck and shoulder regions. A positive and significant correlation was found between students' fatigue and Cornell discomfort scores. When the Cornell questionnaire was divided into two parts (night-day) for participants, it was observed that shoulder risk scores significantly differed

between night-shift and day-shift students[10].

Aydın (2021) conducted an ergonomic risk analysis for employees working in a retail store selling meat and poultry products. The NIOSH equation was used for manual lifting operations, and the REBA method was employed to assess working postures in the store. It was identified that manual lifting during order preparation posed a high risk level, and the recommendation included the use of adjustable pallet jacks. Furthermore, it was emphasized that the loads carried by employees should be reduced through improvements. After implementing the proposed methods, the REBA risk score decreased from 9 to 3[11]. Geniş and Sümer (2021) analyzed the body postures of seasonal workers engaged in seed corn farming, which can lead to musculoskeletal disorders, using the REBA method. They conducted separate evaluations for each work model and provided recommendations for each work model[12].

Kızıgın et al. (2022) investigated the body parts where musculoskeletal disorders are most prevalent among hairdressers and examined the relationship between upper extremity problems and occupational burnout. The study included 78 hairdressers. Musculoskeletal disorders were determined using the Cornell questionnaire, and the level of burnout was assessed using the TÖ-KF form. The study found that the participants experienced the most discomfort in the neck and lower back regions. Additionally, a high and positive correlation was found between upper extremity disorders and occupational burnout.

Protective rehabilitation programs were recommended for hairdressers[13]. Altunel (2022) conducted an ergonomic risk assessment for employees working in both the offices and chemical storage facilities of a company in the chemical sector. The ROSA and CMDQ questionnaires were used for office workers, and the REBA method was

used for chemical storage facility workers. The study involved both observer and participant observations for office workers. The study found that the chairs of office workers were not sufficiently ergonomic, and the workers in the storage facility experienced postural problems due to load lifting activities. Recommendations were provided for addressing non-ergonomic working conditions. Yurdalan et al. (2022) investigated the effects of postures and respiratory exercises on quality of life and potential pain for home and office workers. The study included 61 volunteer workers aged between 20 and 50. According to the CMDQ questionnaire, significant differences were observed in the scores for the lower back, neck, and left forearm among the groups. No significant differences were found in terms of quality of life based on the SF-36 questionnaire. It was observed that exercise-focused physiotherapy approaches resulted in a reduction in musculoskeletal disorders and an improvement in quality of life for the workers[14].

Considering that this study is being conducted in the forest products industry, which is one of the labor-intensive industries, it highlights the importance of ergonomic risk assessment studies for lumber production as well. Like any labor-intensive manufacturing operations, lumber production involves movements that can cause musculoskeletal disorders. The Cornell questionnaire is a self-reporting method. In addition to such ergonomic risk assessment questionnaires, it would be appropriate to analyze the causes and consequences of the problem from a broader perspective by using observation-based methods.

### 3. MATERIAL AND METHOD

The study was conducted for the employees working on the production line of a factory operating in the forest products sector. The factory is comprised of two facilities and has a total of 55 employees, serving both domestic and international markets. Since its

establishment, the factory has been engaged in the production of furniture and construction timber using poplar, fir, and pine as raw materials.

The factory operates from 08:00 to 18:00 with three breaks during the day, including a lunch break. The process flow of timber production is presented in Figure 1. The production of timber begins with the arrival of logs to the log yard and their dimensioning according to customer orders. After cutting, the logs are sent to the resaw machines, where the bark is removed using band saws. The straight-shaped pieces, excluding the bark, are then subjected to multiple ripping, edging, and trimming operations.

Multiple circular saws enable the removal of sides from the timber or the simultaneous production of multiple materials with equal thickness. Next, the timber is sent to the trimming machine for full-length sizing based on the orders. The quarter sawing machine (Markul) cuts the thick caps from the main machine and trims the sides of the parallel-cut timber. Subsequently, the edging/trimming process takes place. The edging machine is used to remove the sides of the parallel-cut timber or to obtain standard construction timber from the similarly processed timber.

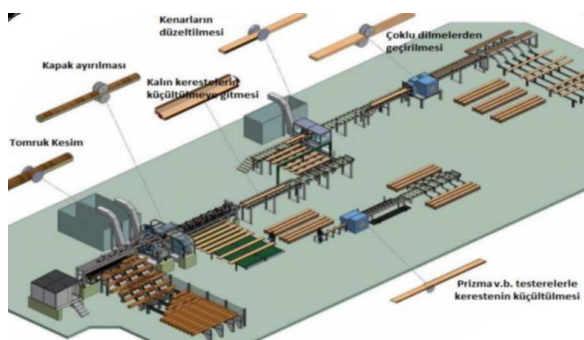


Figure 1. Timber Production Process

In order to directly impact employee health and motivation, non-ergonomic work conditions will also have consequences on work efficiency. In this context, businesses should assess the risk factors that contribute to musculoskeletal disorders (MSDs) and take necessary precautions. There are several

scientific methods available for evaluating ergonomic risk factors. These methods can be broadly classified into three categories, as outlined in Table 1: self-reporting by employees, systematic observation-based methods, and direct measurement methods. Examples of self-reporting methods include the Nordic Musculoskeletal Questionnaire (NMQ), Cornell Musculoskeletal Disorder Questionnaire (CMDQ), and Body Discomfort Diagram (BPDS). Advanced observation-based methods include Rapid Upper Limb Assessment (RULA), Occupational Repetitive Actions (OCRA), Quick Exposure Check (QUE), Working Posture Analysis (OWAS), Builder Model, SANTOS, PoenSim, 3DSSPP, and Ramsis Model. Quantitative assessments using devices such as goniometers, biomechanical analysis, electromyography, and optical tools fall under the category of direct measurement methods. In this study, the REBA method, a simple observation-based method, and the CMDQ questionnaire, a method based on self-reporting by employees, were applied[15].

### 3.1. Cornell Musculoskeletal Disorder Questionnaire (CMDQ)

The Cornell Musculoskeletal Disorder Questionnaire (CMDQ) is a method developed by Dr. Alan Hedge and graduate students in the field of ergonomics at Cornell University's Human Factors and Ergonomics Laboratory. It is a valuable tool for gathering data on musculoskeletal disorders, providing a separate evaluation for each region of the body. The CMDQ questionnaire considers the frequency, severity, and interference of musculoskeletal discomfort in each body region, including their impact on work. This assessment helps evaluate the consequences of discomfort on employees' job performance[7]. The questionnaire has separate forms for individuals working in a standing position and those working in a seated position. In this study, the CMDQ questionnaire form designed for male

individuals working in a standing position, as shown in Figure 2, was used[16].

According to the form, the risk score calculation is based on frequency scores: never felt it = 0 points, felt it 1-2 times per week = 1.5 points, felt it 3-4 times per week = 3.5 points, felt it once a day = 5 points, and felt it multiple times a day = 10 points. Pain severity is scored as follows: mild = 1 point, moderate = 2 points, severe = 3 points. The interference of discomfort with work activities is assessed as follows: no interference = 1 point, slight interference = 2 points, significant interference = 3 points.

**3.2.REBA Method**

REBA method was first proposed in 1998 by Hignett and McAtamney. It is a method

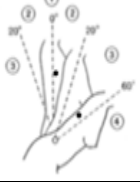
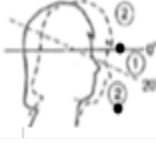

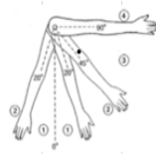
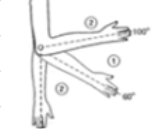

designed for the analysis of strenuous, frequently repetitive, and unpredictable body postures. [17] The method involves assigning scores to each region of the body involved in performing a task to quantify the risks. This method is based on observation, where the evaluator assesses posture positions by reviewing photographs and videos[18]. In REBA analysis, both the right and left sides of the body are evaluated together. The body parts are generally divided into Group A and Group B, as shown in Table 1. Group A includes the assessment of the trunk, neck, and legs, while Group B includes the assessment of the upper arm, forearm, and wrists. Different angle values are assigned for each relevant body part. The total score is obtained by combining the scores from Group A and Group B.

The diagram below shows the approximate position of the body parts referred to in the questionnaire. Please answer by marking the appropriate box.

	During the last work week how often did you experience ache, pain, discomfort in:					If you experienced ache, pain, discomfort, how uncomfortable was this?			If you experienced ache, pain, discomfort, did this interfere with your ability to work?		
	Never	1-2 times last week	3-4 times last week	Once every day	Several times every day	Slightly uncomfortable	Moderately uncomfortable	Very uncomfortable	Not at all	Slightly interfered	Substantially interfered
Neck	<input type="checkbox"/>	<input type="checkbox"/>	<input type="checkbox"/>	<input type="checkbox"/>	<input type="checkbox"/>	<input type="checkbox"/>	<input type="checkbox"/>	<input type="checkbox"/>	<input type="checkbox"/>	<input type="checkbox"/>	<input type="checkbox"/>
Shoulder (Right)	<input type="checkbox"/>	<input type="checkbox"/>	<input type="checkbox"/>	<input type="checkbox"/>	<input type="checkbox"/>	<input type="checkbox"/>	<input type="checkbox"/>	<input type="checkbox"/>	<input type="checkbox"/>	<input type="checkbox"/>	<input type="checkbox"/>
Shoulder (Left)	<input type="checkbox"/>	<input type="checkbox"/>	<input type="checkbox"/>	<input type="checkbox"/>	<input type="checkbox"/>	<input type="checkbox"/>	<input type="checkbox"/>	<input type="checkbox"/>	<input type="checkbox"/>	<input type="checkbox"/>	<input type="checkbox"/>
Upper Back	<input type="checkbox"/>	<input type="checkbox"/>	<input type="checkbox"/>	<input type="checkbox"/>	<input type="checkbox"/>	<input type="checkbox"/>	<input type="checkbox"/>	<input type="checkbox"/>	<input type="checkbox"/>	<input type="checkbox"/>	<input type="checkbox"/>
Upper Arm (Right)	<input type="checkbox"/>	<input type="checkbox"/>	<input type="checkbox"/>	<input type="checkbox"/>	<input type="checkbox"/>	<input type="checkbox"/>	<input type="checkbox"/>	<input type="checkbox"/>	<input type="checkbox"/>	<input type="checkbox"/>	<input type="checkbox"/>
Upper Arm (Left)	<input type="checkbox"/>	<input type="checkbox"/>	<input type="checkbox"/>	<input type="checkbox"/>	<input type="checkbox"/>	<input type="checkbox"/>	<input type="checkbox"/>	<input type="checkbox"/>	<input type="checkbox"/>	<input type="checkbox"/>	<input type="checkbox"/>
Lower Back	<input type="checkbox"/>	<input type="checkbox"/>	<input type="checkbox"/>	<input type="checkbox"/>	<input type="checkbox"/>	<input type="checkbox"/>	<input type="checkbox"/>	<input type="checkbox"/>	<input type="checkbox"/>	<input type="checkbox"/>	<input type="checkbox"/>
Forearm (Right)	<input type="checkbox"/>	<input type="checkbox"/>	<input type="checkbox"/>	<input type="checkbox"/>	<input type="checkbox"/>	<input type="checkbox"/>	<input type="checkbox"/>	<input type="checkbox"/>	<input type="checkbox"/>	<input type="checkbox"/>	<input type="checkbox"/>
Forearm (Left)	<input type="checkbox"/>	<input type="checkbox"/>	<input type="checkbox"/>	<input type="checkbox"/>	<input type="checkbox"/>	<input type="checkbox"/>	<input type="checkbox"/>	<input type="checkbox"/>	<input type="checkbox"/>	<input type="checkbox"/>	<input type="checkbox"/>
Wrist (Right)	<input type="checkbox"/>	<input type="checkbox"/>	<input type="checkbox"/>	<input type="checkbox"/>	<input type="checkbox"/>	<input type="checkbox"/>	<input type="checkbox"/>	<input type="checkbox"/>	<input type="checkbox"/>	<input type="checkbox"/>	<input type="checkbox"/>
Wrist (Left)	<input type="checkbox"/>	<input type="checkbox"/>	<input type="checkbox"/>	<input type="checkbox"/>	<input type="checkbox"/>	<input type="checkbox"/>	<input type="checkbox"/>	<input type="checkbox"/>	<input type="checkbox"/>	<input type="checkbox"/>	<input type="checkbox"/>
Hip/Buttocks	<input type="checkbox"/>	<input type="checkbox"/>	<input type="checkbox"/>	<input type="checkbox"/>	<input type="checkbox"/>	<input type="checkbox"/>	<input type="checkbox"/>	<input type="checkbox"/>	<input type="checkbox"/>	<input type="checkbox"/>	<input type="checkbox"/>
Thigh (Right)	<input type="checkbox"/>	<input type="checkbox"/>	<input type="checkbox"/>	<input type="checkbox"/>	<input type="checkbox"/>	<input type="checkbox"/>	<input type="checkbox"/>	<input type="checkbox"/>	<input type="checkbox"/>	<input type="checkbox"/>	<input type="checkbox"/>
Thigh (Left)	<input type="checkbox"/>	<input type="checkbox"/>	<input type="checkbox"/>	<input type="checkbox"/>	<input type="checkbox"/>	<input type="checkbox"/>	<input type="checkbox"/>	<input type="checkbox"/>	<input type="checkbox"/>	<input type="checkbox"/>	<input type="checkbox"/>
Knee (Right)	<input type="checkbox"/>	<input type="checkbox"/>	<input type="checkbox"/>	<input type="checkbox"/>	<input type="checkbox"/>	<input type="checkbox"/>	<input type="checkbox"/>	<input type="checkbox"/>	<input type="checkbox"/>	<input type="checkbox"/>	<input type="checkbox"/>
Knee (Left)	<input type="checkbox"/>	<input type="checkbox"/>	<input type="checkbox"/>	<input type="checkbox"/>	<input type="checkbox"/>	<input type="checkbox"/>	<input type="checkbox"/>	<input type="checkbox"/>	<input type="checkbox"/>	<input type="checkbox"/>	<input type="checkbox"/>
Lower Leg (Right)	<input type="checkbox"/>	<input type="checkbox"/>	<input type="checkbox"/>	<input type="checkbox"/>	<input type="checkbox"/>	<input type="checkbox"/>	<input type="checkbox"/>	<input type="checkbox"/>	<input type="checkbox"/>	<input type="checkbox"/>	<input type="checkbox"/>
Lower Leg (Left)	<input type="checkbox"/>	<input type="checkbox"/>	<input type="checkbox"/>	<input type="checkbox"/>	<input type="checkbox"/>	<input type="checkbox"/>	<input type="checkbox"/>	<input type="checkbox"/>	<input type="checkbox"/>	<input type="checkbox"/>	<input type="checkbox"/>
Foot (Right)	<input type="checkbox"/>	<input type="checkbox"/>	<input type="checkbox"/>	<input type="checkbox"/>	<input type="checkbox"/>	<input type="checkbox"/>	<input type="checkbox"/>	<input type="checkbox"/>	<input type="checkbox"/>	<input type="checkbox"/>	<input type="checkbox"/>
Foot (Left)	<input type="checkbox"/>	<input type="checkbox"/>	<input type="checkbox"/>	<input type="checkbox"/>	<input type="checkbox"/>	<input type="checkbox"/>	<input type="checkbox"/>	<input type="checkbox"/>	<input type="checkbox"/>	<input type="checkbox"/>	<input type="checkbox"/>

Figure 2. Musculoskeletal Disorder Questionnaire (CMDQ)

Table 1 REBA Score

	Movement	Point	Change Point	Position
Body	Posture	1	Lateral stretch or a twisting movement, add +1 point.	
	0°-20° flexion	2		
	0°-20° stretching			
	20°-60° stretching	3		
	>20° stretching			
>60° flexion	4			
Neck	0°-20° flexion	1	Lateral stretch or a twisting movement, add +1 point.	
	>20° flexion	2		
Legs	If the weight is distributed on both legs while walking or sitting.	1	The knees are bent between 30 degrees and 60 degrees, add +1 point; or the knees are bent >60 degrees, add +2 points.	
	If the weight is on one leg or if there is an unbalanced posture	2		
Upper Arm	0°-20° flexion	1	Extension and rotation movement in the arm add +1; if the shoulders are raised, add +1; if the arms -1	
	0°-20° stretching			
	20°-45° flexion	2		
	>20° stretching			
	45°-90° flexion	3		
>90° flexion	4			
Forearm	60°-100° flexion	1		
	<60° flexion			
	>100° flexion	2		
Wrist	0°-15° flexion		Lateral stretching or rotation in the wrist	
	15 stretching			
	>15° flexion			
	>15° stretching			

When analyzing the photographs and videos of employees' postures, separate scores for the neck, trunk, and legs are determined based on the categories provided in Table 1. These scores are then cross-referenced in Table 2. The load imposed on the employee during the task is assessed based on the load force score in Table 2 and added to obtain the total A score.

Table 2 REBA A Score

Table A		Neck															
		1				2				3							
Legs		1	2	3	4	1	2	3	4	1	2	3	4				
Torso	1	1	2	3	4	1	2	3	4	3	3	5	6				
	2	2	3	4	5	3	4	5	6	4	5	6	7				
	3	2	4	5	6	4	5	6	7	5	6	7	8				
	4	3	5	6	7	5	6	7	8	6	7	8	9				
	5	4	6	7	8	6	7	8	9	7	8	9	9				
Charge/Force Points																	
		0				1				2				+1			
		less than 5 kg				5-10 kg				>more than 10				Add +1 when power usage suddenly or rapidly increases			

In Table 3, the stance scores for the wrist, lower arm, and upper arm in the B cells are crossed over. The total score in Table B is created by adding the second score from Table 3 to the combination score. Scores from Tables A and B are compared to Table C. The REBA score is calculated by adding the activity score from Table 4 to the C score.

In Table A, a cross-referencing is conducted between the scores obtained from the trunk, neck, and leg assessments, and in Table B, the scores obtained for the upper arm, forearm, and wrist assessments. This cross-referencing process is performed in Table C. The appropriate activity score specified in the table is added to the cross-referenced C score. The resulting C score becomes the REBA score.

Table 3 REBA B Score

Table B		Lower Arm					
		1			2		
Wrist		1	2	3	1	2	3
Upper Arm	1	1	2	2	1	2	3
	2	1	2	3	2	3	4
	3	3	4	5	4	5	5
	4	4	5	5	5	6	7
	5	6	7	8	7	8	8
	6	7	8	8	8	9	9
Suitable and reasonable holding forces of the necessary apparatus							0
Adequate but unsatisfactory hand grip supported anywhere on the body							1
No holding hands, but it's possible (weak)							2
Cannot support or hold anything							3



Table 4 REBA C Score

Table C		B Score											
		1	2	3	4	5	6	7	8	9	10	11	12
A Score	1	1	1	1	2	3	3	4	5	6	7	7	7
	2	2	2	2	3	4	4	5	6	6	7	7	8
	3	3	3	3	3	4	5	6	7	7	8	8	8
	4	4	4	4	4	5	6	7	8	8	9	9	9
	5	5	4	4	5	6	7	8	8	9	9	9	9
	6	6	6	6	7	8	8	9	9	10	10	10	10
	7	7	7	7	8	9	9	9	10	10	11	11	11
	8	8	8	8	9	10	10	10	10	10	11	11	11
	9	9	9	9	10	10	10	11	11	11	12	12	12
	10	10	10	10	11	11	11	11	12	12	12	12	12
	11	11	11	11	12	12	12	12	12	12	12	12	12
	12	12	12	12	13	12	12	12	12	12	12	12	12
Score		Definition											
+1		One or more body parts are static											
+1		If there are repeated short-term actions											
+1		If the action causes rapid drastic changes in posture or there is unstable posture											

The risk levels and action levels associated with the calculated REBA risk score are determined according to Table 5. A score of 8-10 points on the REBA scale indicates a high risk level and the need for improvement in the near future. If the score falls within the range of 11-15 points, the risk level is very high, and immediate action should be taken.

Table 5 REBA Risk Scores

Level	REBA Score	Risk Level	Precaution
1	1	Negligible	Not Necessary
2	2-3	Low	May be necessary
3	4-7	Middle	Necessary
4	8-10	High	Necessary in a Short Time
5	11-15	Very High	Needed Immediately

#### 4. APPLICATION

In this study, the physical exertions of individuals during lumber production, such as lifting, dropping, and carrying heavy materials, were evaluated ergonomically. The study consisted of two parts, starting with the selection of 40 male volunteers for the CMDQ questionnaire, which focused on Cornell musculoskeletal disorders. The first

part of the questionnaire collected demographic information of the workers (age, weight, height, education level, industry experience) and work-related details (working style, weight lifted, department worked in). This information is presented in Table 6.

The average age of the 40 participants in the survey is 34.03, with an average height of 173.73 cm and an average weight of 74.03 kg. The average duration of experience in the company is more than 4.5 years. Among the participants, 52% have completed primary school education. The production line is divided into six separate units. The majority of the workers (25%) are involved in the cutting unit, including multiple and secondary-stage cutting, as well as the stacking unit. In terms of work style, 65% of the employees work standing, 25% work walking, and 10% work sitting. Those who work walking are mainly in the sorting unit, while those who work sitting are usually operators. The musculoskeletal disorders of the workers are directly related to the materials they handle and their work style. As the average weight of the produced lumber is 25 kg or more, it is observed that 50% of the workers carry weights exceeding 20 kilograms. Individuals operating the cutting

machine, collecting and stacking small slats or logs, or working as operators are considered to handle materials weighing less than 10 kg.

Table 6 Information for employees

<i>Demographic Information</i>		N	Average	Std. Deflection
Age		40	34.03	10.307
Height		40	173.73	5.782
Weight		40	74.03	13.26
Experienced		40	4.73	4.58
<i>Worked Production Unit</i>		Frequency	Percentage (%)	Cumulative Percentage
Log Cutting		4	0.10	0.10
Longitudinal saw		6	0.15	0.25
Stacking		10	0.25	0.50
Side cut		5	0.13	0.63
Mower		10	0.25	0.88
General		5	0.13	1.00
Total		40	1.00	
<i>How Does an Individual Work?</i>		Frequency	Percentage (%)	Cumulative Percentage
afoot		26	0.65	0.65
On foot		10	0.25	0.90
Sitting down		4	0.10	1.00
Total		40	1.00	
<i>Lifted Weight</i>		Frequency	Percentage (%)	Cumulative Percentage
<10 kg		13	0.33	0.33
10-20 kg		7	0.18	0.50
>20 kg		20	0.50	1.00
Total		40	1.00	

#### 4.1. Cornell Musculoskeletal Disorder Questionnaire (CMDQ) Application

The frequency, severity, and work interference scores obtained from the responses to the Cornell Musculoskeletal System questionnaire by the employees are provided in Table 7.

According to the CMDQ questionnaire, for example, the risk score calculation for the back region is as follows: frequency score  $(140) + (131.5) + (73.5) + (45) + (210) = 84$ , weighted severity score  $(51) + (192) + (23) = 49$ , and work interference discomfort score  $(111) + (132) + (2*3) = 43$ , resulting in a total

discomfort score of 176988 when multiplied together. According to the Cornell questionnaire results, the highest risk scores are attributed to the lower back (31.78%), followed by the back (11.34%), right wrist (10.31%), and right forearm (9.15%). It is observed that the employees experience the highest level of pain in the lower back region (35.90%). Furthermore, work interference is predominantly associated with discomfort in the lower back, upper right leg, and back.

#### 4.2. REBA Method Application

REBA analysis was conducted separately for each unit of the timber production line. Photographs and videos were taken from different angles to assess the employees' postures. Each posture was then examined in detail, and the REBA score was calculated for the posture with the highest level of risk.

The REBA analysis for the stacking unit is presented in Figure 3. Since the load in the employee's hand is heavier than 20 kilograms, a force score of 2 is assigned. The trunk posture is mostly at or above 60 degrees (4 points), with lateral bending and twisting (+1 point) due to picking up the materials from the side. For the neck region, there is a maximum of 20 degrees of flexion (1 point) and stretching (+1 point). Additionally, the weight is distributed on both legs (1 point), and the knees are flexed to a maximum of 60 degrees (+1 point). In the upper arm, there is a maximum of 20 degrees of flexion (+1 point), and abduction or rotation movement is present (+1 point). The forearm exhibits flexion above 60 degrees (2 points), while the wrists have a maximum of 15 degrees of extension. Thus, a Table A score of 7 is obtained for employees in the stacking unit.

Table 7 CMDQ Survey Results

CMDQ SURVEY	How often have you felt aches, pains, discomfort in your body during the past working week?						If you felt aches, pains, discomfort, how severe was it?			Percentage %	Have you experienced pain, ache, or discomfort that prevented you from performing your tasks?			Percentage %	Average Risk Score	Score Percentage (%)
	None	1-2 times a week	3-4 times a week	1 time per day	Many Times Every Day	Little	Middle	Lot	Little		Middle	Lot				
Neck		22	13	4	1	0	7	11	0	0.00	14	4	0	0.00	24563	1.57
Shoulder	Right	24	9	4	3	0	9	6	1	2.56	12	4	0	0.00	20400	1.31
	Left	26	13	1	0	0	9	4	1	2.56	11	3	0	0.00	7820	0.50
Back		14	13	7	4	2	5	19	2	5.13	11	13	2	9.52	176988	11.34
Upper Arm	Right	20	9	7	2	2	5	13	2	5.13	9	10	1	4.76	80512	5.16
	Left	22	11	7	0	0	4	13	1	2.56	9	9	0	0.00	36531	2.34
Waist		11	7	5	11	6	4	11	14	35.90	14	8	7	33.33	495924	31.78
Forearm	Right	14	10	11	4	1	10	13	3	7.69	15	10	1	4.76	142785	9.15
	Left	16	10	11	3	0	9	12	3	7.69	14	9	1	4.76	100695	6.45
Wrist	Right	11	15	10	3	1	11	15	3	7.69	20	8	1	4.76	160875	10.31
	Left	13	13	10	3	1	11	13	3	7.69	19	7	1	4.76	131652	8.44
Hip		32	1	2	0	5	0	8	0	0.00	8	0	0	0.00	7488	0.48
Upper leg	Right	18	10	9	2	1	13	8	1	2.56	15	3	4	19.05	70224	4.50
	Left	20	10	8	2	0	12	7	1	2.56	15	2	3	14.29	43036	2.76
Knee	Right	31	7	1	0	1	8	1	0	0.00	8	1	0	0.00	2400	0.15
	Left	29	8	2	0	1	9	2	0	0.00	10	1	0	0.00	4524	0.29
Lower Leg	Right	26	7	5	2	0	6	8	0	0.00	13	1	0	0.00	12540	0.80
	Left	24	9	5	2	0	6	10	0	0.00	13	3	0	0.00	20254	1.30
Foot	Right	28	3	5	4	0	8	2	2	5.13	10	2	0	0.00	10584	0.68
	Left	28	3	5	4	0	8	2	2	5.13	10	2	0	0.00	10584	0.68


REBA Analysis For Stacking Unit					
Group A		Score A	Score B	Score B	
Torso	5	7	2	Lower Arm	2
Neck	2			Upper Arm	2
Legs	2			Wrist	1
Strength Points		2	0	Grip Score	
<b>Score A</b>		<b>9</b>	<b>2</b>	<b>B Score</b>	
				<b>C Score</b>	<b>9</b>
				Activity Score	<b>1</b>
				<b>REBA Score</b>	<b>10</b>

Figure 3 Stacking Unit REBA Evaluation

The high Table A score is due to the intensive use of the trunk and arms in the process of lifting, carrying, and stacking materials. After obtaining the A and B scores, cross-referencing is done from Table C. Then, based on the nature of the task, a score is added. For this example, since there is no prolonged static posture, no significant rapid changes in posture, and repeated movements within a short period (such as stacking logs at least 3 times per minute), a +1 score is added from Table C, resulting in a total REBA Score of 10. This score indicates a high ergonomic risk level in the relevant unit and the need for prompt action to address the employee's musculoskeletal disorders.


Scores For Longitudinal Unit REBA					
Group A		Score A	Score B	Score B	
Torso	4	6	5	Lower Arm	4
Neck	2			Upper Arm	2
Legs	2			Wrist	1
Strength Points		2	0	Grip Score	
<b>Score A</b>		<b>8</b>	<b>5</b>	<b>B Score</b>	
				<b>C Score</b>	<b>10</b>
				Activity Score	<b>1</b>
				<b>REBA Score</b>	<b>11</b>

Figure 4 Scores for Longitudinal Unit REBA

The REBA analysis for the sizing unit is presented in Figure 4. The employee exhibits a trunk stretching posture of 20 degrees or more (3 points) and also lateral bending or twisting (+1 point). There is a maximum of 20 degrees of flexion in the neck (1 point) and rotational movement to the right and left (+1 point). While walking, the weight is distributed on both legs (1 point), and the knees are flexed between 30 and 60 degrees (+1 point). In the upper arm, there is flexion above 45 degrees (3 points) and abduction movement (+1 point). The lower arm exhibits slight flexion (2 points), and there is slight extension in the wrists (1 point). Since the weight lifted exceeds 20 kilograms, a force score of 2 is assigned, resulting in a total Table A score of 8. The Table B score is 5. Cross-referencing in Table C yields a score of 10, resulting in a total REBA Score of 11. This score indicates a high ergonomic risk level in the relevant unit and the need for immediate action to address it.


Multi-Slitting REBA Scoring					
Group A		Score A	Score B	Score B	
Torso	3	5	2	Lower Arm	2
Neck	2			Upper Arm	2
Legs	2			Wrist	1
Strength Points		2	0	Grip Score	
<b>Score A</b>		<b>7</b>	<b>2</b>	<b>B Score</b>	
				<b>C Score</b>	<b>7</b>
				Activity Score	<b>1</b>
				<b>REBA Score</b>	<b>8</b>

Figure 5 Multi-Slitting REBA Scoring

The multiple cutting REBA analysis is presented in Figure 5. By combining the total A and total B scores for the employee who supplies the material to the machine, a total C score of 8 is obtained. This score indicates a high-risk level within the low range, emphasizing the need for immediate action to address the ergonomic concerns.


Trimming Unit REBA Score					
Group A		Score A	Score B	Score B	
Torso	3	5	2	Lower Arm	2
Neck	2			Upper Arm	2
Legs	2			Wrist	1
Strength Points		2	0	Grip Score	
<b>Score A</b>		7	2	<b>B Score</b>	
				<b>C Score</b>	<b>7</b>
				Activity Score	<b>1</b>
				<b>REBA Score</b>	<b>8</b>

Figure 6 Timber Chopper REBA Evaluation

The REBA analysis conducted for the trimming unit resulted in a Table A score of 7 and a Table B score of 2, as shown in Figure 6. The total REBA score is determined as 8, indicating a high action level and the need for prompt intervention within this unit.


Trimming Unit REBA Score					
Group A		Score A	Score B	Score B	
Torso	3	5	2	Lower Arm	4
Neck	2			Upper Arm	2
Legs	2			Wrist	1
Strength Points		2	0	Grip Score	
<b>Score A</b>		7	6	<b>B Score</b>	
				<b>C Score</b>	<b>9</b>
				Activity Score	<b>1</b>
				<b>REBA Score</b>	<b>10</b>

Figure 7 Markule Unit REBA Scoring

For the operator of the marking machine, the total REBA score is determined as 10, as shown in Figure 7. In this case, the action level is high-risk, indicating the need for prompt intervention within a short period of time.

## 5. RESULTS AND DISCUSSION

In the study, the Cornell Musculoskeletal Discomfort Questionnaire (CMDQ) was used to evaluate the 40 voluntary participants based on their questionnaire responses. The results were analyzed, and the highest risk scores were found to belong to the lower back (31.78%), the upper back (11.34%), the right wrist (10.31%), and the right forearm (9.15%). It was observed that the employees experienced the highest level of pain in the lower back region (35.90%). Furthermore, the highest rate of work interference due to pain was reported in the lower back, right upper leg, and upper back.

The graphical representation of the results obtained from the Cornell Musculoskeletal Discomfort Questionnaire for the employees is presented in Figure 8.

According to the information obtained from the Cornell results, it is observed that the majority of musculoskeletal disorders occur in the lower back region (31.78%). Within the field, except for operators, machine operators, and employees performing light tasks, most employees are required to stand and engage in frequent bending and stooping movements. Activities such as placing materials into the machine, retrieving leftover materials from the machine for evaluation, and transporting them to the storage area pose a risk of musculoskeletal disorders for the employees.

It has been observed that employees generally complain of lower back pain (bel ağrısı) due to the lifting and carrying of heavy materials. To mitigate work interference caused by these ergonomic discomforts and ensure employee health and safety, several breaks are provided throughout the day.

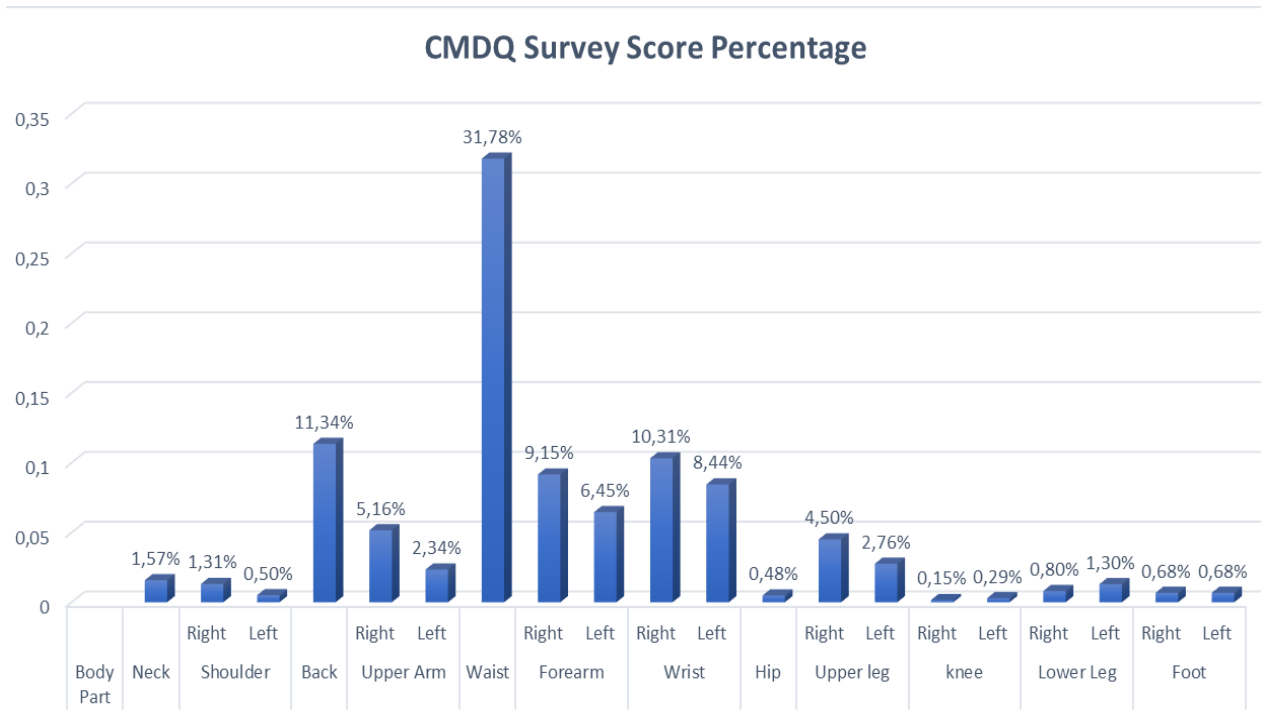


Figure 8 Percentage of CMDQ Survey Risk Scores

After the lower back region, the highest risk scores are observed in the right wrist (sağ el bileği) (10.31%) and the upper back (sırt) (11.34%). The similarity in results between the lower back and upper back regions is due to the use of significant physical effort in handling the large prismatic materials obtained from the multiple cutting machine. Transporting these materials via a conveyor can reduce the workload for workers. Unconscious lifting of heavy loads can also contribute to back and lower back pain. Therefore, it is necessary to provide appropriate training within the company. The least ergonomic risk is associated with the right knee region (sağ diz) (0.15%). Since employees predominantly use their right hand, it is expected that there will be physical strain on their right wrists. The low score for the knee region can be attributed to the absence of physical activities involving squatting. According to Table 8, which shows the calculated REBA action levels for the work units, the trimming unit has the highest risk level. In this unit, the products obtained from multiple cutting are transported to the trimming machine for sizing. The handling of these heavy and bulky materials predominantly involves the use of the trunk

and arms. Immediate measures should be taken to minimize the exposure of employees in this unit to musculoskeletal disorders.

Activities such as placing materials into the machine, retrieving leftover materials from the machine for evaluation, and transporting them to the storage area pose a risk of musculoskeletal disorders for the employees. It has been observed that employees generally complain of lower back and upper back pain due to the handling and transportation of heavy timber materials. Similar to the study conducted by Ünver et al. (2021), automation systems can be implemented in the production process to reduce the workload on employees for repetitive and continuous movements. In the mentioned study, conducted in the chemical industry, autonomous systems were designed for employees handling hazardous substances [19]. Similarly, timber production, like the chemical industry, involves various hazardous machinery in the production process, posing threats to employee safety.

Table 8 REBA Scores

Unit / Body Part	A Score			B Score			REBA Score	
	Torso	Neck	Leg	Upper Arm	Lower arm	Wrist	Risk Score	Risk Level
Longitudinal saw	4	2	2	4	2	1	11	Immediate action must be taken
Stacking	5	2	2	2	2	1	10	Action should be taken as soon as possible
Multiplicity Slitting	3	2	2	2	2	1	8	Action should be taken as soon as possible
Side cut	3	2	2	2	2	1	8	Action should be taken as soon as possible
Markule	3	2	2	4	2	2	10	Action should be taken as soon as possible

## 6. CONCLUSION

With the advancement of technology in modern times, although machines help alleviate the burden on humans in the production processes, complete automation is not always achievable, and the human factor cannot be eliminated. In places where the human factor is present, issues such as occupational health and safety cannot be ignored. Particularly in labor-intensive industries, being aware of the science of ergonomics is crucial for both employees and employers. The exposure of employees to non-ergonomic working conditions directly affects production quality, resulting in reduced profitability and work performance for businesses. Like many other sectors, the forest products industry involves certain ergonomic risks in the primary and secondary processing stages of raw materials. Furthermore, repetitive movements, lifting and carrying heavy materials, and other activities in labor-intensive operations lead to musculoskeletal disorders in employees.

This study was conducted in an enterprise operating in the forest products industry in the Western Black Sea Region. In the first part of the study, musculoskeletal disorders observed

in individuals due to working conditions were evaluated by assessing specific body areas using the Cornell Musculoskeletal Discomfort Questionnaire (CMDQ). Activities such as placing materials into the machine, retrieving leftover materials from the machine for evaluation, and transporting them to the storage area pose a risk of musculoskeletal disorders for the employees. It has been observed that employees generally complain of lower back and upper back pain due to the handling and transportation of heavy timber materials. According to the REBA analysis, the highest occurrence of musculoskeletal disorders was found in the trimming unit. The visual assessment of the employee during the highest ergonomic risk situation in this unit resulted in a risk score of 11. The employee is required to continuously lift and carry materials weighing more than 20 kg while arranging the parts from the multiple cutting machine in front of the trimming machine, which contributes to a high risk score in the trunk category. Due to the intense use of the back, upper back, and arms, the load imposed on the employee's body leads to musculoskeletal disorders and the need for frequent breaks. Transporting the heavy and bulky materials from the multiple cutting machine to the trimming stock area via

conveyors or using forklifts would alleviate the employee's load.

The body areas evaluated in the Cornell questionnaire, such as the lower back and upper back, correspond to the trunk assessment in the REBA method. The questionnaire evaluation and the observation-based analysis in the REBA method reveal non-ergonomic postures for the same body regions. The company provides two breaks of 15 minutes each, at 10:30 AM and 2:30 PM. It was determined that employees become more fatigued within the field and require intermittent rest. Increasing the rest periods for individuals in continuous working conditions would help alleviate body fatigue and enable safe continuation of work. The manner of lifting materials is also crucial. Incorrect grasping and lifting of heavy materials from the floor increase the load on the back and neck.

Practical workplace training sessions on proper material handling techniques should be conducted multiple times a month to raise awareness among employees. Additionally, it was observed that individuals use technological devices such as phones or headphones during production. In occupational health and safety training provided by professionals, it is appropriate to address or prohibit the use of such devices for the sake of safety.

### ***Funding***

The author (s) has no received any financial support for the research, authorship or publication of this study.

### ***Authors' Contribution***

In this study, Author 1 was responsible for the literature review, use of questionnaires, data collection, statistical analysis, writing of the article, and interpretation; Author 2 was involved in idea generation, method selection, model construction, analysis, interpretation, and final control of the findings and results.

### ***The Declaration of Conflict of Interest/ Common Interest***

No conflict of interest or common interest has been declared by the authors.

### ***The Declaration of Ethics Committee Approval***

This study does not require ethics committee permission or any special permission.

### ***The Declaration of Research and Publication Ethics***

The authors of the paper declare that they comply with the scientific, ethical and quotation rules of SAUJS in all processes of the paper and that they do not make any falsification on the data collected. In addition, they declare that Sakarya University Journal of Science and its editorial board have no responsibility for any ethical violations that may be encountered, and that this study has not been evaluated in any academic publication environment other than Sakarya University Journal of Science.

## **REFERENCES**

- [1] Y. Gök, "REBA-RULA, OWAS ve NIOSH Ergonomik Risk Değerlendirme Yöntemlerinin İnşaat Sektörüne Uygulanması ve İncelenmesi", Master Thesis, Dept. OHS, Yeni Yüzyıl Üniv., İstanbul, 2021
- [2] R. Akgönül, "Ergonomik Personel Çizelgeleme Problemi:Savunma Sanayiinde Bir Uygulama", Master Thesis, Dept. OHS, Kırıkkale Univ.,Kırıkkale, 2023
- [3] İ. Demir, "Orman Ürünleri Endüstrisi Çalışanlarında İş Sağlığı ve Güvenliği Farkındalığı", Master Thesis, Dept. OHS, Gaziosmanpaşa Üniv., Tokat, 2021
- [4] F. Altunel, "Kimya Sektöründeki Bir İşletmenin Reba, Rosa ve CMDQ Yöntemleriyle Ergonomik Risklerinin Değerlendirilmesi", Master Thesis,



- Dept. OHS, Üsküdar Üniv., İstanbul, 2022.
- [5] H. Esen, N. Fıđlalı, “Çalıřma duruřu analiz yöntemleri ve çalıřma duruřunun kas-iskelet sistemi rahatsızlıklarına etkileri”, Sakarya University Journal of Science, vol. 17, no. 1, pp. 41-51,2013.
- [6] S. Ünver, A. Kaya, “Orman Fidanlıklarında Fidan Repikaj İşlerinde Çalıřma Durumlarının REBA Yöntemi İle Analiz Edilmesi”, Journal of Engineering Sciences and Designes, vol. 3, no. 3, pp. 157-163,2015.
- [7] D. Gönen, A. Oral, M. A. B. Ocaktan, A.D. Karaođlan, A. Cicibař, “Bir transformatör işletmesinde montaj ünitesinin ergonomik analizi”, Sakarya University Journal Of Science, vol. 21, no. 5, pp. 1067-1080, 2017.
- [8] K.H. Nam, S. Lee, G. Kyung, J. An, S. An, “Development of ergonomic gun barrel cleaning method: Automation and its advantages”, Human Factors and Ergonomics in Manufacturing, vol. 27, pp. 243-248, 2017.
- [9] E. Yalçın, B. Ayvaz, “İřletmelerde İş Sađlıđı ve Güvenliđi açısından Ergonomik Risk Ölçümü:Tekstil Sektöründe Bir Uygulama”, Istanbul Commerce University Journal of Science, vol 17, no. 34, pp. 13-30, 2018.
- [10] D. İde, T. Gündüz, “Koronavirüs Kapanma(Kısıtlama) Döneminde Üniversite Öğrencilerinin Yorgunluk Düzeyleri ve Kas İskelet Sistemi Rahatsızlıkları Arasındaki İliřkinin Bazı Deđişkenler Açısından İcelenmesi”, Ergonomics, vol 4, no. 2, pp. 107-118,2021.
- [11] S. Aydın, “NIOSH ve REBA yöntemleri kullanılarak ergonomik risk analizi vaka çalıřması”, Journal of Balıkesir University Institute of Science and Technology, vol. 23, no. 2, pp. 414-433,2021.
- [12] A. Geniř, S.K. Sümer, “Tohumluk Mısır Üretiminde Çalıřma Duruřlarının REBA Yöntemi ile Ergonomik Risk Analizi”, Journal of Agricultural Machinery Science, vol. 17, no. 3, pp. 127-138,2021.
- [13] Z.Y. Kızgın, K. Üstün, Ö. Bingölbali, Z. Sarı, “Investigation of the Relationship Between Upper Extremity Musculoskeletal Problems and Occupational Burnout in Hairdressers”, Journal of Health Sciences Institute, vol. 7, no. 2, pp. 105-111, 2022.
- [14] S. U. Yurdalan, B. Ünlü, T. B.Güneř, A. Atilla, ř. Aslançı, E. Kabacık, “The Effect of Posture and Breathing Exercises on Pain and Quality of Life in Home-Office Workers”, Kâtip Çelebi University Journal of Health Sciences Faculty, vol. 7, no. 1, pp. 23-32, 2022.
- [15] E. Alp, M. Bozkurt, İ. Bařçıftçi, “Hastane Malzemelerinin Sađlık Çalıřanlarının Postürüne Etkileri”, Sakarya University Journal Of Science, vol. 16, no. 3, pp. 221-226, 2012.
- [16] B. N. Uyal, M. U. Umar, “The Effect Of Classrom Environment On Students’ Academic Performance And Musculoskeletal Discomfort”, Journal Of Industrial Engineering, vol. 33, no. 2, pp. 385-401, 2022.
- [17] ř. Yavuz, G. Berna, A. D. Çakır, D. A. Köse, “Investigation of The Posture Positions of The Apparel Workshop Employees with The Rapid Entire Body Assessment(REBA) and Rapid Upper Limb Assessment(RULA) Method”, Hittite Journal of Science and Engineering, vol. 8, no. 2, pp. 149-160, 2021.

- [18] A. N. Amri, B. I. Putra, “Ergonomic Risk Analysis Of Musculoskeletal Disorders(MSDs) Using Rosa and Reba Methods On Administrative Employees Faculty Of Science1”, Journal of Applied Engineering and Technological Science, vol. 4, no. 1, pp. 104-110, 2022.
- [19] U. C. Doğu, S. Boz, M. Ünver, “Kimya Sektöründe Tehlikeli Madde Taşınmasında Otonom Sistemler ile İş Sağlığı ve Güvenliği”, Journal of Advanced Engineering Studies and Technologies, vol. 2, no. 1, pp. 1-9, 2021.



SAKARYA ÜNİVERSİTESİ

# FEN BİLİMLERİ ENSTİTÜSÜ DERGİSİ

Sakarya University Journal of Science  
SAUJS

ISSN 1301-4048 | e-ISSN 2147-835X | Period Bimonthly | Founded: 1997 | Publisher Sakarya University |  
<http://www.saujs.sakarya.edu.tr/>

Title: Astrophysical Parameters of the Open Cluster NGC 2509

Authors: Talar YONTAN, Seliz Koç

Received: 7.12.2022

Accepted: 2023-07-08 00:00:00

Article Type: Research Article

Volume: 27

Issue: 5

Month: October

Year: 2023

Pages: 1036-1045

How to cite

Talar YONTAN, Seliz Koç; (2023), Astrophysical Parameters of the Open Cluster NGC 2509. Sakarya University Journal of Science, 27(5), 1036-1045, DOI: 10.16984/saufenbilder.1215972

Access link

<https://dergipark.org.tr/tr/journal/1115/issue/80257/1215972>

New submission to SAUJS

<http://dergipark.gov.tr/journal/1115/submission/start>

## Astrophysical Parameters of the Open Cluster NGC 2509

Talar YONTAN<sup>\*1</sup> , Seliz Koç<sup>2</sup> 

### Abstract

This study presents structural and fundamental astrophysical parameters of poorly studied open cluster NGC 2509. We used the third photometric and astrometric data release of the *Gaia* (*Gaia* DR3) to perform analyses. By taking into account the *Gaia* DR3 astrometric data, we calculated the membership probabilities of the stars in the region of NGC 2509. As a result of the membership analysis, 244 stars with membership probabilities  $P \geq 50\%$  were determined as the physical members of the cluster. The colour excess, distance and age were obtained simultaneously by fitting solar metallicity PARSEC isochrones to  $G \times G_{BP} - G_{RP}$  colour-magnitude diagram. We considered the most likely cluster member stars during the fitting procedure and calculated the colour excess, distance and age of the NGC 2509 as  $E(G_{BP} - G_{RP}) = 0.100 \pm 0.184$  mag,  $d = 2518 \pm 667$  pc and  $t = 1.5 \pm 0.1$  Gyr, respectively.

**Keywords:** Galaxy: open cluster and associations: individual: NGC 2509, Galaxy: Disc, stars: Hertzsprung Russell (HR) diagram

### 1. INTRODUCTION

Open star clusters (OCs) are the celestial bodies which consist of tens of to thousands of stars that share similar physical properties under the weak gravitational forces. These objects are located through the Galactic disc within the different distances and have a vast age range from a few million years to a few billion years. Because of the components stars of OCs are formed from collapsing of the same molecular cloud, their age, heliocentric distance, metallicities are similar [1]. These

properties make OCs important tools to study star formation process, stellar evolution as well as the formation and chemical evolution of the Galactic disc ([2-4]). Due to their same formation origin, the movement vectors of proper-motion components of cluster stars are similar. This knowledge is useful to define the membership properties of stars in the direction of open cluster ([5]). Moreover, astrometric, photometric and spectroscopic data of *Gaia* observations provided essential results for OCs and Milky Way Galaxy (e.g., [6-10]).

\* Corresponding author: talar.yontan@istanbul.edu.tr (T. YONTAN)

<sup>1</sup> Istanbul University, Faculty of Science, Department of Astronomy and Space Sciences, Istanbul, Türkiye.

<sup>2</sup> Istanbul University, Institute of Graduate Studies in Science, Programme of Astronomy and Space Sciences, Istanbul, Türkiye.

E-mail: seliskoc@gmail.com

ORCID: <https://orcid.org/0000-0002-5657-6194>, <https://orcid.org/0000-0001-7420-0994>



Table 1 Fundamental parameters for NGC 2509 estimated in this study and compiled from the literature. Columns denote the colour excess ( $E(B-V)$ ), metallicity ( $[Fe/H]$ ), distance moduli and distance ( $\mu$ ,  $d$ ), age ( $t$ ), proper-motion components ( $\mu_{\alpha\cos\delta}$ ,  $\mu_{\delta}$ ) and trigonometric parallaxes ( $\varpi$ ). Errors of the parameters are shown in parenthesis

$E(B-V)$ (mag)	$[Fe/H]$ (dex)	$\mu$ (mag)	$d$ (pc)	$t$ (Gyr)	$\mu_{\alpha\cos\delta}$ (mas/yr)	$\mu_{\delta}$ (mas/yr)	$\varpi$ (mas)	Reference
0.15	---	---	912 (15)	8	---	---	---	[11]
0.1	---	12.5 (0.10)	2900	1.2	---	---	---	[12]
0.104	---	11.2	1711	1.6	-3.82	4.24	---	[13]
0.104	---	---	1711	1.6	---	---	---	[14]
---	---	---	2549 (695)	---	-2.708 (0.076)	0.764 (0.075)	0.363 (0.039)	[6]
---	---	---	---	2.3 (0.140)	-2.712 (0.160)	0.771 (0.138)	0.369 (0.032)	[15]
0.1	---	11.72	---	1.8	---	---	---	[16]
---	---	---	2549 (695)	---	-2.708 (0.076)	0.764 (0.075)	0.363 (0.039)	[17]
0.074	---	11.99	2495	1.5	-2.708 (0.076)	0.764 (0.075)	0.363 (0.039)	[18]
0.242	---	12.36	---	0.86	---	---	---	[19]
0.105 (0.021)	0.082 (0.137)	---	2411 (118)	1.5	-2.708 (0.098)	0.766 (0.089)	0.364 (0.041)	[20]
0.071 (0.130)	0.00	12.191 (0.509)	2518 (667)	1.5 (0.1)	-2.718 (0.002)	0.803 (0.002)	0.37 (0.03)	This study

NGC 2509 ( $\alpha_{2000.0} = 08^{\text{h}}00^{\text{m}}48^{\text{s}}.2$ ,  $\delta_{2000.0} = -19^{\circ}03'22''$ ;  $l = 237^{\circ}.8442$ ,  $b = 05^{\circ}.8465$ ) [17] is an intermediate age open cluster located in the second Galactic quadrant towards the Galactic anti-centre region. Due to the cluster is situated very close to the Galactic disc, its embedded in field star contamination. [13] found reddening, distance and age of the cluster as  $E(B-V) = 0.104$  mag,  $d = 1711$  pc,  $\log t = 9.2$  yr, respectively. [18] used *Gaia* DR2 astrometric and photometric data and determined distance and age of NGC 2509 as  $d = 2495$  pc and  $\log t = 9.18$  yr, respectively. They obtained extinction in the cluster direction as  $A_V = 0.23$  which corresponds colour excess to be  $E(B-V) = 0.074$  mag. Also, researchers calculated mean proper-motion components of the NGC 2509 as  $(\mu_{\alpha\cos\delta}, \mu_{\delta}) = (-2.708 \pm 0.076, 0.764 \pm 0.075)$  mas/yr. [19] found extinction, distance and age of the cluster as  $A_V = 0.75$ , which corresponds  $E(B-V)$  to be 0.242 mag,  $\mu = 12.36$  mag and  $t = 860$  Myr, respectively. [20] using *Gaia* DR2 astrometric and photometric data obtained the extinction, metallicity, distance and age of the cluster as  $A_V = 0.23$  mag, which corresponds  $E(B-V)$  to be 0.105 mag,  $[Fe/H] = 0.082 \pm 0.137$  dex,  $d = 2411 \pm 118$  pc

and  $\log t = 9.18$  yr, respectively. Moreover, in the study researchers determined mean proper-motion components as  $(\mu_{\alpha\cos\delta}, \mu_{\delta}) = (-2.708 \pm 0.098, 0.766 \pm 0.089)$  mas/yr. For detailed literature study results see Table 1.

In this study, we used *Gaia*'s the third release (hereafter *Gaia* DR3, [21]) of astrometric and photometric data to analyse NGC 2509 open cluster. To remove field star contamination and perform precise selection of cluster members we used *Gaia* DR3 proper-motion components ( $\mu_{\alpha\cos\delta}$ ,  $\mu_{\delta}$ ), trigonometric parallaxes ( $\varpi$ ) and their uncertainties for each star in cluster region and calculated their membership probabilities. We took into account the stars with the membership probabilities  $P \geq 50\%$  as the most likely cluster members and used them to determine astrometric ( $\mu_{\alpha\cos\delta}$ ,  $\mu_{\delta}$ ,  $\varpi$ ) and astrophysical (reddening, distance modulus and age) parameters of the NGC 2509.

### 1.1. Astrometric and Photometric Data

We used photometric and astrometric data of *Gaia* DR3 ([21]) to analyse NGC 2509 open

cluster. We created the catalogue of NGC 2509 by considering 20 arcmin radius circular field from the cluster centre ( $\alpha_{2000.0} = 01^{\text{h}}51^{\text{m}}12^{\text{s}}.7$ ,  $\delta_{2000.0} = 61^{\circ}03'40''$ ; [17]). Thus, we found 20,391 stars within the magnitude range  $7 < G \leq 22$  mag in cluster region. Generated catalogue contains positions ( $\alpha$ ,  $\delta$ ), photometric magnitude and colours ( $G$ ,  $G_{\text{BP}} - G_{\text{RP}}$ ), proper-motion components ( $\mu_{\alpha} \cos \delta$ ,  $\mu_{\delta}$ ) and trigonometric parallaxes ( $\varpi$ ). Identification map of the open cluster NGC 2509 is shown in Figure 1. *Gaia* DR3 ([21]) provides high quality astrometric and photometric data more than 1.5 billion celestial objects. The uncertainties in *Gaia* DR3 are 0.01-0.02 mas for  $G \leq 15$  mag, and reach about 1 mas at  $G = 21$  mag. The uncertainties of trigonometric parallax are 0.02-0.07 mas for  $G \leq 17$  mag, 0.5 mas for  $G = 20$  mag and reach 1.3 mas for at  $G = 21$  mag. For sources with  $G \leq 17$  mag the proper motion uncertainties are 0.02-0.07 mas/yr reaching 0.5 mas mas/yr at  $G = 20$ , and 1.4 mas/yr at  $G = 21$  mag. For sources within  $G \leq 17$  mag the  $G$ -band photometric uncertainties are 0.3-1 mmag, increasing to 6 mmag at  $G = 20$  mag, allowing such separations to be made more accurately ([7, 22]).

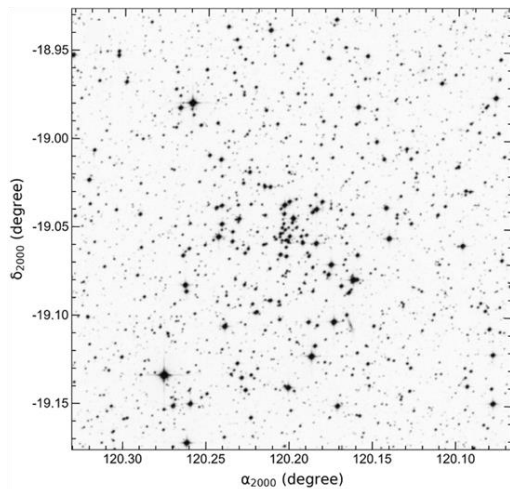


Figure 1 Identification chart of stars located through the area of NGC 2509. Field of view of the optical chart is  $20' \times 20'$ . North and East correspond to the up and left directions, respectively

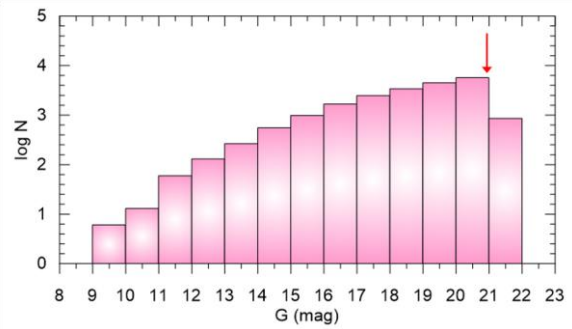


Figure 2 Number of stars versus interval  $G$  magnitudes. The red arrow represents the faint limit magnitude of the NGC 2509

Table 2 Mean photometric errors for  $G$  magnitude and  $G_{\text{BP}} - G_{\text{RP}}$  colour index as  $G$  mag function.  $N$  indicates the number of stars within the selected  $G$  magnitude intervals

$G$ (mag)	$N$	$\sigma_G$ (mag)	$\sigma_{G_{\text{BP}}-G_{\text{RP}}}$ (mag)
(6, 12]	79	0.003	0.005
(12, 14]	395	0.003	0.005
(14, 15]	552	0.003	0.005
(15, 16]	967	0.003	0.006
(16, 17]	1643	0.003	0.008
(17, 18]	2474	0.003	0.016
(18, 19]	3418	0.003	0.034
(19, 20]	4456	0.004	0.074
(20, 21]	5563	0.009	0.188
(21, 23]	844	0.024	0.383

To perform precise analyses, we investigated photometric completeness limit for the cluster. For this, we determined number of stars in interval  $G$  magnitudes. The star count histogram versus interval  $G$  magnitude is shown in Figure 2. It can be seen from the figure that number of stars increase up to  $G = 21$  mag and start to decrease after this limit where the stellar incompleteness has set in. This value is adopted photometric completeness limit for NGC 2509. We considered the stars fainter than this limit to utilize analyses of the cluster. We also investigated mean photometric errors of  $G$  magnitudes and  $G_{\text{BP}} - G_{\text{RP}}$  colour indices as function of  $G$  interval magnitudes and listed in

Table 2. It can be seen from Table 2 that the mean errors of  $G$  magnitude and  $G_{BP}-G_{RP}$  colour indices of the stars reach up to 0.01 and 0.2 mag for completeness limit  $G = 21$  mag, respectively

### 3 CONCLUSIONS AND DISCUSSION

#### 3.1. Structural Parameters of the NGC 2509

In order to estimate structural parameters of NGC 2509, we visualized the Radial Density Profile (RDP) for NGC 2509 using the centre coordinates given by [17]. The cluster area was divided into concentric circles around the adopted centre. Stellar densities ( $\rho_i$ ) in each  $i^{\text{th}}$  ring were calculated by using the expression  $\rho_i = N_i/A_i$ , where  $N$  is the number of stars and  $A$  is the area of  $i^{\text{th}}$  ring. Those calculated stellar densities ( $\rho$ ) were plotted as a function of radius from the cluster centre (Figure 3). We fitted RDP model of [23] to this distribution considering  $\chi^2$  minimization. The RDP model is formulized as  $\rho(r) = f_{bg} + (f_0 / (1 + (r/r_c)^2))$ , where  $r$  represents the radius from the cluster centre,  $f_{bg}$ ,  $f_0$  and  $r_c$  describe the background stellar density, the central density and the core radius, respectively. RDP of the cluster with best fit is shown in Figure 3. As a result of analyses, we estimated the core radius, background stellar density and central density of the NGC 2509 as  $r_c = 0.578 \pm 0.113$  arcmin,  $f_{bg} = 15.816 \pm 0.511$  stars/arcmin<sup>2</sup> and  $f_0 = 32.334 \pm 3.236$  stars/arcmin<sup>2</sup>, respectively. Also, with visual review of RDP, we obtained limiting radii ( $r_{lim}$ ) of the cluster. We described the  $r_{lim}$  as the radius that cluster density almost meets the background density (Figure 3 grey horizontal line). We considered this limit to be  $r_{lim} = 7'$  ( $5.13 \pm 1.35$  pc) for the cluster, and we used the stars inside this limiting radius for the determination of fundamental parameters of it.

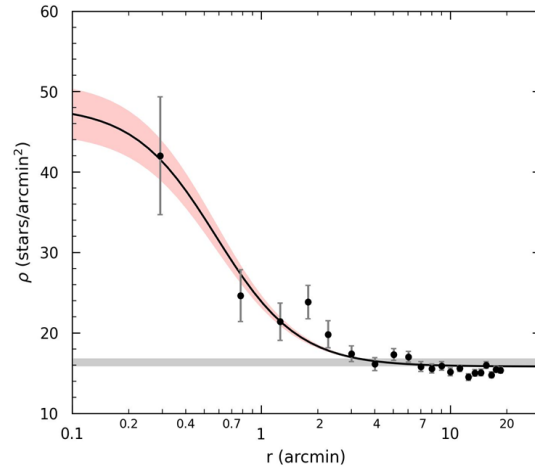


Figure 3 RDP of NGC 2509. Errors were calculated from sampling statistics  $1/\sqrt{N}$ , where  $N$  is the number of stars used in the density estimation. The smooth line shows the best fit profile of [23]. The background density level and its errors are represented with the horizontal grey bands. The King fit uncertainty ( $1\sigma$ ) is shown by the red shaded region

#### 3.2. Membership Analyses

OCs are distributed through the densely populated Galactic plane and are mostly affected by foreground/background stars. It is necessary to separate cluster members from field stars to determine more precise fundamental parameters of the OCs. As for the cluster members have same origin, their motion vectors in the sky point in the same direction. Therefore, proper-motion components are useful tools to discriminate cluster members from field stars. The membership analyses carried from astrometric data of *Gaia* catalogue give more reliable results than ground-based data ([24]). We utilized UPMASK (Unsupervised Photometric Membership Assignment in Stellar Clusters; [29]) method by using astrometric data of *Gaia* DR3 for membership analyses. This methodology previously used in many studies ([6, 17, 25-27]). UPMASK is the method of clustering algorithm and detects spatially populated groups and identifies membership probabilities of stars. This clustering method is described as k-means clustering which is the integer number and varies within 5 to 25 and is not set directly by the user ([17, 28]). We used five-dimensional

astrometric parameters as inputs which include stars' positions ( $\alpha$ ,  $\delta$ ), proper-motion components ( $\mu_\alpha \cos \delta$ ,  $\mu_\delta$ ), trigonometric parallaxes ( $\varpi$ ) and their uncertainties. In the method of UPMASK, membership probabilities ( $P$ ) of stars are described as the frequency with which star belongs to a clustered group. Program was run 1000 iterations during the utilization. Best solution was adopted when k-means value was set to 15 for NGC 2509. We considered the stars with membership probability  $P \geq 50\%$  as possible cluster members. Moreover, to determine cluster members more precision and get reliable astrometric parameters for NGC 2509, we filtered possible members which brighter than completeness limit  $G \leq 21$  mag and within the cluster limiting radius ( $r_{\text{lim}} = 7'$ ). Thus, with these criteria we identified a total of 244 stars with probability  $P \geq 50\%$ . We plotted proper-motion distribution of stars to image the position of the cluster as regards to field stars and shown it in Figure 4.

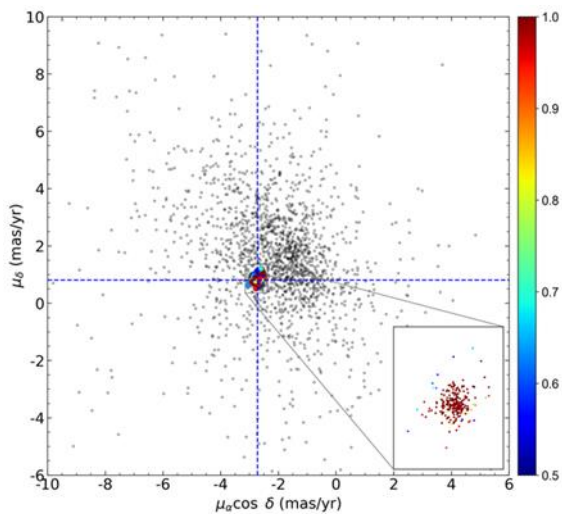


Figure 4 *Gaia* DR3 data based proper-motion distribution of NGC 2509. Colour bar shows the scale of membership probabilities of the stars. Zoomed region shows the location where the cluster is condensed. The intersection of the dashed blue lines is the point of mean proper-motion values

It can be seen in the figure that NGC 2509 is embedded in field stars. In Figure 4, the intersection of blue dashed lines represents the values of mean proper-motion components

calculated from the most probable cluster members (244 stars with  $P \geq 50\%$ ). These values were determined as  $(\mu_\alpha \cos \delta, \mu_\delta) = (-2.718 \pm 0.002, 0.803 \pm 0.002)$  mas/yr, which are compatible with the results of all studies performed with *Gaia* observations for the NGC 2509 (see Table 1). To estimate mean trigonometric parallax  $\langle \varpi \rangle$  of NGC 2509, we took into account the most likely member stars with relative parallax error ( $\sigma_\varpi / \varpi$ ) less than 0.15 and plotted the histogram for number of stars ( $N$ ) versus trigonometric parallax ( $\varpi$ ) as shown in Figure 5. We fitted Gaussian function to this distribution and it provided the mean trigonometric parallax  $\langle \varpi \rangle$  to be  $0.37 \pm 0.03$  mas. By using the expression of linear equation  $d$  (pc) =  $1000 / \varpi$  (mas) we calculated trigonometric parallax-based distance of the NGC 2509 as  $d_\varpi = 2703 \pm 190$  pc.

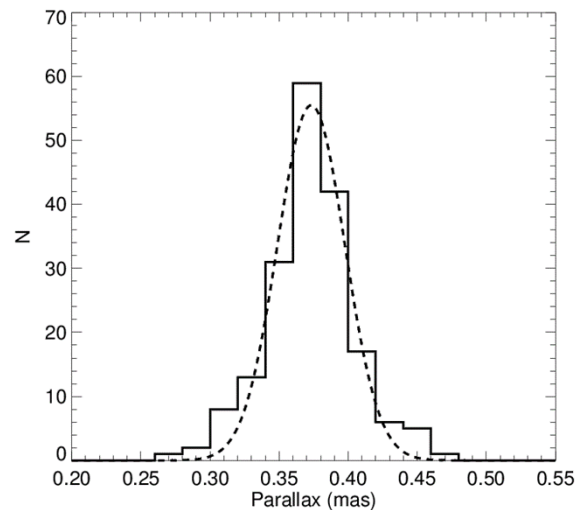


Figure 5 *Gaia* DR3 based trigonometric parallax histogram for NGC 2509. Applied Gaussian fit is shown in black dashed curve

### 3.3. Fundamental Parameters of NGC 2509

Colour-magnitude diagrams of OCs are important tools to examine morphology of the cluster, as well as to obtain their fundamental parameters such as reddening, metallicity, age and distance.

The reddening, metallicity age and distance of NGC 2509 were derived simultaneously by fitting PARSEC isochrones of [29] to the



observed colour-magnitude diagram as shown in Figure 6. During the fitting procedure we concentrated on most likely stars that contain main-sequence, turn-off point and giant region of the cluster. Different age values  $\log t = 8.15, 8.18$  and  $8.20$  yr with metallicity  $z = 0.0152$  of isochrones were superimposed on observable colour-magnitude diagram. Best fit isochrone resulted the reddening, age and isochrone distance of the NGC 2509 to be  $E(G_{BP}-G_{RP}) = 0.100 \pm 0.184$  mag,  $d_{iso} = 2518 \pm 667$  pc and  $t = 1.5 \pm 0.1$  Gyr, respectively (see Table 1). To compare with literature, we transformed *Gaia* based reddening to *UBV* based value by using  $E(G_{BP}-G_{RP}) = 1.41 \times E(B-V)$  equation given by [30]. This equation was used in the studies recently presented [31, 32] and resulted successfully. Thus, we calculated *UBV* based reddening as  $E(B-V) = 0.071 \pm 0.130$  mag. The  $E(B-V)$  colour excess and age of the cluster derived in the study are in a good agreement with many values given in the literature (see Table 1). Moreover, the distance value ( $d_{iso} = 2518 \pm 667$  pc) found in study is compatible with the values those of represented in *Gaia* era (see Table 1), and with the distance that calculated from trigonometric parallaxes of most likely members in the study. This shows that the cluster's all astrophysical parameters derived in the study are acceptable. Also, results of the study listed in Table 3.

#### 4 CONCLUSION

We performed *Gaia* DR3 astrometric and photometric data-based study of intermediate-age open cluster NGC 2509. We calculated membership probabilities of stars in the region of cluster and classified 244 most likely members with membership probabilities  $P \geq 50\%$ . We considered these members to estimate astrophysical parameters. The main results of the analyses are as follows:

- Taking into account the RDP results, the limiting radius of the cluster is obtained as  $r_{lim} = 7'$  ( $5.13 \pm 1.35$  pc)

- Using the distribution of proper-motion components, we determined mean proper-motion of NGC 2509 as  $(\mu_{\alpha} \cos \delta, \mu_{\delta}) = (-2.718 \pm 0.002, 0.803 \pm 0.002)$  mas/yr.

- On the basis of most likely cluster stars with relative parallax error ( $\sigma_{\varpi}/\varpi$ ) less than 0.15, we calculated trigonometric parallax of the cluster as  $\langle \varpi \rangle = 0.37 \pm 0.03$  mas, which corresponds the parallax distance to be  $d_{\varpi} = 2703 \pm 190$  pc.

- PARSEC isochrones of [30] provide an age of  $t = 1.5 \pm 0.1$  Gyr and isochrone distance of  $d_{iso} = 2518 \pm 667$  pc with the solar metallicity ( $z = 0.015$ ) for the cluster. Because of astrophysical parameters estimated simultaneously on CMD, the best fit isochrone gives the *Gaia* based reddening as  $E(G_{BP}-G_{RP}) = 0.100 \pm 0.184$  mag for NGC 2509.

Table 3 Astrophysical parameters of NGC 2509 estimated in the study

Parameter	Value
$\alpha$ (hh:mm:ss.s)	08:00:48.2
$\delta$ (dd:mm:ss.s)	-19:03:22.0
$l$ ( $^{\circ}$ )	237.8442
$b$ ( $^{\circ}$ )	05.8465
$f_0$ (star/arcmin $^2$ )	$32.334 \pm 3.236$
$r_c$ (arcmin)	$0.578 \pm 0.113$
$f_{bg}$ (star/arcmin $^2$ )	$15.816 \pm 0.511$
$r_{lim}$ (arcmin)	7
$r$ (pc)	$5.13 \pm 1.35$
$\mu_{\alpha} \cos \delta$ (mas/yr)	$-2.718 \pm 0.002$
$\mu_{\delta}$ (mas/yr)	$0.803 \pm 0.002$
Cluster members ( $P \geq 50\%$ )	244
$\varpi$ (mas)	$0.37 \pm 0.03$
$d_{\varpi}$ (pc)	$2703 \pm 190$
$E(G_{BP} - G_{RP})$ (mag)	$0.100 \pm 0.184$
$E(B-V)$ (mag)	$0.071 \pm 0.130$
[Fe/H] (dex)	0.0152
Age (Gyr)	$1.5 \pm 0.1$
Distance module (mag)	$12.191 \pm 0.509$
Isochrone distance (pc)	$2518 \pm 667$
$X$ (pc)	-1333
$Y$ (pc)	-2121
$Z$ (pc)	256
$R_{gc}$ (kpc)	9.57

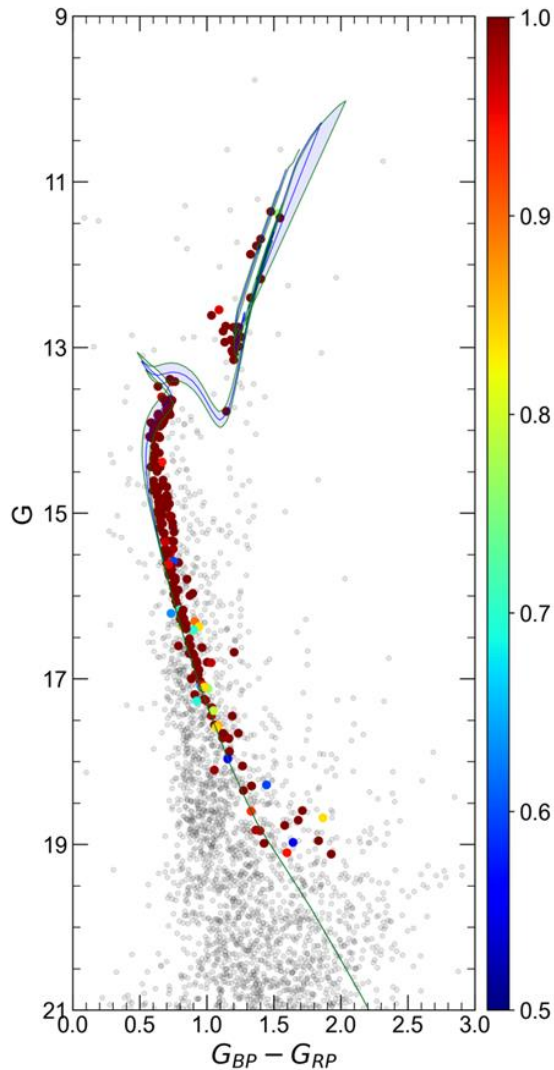


Figure 6 Colour-magnitude diagram with best fit PARSEC isochrones. Colour scaled represent the membership probabilities of stars according to colour bar in right panel. Gray circles show field stars. Blue and green solid lines represent errors in age, with isochrone that best represent cluster parameters, respectively

### ***Acknowledgments***

This study has been supported in part by the Scientific and Technological Research Council (TÜBİTAK) 122F109. We also made use of VizieR and Simbad databases at CDS, Strasbourg, France. We made use of data from the European Space Agency (ESA) mission Gaia, processed by the Gaia Data Processing and Analysis Consortium (DPAC). Funding for DPAC has been provided by national institutions, in particular the institutions participating in the Gaia Multilateral Agreement.

### ***Authors' Contribution***

Concept: T.Y., S.K., Design: T.Y., S.K., Data Collection or Processing: T.Y., S.K., Analysis or Interpretation T.Y., S.K., Literature Search: T.Y., S.K., Writing: T.Y., S.K.

### ***The Declaration of Conflict of Interest/ Common Interest***

The study is complied with research and publication ethics.

### ***The Declaration of Ethics Committee Approval***

This study does not require ethics committee permission or any special permission.

### ***The Declaration of Research and Publication Ethics***

The authors of the paper declare that they comply with the scientific, ethical and quotation rules of SAUJS in all processes of the paper and that they do not make any falsification on the data collected. In addition, they declare that Sakarya University Journal of Science and its editorial board have no responsibility for any ethical violations that may be encountered, and that this study has not been evaluated in any academic publication environment other than Sakarya University Journal of Science.

### **REFERENCES**

- [1] Yadav, R. K. S., Glushkhova, E. V., Sariya, D. P., Porokhova, A. V., Kumar, B., Sagar, R., "Optical Photometric Study of the Open Clusters Kaposov 12, Kaposov 53 and Kaposov 77", Monthly Notices of the Royal Astronomical Society, vol. 414, pp. 652-658, 2011.
- [2] Lada, C. J., Lada, E. A., "Embedded Clusters in Molecular Clouds", Annual Review of Astronomy and Astrophysics, vol. 41, pp. 57-115, 2003.
- [3] Kim, S. C., Kyeong, J., Park, H. S., Han, I., Lee, J. H., Moon, D., Lee, Y., Kim, S., "BVI Photometric Study of the Old

- Open Cluster Ruprecht 6”, *Journal of the Korean Astronomical Society*, vol. 50, pp. 79-92, 2017.
- [4] He, Z.-H., Xu, Y., Hou, L.-G., “A Catalogue of 74 New Open Clusters Found in Gaia Data Release 2”, *Research in Astronomy and Astrophysics*, vol. 21, article id.A93, pp. 1-9, 2021.
- [5] Bisht, D., Elsanhoury, W. H., Zhu, Q., Sariya, D. P., Yadav, R. K. S., Rangwal, G., Durgapal, A., Jiang, I.-G., “An Investigation of Poorly Studied Open Cluster NGC 4337 Using Multicolor Photometric and Gaia DR2 Astrometric Data”, *The Astronomical Journal*, vol. 160, pp. 1-14, 2020.
- [6] Cantat-Gaudin, T., Jordi, C., Vallenari, A., Bragaglia, A., Balaguer-Núñez, L., Soubiran, C., Bossini, D., Moitinho, A., Castro-Ginard, A., Krone-Martins, A., Casamiquela, L., Sordo, R., Carrera, R., “A Gaia DR2 View of the Open Cluster Population in the Milky Way”, *Astronomy and Astrophysics*, vol. 618, article id.A93, pp. 1-16, 2018.
- [7] Soubiran, C., Cantat-Gaudin, T., Romero-Gómez, M., Casamiquela, L., Jordi, C., Vallenari, A., Antoja, T., Balaguer-Núñez, L., Bossini, D., Bragaglia, A., Carrera, R., Castro-Ginard, A., Figueras, F., Heiter, U., Katz, D., Krone-Martins, A., Le Campion, J. -F., Moitinho, A., Sordo, R., “Open Cluster Kinematics with Gaia DR2”, *Astronomy and Astrophysics*, vol. 619, article id.A155, pp. 1-11, 2018.
- [8] Castro-Ginard, A., Jordi, C., Luri, X., Cantat-Gaudin, T., Balaguer-Núñez, L., “Hunting for Open Clusters in Gaia DR2: The Galactic Anticentre”, *Astronomy and Astrophysics*, vol. 627, article id.A35, pp. 1-8, 2019.
- [9] Ding, X., Ji, K.-F., Li, X.-Z., Cheng, Q.-Y., Wang, J.-L., Yu, X.-G., Liu, H., “Fundamental Parameters for 30 Faint Open Clusters with Gaia EDR3 Based on the More Reliable Members”, *Publications of the Astronomical Society of Japan*, vol. 73, pp.1486-1496, 2021.
- [10] Belokurov, V., Kravtsov, A., “From Dawn Till Disc: Milky Way’s Turbulent Youth Revealed By The APOGEE+Gaia Data”, *Monthly Notices of the Royal Astronomical Society*, vol. 514, pp. 689-714, 2022.
- [11] Sujatha, S., Babu, G. S. D., “Study of Open Cluster NGC 2509”, *Bulletin of the Astronomical Society of India*, vol. 31, pp. 9-18, 2003.
- [12] Carraro, G., Costa, E., “Photometry of the Five Marginally Studied Open Clusters Collinder 74, Berkeley 27, Haffner 8, NGC 2509, and VdB-Hagen 4”, *Astronomy and Astrophysics*, vol. 464, pp. 573-580, 2007.
- [13] Kharchenko, N.V., Piskunov, A.E., Roeser, S., Schilbach, E., Scholz, R.-D. “Global Survey of Star Clusters in the Milky Way, II. The Catalogue of Basic Parameters”, *Astronomy and Astrophysics*, vol. 558, article id.A53, pp. 1-8, 2013.
- [14] Joshi, Y. C., Dambis, A. K., Pandey, A. K., Joshi, S., “Study of Open Clusters within 1.8 kpc and Understanding the Galactic Structure”, *Astronomy and Astrophysics*, vol. 593, article id.A116, pp. 1-13, 2016.
- [15] Liu, L., Pang, X., “A Catalog of Newly Identified Star Clusters in Gaia DR2”, *The Astrophysical Journal Supplement Series*, vol. 245, article id.A32, pp. 1-13, 2019.

- [16] Siegel, M. H., LaPorte, S. J., Porterfield, B. L., Hagen, L. M. Z., Gronwall, C. A., “The Swift UVOT Stars Survey. III. Photometry and Color-Magnitude Diagrams of 103 Galactic Open Clusters”, *The Astronomical Journal*, vol. 158, article id.A35, pp. 1-27, 2019.
- [17] Cantat-Gaudin, T., Anders, F. “Clusters and Mirages: Cataloguing Stellar Aggregates in the Milky Way”, *Astronomy and Astrophysics*, vol. 633, article id.A99, pp. 1-22, 2020.
- [18] Cantat-Gaudin, T., Anders, F., Castro-Ginard, A., Jordi, C., Romero-Gómez, M., Soubiran, C., Casamiquela, L., Tarricq, Y., Moitinho, A., Vallenari, A., Bragaglia, A., Krone-Martins, A., Kounkel, M., “Painting a Portrait of the Galactic Disc with its Stellar Clusters”, *Astronomy and Astrophysics*, vol. 640, article id.A1, pp. 1-17, 2020.
- [19] de Juan Ovelar, M., Gossage, S., Kamann, S., Bastian, N., Usher, C., Cabrera-Ziri, I., Dotter, A., Conroy, C., Lardo, C., “Extended Main Sequence Turnoffs in Open Clusters as Seen by Gaia - II. The Enigma of NGC 2509”, *Monthly Notices of the Royal Astronomical Society*, vol. 491, pp. 2129-2136, 2020.
- [20] Dias, W. S., Monteiro, H., Moitinho, A., Lépine, J. R. D., Carraro, G., Paunzen, E., Alessi, B., Villela, L. “Updated Parameters of 1743 Open Clusters Based on Gaia DR2”, *Monthly Notices of the Royal Astronomical Society*, vol. 504, pp. 356-371, 2021.
- [21] Gaia Collaboration, Vallenari, A., Brown, A. G. A., Prusti, T., de Bruijne, J. H. J., Arenou, F., Babusiaux, C., Biermann, M., Creevey, O. L., Ducourant, C., Evans, D. W., Eyer, L., Guerra, R., Hutton, A., Jordi, C., Klioner, S. A., Lammers, U. L., Lindegren, L., Luri, X., Mignard, F., et al., “Gaia Data Release 3: Summary of the Content and Survey Properties”, *Astronomy and Astrophysics*, vol. 674, article id.A1, pp.1-22, 2023.
- [22] Monteiro, H., Dias, W. S., “Distances and Ages From Isochrone Fits of 150 Open Clusters Using Gaia DR2 Data”, *Monthly Notices of the Royal Astronomical Society*, vol. 487, pp. 2385-2406, 2019.
- [23] King, I. R., “The Structure of Star Clusters. I. An Empirical Density Law”, *Astronomical Journal*, vol. 67, pp. 471-485, 1962.
- [24] Dias, W. S., Monteiro, H., Lépine, J. R. D., Prates, R., Gneiding, C. D., Sacchi, M., “Astrometric and Photometric Study of Dias 4, Dias 6, and Other Five Open Clusters Using Ground-Based and Gaia DR2 Data”, *Monthly Notices of the Royal Astronomical Society*, vol. 481, pp. 3887-3901, 2018.
- [25] Banks, T., Yontan, T., Bilir, S., Canbay, R., “Vilnius photometry and Gaia astrometry of Melotte 105”, *Journal of Astrophysics and Astronomy*, vol. 41, article id.A6, pp. 1-24, 2020.
- [26] Koç, S., Yontan, T., Bilir, S., Canbay, R., Ak, T., Banks, T., Ak, S., Paunzen, E., “A Photometric and Astrometric Study of the Open Clusters NGC 1664 and NGC 6939”, *The Astronomical Journal*, vol. 163, article id.A191, pp. 1-22, 2022.
- [27] Yontan, T., “An Investigation of Open Clusters Berkeley 68 and Stock 20 Using CCD UBV and Gaia DR3 Data”, *Astronomical Journal*, vol. 165, article id.A79, pp. 1-20, 2023.
- [28] Krone-Martins A., Moitinho A., “UPMASK: Unsupervised Photometric Membership Assignment in Stellar Clusters”, *Astronomy and*

Astrophysics, vol. 561, article id.A57,  
pp. 1-12, 2004.

- [29] Bressan, A., Marigo, P., Girardi, L., Salasnich, B., Dal Cero, C., Rubele, S., Nanni, A., “PARSEC: Stellar Tracks and Isochrones with the Padova and Trieste Stellar Evolution Code”, Monthly Notices of the Royal Astronomical Society, vol. 427, pp. 127-145, 2012.
- [30] Sun, M., Jiang, B., Yuan, H., Li, J., “The Ultraviolet Extinction Map and Dust Properties at High Galactic Latitude”, The Astrophysical Journal Supplement Series, vol. 254, article id.38, pp.1-12, 2021.
- [31] Taşdemir, S, Yontan, T., “Analysis of the Young Open Cluster Trumpler 2 Using Gaia DR3 Data”, Physics and Astronomy Reports, vol. 1, no. 1, pp. 1-10, 2023.
- [32] Koç, S., Yontan, T., “Astrophysical Parameters of the Open Cluster Berkeley 6”, Bitlis Eren Üniversitesi Fen Bilimleri Dergisi, vol. 12, no. 2, pp. 369-375, 2023.



SAKARYA ÜNİVERSİTESİ

# FEN BİLİMLERİ ENSTİTÜSÜ DERGİSİ

Sakarya University Journal of Science  
SAUJS

ISSN 1301-4048 | e-ISSN 2147-835X | Period Bimonthly | Founded: 1997 | Publisher Sakarya University |  
<http://www.saujs.sakarya.edu.tr/>

Title: Topology Optimization of Spinal Cage Designs for Improved Stress Distribution and Bone Graft Window

Authors: Meltem ERYILDIZ

Received: 11.05.2023

Accepted: 2023-07-12 00:00:00

Article Type: Research Article

Volume: 27

Issue: 5

Month: October

Year: 2023

Pages: 1046-1054

How to cite

Meltem ERYILDIZ; (2023), Topology Optimization of Spinal Cage Designs for Improved Stress Distribution and Bone Graft Window. Sakarya University Journal of Science, 27(5), 1046-1054, DOI: 10.16984/saufenbilder.1295714

Access link

<https://dergipark.org.tr/tr/journal/1115/issue/80257/1295714>

New submission to SAUJS

<http://dergipark.gov.tr/journal/1115/submission/start>

## Topology Optimization of Spinal Cage Designs for Improved Stress Distribution and Bone Graft Window

Meltem ERYILDIZ \*<sup>1</sup> 

### Abstract

Interbody fusion is utilized as a treatment for spinal degenerative diseases. Spinal cages, also known as intervertebral cages or interbody fusion devices, are implants employed in spinal surgery to address these conditions and promote spinal stability. These cages are inserted into the intervertebral space between adjacent vertebrae, replacing the damaged or degenerated disc. Spinal cages aid in the distribution of loads and stress at the fusion site and often incorporate a dedicated area for bone graft material. In this study, a topology optimization approach was employed to develop distinct spinal cages featuring a bone graft window. The mechanical behavior of the spinal cages under loading conditions was simulated and evaluated using finite element analysis. Following optimization, a finite element model analysis estimated the maximum stresses and compared them to the initial model. For topology optimization, reductions of 30%, 50%, and 70% in mass were defined. Both the 50% and 70% mass-reduced designs, featuring an open window, are deemed suitable for bone graft placement and stress distribution.

**Keywords:** Interbody fusion, spinal cage, topology optimization, FEA, mass reduction

### 1. INTRODUCTION

A crucial component of the human body for connecting and supporting weight is the spine. The prevalence of spinal degenerative disorder has gradually increased with the aging of the population. Patients with spinal degenerative disorders who do not respond to conservative treatment frequently require surgical treatment. Spinal degenerative disorders can be effectively treated using interbody fusion [1]. The insertion of a fusion cage between the vertebrae is necessary for interbody fusion. The spinal interbody fusion cage is a small, porous, hollow implant with a

form that can be either cylindrical or almost cuboid. It can restore physiological disc height by replacing the degenerative disc and disengaging the intervertebral body. The hollow and porous cage can be filled with bone grafts, which will allow bone to grow through the cage and lead to bony fusion. Additionally, it can boost fusion speed and mechanical strength [2]. The interbody fusion cage's size, shape, and bone-grafting capacity are crucial elements impacting how well the fusion will work. However, the majority of fusion cages currently in use have a universal design and merely vary in size. The use of universal interbody fusion cages may

\* Corresponding author: meltemeryildiz@beykent.edu.tr (M. ERYILDIZ)

<sup>1</sup> Department of Mechanical Engineering, Istanbul Beykent University, Istanbul, Türkiye,

ORCID: <https://orcid.org/0000-0002-2683-560X>



decrease the fusion rate and raise the likelihood of surgical failure due to mismatched sizes, shapes, and volumes of the bone graft window because of the wide variation in the pathological environments of patients. As a result, scientists are now concentrating primarily on designing interbody fusion cages [3].

Topology optimization is a computational design process used to optimize the material distribution within a given design space to achieve the best possible performance. It is commonly employed in engineering disciplines, such as mechanical, structural, and aerospace engineering [4, 5]. The goal of topology optimization is to determine the optimal layout or distribution of material within a predefined design domain, subject to specified constraints and objectives. The process starts with an initial design space, which represents the overall shape and boundaries of the structure or component being optimized [4-6].

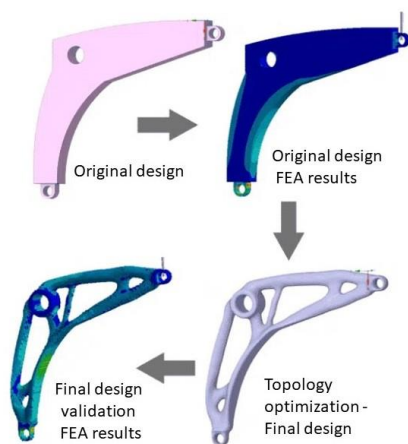


Figure 1 Topology optimization process

Using numerical methods and algorithms, topology optimization iteratively redistributes material within the design domain to maximize performance while satisfying design criteria. During the optimization process, regions with excessive material that do not contribute significantly to the desired performance are systematically removed or minimized, resulting in a more efficient design. At the same time, material is added or

reinforced in areas where it is necessary to meet the performance requirements. Topology optimization considers various factors such as loads, boundary conditions, material properties, and manufacturing constraints. It often utilizes finite element analysis (FEA) techniques to simulate and evaluate the structural behavior under different conditions. As shown in the topology optimization process in Figure 1, the majority of topology optimization techniques are carried out by combining the concepts of CAD (Computer Aided Design), FEA, and various optimization algorithms in consideration of various manufacturing techniques [6, 7].

Topology-optimized structures exhibit complicated geometric configurations. Due to the difficulty of producing these novel structures using traditional methods (such as casting or machining), additive manufacturing offers a strong opportunity for topology optimization [8].

It has been demonstrated that topology optimization of fusion cages effectively increases the available area for bone grafts; however, stress shielding remains a concern [9, 10]. Zhong et al. [11] utilized topology optimization to design a new cage and investigate stress distribution in the lumbar spine. Tovar et al. [12] utilized finite element-based optimization techniques to achieve an optimal design for interbody implants. Chuah et al. [13] employed topology optimization to reduce the stress-shielding effect in spinal interbody cages by removing ineffective material from the design domain. The stress shielding effect can be minimized by designing porous implants that allow bone to grow into the implant. However, studies in this area are still insufficient and ongoing, so further investigation is needed. The aim of this study was to design a cage that minimizes the stress shielding effect while also maintaining its mechanical strength. To achieve this, a novel fusion cage with a bone graft window was designed using a topology optimization approach. The study also aimed



to simulate and evaluate the mechanical behavior of the spinal cages under loading conditions through finite element analysis (FEA) and topology optimization methods. The specific objectives were to optimize the cage design by reducing its mass by 30%, 50%, and 70%, and to assess the resulting stress distribution and deformation.

## 2. MATERIAL AND METHODS

### 2.1. Initial Design of Spinal Cage

Spinal cages are typically implantable devices that are inserted into the intervertebral space, which is the area between two adjacent vertebrae in the spine. The primary purpose of a spinal cage is to provide stability, decompression, and support to the spine while promoting proper alignment and fusion of the vertebral segments. The spinal cage is a small, hollow, or partially hollow structure with a form that can be either cylindrical or almost cuboid. Key considerations in spinal cage design include the choice of materials, geometry, and biomechanical properties.

Solid models of the L3-L4 vertebrae and spinal cage were created using the CATIA V5R20 program. The dimensions of the cage rely on the usual distance between the L3-L4 vertebrae according to the model. As seen in Figure 2, the initial spinal cage design was created based on the L3-L4 vertebrae model. The standard type of XLIF cage has 18 mm of width. [14]. The cage height and length were chosen to preserve disc space and lordosis according to the L3-L4 model.

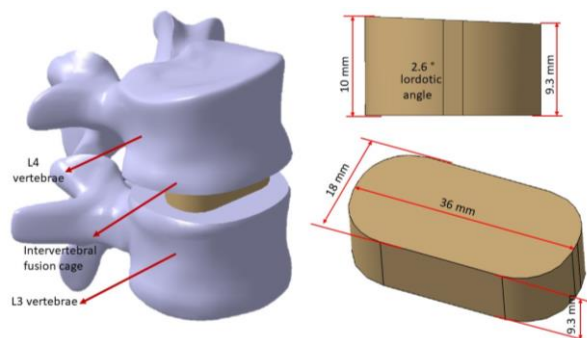


Figure 2 Initial spinal cage design

The materials used for spinal cages are usually biocompatible and can include titanium, stainless steel, or polymer-based composites. These materials should possess adequate strength and durability to withstand the forces exerted on the spine. In this study, stainless steel material was chosen due to its strength, durability, biocompatibility, radiopacity, and cost-effectiveness [15]. The total mass of the initial design was 0.450 kg.

### 2.2. Finite Element Model

After designing the spinal cage's CAD model, geometry was loaded into ANSYS Workbench 2022 R2 simulation software to build a finite element model. Statistical structural analysis was performed. Automatic meshing was applied to the model with resolution 7. Stainless steel was chosen as a material for the analysis and the material properties are shown in Table 1.

Table 1 The properties of stainless steel

Properties	Unit
Young modulus	195 GPa
Poisson's Ratio	0.27
Yield Strength	250 MPa
Tensile Ultimate Strength	565 MPa
Density	7969 kg/m <sup>3</sup>

Ansys was used to define the loads and boundary conditions that were applied to the spinal cage. A static, axial compressive force along the y-axis of 750 N was applied uniformly throughout the surface of L3 vertebrae, fixing L4 vertebrae as shown in Figure 3. The highest in vivo force recorded in a patient's lumbar spine when they were getting up from a chair was used to determine the load [16].

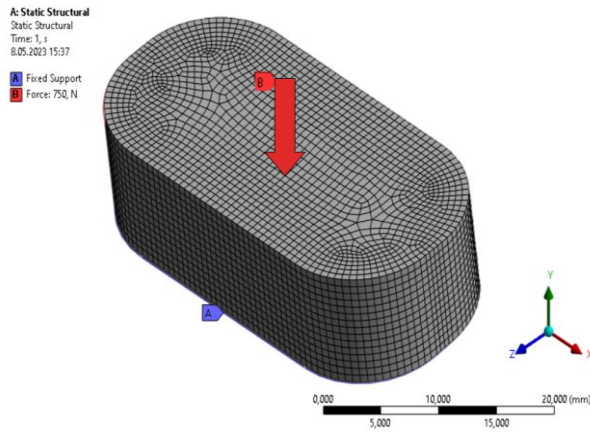


Figure 3 Finite element model of the spinal cage

### 2.3. Topology Optimization for Designing a Spinal Cage

The most effective design is produced using structural optimization methods using ANSYS that take into account several factors, such as mass, volume, strength, cost, etc. The objective of the structural optimization method is to create optimal designs that meet specific criteria. This method has the advantage of reducing time and money lost [17].

The design space was defined according to the dimensions of the spinal cage. The entire cage model was chosen as the design region and there was no exclusion region. 30%, 50%, and 70% mass reduction was defined for topology optimization. Minimizing compliance was stated as the goal. The maximum number of iterations was set at 100. The topology-optimized designs are shown in Figure 4.

## 3. RESULTS AND DISCUSSION

A structural analysis was performed to assess the effectiveness of the initial spinal cage design, revealing a displacement of 1.083 mm and a maximum von Mises stress of 3.0157 MPa. To verify the ability of the topology-optimized designs to withstand the applied load case, another structural analysis was conducted, as depicted in Figure 5, Figure 6, and Figure 7. The FEA and topology optimization results of the spinal cage designs

are presented in Table 2. According to Table 2, the 50% mass-reduced spinal cage design exhibited the minimum von Mises stress

With a 70% reduction in mass, a weight loss of 29.14 g was achieved, but the maximum stress value did not decrease as significantly as in the 50% mass-reduced spinal cage, which had a weight loss of 19.99 g. A stiffer structure typically experiences lower deformations and displacements under the same applied load, while a less stiff structure tends to undergo larger deformations (Figure 5, Figure 6, and Figure 7). The stiffer design was created with a 30% mass reduction, while the least stiff design was achieved through a 70% mass reduction. Areas with lower stiffness may experience higher stresses due to increased deformation or localized load concentrations [18]. The findings of Zhong et al. [11] align with our results, supporting the general understanding that a stiffer structure tends to exhibit reduced deformations and displacements.

Moreover, an increase in volume can result in an increase in stiffness, assuming all other factors remain equal. When the volume of a structure increases, assuming the material properties remain the same, the additional material contributes to a higher resistance against deformation. This increased material volume leads to a higher stiffness or rigidity of the structure [19]. Srinivasan et al. [20] reported that an increase in the infill percentage results in the provision of more material, thereby leading to an improvement in strength. These findings align with the results obtained in our study.

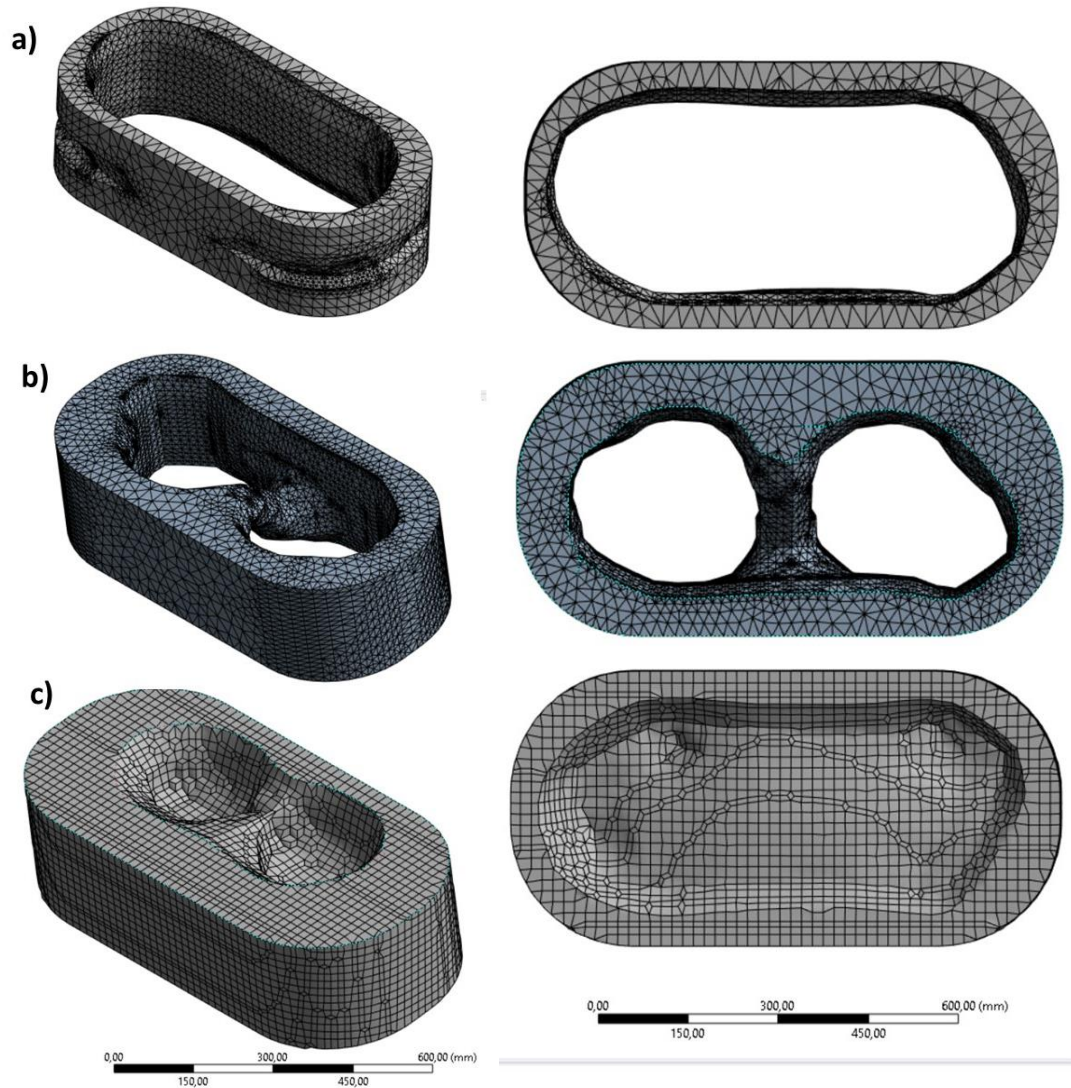


Figure 1 Topology-optimized spinal cages with varying levels of mass reduction: a) 30%, b) 50%, and c) 70%

Table 2 FEA results of the topology optimized the spinal cage designs

	Initial design	70% mass reduction	50% mass reduction	30% mass reduction
Von Mises Stress (MPa)	3.016	0.036	0.013	0.079
Deformation (mm)	1.082900	0.000054	0.000012	0.000008
Mass (g)	45.09	15.95	26.10	35.59
Volume (cm <sup>3</sup> )	5743.7	2031.5	3324.5	4533.9
Weight loss (g)	-----	29.14	18.99	9.5

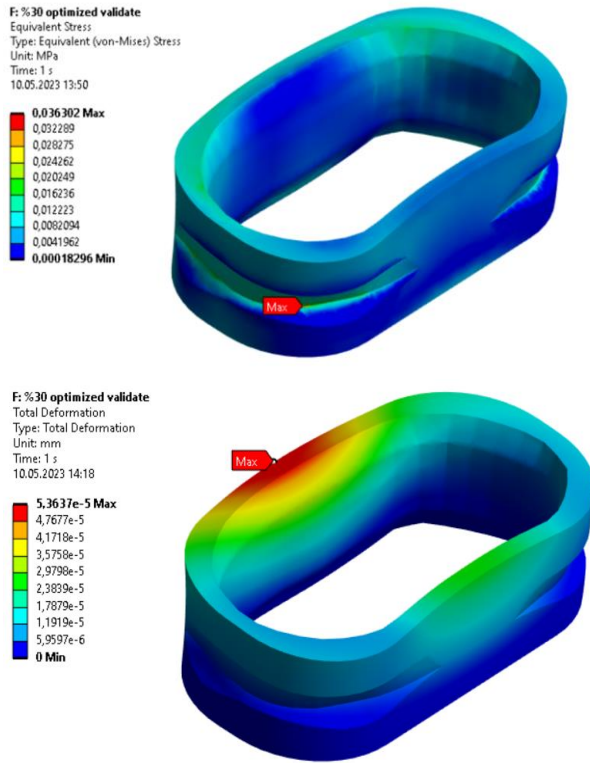


Figure 5 FEA results of 70% mass-reduced spinal cages: a) von Mises stress, b) total deformation

However, after a 50% mass reduction, this value decreased to 0.013 MPa. The maximum von Mises stress remains below the endurance limit of the material, typically ranging between 30% and 45% of its ultimate tensile strength, as indicated by the study conducted by Gültekin and Vahşi [21].

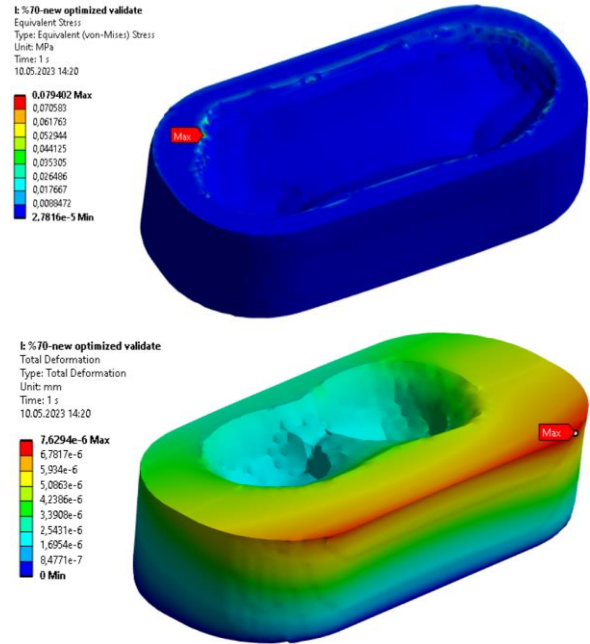


Figure 7 FEA results of 30% mass-reduced spinal cages: a) von Mises stress, b) total deformation

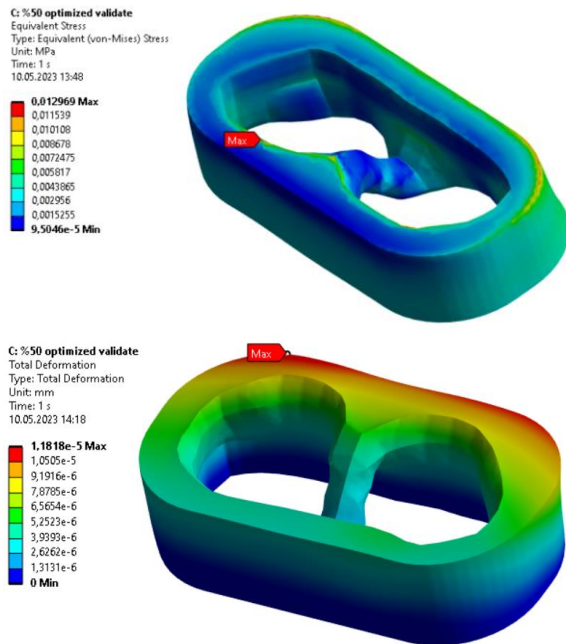


Figure 6 FEA results of 50% mass-reduced spinal cages: a) von Mises stress, b) total deformation

Both the 50% and 70% mass-reduced designs, featuring an open window, are considered suitable for bone graft placement. These designs have achieved a reduction in mass while maintaining the necessary structural integrity and functionality for their intended purpose. The presence of an open window indicates that a portion of the design has been modified or removed to allow for bone graft placement. During a spinal fusion procedure, the bone graft is typically inserted inside the spinal cage, promoting bone growth and facilitating fusion between adjacent vertebrae. [3, 9, 10] This modification ensures that the bone graft can be properly positioned and secured within the design.

The strength of the topology-optimized spinal cage can still be considered acceptable. Under the load condition, the maximum von Mises stress of the initial design was 3.016 MPa.

#### 4. CONCLUSION

This work proposes the design concept of a human spinal cage used for people with a spinal degenerative disorder. In order to determine the best material distribution, the spinal cage's topology was optimized. This resulted in a mass reduction of around 36 g as well as stress and deformation that met acceptance criteria. While retaining the essential structural integrity and functionality for the intended purpose, these designs had undergone a mass reduction. The window for the bone graft could be obtained through topological optimization. This bone graft window makes sure that the bone graft may be positioned and fixed within the design in the appropriate manner.

##### *Funding*

The author has not received any financial support for the research, authorship, or publication of this study.

##### *Authors' Contribution*

The author was responsible for the conception, design, data collection, analysis, interpretation of the research and, the author also drafted the manuscript and approved the final version for publication.

##### *The Declaration of Conflict of Interest/ Common Interest*

No conflict of interest or common interest has been declared by the author.

##### *The Declaration of Ethics Committee Approval*

This study does not require ethics committee permission or any special permission.

##### *The Declaration of Research and Publication Ethics*

The author of the paper declares that she complies with the scientific, ethical, and quotation rules of SAUJS in all processes of the paper and that she does not make any falsification of the data collected. In addition, she declares that Sakarya University Journal of Science and its editorial board have no

responsibility for any ethical violations that may be encountered and that this study has not been evaluated in any academic publication environment other than Sakarya University Journal of Science.

#### REFERENCES

- [1] C. Y. Lin, T. Wirtz, F. LaMarca, S. J. Hollister, "Structural and mechanical evaluations of a topology optimized titanium interbody fusion cage fabricated by selective laser melting process," *Journal of Biomedical Materials Research Part A: An Official Journal of The Society for Biomaterials*, vol. 83, no. 2, pp. 272-279, 2007.
- [2] T. A. Zdeblick, F.M. Phillips, "Interbody cage devices," *Spine*, vol. 28, no. 15S, pp. S2-S7, 2003.
- [3] Z. Wang, J. Jiang, F. Jian, Z. Chen, X. Wang, W. Duan, W. Zhang, "Interbody Fusion Cage Design Driven by Topology Optimization," *World Neurosurgery*, 2023.
- [4] G. I. Rozvany, "A critical review of established methods of structural topology optimization," *Structural and multidisciplinary optimization*, vol. 37, pp. 217-237, 2009.
- [5] Z. Sun, Y. Wang, Z. Gao, Y. Luo, "Topology optimization of thin-walled structures with directional straight stiffeners," *Applied Mathematical Modelling*, vol. 113, pp. 640-663, 2023.
- [6] R. D. Kundu, X. S. Zhang, "Stress-based topology optimization for fiber composites with improved stiffness and strength: Integrating anisotropic and isotropic materials," *Composite Structures*, pp. 117041, 2023.
- [7] M. Bi, P. Tran, L. Xia, G. Ma, Y. M. Xie, "Topology optimization for 3D concrete printing with various

- manufacturing constraints,” *Additive Manufacturing*, vol. 57, pp. 102982, 2022.
- [8] A. L. R. Prathyusha, G. R. Babu, “A review on additive manufacturing and topology optimization process for weight reduction studies in various industrial applications,” *Materials Today: Proceedings*, vol. 62, pp. 109-117, 2022.
- [9] H. Wang, Y. Wan, Q. Li, Y. Xia, X. Liu, Z. Liu, X. Li, “Porous fusion cage design via integrated global-local topology optimization and biomechanical analysis of performance,” *Journal of the Mechanical Behavior of Biomedical Materials*, vol. 112, pp. 103982, 2020.
- [10] N. Li, Y. Zhang, Q. Tang, H. Wang, D. He, Y. Yao, Y. Fan, “Porous interbody fusion cage design via topology optimization and biomechanical performance analysis,” *Computer Methods in Biomechanics and Biomedical Engineering*, vol. 26, no. 6, pp. 650-659, 2023.
- [11] Z. C. Zhong, S. H. Wei, J. P. Wang, C. K. Feng, C. S. Chen, C. H. Yu, “Finite element analysis of the lumbar spine with a new cage using a topology optimization method,” *Medical Engineering & Physics*, vol. 28, no. 1, pp. 90-98, 2006.
- [12] A. Tovar, S. E. Gano, J. J. Mason, J. E. Renaud, “Optimum design of an interbody implant for lumbar spine fixation”, *Advances in Engineering Software*, vol. 36, no. 9, pp. 634-642, 2005.
- [13] H. G. Chuah, I. A. Rahim, M. I. Yusof, “Topology optimisation of spinal interbody cage for reducing stress shielding effect”. *Computer methods in biomechanics and biomedical engineering*, vol. 13, no. 3, pp. 319-326, 2010.
- [14] S. J. Kim, Y. S. Lee, Y. B. Kim, S. W. Park, V. T. Hung, “Clinical and radiological outcomes of a new cage for direct lateral lumbar interbody fusion,” *Korean Journal of Spine*, vol. 11, no. 3, pp. 145, 2014.
- [15] A. Warburton, S. J. Girdler, C. M. Mikhail, A. Ahn, S.K. Cho, “Biomaterials in spinal implants: a review,” *Neurospine*, vol. 17, no. 1, pp. 101, 2020.
- [16] L. S. Chatham, V. V. Patel, C. M. Yakacki, R. Dana Carpenter, “Interbody spacer material properties and design conformity for reducing subsidence during lumbar interbody fusion,” *Journal of biomechanical engineering*, vol. 139, no.5, pp.1-7, 2017.
- [17] J. Ma, Y. He, Z. L. Zhao, Y. M. Xie, “Topology optimization of ribbed slabs and shells,” *Engineering Structures*, vol. 277, pp. 115454, 2023.
- [18] J. Y. Zheng, M. W. Fu, F. Zeng, “Design and Development of Multi-Scaled Metallic Parts and Structures”, 2022.
- [19] Q. Wang, “Simulations of the bending rigidity of graphene,” *Physics Letters A*, vol. 374, no. 9, pp. 1180-1183, 2010.
- [20] R. Srinivasan, W. Ruban, A. Deepanraj, R. Bhuvanesh, T. Bhuvanesh, “Effect on infill density on mechanical properties of PETG part fabricated by fused deposition modelling,” *Materials Today: Proceedings*, vol. 27, pp. 1838-1842, 2020.
- [21] E. Gültekin, M. A. Yahşi, “A Study About Shape and Topology Optimizations on A Connecting Rod,”

International Journal of Automotive  
Science And Technology, 5(2), 141-  
146, 2021.



SAKARYA ÜNİVERSİTESİ

# FEN BİLİMLERİ ENSTİTÜSÜ DERGİSİ

Sakarya University Journal of Science  
SAUJS

ISSN 1301-4048 | e-ISSN 2147-835X | Period Bimonthly | Founded: 1997 | Publisher Sakarya University |  
<http://www.saujs.sakarya.edu.tr/>

Title: The Influence of Building Form Compactness on Energy Efficiency in Accommodation Structures: The Case of Türkiye

Authors: Özlem KAHRAMAN, Erdem KÖYMEN

Received: 2023-02-19 00:00:00

Accepted: 13.07.2023

Article Type: Research Article

Volume: 27

Issue: 5

Month: October

Year: 2023

Pages: 1055-1078

How to cite

Özlem KAHRAMAN, Erdem KÖYMEN; (2023), The Influence of Building Form Compactness on Energy Efficiency in Accommodation Structures: The Case of Türkiye. Sakarya University Journal of Science, 27(5), 1055-1078, DOI: 10.16984/saufenbilder.1253136

Access link

<https://dergipark.org.tr/tr/journal/1115/issue/80257/1253136>

New submission to SAUJS

<http://dergipark.gov.tr/journal/1115/submission/start>



## The Influence of Building Form Compactness on Energy Efficiency in Accommodation Structures: The Case of Türkiye

Özlem KAHRAMAN<sup>\*1</sup> , Erdem KÖYMEN<sup>1</sup> 

### Abstract

Based on the information found in the literature, which suggests that "more compact forms closer to squares are preferred in building designs in cold climate regions," this study investigates to what extent the existing theoretical knowledge of compactness is practically followed in the shaping of winter tourism accommodation structures and how the differences in building form based on regions affect the amount of energy consumption. Cold climate region structures were preferred because compactness is more comparable in terms of form and provides a constraining plane. In this study, 50 accommodation structures in different regions that are most preferred for winter tourism were evaluated based on compactness. The existing and compact projections of the selected structures were measured, and then these plan projections were superimposed to obtain compactness ratios. Additionally, the structures were 3D modeled in both the existing and compact forms, and the energy consumption amounts for both forms were measured using the "Energy Plus" energy simulation engine with the assistance of the "Ladybug" plugin, which operates in the Rhinoceros3D/Grasshopper3D environment. Furthermore, data such as the facade opening ratio, main facade direction, and number of floors were determined and compiled into a table. As a result, it was found that increasing the surface area significantly affects the compactness ratio in accommodation structures with relatively small floor areas. There is a linear relationship between the increase in floor area and the number of floors. It was determined that there is no specialized building form or main facade direction for any region. In regional evaluations, it was observed that the difference in projection is low in regions where the difference in energy consumption between the existing and compact forms is also low.

**Keywords:** Accommodation structures, compactness, energy-efficient, winter tourism

### 1. INTRODUCTION

Since the Industrial Revolution, the need for energy has been steadily increasing [1]. This situation is significant not only for all fields but also for the discipline of architecture, and

the increasing number of studies on the effective use of energy demonstrates this.

Energy-efficient design aims to ensure that a building consumes energy in the least amount and most beneficial way by utilizing physical

\* Corresponding author: ozlem.kahraman@std.izu.edu.tr (Özlem KAHRAMAN)

<sup>1</sup> Istanbul Sabahattin Zaim University, İstanbul, Türkiye

E-mail: erdemkoymen@yahoo.com

ORCID: <https://orcid.org/0000-0002-6874-6779>, <https://orcid.org/0000-0002-6924-421X>



environment and climate data [2]. Achieving energy efficiency in buildings occurs in two stages. The first stage can be achieved during the design phase, known as passive systems, by evaluating factors such as topography and orientation. The second stage generally involves incorporating mechanical and technologically adaptable system elements into the building materials and facades [3]. The literature review reveals that energy efficiency is predominantly approached within this second scope.

Research has highlighted the necessity of diversifying building forms based on climatic regions and emphasized the context of thermal effects in exploring the architectural expression of buildings [4]. In cool regions, where temperatures are lower, the principle of elongating structures in the East-West direction to mitigate the effects of the sun is challenged, thereby necessitating the creation of forms closer to squares. The upper limit in this context is a "rectangular" shape determined based on the East-West direction and climate, while the lower limit is a "square" shape [5]. Additionally, research conducted by Lütfü Zeren suggests an optimum ratio of 1:1.2 for building form parameters in cold climate regions [6]. Architect Richard L. Crowther has also recommended enclosed compact forms for structures in cold climate regions [7]. In hot climate regions, courtyard building forms are commonly observed, with the aim of providing natural ventilation and creating circulation spaces to maintain a cool environment and enhance indoor air quality [8]. Therefore, building form is an important factor that influences energy consumption and determines the level of utilization of the physical environment. In this regard, the analysis of these environmental effects becomes crucial during the process of determining the form. As seen in the shared literature, experts suggest that architectural forms should be kept as compact as possible, approaching basic rectangular shapes, to minimize heat loss.

Compactness in architectural design is one of the powerful tools that can be used for energy-efficient building design due to its impact on understanding and managing the process of form-space formation. With this feature, compactness can complement the evaluation of the thermal resistance of building components in order to control heat loss and gain in the architectural design process. In architectural design, compactness defines the degree of merging and connecting building areas. Although compactness in architectural design has not been studied as an independent subject, many researchers have addressed the impact of compactness factor when examining environmental design or conducting cost analysis of energy consumption, and have concluded that the external envelope of a building changes according to the building's shape and a compact building has a minimum perimeter and a maximum floor area [9]. Various studies related to the scope of research topics and their correlations with the field have been summarized below, providing motivation for this study.

In Demir's study, the aim was to create a database to contribute to the formation of qualified architectural groups in a mountainous environment where winter tourism takes place. The Tekir Plateau in Mount Erciyes was chosen as the application area. All the necessary criteria for design, from the organization of buildings to environmental factors, from the plan scheme to the building form, were determined to create a basic handbook [10].

In Kun's study, a comparison was made regarding the cooling loads of hotel buildings based on predetermined plan typologies in the case of Kuşadası. Using the Ecotect program, the 7 predetermined plan typologies were ranked from most efficient to least efficient. Thus, a recommendation is provided for future hotel buildings in Kuşadası [11].

In Demirtaş's study, which aimed to find the most efficient building form for five pilot

cities selected from different climatic regions of Türkiye, an analysis was conducted based on eight preferred plan types for hotel buildings, including courtyard and courtyardless designs. The Designbuilder program was used to calculate heating and cooling loads. As a result, it was determined that the courtyardless square form yielded the lowest heating and cooling loads for Ankara, Istanbul, and Erzurum, while the double-oriented staggered form was found to be the most efficient for Antalya and Diyarbakır [12].

D'Amico and Pomponi investigated the relationship between surface area and interior space to address the sustainability of building forms. Firstly, an optimal form was obtained, and then, since a single specific form is of limited practical use, a scale-independent metric was developed to measure the optimality degree of building forms and demonstrate their practical application. This new metric system, which is expected to be highly beneficial in the early design stage, allows for measuring how far a building form deviates from optimality and generating the closest alternative geometries [13].

Başaran's study focused on reducing heating loads and determining the optimal architectural forms that provide the highest solar gains specific to the climatic region. Ankara was chosen as the study area. By conducting solar radiation analysis using the Designbuilder program, shape revisions were made based on prime geometric forms and organic forms. The results showed that curved organic forms shaped by tracking the movement axis of the sun horizontally and the angle between the sun and the earth vertically resulted in higher solar energy gains [14].

In the studies of Karadağ and Keskin; The performance and adequacy of the Radiance simulation engine integrated into DaylightX were measured for daylight optimization during the early design phase. Although the Radiance simulation engine is the most widely used and approved simulation engine,

it has been integrated with DaylightX due to the difficulty of processing input parameters. Simulation experiments were carried out on a selected container house in the California sample, and a modeling and workflow prototype was developed [15]. In the studies of Karadağ and Serteser; has developed a particle-based algorithm in which the flow properties of the air to be taken into the building can be evaluated in the early design phase. The functionality of this algorithm has been tested on three commonly seen natural ventilation conditions. While the features such as real-time operation and non-relativism of the algorithm produced as a result of the studies highlight the algorithm, it is stated that it has a guiding argument that can be used in the early design phase [16]. The software techniques used in these two studies were found to be remarkable in terms of directing and expanding the research within the scope of the article.

### **1.1. Limitation & Assumption in The Case Study**

The concept of "compactness," which is a geometric sub-concept related to building form, is an important parameter in terms of heat loss and gain of buildings and forms the main motivation of this research. The study investigates the adherence to theoretical knowledge of compactness in the formation of winter tourism accommodation structures and the differences in building forms that arise according to regions.

This study is limited to examining the compactness of 50 accommodation structures located in the cold climate zones of different climatic regions in Türkiye's prominent ski resorts, in relation to their energy consumption. Initially, the projection of the 50 structures were extracted, and their areas and main facade orientations were calculated. Then, based on the number of floors of these structures, estimated 3D models were created, and openings in the form of transparency were added to the 3D models as estimations. Subsequently, "compact plan projection"

were drawn based on the projection of each structure. The same process was repeated based on these new plan projection, and 3D models representing the most compact forms of the structures were obtained.

Then, openings were added to these compact 3D models again, matching the amount of openings in the existing forms. Finally, annual heating and cooling energy consumption analyses were conducted based on the obtained existing and compact 3D models, considering thermal comfort. Factors such as building elements, material properties, and heating/cooling system settings were assumed to be equal for better understanding of the compactness ratio of the buildings.

The energy model used in the analysis was built in the Rhinoceros3D/Grasshopper3D environment using the "Energy Plus" energy simulation engine and the "Ladybug" plugin. It was assumed that each structure in the analysis used the same mechanical HVAC system. Although the structures were located in different climatic regions, they were considered to be in their local "cold climate" extremes.

## 2. WINTER TOURISM IN TÜRKİYE

With the changing perception of vacations in recent years, alternative tourism activities have come to the forefront, and winter tourism, in particular, has gained significant interest. Winter tourism, also known as mountain tourism in the literature, is seen as an important tourism type for the development of mountainous areas, regional development, and achieving balance between regions. It is also important in terms of sustainability, minimizing harm to natural assets, and contributing to economic and social aspects [17]. Conceptually, winter tourism focuses primarily on winter sports, mainly skiing, and involves accommodation and other services provided in snowy and mountainous regions, depending on suitable slope, aspect, and geographical conditions [18].

Winter tourism has economic, social, and various other advantages. Firstly, the investments in infrastructure and facilities contribute to the development of the region. Thus, both during the construction phase and in the service process, employment opportunities are created for the local population. Extending the tourism season throughout the year contributes to the economy of the region and the country as a whole. The disadvantages arising from the climate can be turned into advantages. Additionally, it provides a unique experience for those seeking a different vacation alternative and adventure enthusiasts [17].

Türkiye, a significant portion of which is composed of mountainous areas within the Alp-Himalaya mountain system, has a great potential for winter tourism. Winter tourism in Türkiye first began in the 1930s in Uludağ. With the interest of local residents and tourists from Istanbul, many hotels and ski lodges were opened. Subsequently, centers such as Elmadağ, Erciyes, Sarıkamış, and Palandöken became operational. This new understanding of tourism led to the enactment of incentive laws and the preparation of master plans [18].

According to data from the Ministry of Culture and Tourism, there are 29 ski resorts in Türkiye. Of these, 9 are operational (Davraz, Erciyes, Ilgaz, Kartalkaya, Kartepe, Palandölen, Sarıkamış, Uludağ, Yıldız Dağı), 7 are semi-operational (Yıldıztepe, Uğurludağ, Kop Dağı, Zigana, Ergan, Bozdağ, Ladik), and the rest are centers that are not yet operational [19, 20]. The most popular ski resorts in terms of demand are Uludağ, Kartalkaya, Erciyes, Sarıkamış, Kartepe, Palandöken, and Ilgaz [21].

The current bed capacity in Türkiye is 11,459, while the target is 80,175. When looking at the provinces, Erzurum ranks first with a capacity of 2,466 beds, followed by Bursa with 2,250 beds, Bolu with 1,713 beds, and Kayseri with 1,072 beds [19]. When examining the participation demand for

winter tourism, it is known that 20% of visits are for day trips, while the remaining 80% prefer accommodation-based vacations. Winter sports enthusiasts constitute 75% of the visitors, while the domestic profile consists mainly of singles and families with children [22].

### **2.1. Winter Tourism Accommodation Buildings**

Winter tourism facilities multiple functions within their structures. Social and sports facilities include clubs where winter sports training courses are offered and various events are organized. Mechanical facilities consist of technical infrastructure units related to winter sports, such as chairlifts, gondolas, ski lifts, cable cars, mountain trains, and baby lifts. These are followed by recreational facilities such as ski areas, accommodation and service facilities, day-use facilities, golf courses, polo fields, bowling alleys, paragliding sites, ice skating rinks, and more. Among these units, mechanical facilities and accommodation facilities are the most important. In mechanical facilities, the main goal is to ensure that sports activities are carried out smoothly and efficiently, while in accommodation facilities, the aim is to provide a comfortable stay for domestic and foreign visitors in units where they will temporarily reside. Accommodation facilities for winter tourism and winter sports include hotels, motels, holiday villages, guesthouses, timeshare properties, and apartment hotels, offering visitors a variety of options [10].

### **2.2. Form in Winter Tourism Buildings**

Building form can be defined by geometric variables such as shape factor (ratio of building facade depth), building height, roof type (flat, gable, hipped), floor type (ground-bearing floor, open underside floor), roof pitch, and facade inclination [14]. The architectural form should be designed in a way that carries aesthetic value visually and contributes to sustainability.

In architectural design, form is one of the most influential factors in the energy performance of a structure. Therefore, the primary objective in sustainable building design is to create a building envelope that can maintain optimum levels of heat gain [23]. Decisions should be made in the design phase considering factors directly related to the building, such as climatic conditions, wind direction/intensity, and maximum utilization time from the sun. In this context, design decisions can help alleviate heating loads, especially in high mountainous areas with winter tourism and winter sports where snow cover is intense. The wind, which is effective for more than half of the year in cold climate regions, causes heat losses [24].

Therefore, consideration of wind directions should be taken into account during the form-making process. Another important criterion is to maximize the utilization of sunlight. Depending on local climate conditions, in Türkiye, south-facing slopes receive more sunlight during winter, so a design can be envisaged along the south axis in linear building configurations [10].

Compactness is one of the most important factors in terms of the building's heat loss and gain. When the surface area is increased while keeping the volume constant, compactness decreases, and the amount of heat lost from the surface areas increases. Protrusions, recesses, or fragmentation in the floor plan can cause unnecessary expansion of the building and an increase in surface area, which negatively affects compactness. Therefore, compact building forms should be preferred for energy conservation in cold climate regions [25]. In terms of internal heat preservation, the most efficient building form is a square with a small surface area and a large interior volume. Therefore, it is more appropriate to design winter tourism accommodation facilities in the form of individual houses or adjacent buildings in a back-to-back arrangement [10]. For L, T, H, and U-shaped building forms, it has been determined that the most appropriate

orientations are Southeast-Northwest or Northeast-Southwest [26].

Winter tourism facilities are exposed to heavy snowfall and wind accumulation, so the roof pitches should be steep, and materials that prevent snow accumulation should be chosen. The facility structures should be constructed close to each other. In accommodation units, designs such as courtyards, backyards, canopies, and overhangs should be implemented to protect visitors from rain and snow [10].

### **3. ANALYSIS OF ACCMODATION STRUCTURES IN TURKISH WINTER TOURISM IN THE CONTEXT OF “COMPACTNESS”**

The main motivation of the study is to investigate the impact of compactness on the energy efficiency of tourism-oriented accommodation building forms in cold climate regions in Türkiye. Additionally, the study aims to explore how the parameters of these buildings, based on the obtained mathematical data, statistically affect each other in different regions.

Within the scope of the study, accommodation structures located in various regions of Türkiye such as Palandöken, Erciyes, Sarıkamış, Kartalkaya, Kartepe, Ilgaz, Uludağ, and Davraz, which are popular ski resorts, were selected, and these structures were analyzed in terms of form and energy consumption within the context of compactness. Fifty prominent accommodation buildings in the selected resorts were first transformed into their most basic forms based on the plan projection. Subsequently, measurements of compact projection were conducted by comparing the existing plan projection with the obtained compact projection, leading to a compactness

percentage. While producing the plan projections, compactness measurements were conducted for both the ground floor and typical floor plans in cases where there was a difference between them.

However, compactness measurements were not conducted for building sections that were added to the ground floor after the original version of the structure. Roof slopes and attic floor plans were disregarded in these measurements. Afterwards, based on the generated plan projections, both the existing and compact forms of the buildings were 3D modeled with similar volumes. The purpose of this modeling process was to obtain a substrate that allows for more realistic measurements and energy simulations based on the building forms. In order to achieve accurate results in the analysis, the opaque and transparent surfaces of the buildings were considered and added to the building models, resembling their approximate proportions.

As a result, very close transparency ratios were achieved for both the normal and compact forms of the buildings. Finally, the superimposed plan drawings, opening ratios, orientation calculations, and images of the existing and compact forms, as summarized in this section, were transferred to a table.

#### **3.1. Energy Model and Energy Input Parameters**

A total of 100 building models were obtained in the Rhino/Grasshopper3D environment, and an extension was developed for processing the models. With the developed extension, a system was created where the "Energy Plus" energy simulation engine could measure energy consumption quantities with the help of the "Ladybug" plugin (Figure 1).

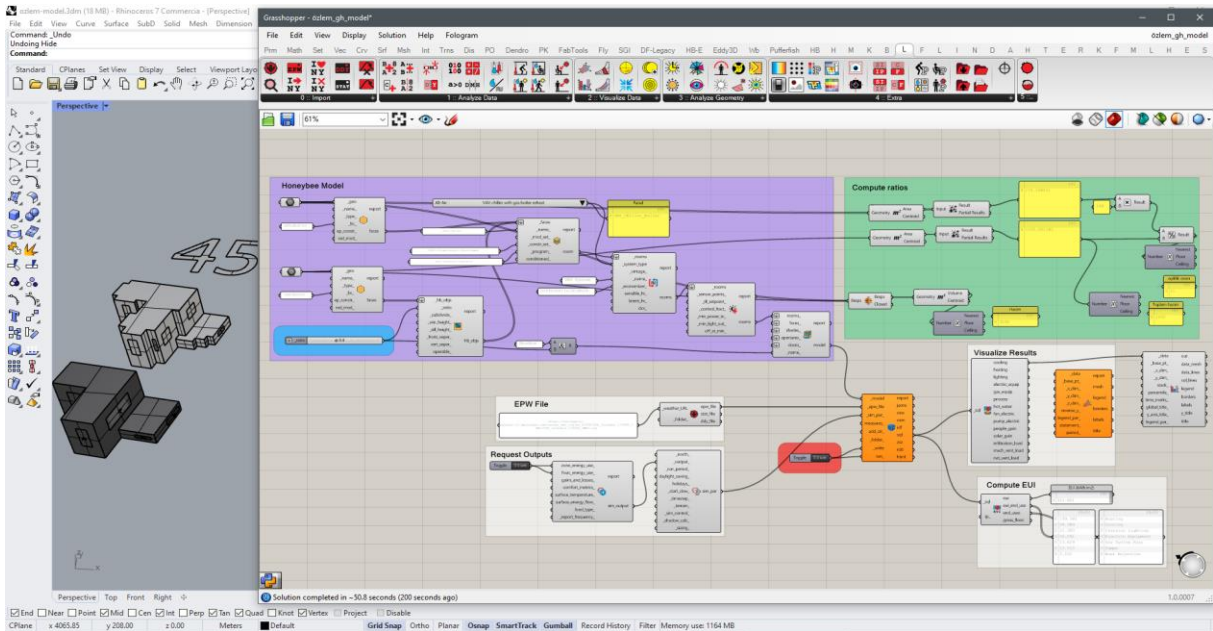


Figure 1 The model constructed in the Grasshopper3D environment for the analysis of building energy consumption quantities

In the developed extension in Grasshopper, various input parameters have been defined to convert form-based 3D models into input data

and to incorporate climatic and structural variables into the system.

Table 1 Layering of the structural components used in the models

Structural Components	Material	Thermal Conductivity {W/m-K}	Specific Heat {J/kg-K}	Density {kg/m <sup>3</sup> }	Thickness {m}	r {m <sup>2</sup> -K/W}	U {W/m <sup>2</sup> -K}
Exterior Walls	25mm Plaster						
	15mm Gypsum Board® Typical	0.159	1089	800	0.0159		
	Insulation-R19					3.346	
	15mm Gypsum Board®	0.159	1089	800	0.0159		<b>0.267</b>
Interior Floor	Interior Floor Typical					0.704	
	Insulation-R4					0.216	
	Concrete Floor Typical Carpet Pad	2.308	831	2322	0.203		<b>0.852</b>
Roof	Roof Gypsum Board Insulation-R47	0.159	1089	800	0.0159	8.277	<b>0.117</b>
Windows	Windows Low E. Glass Air Glass	0.899			0.006		
		0.899			0.0127		<b>1.784</b>

The intended structural characteristics for the building models used in the analysis are provided in Table 1. Since the specific structural properties of each building were not determined, average values were defined for each structural feature. For the model, the total thermal transmittance (U-value) of the external wall layer was taken as 0.267 W/m<sup>2</sup>-

K, the internal floor as 0.852 W/m<sup>2</sup>-K, the roof as 0.117 W/m<sup>2</sup>-K, and the windows as 1.784 W/m<sup>2</sup>-K. The analysis utilized data specific to cold climate regions. Additionally, it was assumed that each analyzed building had mechanical HVAC systems using “VAV (Variable air Volume) chiller gas boiler reheat.”

Subsequently, the visuals of the buildings, their respective locations, number of floors, superimposed drawings of the existing and compact floor plans, area measurements/ratios derived from these drawings, energy consumption quantities for both forms of the buildings, ratios of opaque/transparent surfaces, volumes included in the energy consumption analysis, and deviations of the main facades from the north direction were compiled in a table (Table 2). This allowed for the creation of a

comprehensive database where all the data could be tracked. The obtained data was then interpreted in the context of "compactness

### 3.2. Energy Simulation Results and Energy Analyses

The results of the energy consumption analysis conducted on the existing and compact forms of the structures included in the study have been added to Table 2.

Table 2 (Continue). Data and analysis results for selected accommodation structures



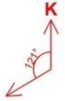











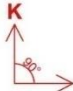



Visual representation and name of the structure	Location	Number of Floor	Overlapping floor plan diagram	Measurements (m)	Energy consumption (kWh/m <sup>2</sup> )	Ratios(%)	Main Facade Direction
	Eastern Anatolia Region	Ground floor +5		Compact Projection 47.43	Compact 181.763	Compactness Ratio %81.41	
				Existing Projection 58.26	Existing 188.71	Facade Opening Ratio %16	
	Eastern Anatolia Region	Ground floor +5		Compact Projection 198.35	Compact 311.773	Compactness ratio %83.62	
				Existing Projection 237.2	Existing 338.902	Facade Opening Ratio %9	
	Eastern Anatolia Region	Ground floor +4		Compact Projection 106.61	Compact 279.347	Compactness ratio %100	
				Existing Projection 106.61	Existing 279.437	Facade Opening Ratio %12	
	Eastern Anatolia Region	Ground floor +8		Compact Projection 271.11	Compact 316.989	Compactness ratio %86.19	
				Existing Projection 314.52	Existing 357.094	Facade Opening Ratio %8	
	Eastern Anatolia Region	Ground floor +6		Compact Projection 77.16	Compact 639.912	Compactness ratio %77.22	
				Existing Projection 99.92	Existing 680.975	Facade Opening Ratio %15	
	Eastern Anatolia Region	Ground floor +4		Compact Projection 129.71	Compact 623.585	Compactness ratio %87.60	
				Existing Projection 148.07	Existing 638.462	Facade Opening Ratio %14	
		Ground floor +4	Compact Projection 105.84	Compact 413.836	Compactness ratio %71.05		



Table 2 (Continue). Data and analysis results for selected accommodation structures


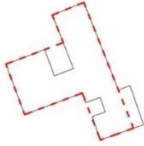


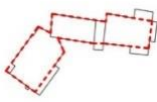


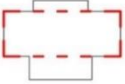


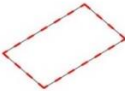


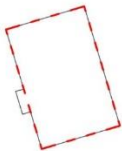


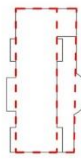


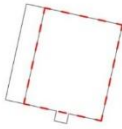


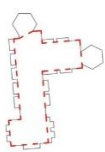

Visual representation and name of the structure	Location	Number of Floor	Overlapping floor plan diagram	Measurements (m)	Energy consumption (kWh/m <sup>2</sup> )	Ratios(%)	Main Facade Direction
 <p>7. Snowdora Ski Resort Hotel</p>				Existing Projection 148.95	Existing 476.398	Facade Opening Ratio %11	
 <p>8. Dedeman Palandöken Hotel</p>	Eastern Anatolia Region	Ground floor +6		Compact Projection 157.32 Existing Projection 222.97	Compact 465.081 Existing 483.856	Compactness ratio %70.55 Facade Opening Ratio %11	
 <p>9. Ve Hotels Palandöken</p>	Eastern Anatolia Region	Ground floor +4		Compact Projection 41.08 Existing Projection 64.63	Compact 523.845 Existing 576.316	Compactness ratio %63.56 Facade Opening Ratio %12	
 <p>10. Library Hotels Erciyes</p>	Central Anatolia Region	Ground floor +2		Compact Projection 57.50 Existing Projection 57.50	Compact 328.604 Existing 328.604	Compactness ratio %100 Facade Opening Ratio %14	
 <p>11. Mirada Del Monte Hotel</p>	Central Anatolia Region	Ground floor +2		Compact Projection 60.28 Existing Projection 66.24	Compact 295.385 Existing 302.615	Compactness ratio %91 Facade Opening Ratio %16	
 <p>12. Grand Eras Erciyes Hotel</p>	Central Anatolia Region	Ground floor +5		Compact Projection 129.90 Existing Projection 174.11	Compact 333.316 Existing 342.125	Compactness ratio %74.60 Facade Opening Ratio %9	
 <p>13. Zümrüt Palas Hotel</p>	Central Anatolia Region	Ground floor +4		Compact Projection 56.49 Existing Projection 83.90	Compact 430.613 Existing 475.178	Compactness ratio %67.33 Facade Opening Ratio %12	
 <p>14. Mirada Del Logo Hotel</p>	Central Anatolia Region	Ground floor +3		Compact Projection 70.10 Existing Projection 151.71	Compact 613.81 Existing 656.859	Compactness ratio %46.20 Facade Opening Ratio %12	
<p>15. Ace Kite Hotel</p>	Central Anatolia Region	Ground floor +3		Compact Projection 46.83	Compact 467.413	Compactness ratio %100	

Table 2 (Continue). Data and analysis results for selected accommodation structures



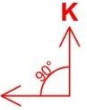

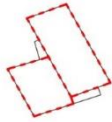


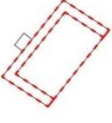


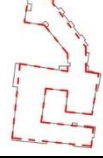
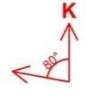

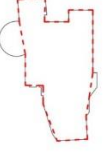
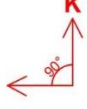

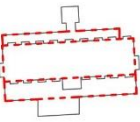


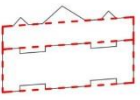


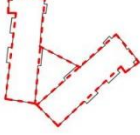


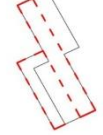
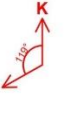
Visual representation and name of the structure	Location	Number of Floor	Overlapping floor plan diagram	Measurements (m)	Energy consumption (kWh/m <sup>2</sup> )	Ratios(%)	Main Facade Direction
				Existing Projection 46.83	Existing 467.413	Facade Opening Ratio % 15	
16. Erciyes Hill Hotel 	Central Anatolia Region	Ground floor +4		Compact Projection 113.76 Existing Projection 130.54	Compact 261.099 Existing 319.639	Compactness ratio %87.14 Facade Opening Ratio % 13	
17. X Mountain Lodge Hotel 	Central Anatolia Region	Ground floor +3		Compact Projection 153.86 Existing Projection 163.66	Compact 278.654 Existing 280.558	Compactness ratio %94.01 Facade Opening Ratio % 10	
18. Ağaoğlu My Mountain Hotel 	Marmara Region	Ground floor +8		Compact Projection 143.05 Existing Projection 203.61	Compact 1110.206 Existing 1134.575	Compactness ratio %70.25 Facade Opening Ratio % 14	
19. BOF Hotels Uludağ Ski&Resort 	Marmara Region	Ground floor +8		Compact Projection 96.71 Existing Projection 123.74	Compact 722.444 Existing 725.338	Compactness ratio %78.15 Facade Opening Ratio % 15	
20. Kaya Uludağ Hotel 	Marmara Region	Ground floor +3		Compact Projection 101.07 Existing Projection 217.93	Compact 241.681 Existing 337.928	Compactness ratio %46.37 Facade Opening Ratio % 6	
21. Karinna Hotel 	Marmara Region	Ground floor + 10		Compact Projection 119.99 Existing Projection 152.25	Compact 333.37 Existing 458.909	Compactness ratio %78.81 Facade Opening Ratio % 14	
22. Monte Baia Hotel 	Marmara Region	Ground floor +4		Compact Projection 176.92 Existing Projection 220.22	Compact 450.323 Existing 469.974	Compactness ratio %80.33 Facade Opening Ratio % 13	
23. Jura Hotels Kervansaray 	Marmara Region	Ground floor +5		Compact Projection 89.81 Existing Projection 121.55	Compact 665.615 Existing 756.642	Compactness ratio %73.88 Facade Opening Ratio % 15	
24. Trendlife Hotel	Marmara Region	Ground floor +5		Compact Projection 69.33	Compact 551.762	Compactness ratio %100	

Table 2 (Continue). Data and analysis results for selected accommodation structures



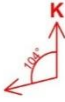

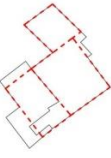


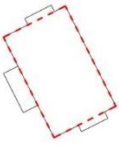


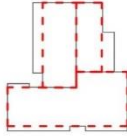





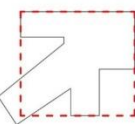





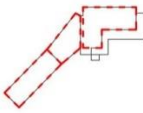

Visual representation and name of the structure	Location	Number of Floor	Overlapping floor plan diagram	Measurements (m)	Energy consumption (kWh/m <sup>2</sup> )	Ratios(%)	Main Facade Direction
				Existing Projection 69.33	Existing 591.923	Facade Opening Ratio %6	
25. Grand Yazıcı Hotel 	Marmara Region	Ground floor +7		Compact Projection 158.45 Existing Projection 237.98	Compact 496.9 Existing 555.941	Compactness ratio %66.58 Facade Opening Ratio %12	
26. Beceren Hotel 	Marmara Region	Ground floor +5		Compact Projection 89.54 Existing Projection 129.91	Compact 388.206 Existing 389.482	Compactness ratio %68.92 Facade Opening Ratio %12	
27. Fahri Hotel 	Marmara Region	Ground floor +5		Compact Projection 117.47 Existing Projection 172.10	Compact 421.646 Existing 450.186	Compactness ratio %68.25 Facade Opening Ratio %9	
28. Kaya Palazzo Ski&Mountain Resort 	West Blacksea Region	Ground floor + 10		Compact Projection 73.96 Existing Projection 73.96	Compact 882.768 Existing 888.527	Compactness ratio %100 Facade Opening Ratio %19	
29. Golden Key Hotel 	West Blacksea Region	Ground floor +3		Compact Projection 93.33 Existing Projection 121.71	Compact 271.945 Existing 388.315	Compactness ratio %77.22 Facade Opening Ratio %10	
30. Dorukkaya Ski&Mountain Resort 	West Blacksea Region	Ground floor +6		Compact Projection 212.45 Existing Projection 253.80	Compact 421.603 Existing 460.59	Compactness ratio %83.70 Facade Opening Ratio %12	
31. Kartal Otel 	West Blacksea Region	Ground floor +5		Compact Projection 110.34 Existing Projection 145.76	Compact 543.98 Existing 631.294	Compactness ratio %75.69 Facade Opening Ratio %14	

Table 2 (Continue). Data and analysis results for selected accommodation structures


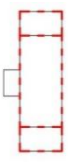


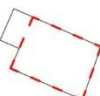
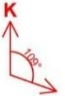

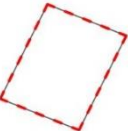


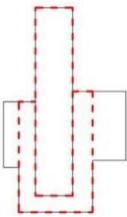
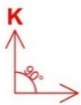




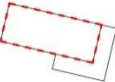


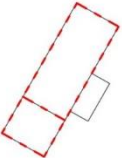


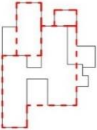


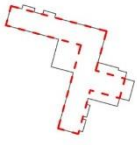


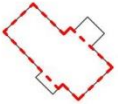


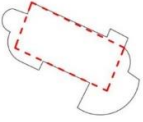

Visual representation and name of the structure	Location	Number of Floor	Overlapping floor plan diagram	Measurements (m)	Energy consumption (kWh/m <sup>2</sup> )	Ratios(%)	Main Facade Direction
 <p>32. Grand Kartal Hotel</p>	West Blacksea Region	Ground floor + 11		Compact Projection 91.85 Existing Projection 103.86	Compact 532.812 Existing 618.875	Compactness ratio %88.43 Facade Opening Ratio %18	
 <p>33. Kaya Palazzo Luxury Chalet</p>	West Blacksea Region	Ground floor +1		Compact Projection 33.45 Existing Projection 43.04	Compact 354.339 Existing 376.117	Compactness ratio %77.71 Facade Opening Ratio %9	
 <p>34. Kartaltepe Boutique Hotel</p>	West Blacksea Region	Ground floor +2		Compact Projection 58.46 Existing Projection 58.46	Compact 319.998 Existing 319.998	Compactness ratio %100 Facade Opening Ratio %10	
 <p>35. The Green Park Kartepe Resort&amp;Spa</p>	Marmara Region	Ground floor + 11		Compact Projection 157.07 Existing Projection 205.36	Compact 395.485 Existing 452.389	Compactness ratio %76.48 Facade Opening Ratio %13	
 <p>36. Ferko Ilgaz Mountain Hotel&amp;Resort</p>	West Blacksea Region	Ground floor +5		Compact Projection 49.99 Existing Projection 54.16	Compact 724.277 Existing 819.528	Compactness ratio %92.3 Facade Opening Ratio %15	
 <p>37. Dağbaşı Hotel</p>	West Blacksea Region	Ground floor +3		Compact Projection 63.70 Existing Projection 96.58	Compact 422.912 Existing 429.048	Compactness ratio %65.95 Facade Opening Ratio %8	
 <p>38. Ilgaz Hotel</p>	West Blacksea Region	Ground floor +5		Compact Projection 81.93 Existing Projection 97.51	Compact 393.356 Existing 465.773	Compactness ratio %84.02 Facade Opening Ratio %9	
 <p>39. Duja Chalet Ski Center</p>	Eastern Anatolia Region	Ground floor +4		Compact Projection 133.78 Existing Projection 175.20	Compact 433.733 Existing 1003.401	Compactness ratio %76.35 Facade Opening Ratio %8	
<p>40. Sarpino Mountain Hotel</p>	Eastern Anatolia Region	Ground floor +5		Compact Projection 71.39	Compact 664.385	Compactness ratio %80.66	

Table 2 (Continue). Data and analysis results for selected accommodation structures

Visual representation and name of the structure	Location	Number of Floor	Overlapping floor plan diagram	Measurements (m)	Energy consumption (kWh/m <sup>2</sup> )	Ratios(%)	Main Facade Direction
				Existing Projection 88.5	Existing 759.785	Facade Opening Ratio % 12	
41. Kayı Snow Hotel 	Eastern Anatolia Region	Ground floor +3		Compact Projection 78.21	Compact 420.865	Compactness ratio %90.27	
Existing Projection 86.64				Existing 479.11	Facade Opening Ratio % 14		
42. White Park Hotel 	Eastern Anatolia Region	Ground floor +3		Compact Projection 46.37	Compact 465.128	Compactness ratio %66.78	
Existing Projection 69.43				Existing 472.139	Facade Opening Ratio % 10		
43. Habitat Otel Sarıkamış 	Eastern Anatolia Region	Ground floor +4		Compact Projection 56.82	Compact 408.097	Compactness ratio %74.08	
Existing Projection 76.70				Existing 470.099	Facade Opening Ratio % 14		
44. Snowflake Dağ Oteli 	Eastern Anatolia Region	Ground floor +3		Compact Projection 40.16	Compact 521.12	Compactness ratio %100	
Existing Projection 40.16				Existing 521.12	Facade Opening Ratio % 15		
45. Çamkar Hotel 	Eastern Anatolia Region	Ground floor +3		Compact Projection 100.33	Compact 321.861	Compactness ratio %78.96	
Existing Projection 127.05				Existing 381.223	Facade Opening Ratio %8		
46. Efsane Group Sarıkamış Hotel 	Eastern Anatolia Region	Ground floor +2		Compact Projection 39.21	Compact 489.229	Compactness ratio %100	
Existing Projection 39.21				Existing 489.229	Facade Opening Ratio % 12		
47. Sarıkamış Kar Hotel 	Eastern Anatolia Region	Ground floor +2		Compact Projection 31.52	Compact 549.433	Compactness ratio %76.20	
Existing Projection 41.36				Existing 587.321	Facade Opening Ratio % 13		
48. Sirene Davraz Hotel	Mediterranean Region	Ground floor +4		Compact Projection 94.18	Compact 675.321	Compactness ratio %64.28	

Table 2 (Continue). Data and analysis results for selected accommodation structures

Visual representation and name of the structure	Location	Number of Floor	Overlapping floor plan diagram	Measurements (m)	Energy consumption (kWh/m <sup>2</sup> )	Ratios(%)	Main Facade Direction
				Existing Projection 146, 50	Existing 833.097	Facade Opening Ratio %13	
49. İşperia Davraz 	Mediterranean Region	Ground floor +1		Compact Projection 67.42 Existing Projection 91.34	Compact 246.039 Existing 252.489	Compactness ratio %73.81 Facade Opening Ratio %7	
50. Süleyman Demirel Üniversitesi Uygulama Oteli 	Mediterranean Region	Ground floor +4		Compact Projection 73.15 Existing Projection 127.33	Compact 424.434 Existing 430.512	Compactness ratio %57.44 Facade Opening Ratio %8	

Various assessments will be made below based on the analysis data in table 2, which presents the energy consumption quantities of the "existing" and "compact" forms for 50 structures in kWh/m<sup>2</sup>. These evaluations will be made using the ratios obtained from the projection of both forms of the structures.

Figure 2 and Figure 3 present sample graphs showcasing the analysis results of the daily and monthly heating and cooling loads for Structure 45, named "Çamkar Hotel," located in the Eastern Anatolia Region.

### 3.3. Interpreting Analysis Results Based on Regions

In this section, the results obtained from the analysis of each form of the structures are interpreted while considering their geographical locations. Special emphasis is given to the main facades and mass orientations of the structures. Additionally, regional classification is used to determine the average compactness, as well as structures with the lowest and highest compactness ratios. The structures with the highest energy consumption in both existing and compact forms, along with the widest gap between these two values, are identified. By evaluating the relationships between these data, findings are derived and conclusions are drawn.

#### Eastern Anatolia Region

In Table 2, it can be observed that the accommodation structures located in the Palandöken ski resort have a diverse range of

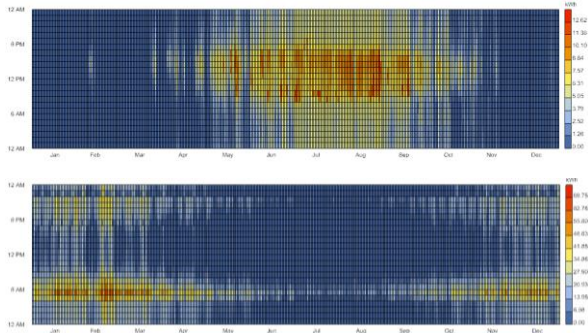


Figure 2 Hourly graph illustrating the cooling load (above) and heating load (below) for Structure 45

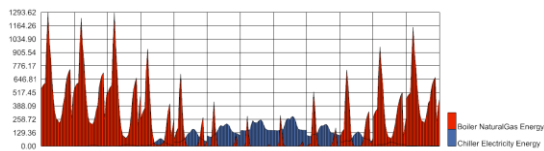


Figure 3 Monthly graph illustrating the cooling and heating loads for Structure 45

main facade orientations, including NE, N, SE, SW, E, NW, and W. The mass orientations of the structures are along the NE-SW (3), E-W (2), NW-SE (2), and N-S (2) axes. The average compactness ratio for the selected 9 sample structures is 80.13%. The lowest ratio belongs to Ve Hotels Palandöken with 63.56%. Although it appears relatively compact in the plan view, the relatively smaller size of the structure resulted in a decrease in the ratio due to the movement made in the form. The highest ratio is 100% for Dedeman Ski Lodge.

Despite having a smaller projection compared to other buildings, it is designed closest to the fundamental form, resulting in no additional surface areas that would increase heat loss and thus having the highest compactness value. Looking at the facade opening ratios, the average is 12%, with The Erzurum Hotel having the highest ratio of 16% and Polat Palandöken Hotel having the lowest ratio of 8%. The structure with the highest energy consumption in both the existing (680.975 kWh/m<sup>2</sup>) and compact (639.912 kWh/m<sup>2</sup>) forms is Palan Hotel. Based on these results, no significant relationship was found between the facade opening ratio, energy consumption, and compactness ratio. This is believed to be due to the structures not having the same volume and plan projection.

Similarly, as seen in Table 2, the hotels selected from the Sarıkamış ski resort have main facade facing the D, NE, SE, NW, N and SW directions. Just like in Palandöken, no dominant main facade orientation could be determined in this resort either. The accommodation structures are mostly positioned along the NE-SW(5) axis, followed by the NW-SE(2) and N-S(2) axes in terms of mass orientation. The average compactness ratio for the selected structures is 82.58%, with Efsane Group Sarıkamış Hotel and Snowflake Mountain Hotel having the highest compactness ratios of 100%. White Park Hotel has the lowest ratio of 66.78%. Despite having a smaller plan projection compared to other structures, the

design features introduced in the form caused a decrease in the ratio. In this regard, it is similar to the example in Palandöken.

The average facade opening ratio for the hotels selected from the Sarıkamış ski resort is 10.88%. Snowflake Mountain Hotel has the highest facade opening ratio of 15%, while Duja Chalet Ski Center and Çamkar Hotel have the lowest ratios of 8%. In terms of energy consumption, Duja Chalet Ski Center has the highest value of 1003.401 kWh/m<sup>2</sup> for the existing energy consumption, while Sarpino Mountain Hotel has the highest value of 664.385 kWh/m<sup>2</sup> for the compact energy consumption. The structure with the widest gap between the existing and compact energy consumption is Duja Chalet Ski Center with a value of 569.668 kWh/m<sup>2</sup>.

### Central Anatolia Region

According to the results derived from Table 2, the accommodation structures selected from the Erciyes ski resort generally have main facades facing the west direction, such as SW (3), W (3), and NW (2). The mass orientation is predominantly along the N-S (5), NW-SE (2), and NE-SW axes, indicating that most of the structures are volume-oriented along the north-south axis. The average compactness ratio for the 8 selected structures is 82.53%, with Mirada Del Logo Hotel having the lowest ratio of 46.2% and Ace Kite Hotel and Library Hotel having the highest ratio of 100%. Unlike the examples in Sarıkamış and Palandöken, it can be observed that the structure with a larger projection has the lowest ratio. This is believed to be due to the L-shaped form of the structure and the presence of movable facades on all sides. Mirada Del Logo Hotel, which has the lowest compactness ratio, has the highest values in both compact (613.81 kWh/m<sup>2</sup>) and existing (656.859 kWh/m<sup>2</sup>) energy consumption.

For the Central Anatolia Region, the average facade opening ratio is 12.62%. Mirada Del Monte Hotel has the highest value of 16%, while Grand Eras Erciyes Hotel has the lowest value of 9%.

## Marmara Region

Based on the deductions made from Table 2, it is determined that the hotels in Uludağ ski resort have main facades facing the directions of NW, W, N (2), SW (4), NE, and E. The building orientations are shaped along the N-S (3), NW-SE (2), NE-SW (2), and SE-NW (3) axes. The average compactness value for these selected structures is 73.15%. The highest ratio is 100% for Trendlife Hotel, while the lowest ratio is 46.37% for Kaya Uludağ Hotel. Although Kaya Uludağ Hotel has a plan projection that is close to a compact form, the surface area has been increased by incorporating indentations and protrusions. This is believed to have moved the structure away from compactness.

For this region, the average facade opening ratio is 11.6%. The lowest value of 6% is attributed to Trendlife Hotel and Kaya Uludağ Hotel, while the highest value of 15% belongs to BOF Hotels Uludağ Ski & Resort and Jura Hotels Kervansaray. The structure with the highest energy consumption in terms of both existing (1134.575 kWh/m<sup>2</sup>) and compact (1110.206 kWh/m<sup>2</sup>) is BOF Hotels Uludağ Ski & Resort. When examining the selected examples from Uludağ ski resort, no correlation is found between compactness ratio, facade opening ratio, and energy consumption quantities.

## West Blacksea Region

Based on Table 2, it can be seen that the accommodation structures in Kartaltepe ski center have main facades facing the directions of N, SW (2), SE (2), W, and E. The mass orientations are mostly shaped along the SW-NE (5) axis, followed by the N-S and SE-NW axes. The average compactness ratio of the structures is 86.10%, with the most compact hotels being Kartaltepe Boutique Hotel and Kaya Palazzo Ski & Mountain Resort with a ratio of 100%. The least compact hotel is Kartal Otel with a ratio of 75.69%. It is believed that both the basic plan geometry and later additions made to the ground floor have caused the ratio to decrease.

For this region, the average facade opening ratio is 13.12%. The highest ratio of 19% belongs to Kaya Palazzo Ski & Mountain Resort, while the lowest value of 9% is attributed to Kaya Palazzo Luxury Chalet. When examining the existing and compact energy consumption quantities, Kaya Palazzo Ski & Mountain Resort stands out with values of 888.527 kWh/m<sup>2</sup> and 882.768 kWh/m<sup>2</sup>, respectively. Despite having a compactness ratio of 100%, the high energy consumption is believed to be due to its larger volume compared to other structures because of its multi-story nature. However, once again, no correlation is found between the compactness ratio, facade opening ratio, and energy consumption quantities for the selected examples.

According to the results obtained from Table 2, the main facades in Ilgaz ski center also show diversity. The main entrances are provided from the facades facing NE, SW, and SE for the three examined examples. The average compactness ratio of the structures is quite high at 80.75%. The structure with the lowest compactness percentage is Dağbaşı Otel with a ratio of 65.95% due to the areas added later on the ground floor. The average facade opening ratio is 10.66%. In terms of energy consumption, Ferko Ilgaz Mountain Hotel & Resort has the highest values in both existing (819.528 kWh/m<sup>2</sup>) and compact (724.277 kWh/m<sup>2</sup>) consumption.

## Mediterranean Region

Table 2 provides examples of three accommodation structures in Davraz ski center. As observed in all the regions examined so far, there is no single specialized main facade orientation in this area as well. However, in terms of mass orientation, the GD-KB axis is common among all the examined structure examples. The average compactness ratio of the structures is 65.17%. This result is consistent with the preference for dynamic building forms that heavily utilize projections and recesses.



When examining the average facade opening ratio, it is found to be 9.33%, and the highest value of 13% belongs to Sirena Davraz Hotel. Further analysis of Sirena Davraz Hotel reveals that its existing energy consumption is measured at 833.097 kWh/m<sup>2</sup>, while the compact energy consumption is 675.321 kWh/m<sup>2</sup>, making it the structure with the highest values among the selected buildings in the region. When looking at the difference between the compact and existing energy consumption, Sirena Davraz Hotel also has the highest value of 157.776 kWh/m<sup>2</sup>. From this perspective, it can be said that the facade opening ratio for the examined group of structures in the region follows a proportional relationship with energy consumption.

### 3.4. General Overview Based on Analysis Findings

In this section, various analyses and the results of the corresponding investigations have been presented and interpreted with the support of graphs. All the data obtained from the energy analysis, along with other relevant data, have been processed using the statistical data processing software SPSS 26. As a result, graphs have been generated, enabling the comprehensive interpretation of all the collected data."

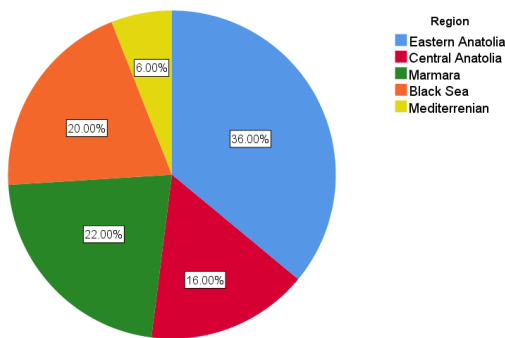


Figure 4 Graph illustrating the distribution of the included structures by regions in the research

Firstly, the research was conducted on a total of 50 winter tourism accommodation structures from 5 different geographical regions in Türkiye. Within the scope of the study, 36% of the examined structures are located in Eastern Anatolia, 16% in Central

Anatolia, 22% in Marmara, 6% in the Mediterranean, and 20% in the Black Sea region (Figure 4).

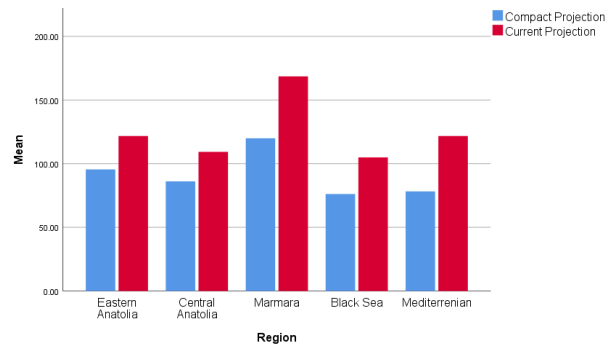


Figure 5 Average existing and compact projection ratios of structures according to regions

In Figure 5, the average existing and compact projection ratios of structures are presented together according to geographical regions. In this comparison conducted based on regions, the difference between the average existing and compact projection is highest in the Marmara Region, while it is the lowest in the Central Anatolia Region. The higher average projection in the Marmara Region indicates that structures in this region tend to have larger ground areas. Additionally, the higher average projection difference in this region can be interpreted as a preference for structures with more protrusions and recesses. The smaller projection difference in the Eastern Anatolia and Central Anatolia Regions suggests a preference for more stable forms with fewer protrusions and recesses.

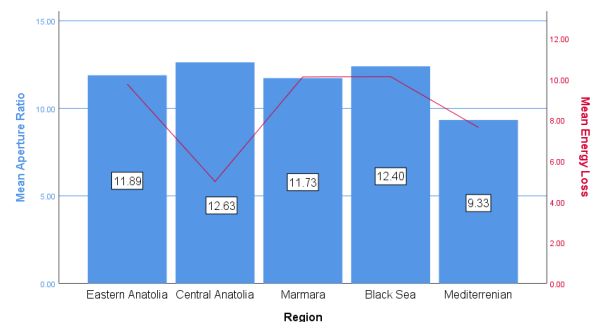


Figure 6 Illustration of the energy consumption differences between the average opacity values and the current-compact forms of the structures, categorized according to geographical regions

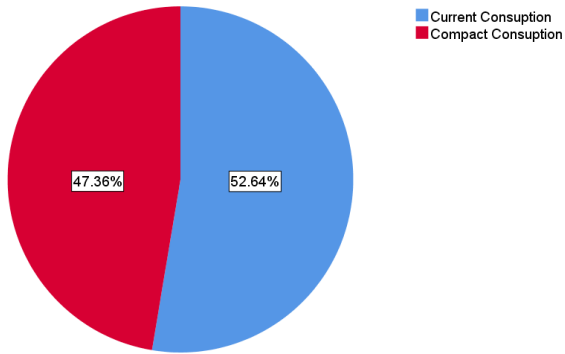


Figure 7 Graph illustrating the ratio between the average current and compact energy consumption quantities of all the structures

As can be observed in Figures 6-7, it is expected that the average quantity of normal energy consumption of all structures exceeds the average quantity of compact energy consumption. The difference between the two ratios is 5.28%. The increase or decrease of this difference can vary depending on how the compact projection are determined. In this study, the selected structures were determined to have compact projection with minimal intervention in their current forms. It is believed that the relatively small difference can be attributed to this factor.

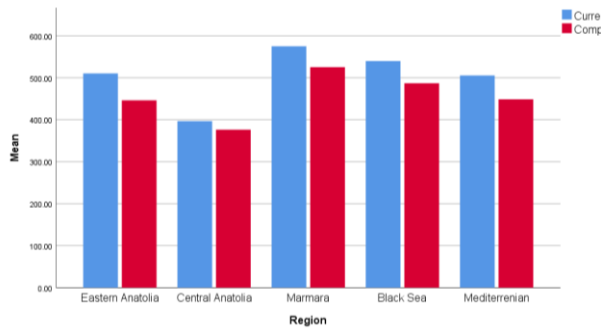


Figure 8 Clustered bar mean of current consumption and compact consumption by region

According to Figure 12, the region with the least difference between current and compact energy consumption is Inner Anatolia, while the other regions show a similar level of difference. In Figure 8, the individual representation of the energy consumption quantities of the structures, examined in terms of geographical regions in the previous graph, can be observed. When comparing the energy consumption quantities of the current and compact forms, the structure with the largest

difference is Duja Chalet Ski Center, while the structure with the smallest difference is Ace Kite Hotel. When analyzing the compactness ratios, it is noticed that Beceren Hotel has a very low value of 68.92%, and the difference between its compact and current energy consumption values is also very low. This is believed to be due to the fact that compactness ratio is not the sole factor related to energy efficiency.

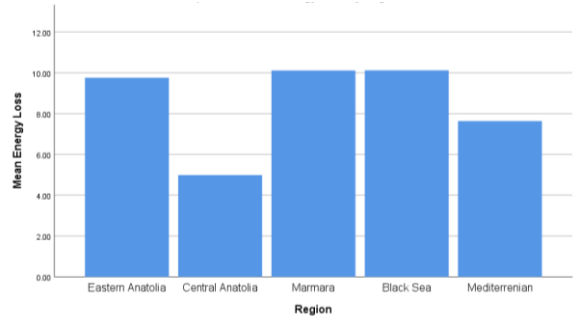


Figure 9 Energy loss percentages due to compactness factor in buildings by regions

In Figure 9, the percentages of energy loss due to the compactness factor are shown according to regions. According to this, it can be observed that the region with the least loss is Inner Anatolia with approximately 4.5%, while the highest loss is in the winter tourism accommodation structures in the Marmara and Black Sea regions. Based on these data, it can be inferred that the winter tourism accommodation structures in Inner Anatolia are designed in more compact forms compared to structures in other regions. In Marmara and Western Black Sea regions, on the other hand, it is observed that more flexible designs are preferred.

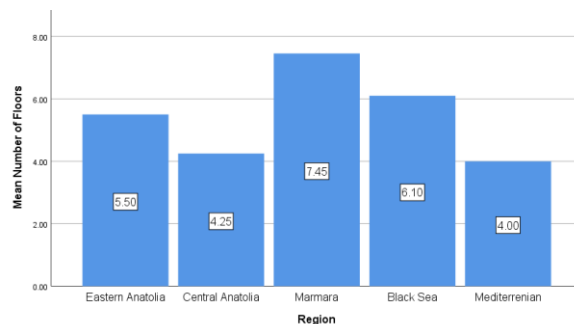


Figure 10 Table showing average number of building floors by geographical regions

As evident from Figure 10, in the evaluation based on the average number of floors, it can be observed that higher-rise structures are preferred in the Marmara Region, while lower-rise structures are preferred in the Mediterranean Region. It is known that compactness and energy efficiency are directly related to volume. Therefore, it can be said that in cold climate regions, the number of floors is kept lower to reduce the volume, while more flexible decisions are made in more temperate climate regions. In this regard, the higher average number of floors in the Marmara Region is in line with expectations.

However, it is unexpected that the average number of floors remains at the lowest level in the Mediterranean Region, despite its mild climate. This is thought to be due to economic concerns and ease of operation associated with the Mediterranean region being a relatively new development in winter tourism, thus making it a pilot region where lower-rise structures are preferred.

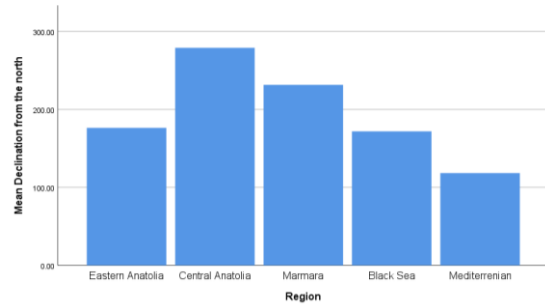


Figure 11 Table showing average deviation of building main facades from the north direction by regions

Figure 11 provides a comparison of the deviation rates of the main facades of the structures from the north direction based on geographical regions. According to the graph, winter tourism accommodation structures in the Central Anatolia region have the highest deviation from the north direction compared to other regions, placing it in the first position. On the other hand, structures in the Mediterranean region have the closest main facade direction to the north.

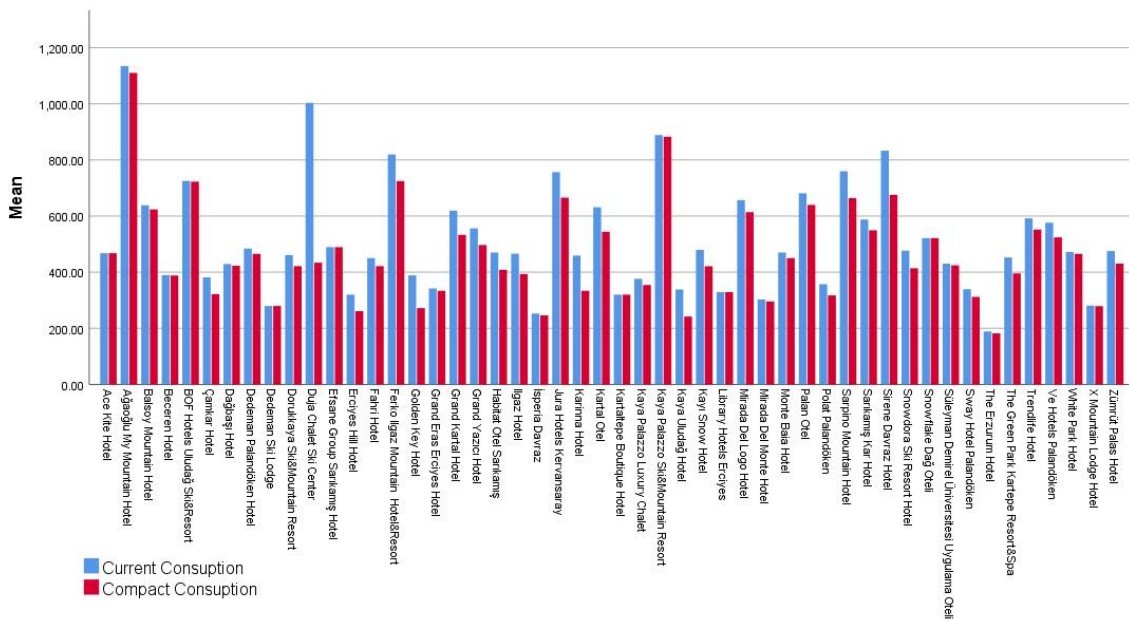


Figure 12 Comparison of energy consumption amounts for current and compact forms of buildings

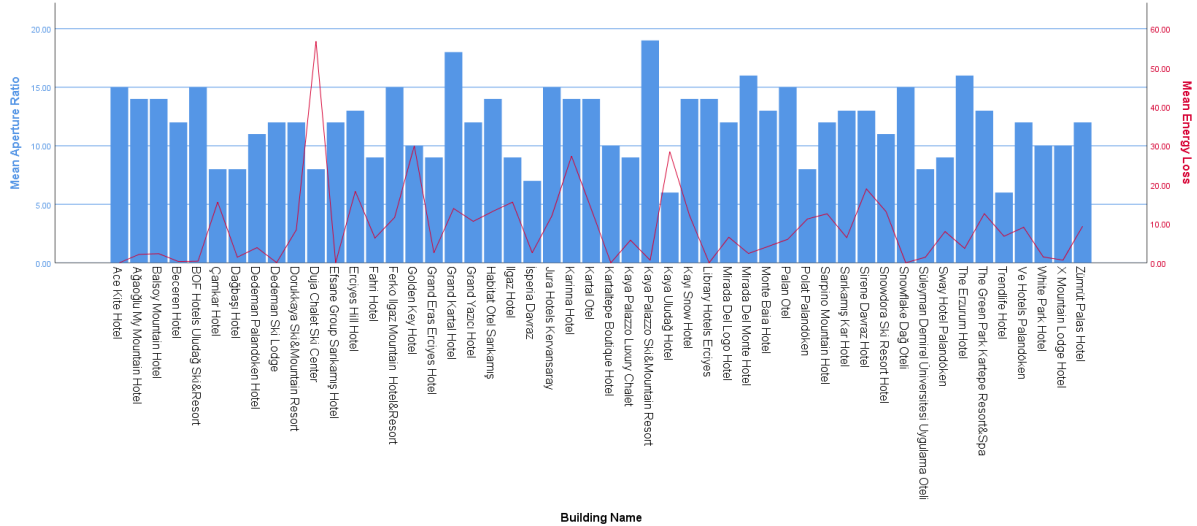


Figure 13 Displays the graph representing the energy loss amounts between the openness ratios of the structures and the current-compact forms

When examining the opacity ratios of the structures by geographical regions, the Central Anatolia Region ranks first, followed by the Western Black Sea Region in second place. They are then followed by the Eastern Anatolia, Marmara, and Mediterranean Regions. Considering that opacity is directly related to the facade openness ratio, it can be observed that the Mediterranean Region, which has the lowest opacity, has a higher facade openness ratio compared to other regions. This is a predictable result,

considering the relatively milder climate of the Mediterranean Region compared to other regions. Additionally, the average energy losses vary proportionally with the openness ratios according to the geographical regions. Thus, the impact of openness ratios on energy loss becomes evident (Figure 6). Figure 13, on the other hand, illustrates the individual representation of the facade openness ratios of the structures as examined in the previous graph.

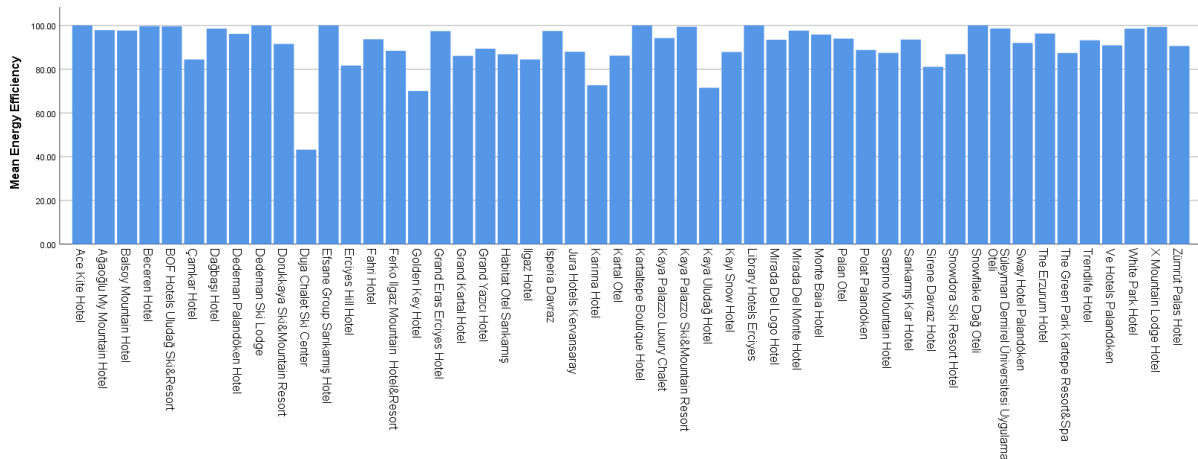


Figure 14 Table showing energy efficiency of buildings based on current and compact energy consumption

In Figure 14, the current and compact energy consumption quantities of each structure have

been analyzed in terms of energy efficiency. This graph was generated by considering the

compact forms of the structures as 100% efficient, and the efficiency ratios of each form were defined based on the deviation from compactness. According to this approach, it was observed that only 4 out of the 50 structures had an energy efficiency below 80% within the sample set.

#### 4. CONCLUSION

Considering the global trends in the new tourism paradigm, it is evident that our country, which largely consists of mountainous areas, has significant potential for winter tourism. In the design of winter tourism structures located in cold climate regions with complex activities, attention should be given to energy efficiency and the production of appropriate building envelopes. In this context, the motivation to examine the energy performance of winter tourism structures in our country has emerged. With this fundamental motivation, this study focuses on the concept of "compactness," which is highly important in the thermal balance and energy performance of buildings. Measurements of compactness were conducted based on the projections of 50 selected winter tourism accommodation structures from different regions, and various results were obtained using statistical research methods.

Examining the general findings of the study, it was observed that the compactness ratios ranged from 46.2% to 100%, with an average of 77.88%. In terms of regional compactness data, the Eastern Anatolia, Central Anatolia, and Western Black Sea regions exhibited ratios of 80% and above, while the Marmara and Mediterranean regions, which have higher average temperatures and a more temperate climate, showed lower ratios. Therefore, it can be concluded that these two regions contribute to the decrease in the overall compactness average. Additionally, it was found that increasing the surface area significantly affects the compactness ratio in accommodation structures with relatively

small floor areas, while in larger floor area buildings, this can be more tolerable.

Although certain directions were occasionally preferred in terms of the main facade orientations, no dominant direction was determined. Similarly, no discernible dominant direction was found regarding mass orientation. These findings suggest a mismatch between theoretical knowledge and practical application. It is believed that factors such as the size of the plot, its location, and its relationship with the road influence the results. Furthermore, no significant relationship was found between the compactness ratio, main facade orientation, and number of floors. In other words, it is not possible to speak of specialized main facade orientations and compactness ratios specific to a particular region.

In the evaluation based on the average number of floors, it is observed that the selected structures from the Marmara Region have higher floors, while the ones from the Mediterranean region have fewer floors compared to other regions. It is expected that the Marmara Region, which has a moderate climate, would prefer taller buildings, while it is unexpected for the selected structures from the Mediterranean Region with a similar climate to be low-rise. It is believed that this is due to economic concerns and operational convenience arising from the fact that winter tourism in the Mediterranean region is still in its early stages and it is considered a pilot region.

The structures selected from the Marmara Region have the highest difference between the existing and compact projections, while the structures selected from the Central Anatolia Region have the lowest difference. The preference for dynamic building forms contributes to a larger difference, while incorporating more stable forms reduces the difference. The Central Anatolia Region has the lowest difference between the existing and compact energy consumption. This supports the fact that the amount of energy lost due to the compactness factor is the lowest in the

Central Anatolia Region. Another reason for the high energy consumption is the wide floor area and the higher number of floors.

Building opacity is directly related to the facade opening. Therefore, the opacity of accommodation centers selected from the Mediterranean Region, which has relatively favorable climatic conditions, is found to be the lowest compared to other centers.

In the examinations conducted, it was observed that even in structures with a 100% compactness ratio, there could still be a difference between the existing and compact energy consumption. This is due to the overall increase in the structure. For example, the Kartaltepe Boutique Hotel, which has a 100% compactness ratio, has the same ground floor and regular floor plans, so there is no difference between the existing and compact energy consumption. However, in the Kaya Palazzo Ski & Mountain Resort, which also has a compactness average of 100%, the first two floors are the same, but as the floor level increases, the floor area decreases. Another notable observation is that, despite the low compactness ratio in the Beceren Hotel example, the difference between the existing and compact energy consumption values can be very small. This is presumed to be due to other influential factors such as facade opening ratio, main facade orientation, and mass orientation.

The study conducted energy simulations to examine the impact of mass design on the climatic comfort performance of winter accommodation structures affected by cold climates. The analyses revealed that the mass of the structures influenced their energy consumption based on thermal comfort. In this context, the study highlighted the significance of mass design in the climatic comfort performance of accommodation structures, contributing to the existing literature. For future research, it is recommended to explore the effects of different structural factors, along with mass design, on climatic comfort in various climate

conditions for accommodation structures. Consequently, this study offers a method for architectural designers to reduce energy consumption and enhance climatic comfort.

### ***Acknowledgements***

We would like to thank Enes Yaşa and Agah Taştemir for their contributions to the article.

### ***Funding***

The authors has no received any financial support for the research, authorship or publication of this study.

### ***Authors' Contribution***

The authors contributed equally to the study.

### ***The Declaration of Conflict of Interest/ Common Interest***

No conflict of interest or common interest has been declared by the authors.

### ***The Declaration of Ethics Committee Approval***

This study does not require ethics committee permission or any special permission.

### ***The Declaration of Research and Publication Ethics***

The authors of the paper declare that they comply with the scientific, ethical and quotation rules of SAUJS in all processes of the paper and that they do not make any falsification on the data collected. In addition, they declare that Sakarya University Journal of Science and its editorial board have no responsibility for any ethical violations that may be encountered, and that this study has not been evaluated in any academic publication environment other than Sakarya University Journal of Science.

## **REFERENCES**

- [1] M. Yılmaz, "Türkiye's energy potential and the importance of renewable energy sources in terms of electricity generation," Ankara University Journal of Environmental Sciences, vol.4, no. 2, pp.33-54, 2012.

- [2] C. B. Dikmen, "Sampling of energy efficient building design criteria," *Polytechnic*, vol. 14, no. 2, pp. 121-134, 2011.
- [3] F. P. Basaran, "Building morphology and optimum form analysis in the context of solar energy gain in energy efficient architectural design," Ph.D. dissertation, Gazi Univ., Ankara, Türkiye, 2021.
- [4] V. Olgyay, *Design With Climate*. Princeton University Press, New Jersey, 1963.
- [5] M. Aysan, "A research on optimum utilization of solar energy in urban design and various application examples in Istanbul," Ph.D. dissertation, Istanbul Technical Univ., Istanbul, Türkiye, 1983.
- [6] L. Zeren, "Climate-balanced architectural practice in Türkiye," in *Conf. Tübitak 6th Science Congress*, İzmir, 1977.
- [7] R. L. Crowther, *Sun Earth: How to Solar and Climatic Energies Today: First Edition*, New York, 1976.
- [8] G. Manioğlu, "Climate compatible buildings in traditional architecture: a student workshop in Mardin," in *Conf. 8th National Installation Engineering Congress*, İzmir, 2007, pp. 79-92.
- [9] M. M. Saeed, "A Scale For Architectural Design Compactness: A Mathematical Approach," *Sustainable Development And Planning V*, vol.150, pp.397-408, 2011.
- [10] K. Demir, "Database Model for Winter Tourism and Winter Sports Facilities Formation Process," Ph.D. dissertation, Yıldız Technical Univ., Istanbul, Türkiye, 2000.
- [11] F. Kun, "Evaluation of Tourism-Purpose Buildings in terms of Cooling Load in the Scope of Climate Balanced Design: The Case of Kuşadası" Master dissertation, Yıldız Technical Univ., Istanbul, Türkiye, 2005.
- [12] A. Demirtas, "Comparison of Hotel Buildings in Different Climate Regions in terms of Heating and Cooling Loads," Master dissertation, Yıldız Technical Univ., Istanbul, Türkiye, 2011.
- [13] B. D'Amico, F. Pomponi, "A Compactness Measure of Sustainable Building Forms," *Royal Society Open Science* vol.6, no.6, 2019.
- [14] F. P. Basaran, "Solar Energy Gain Analysis in the Context of Energy Efficient Design of Architectural Forms," *Online Journal of Art and Design*, vol. 10, no. 2, pp. 191-206, 2022.
- [15] İ. Karadağ, Z. Keskin, "Development of a Daylight Simulation Software for Early Design Stage: A Case Study of a Container House," *Periodica Polytechnica Architecture*, vol.52, no. 1, pp. 102-111, 2021.
- [16] İ. Karadağ, N. Serteser, "Estimation of Airflow Characteristics of Indoor Environments in the Early Design Stage," *A|Z ITU Journal of the Faculty of Architecture*, vol.16, no.1, pp. 1-9, 2019.
- [17] E. Bozdemir, "Competition and Positioning Strategies of Accommodation Businesses Operating in Winter Tourism: The Case of Türkiye," Master dissertation, Sakarya Univ., Sakarya, Türkiye, 2021.
- [18] Z. Çokal, F. Yılmaz, S. Yetis, "Winter Tourism as an Alternative Tourism Type and Its Importance for Türkiye," in *Conf. International Sivas Tourism Congress*, Sivas, 2018, pp. 149-157.

- [19] T.C. Ministry of Culture and Tourism (2022, Nov) General information of winter sports tourism center[Online]. Available: <https://yigm.ktb.gov.tr/TR-10177/kis-sporlari-turizm-merkezsinde-iliskin-genel-bilgiler.html>.
- [20] G. Özbay, “Winter Tourism in Alternative Tourism Policies: A Swot Analysis for Türkiye,” *The Journal of International Lingual, Social and Educational Sciences*, vol.4, no.2, pp. 203-213, 2018.
- [21] Setur (2022, Dec) [Online]. Available: [https://www.setur.com.tr/ski-hotels?gclid=Cj0KCQiAnNacBhDvARIsABnDa6-A3U53uZgVvga2sWTDGsTGo-zhg9NXLnPkSN4cfi\\_gbIGpiWMkrpAaan6PEALw\\_w](https://www.setur.com.tr/ski-hotels?gclid=Cj0KCQiAnNacBhDvARIsABnDa6-A3U53uZgVvga2sWTDGsTGo-zhg9NXLnPkSN4cfi_gbIGpiWMkrpAaan6PEALw_w)
- [22] N. Ayaz, Ö. C. Apak, “Travel Behaviors of Domestic Visitors Participating in Winter Tourism: Example of Erciyes Ski Resort,” *Journal of Erciyes University Faculty of Economics and Administrative Sciences*, vol. 49, no. 27, pp. 27-73, 2017.
- [23] E. Özmehmet, “A Building Model Proposal for the Mediterranean Climate Type in the Context of Sustainable Architecture,” Ph.D. dissertation, Dokuz Eylül Univ., İzmir, Türkiye, 2005.
- [24] K. Lynch, *Site Planning*, Mass: Second Edition, The Mit Press, Cambridge, 1971.
- [25] S. Soysal, “The Relationship Between Design Parameters and Energy Consumption in Residential Buildings” Master dissertation, Gazi Univ., Ankara, Türkiye, 2008.
- [26] J. E. Aronin, *Climate and Architecture*, Reinhold, 1953.





SAKARYA ÜNİVERSİTESİ

# FEN BİLİMLERİ ENSTİTÜSÜ DERGİSİ

Sakarya University Journal of Science  
SAUJS

ISSN 1301-4048 | e-ISSN 2147-835X | Period Bimonthly | Founded: 1997 | Publisher Sakarya University |  
<http://www.saujs.sakarya.edu.tr/>

Title: Estimating Human Poses Using Deep Learning Model

Authors: Fırgat MURADLI, Serap ÇAKAR, Feyza SELAMET, Gülüzar ÇİT

Received: 2023-06-07 00:00:00

Accepted: 2023-07-17 00:00:00

Article Type: Research Article

Volume: 27

Issue: 5

Month: October

Year: 2023

Pages: 1079-1087

How to cite

Fırgat MURADLI, Serap ÇAKAR, Feyza SELAMET, Gülüzar ÇİT; (2023), Estimating Human Poses Using Deep Learning Model. Sakarya University Journal of Science, 27(5), 1079-1087, DOI: 10.16984/saufenbilder.1311198

Access link

<https://dergipark.org.tr/tr/journal/1115/issue/80257/1311198>

New submission to SAUJS

<http://dergipark.gov.tr/journal/1115/submission/start>

## Estimating Human Poses Using Deep Learning Model

Fırgat MURADLI<sup>1</sup> , Serap ÇAKAR<sup>\*2</sup> , Feyza SELAMET<sup>2</sup> , Gülüzar ÇİT<sup>3</sup> 

### Abstract

Over the past decade, extensive research has focused on the extraction of 3D human poses from images. The existing datasets must effectively address common challenges related to pose estimation. These datasets serve as valuable resources for evaluating, informing, and comparing different models. Deep learning models have gained widespread adoption and have demonstrated impressive performance across various domains of research and engineering. In this study, we employ these models, leveraging the open-source libraries OpenCV and Keras. To enhance the diversity and complexity of the training and testing process, we utilize the MPII Human Pose dataset. Specifically, we train and test the ResNet50 and VGG16 models using this dataset, resulting in significant improvements. The model's performance is evaluated based on the validation rate of the dataset and the accuracy of our model was 88.8 percent for VGG16 and 67 percent for ResNet50.

**Keywords:** 2D human pose, convolutional neural network, transfer learning

### 1. INTRODUCTION

Estimating the precise pixel locations of significant key points on the human body is known as "human pose estimation." Estimating human pose techniques forecast model parameters from training data by using complex view models and learning algorithms [1]. Human pose estimation algorithms have a wide range of applications in various fields where detecting and tracking human movements is important such as sports

analysis, augmented reality and virtual reality, gaming, robotics and healthcare [1-3]. The availability of annotated training images representing human clothing, strong articulation, partial (self) occlusion, and cutting at image boundaries are all essential factors in the performance of these approaches. While there are training sets for particular situations, such as sports scenes and upright people, the variety and variability of the represented activities still need improvement. Since people usually wear tight

\* Corresponding author: scakar@sakarya.edu.tr (S. ÇAKAR)

<sup>1</sup> Sakarya University, Faculty of Computer and Information Sciences, Sakarya, TURKIYE

<sup>2</sup> Sakarya University, Faculty of Computer and Information Sciences, Department of Computer Engineering, Sakarya, TURKIYE

<sup>3</sup> Sakarya University, Faculty of Computer and Information Sciences, Department of Software Engineering, Sakarya, TURKIYE

E-mail: firgat.muradli@ogr.sakarya.edu.tr, feyzacerezci@sakarya.edu.tr, gulizar@sakarya.edu.tr

ORCID: <https://orcid.org/0000-0001-6340-0149>, <https://orcid.org/0000-0002-3682-0831>, <https://orcid.org/0000-0002-1596-1109>, <https://orcid.org/0000-0002-1220-0558>



sportswear, sports scene datasets typically provide highly articulated poses but are limited in various looks. Datasets such as "Fashion Pose" and "Armllets", on the other hand, tend to capture images of people dressed in various outfits and occlusions and cuts.

The objective of estimating human pose can change. Studies have been done to use a single 2D image to create a 3D body pose prediction and a 2D depth image to generate a 3D body pose prediction [2, 3]. The location of articulation points (such as the neck, knees, elbows, etc.) in 2D coordinate space is used to represent a pose [3]. For most action recognition issues, this representation paradigm is adequate. The model is also the simplest way to describe the anatomy of the human body. The number of articulation points in the literature is not standardized. From dataset to dataset, the point count frequently varies [4-6].

This research aims to predict a human body pose from a single 2D image and to see how the Keras model can predict human body posture using deep convolutional neural networks (DCNN). Since VGG16 and ResNet50 are frequently used for detecting and tracking complex structures like the human body, they were chosen for this study as well.

The article is organized as follows; Section 1 describes the motivation of our study, Section 2 mentions related works, and Section 3 explains the experiments and summarizes the results. Finally, the conclusion is discussed in Section 4.

## 2. LITERATURE REVIEW

Human pose prediction is a significant research subject for the computer vision group. Researchers have primarily performed research because of its importance in various fields, including human-computer interaction, action detection, surveillance, image interpretation and threat prediction. As a result, multiple studies have been carried out,

beginning with the first realistic models for predicting human pose, using the most well-known deep learning approaches to provide a brief analytical analysis of the most successful methods.

Tekin et al. [7] suggested an effective method for saving humans' three-dimensional (3D) poses by using motion information from consecutive frames of a video series. In the study, a direct return was made from the spatial seal volume of the bounding boxes to the 3D pose in the main frame. The Human 3.6 m and KTH Multiview Football 3D datasets have effectively overcome uncertainties, and the latest technology has been achieved with a significant difference compared to the human pose prediction criteria.

Pavlokos et al. [8] addressed the question of 3D human pose estimation from a monochrome image. The proposed method reduces relative error by more than 30% on average, outperforming all state-of-the-art approaches in standard comparisons. In addition, research has been done using volumetric representations in a related architecture that is not optimal according to the end-to-end process.

A learning-based motion-capture model for single-camera input is proposed by Tung et al. [9]. The model is trained from synthetic data in an end-to-end frame using robust control and self-control from different manipulations of skeleton key points, extreme 3D grid motion, and human context segmentation. It was determined that low-error solutions were approached with the proposed model, while previous optimization methods were unsuccessful.

Zhou et al. [10] investigated estimating three-dimensional human poses in the wild. In monitored laboratory settings, images captured in the wild were transferred to a 3D exposure mark. Both 2D and 3D experiments yielded competitive results at the end of the analysis.

Kanazawa et al. [11] used the Human Mesh Recovery method to recreate a complete 3D file of a human body from a single RGB image by defining an end-to-end frame. The model has demonstrated approaches to various optimization-based methods that have previously been used, exist in nature and are carried out outside.

Mu et al. [12] describe the techniques used in human exposure estimation and list some applications and the flaws encountered in pose estimation.

Chen et al. [13] propose a transformer-like model called ShiftPose, a regression-based approach whose result on the COCO dataset is 72.2 mAP.

### 3. EXPERIMENTS

#### 3.1. Dataset

In this study, the MPII Human Pose dataset is used to estimate the human pose. The MPII Human Posture dataset has 25K images containing 40000 people with 2D body joint descriptions [2]. The dataset includes 410 human activities, and each image has an activity label. There is no 3D information about human key points. The images have been collected in several daily activities. Annotations are provided in an Anaconda Jupyter. Each image is taken from a YouTube video (Figure 1).



Figure 1 Examples of images from the MPII dataset showing some common human activities

#### 3.2. Deep Learning Methods

DCNN (Deep Convolutional Neural Network): Deep Convolutional Neural Networks (DCNNs) are a type of neural network architecture specifically designed for processing visual data, such as images. They are composed of multiple layers of convolutional, pooling, and fully connected layers. DCNNs leverage the idea of local receptive fields, weight sharing, and hierarchical representations to extract meaningful features from input images.

ResNet50: ResNet50 is a variant of the ResNet (Residual Network) architecture. ResNet introduced the concept of residual learning, which addresses the problem of vanishing gradients in deep neural networks. ResNet50 specifically refers to a ResNet model with 50 layers, consisting of convolutional layers, batch normalization, and skip connections. Skip connections allow the network to learn residual mappings, which helps in training deeper networks more effectively.

VGG16: VGG16 is a convolutional neural network architecture developed by the Visual Geometry Group at the University of Oxford. It gained popularity due to its simplicity and strong performance on various image recognition tasks. VGG16 consists of 16 layers, including 13 convolutional layers and 3 fully connected layers. It uses small receptive fields (3x3 convolutional filters) and max pooling layers to progressively extract more complex features from input images.

Both ResNet50 and VGG16 have been widely used as pre-trained models for transfer learning. Transfer learning involves using a pre-trained model on a large dataset, such as ImageNet, and fine-tuning it on a smaller dataset specific to the target task. This approach allows leveraging the learned representations from the pre-trained models and achieving good performance even with limited training data.

These methods have been instrumental in various computer vision tasks, including image classification, object detection, and image segmentation, and have significantly contributed to the advancements in the field of deep learning.

### 3.3. Details of Training

The image resolution varies in the MPII dataset. The original images were cropped and resized to 256x256 before being sent to CNN. Resizing and cropping can be done in various ways, and you can choose whether or not to include obscured key points in the training data. The weights of a filter are distributed throughout the image in CNNs. Small filter sizes and sharing weights allow CNNs to have fewer weights than fully connected layers. A 3x3 filter size convolutional layer with 128 features, for instance, will have weights of  $3 \times 3 \times 3 \times 128 = 3456$  in a 256x256x3 sample image. In so-called deep CNNs, many layers may be stacked on top of one another while still using less memory. This has been shown to be beneficial when the network needs to learn more difficult and abstract tasks [14]. Three different preprocessing methods were introduced and tested as part of the effort to enhance CNN's results. All preprocessing techniques crop the image using a boundary square to maintain the aspect ratio. Anaconda Jupyter, a commercial software package, was used for preprocessing.

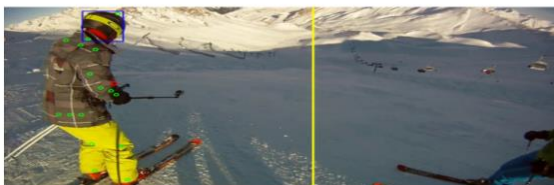


Figure 2 Original image before preprocessing [14]

The original image before preprocessing is shown in Figure 2. In the preprocessing method, the bounding frame cannot be outside the original image. If the edge of the bounding frame is larger than the image, it is set to the minimum (width, height). Cropping the image in this way does not mean that we ensure that the person is in the center of the image.

The only joints with ground truth annotations in the training data version were those visible. The ground truth was ignored and set to zero for the occluded joints, as shown in Figure 3. The key points that are obscured cannot provide the network with information about the pose, which is why they were removed. So they can be taken out of the training data. With this method, the network receives fewer key point annotations during training and is not allowed to develop the ability to predict obscured key points.

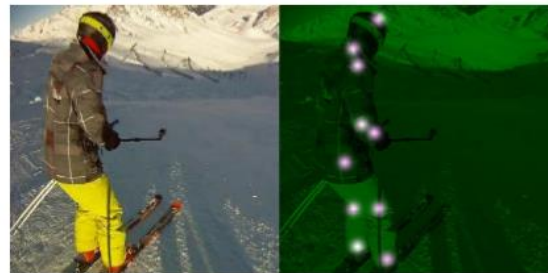


Figure 3 Training image not centered without covering key points [14]

Figure 4 shows the body's main joints, including the elbow, wrist, shoulder, knee, ankle, hip, upper part of the head, rib cage, pelvis, and neck. Calculating these joints' image coordinates is the task at hand.



Figure 4 The key points that make up the pose [14]

There are about 24K annotations; we only use those from sufficiently distant individuals. The validation process involved using about 2400 of these images. Before the training started, each image in the dataset was transformed into 16 labeled images. These images are 64x64 in size, one for each annotation. Each labeled image had a 2D Gaussian hill with 7 pixels in diameter and 1 standard deviation. Each hill was positioned at the x-y coordinate of the corresponding joint.

A label volume of  $16 \times 64 \times 64$  was created for each training image (Figure 5). During instruction, the stack of labeled images served as ground reality.

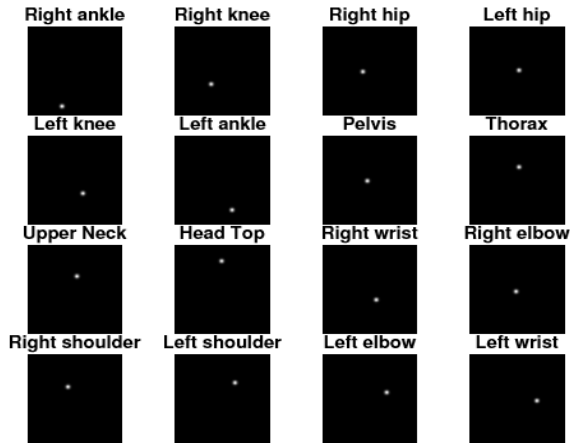


Figure 5 The 16 ground truth images for the key points [14]

### 3.4. Experimental Results

We tested our application on two models (ResNet50 and VGG16). Only sufficiently reserved people's annotations were used, and there are about 24000 annotations in total. Roughly 24000 of the images were used for the ResNet50 model, of which 20000 were used for training and the remaining 4000 for testing. We ran our model as 50 epochs, and the accuracy of our model is 67 percent.

We again used 24000 annotations for our second model, the VGG16. 20000 of them were used for training and the rest for testing. We still ran our model as 50 epochs, and this time the accuracy of our model was 88.8 percent.

Since our VGG16 model gave better results, we showed these graphically in Figures 6 and 7. VGG16 model trial results are shown in Figure 8. The comparison of our model with other studies is shown in Table 1 [1, 7-11, 15-22]. Accuracy values were compared with reference to parameters such as the studies in the literature, the method used, the database, and the number of data. As can be seen in Table 1, although the number of data in the references [18] and [19] made with the MPII dataset used in our study is high, the accuracy rate is lower than in our study.

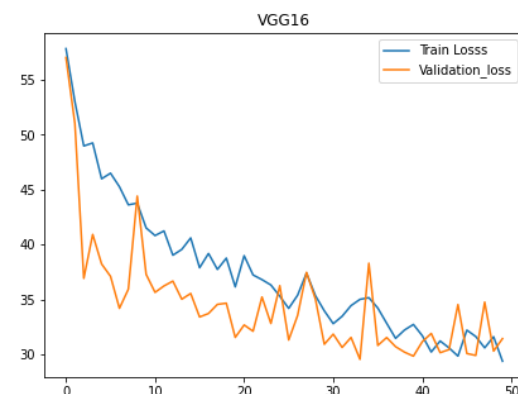


Figure 6 Period and loss charts for training and validation data of the VGG16 model

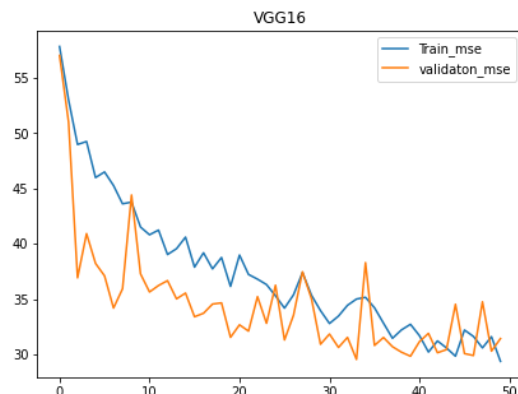


Figure 7 Period and MSE charts for training and validation data of the VGG16 model

```

Epoch 00045: val_loss did not improve from 32.20763
Epoch 46/50
24000/24000 [=====] - 3960s 2s/step - loss: 16.9487 - mean_absolute_error: 16.9487 - val_loss: 18.9701 -
val_mean_absolute_error: 18.9701

Epoch 00046: val_loss did not improve from 32.20763
Epoch 47/50
24000/24000 [=====] - 1792s 747ms/step - loss: 14.1661 - mean_absolute_error: 14.1661 - val_loss: 17.6563 -
val_mean_absolute_error: 17.6563

Epoch 00047: val_loss did not improve from 32.20763
Epoch 48/50
24000/24000 [=====] - 12077s 5s/step - loss: 12.3580 - mean_absolute_error: 12.3580 - val_loss: 15.3882 -
val_mean_absolute_error: 15.3882

Epoch 00048: val_loss did not improve from 32.20763
Epoch 49/50
24000/24000 [=====] - 1827s 761ms/step - loss: 09.1432 - mean_absolute_error: 09.1432 - val_loss: 12.5477 -
val_mean_absolute_error: 12.5477

Epoch 00049: val_loss did not improve from 32.20763
Epoch 50/50
24000/24000 [=====] - 1820s 758ms/step - loss: 08.0439 - mean_absolute_error: 08.0439 - val_loss: 10.2381 -
val_mean_absolute_error: 10.2381

Epoch 00050: val_loss did not improve from 32.20763

```

Figure 8 VGG16 model trial results

Table 1 The methods and results of the studies conducted in the literature review

Research	Method	Database	Number of Images	Accuracy
Pavlokos et al. [1]	RSTV+KDE	KTH Football II	800	71.9 %
Tekin et al. [7]	RSTV + KRR	HumanEva-I/II	3000	85.3 %
Pavlakos et al. [8]	PCK3D	MPII and LSP	26000	76.5 %
Tung et al. [9]	SFM	H3.6M	3600000	98.4 %
Zhou et al. [10]	3D+2D/wgeo	MPI-INF-3DHP	2929	64.9 %
Kanazawa et al. [11]	SMPLify	MPI-INF-3DHP	2929	82.5 %
Zhang et al. [15]	FPD	MPII and LSP	26000	88.1 %
Belagiannis et al. [16]	PCKh	MPII and LSP	26000	85.2 %
Xiao et al. [17]	IEF	Human3.6M+MPII	3625000	75.4 %
Carreira et al. [18]	AAMs	MPII	27000	73.8 %
Newell et al. [19]	SFM	MPII	27000	83.6 %
Li et al. [20]	MSPN	COCO and MPII	352000	92.6 %
Zhang et al. [21]	PCKh	MPII and LSP	26000	91.7 %
Sun et al. [22]	VGGNet	MPII and COCO	352000	85.7 %
Our research	VGG16	MPII	24000	88.8%
Our research	Resnet50	MPII	24000	67.0%

It is clear that the loss drops of a model are taken quickly and with reasonable accuracy; they are quite fast in inference. This is a good illustration of how effective and easy transfer learning can be.

### 3.5. Evaluation

Performance during training and validation is fairly good, but performance on unseen data is unclear. Our original data set was divided into two separate sections. It's crucial to keep in mind that the test dataset requires the same preprocessing steps as the training dataset. We

scale the test dataset before passing it to the method to adjust for this.

## 4. CONCLUSIONS

This article uses deep learning-based models to predict 2D human pose from single-color images in the MPII human pose dataset. The final analysis of the poses in the MPII dataset focuses on separating the poses into different categories and perspective sets. This is done to evaluate how state-of-the-art networks perform under different types of exposure and viewpoints. We conducted our inspections

using 24000 data on VGG16 and Resnet50 models. The accuracy of our model is 67% for ResNet50 and 88.8% for VGG16. The results support the findings in this study that poses with higher exposure scores are harder to predict. The CNN models used in this study have disadvantages such as high computational cost, large memory requirement and overfitting. We can get better results by increasing the training and test data. The overfitting problem can also be addressed with a wider variety of poses, preferably by increasing training data.

#### ***Funding***

The authors received no financial support for the research, authorship, or publication of this work.

#### ***The Declaration of Conflict of Interest/ Common Interest***

No conflict of interest or common interest has been declared by the authors.

#### ***Authors' Contribution***

F. M: Literature research, data collection, data processing, organizing the execution of the study, contribution to article writing and study. S. C., F. S., G. C.: Contribution to article writing and study, literature research, and creation of the idea.

#### ***The Declaration of Ethics Committee Approval***

The authors declare that this document does not require an ethics committee approval or any special permission.

#### ***The Declaration of Research and Publication Ethics***

The authors of the paper declare that they comply with the scientific, ethical, and quotation rules of SAUJS in all paper processes and that they do not make any falsification on the data collected. In addition, they declare that Sakarya University Journal of Science and its editorial board have no responsibility for any ethical violations that may be encountered and that this study has not been evaluated in any academic publication environment other than Sakarya University Journal of Science.

## **REFERENCES**

- [1] G. Pavlakos, X. Zhou, K. G. Derpanis, K. Daniilidis, "Coarse-to-Fine Volumetric Prediction for Single-Image 3D Human Pose", Proceedings of the 30th IEEE Conference on Computer Vision and Pattern Recognition, CVPR 2017, pp. 1263–1272, 2017.
- [2] M. Andriluka, L. Pishchulin, P. Gehler, B. Schiele, "2D Human Pose Estimation: New Benchmark and State of the Art Analysis", Proceedings of the IEEE Computer Society Conference on Computer Vision and Pattern Recognition, pp. 3686–3693, 2014.
- [3] H. Yasin, U. Iqbal, B. Kruger, A. Weber, J. Gall, "A Dual-Source Approach for 3D Pose Estimation from a Single Image", Proceedings of the IEEE Computer Society Conference on Computer Vision and Pattern Recognition, pp. 4948–4956, 2016.
- [4] P. F. Felzenszwalb, D. P. Huttenlocher, "Pictorial Structures for Object Recognition," International Journal of Computer Vision, vol. 61, no. 1, pp. 55–79, 2005.
- [5] C. Szegedy, W. Liu, Y. Jia, P. Sermanet, S. Reed, D. Anguelov, D. Erhan, V. Vanhoucke, A. Rabinovich, "Going Deeper with Convolutions", Proceedings of the IEEE Computer Society Conference on Computer Vision and Pattern Recognition, pp. 1–9, 2015.
- [6] K. He, X. Zhang, S. Ren, J. Sun, "Deep Residual Learning For Image Recognition", Proceedings of the IEEE Computer Society Conference on Computer Vision and Pattern Recognition, pp. 770–778, 2016.
- [7] B. Tekin, A. Rozantsev, V. Lepetit, P. Fua, "Direct Prediction of 3D Body Poses from Motion Compensated Sequences",



- Proceedings of the IEEE Computer Society Conference on Computer Vision and Pattern Recognition, pp. 991–1000, 2016.
- [8] G. Pavlakos, X. Zhou, K. Daniilidis, "Ordinal Depth Supervision for 3D Human Pose Estimation", Proceedings of the IEEE Conference on Computer Vision and Pattern Recognition, pp. 7307-7316, 2018.
- [9] H. Y. F. Tung, H. W. Tung, E. Yumer, K. Fragkiadaki, "Self-Supervised Learning of Motion Capture", Advances in Neural Information Processing Systems, pp. 5237–5247, 2017.
- [10] X. Zhou, Q. Huang, X. Sun, X. Xue, Y. Wei, "Towards 3D Human Pose Estimation in the Wild: A Weakly-Supervised Approach", Proceedings of the IEEE Conference on Computer Vision, pp. 398–407, 2017.
- [11] A. Kanazawa, M. J. Black, D. W. Jacobs, J. Malik, "End-to-End Recovery of Human Shape and Pose", Proceedings of the IEEE Conference on Computer Vision and Pattern Recognition, pp. 7122–7131, 2018.
- [12] T. L. Munea, Y. Jembre, H. Weldegebriel, L. Chen, C. Huang, C. Yang, "The Progress of Human Pose Estimation: A Survey and Taxonomy of Models Applied in 2D Human Pose Estimation", IEEE Access, vol. 8, pp. 133330-133348, 2020.
- [13] H. Chen, X. Jiang, Y. Dai, "Shift Pose: A Lightweight Transformer-like Neural Network for Human Pose Estimation", Sensors 22, vol. 22, no. 19, pp. 7264, 2022.
- [14] S. A. Runing, "An Evaluation of Human Pose Estimation Using a Deep Convolutional Neural Network", Master's Thesis, 2017.
- [15] F. Zhang, X. Zhu, M. Ye, "Fast Human Pose Estimation", Proceedings of the IEEE/CVF Conference on Computer Vision and Pattern Recognition, pp. 3517-3526, 2019.
- [16] V. Belagiannis and A. Zisserman, "Recurrent Human Pose Estimation," 2017 12th IEEE International Conference on Automatic Face & Gesture Recognition (FG 2017), Washington, DC, USA, pp. 468-475, 2017.
- [17] S. Xiao, J. Shang, S. Liang, Y. Wei, "Compositional Human Pose Regression", Proceedings of the IEEE International Conference on Computer Vision, pp. 2602-2611, 2017.
- [18] J. Carreira, P. Agrawal, K. Fragkiadaki, J. Malik, "Human Pose Estimation with Iterative Error Feedback", Proceedings of the IEEE Conference on Computer Vision and Pattern Recognition, pp. 4733-4742. 2016.
- [19] A. Newell, K. Yang, J. Deng, "Stacked Hourglass Networks For Human Pose Estimation", Lecture Notes Computer Science (Including Subseries Lecture Notes Artificial Intelligence Lecture Notes in Bioinformatics), vol. 9912 LNCS, pp. 483–499, 2016.
- [20] W. Li, Z. Wang, B. Yin, Q. Peng, Y. Du, T. Xiao, G. Yu, H. Lu, Y. Wei, J. Sun, "Rethinking on Multi-Stage Networks for Human Pose Estimation", January 2019, [Online]. Available: <http://arxiv.org/abs/1901.00148>.
- [21] H. Zhang, H. Ouyang, S. Liu, X. Qi, X. Shen, R. Yang, J. Jia, "Human Pose Estimation with Spatial Contextual Information", January 2019, [Online]. Available: <http://arxiv.org/abs/1901.01760>.

- [22] K. Sun, B. Xiao, D. Liu, J. Wang, "Deep High-Resolution Representation Learning for Human Pose Estimation", [Online]. Available: <https://github.com/leoxiaobin/>, Last Accessed :05.11.2022



SAKARYA ÜNİVERSİTESİ

# FEN BİLİMLERİ ENSTİTÜSÜ DERGİSİ

Sakarya University Journal of Science  
SAUJS

ISSN 1301-4048 | e-ISSN 2147-835X | Period Bimonthly | Founded: 1997 | Publisher Sakarya University |  
<http://www.saujs.sakarya.edu.tr/>

Title: Investigation of the Usage Properties of Steel Slag as Pigment in Low-Temperature Glaze

Authors: Muhterem KOÇ, Eda TAŞÇI

Received: 13.03.2023

Accepted: 22.07.2023

Article Type: Research Article

Volume: 27

Issue: 5

Month: October

Year: 2023

Pages: 1088-1096

How to cite

Muhterem KOÇ, Eda TAŞÇI; (2023), Investigation of the Usage Properties of Steel Slag as Pigment in Low-Temperature Glaze. Sakarya University Journal of Science, 27(5), 1088-1096, DOI: 10.16984/saufenbilder.1264392

Access link

<https://dergipark.org.tr/tr/journal/1115/issue/80257/1264392>

New submission to SAUJS

<http://dergipark.gov.tr/journal/1115/submission/start>

## Investigation of the Usage Properties of Steel Slag as Pigment in Low-Temperature Glaze

Muhterem KOÇ<sup>1</sup>, Eda TAŞÇI<sup>\*2</sup>

### Abstract

The evaluation of industrial wastes in the ceramics industry has been the subject of research studies in recent years. This study investigated the use of steel slag as a colouring pigment in ceramic glazes. The colour effects of 45 compositions created with a triple-phase diagram with steel slag, CoO, and Cr<sub>2</sub>O<sub>3</sub> on low-temperature glaze composition were determined. The microstructural evaluation of the selected colours by SEM and EDX analysis were carried out. The prepared glaze compositions were applied by pouring on the high silica ceramic body. Glazed tiles were sintered in a muffle furnace at 950 °C and then L\*a\*b colour and gloss brightness values were measured. By using steel slags instead of Fe<sub>2</sub>O<sub>3</sub>, black glazes were obtained in the triple diagram.

**Keywords:** Low-temperature coloured glaze, steel slag, high silica-containing body, L\*a\*b

### 1. INTRODUCTION

Glazes are called glassy surfaces that adhere to the ceramic material and provide basic properties such as permeability, semi-permeability, opacity, matte appearance, necessary thermal expansion and chemical resistance. They can be prepared as a powder or liquid suspension. They are applied to ceramic body surfaces by dipping, spraying or sprinkling methods. Glazes can be applied on the ceramic body as raw or fritized, wet or dry. They may have contained different compositions depending on the purpose of use [1]. In addition, they provide a shiny and smooth surface to the body on which they are applied, they do not have gas permeability,

their mechanical strength is high, they are resistant to abrasion, scratching and chemicals, and they are easy to clean. They create a decorative effect by reflecting matte, glossy and crystalline properties on the surface of the products [2].

The most important feature of ceramic glazes, which are formed by mixing chemically alkali and alkaline earth oxides with inappropriate recipe ratios and sintering at the appropriate temperature, is that they can form physical and chemical bonds with the ceramic body on which they are applied, under normal conditions [3]. In the formation of glaze types, classification can be made according to the structure of the body in which the glaze is

\* Corresponding author: eda.tasci@dpu.edu.tr (E.TAŞÇI)

<sup>1</sup> Kütahya Dumlupınar University, Department of Industrial Design, Kütahya, Türkiye

<sup>2</sup> Kütahya Dumlupınar University, Department of Metallurgical and Materials Engineering, Kütahya, Türkiye

E-mail: muhterem.koc@dpu.edu.tr

ORCID: <https://orcid.org/0000-0003-3661-4410>, <https://orcid.org/0000-0003-3346-8833>



applied, the variety of industrial or artistic applications, and most importantly, according to the firing temperatures [4]. Natural and synthetic oxides and pigments are used in the colouring of ceramic glazes. Natural pigments exist in nature as simple oxides. Among natural pigments, iron oxides, which can impart different colours, are widely used especially in the ceramic industry [4].

Natural and synthetic inorganic-based pigments, glazes containing homogeneous mixtures that disperse without dissolution and chemical reaction at high temperatures; They are widely used for the bulk colouring of various ceramic products, including glass, ceramic body and porcelain enamel. The use of blending systems for raw materials or colourants in the development of a new glaze composition is important for a systematic study.

Ceramic production is increasing rapidly in our country and throughout the world. In the 21st century, in line with the developing technology and industrialization and sustainable development goals, the correct use of by-products and wastes generated during production processes all over the world gains importance. Along with this increase in production, the world reserves decreasing over time not only restrict the use of high-quality raw material stocks in the ceramic industry, but also cause an increase in costs. Therefore, the importance of R&D studies on the use of industrial waste materials, as an alternative to the use of natural raw material reserves, is increasing day by day. The recycling of industrial wastes in this direction is widely used in both sectoral and academic studies. In addition, considering the economic effects of the reuse of wastes, it provides significant gains to the ceramics industry.

The studies carried out cover the subjects of recycling, conservation of natural resources, reducing the demand for landfills and waste management [4-5]. In the ceramics industry, there are studies on the use of industrial

wastes as alternative raw materials in ceramic glazes [6-10], ceramic tile bodies [6-9], ceramic pigments [8-12] and concrete building materials [13-14].

In addition, studies are carried out on the use of solid wastes generated as a result of industrial production as starting raw materials for use in ceramic pigment, glaze or body colouring. In this regard, colourants, which are quite expensive in terms of production cost and in which heavy metal oxides and mixtures containing heavy metal oxides are used, take the first place [15-16]. Apart from these, On the other hand, many studies are carried out to reduce the damage caused by industrial wastes to nature by recycling and to make them reusable in the development of ceramic glazes. With the use of industrial wastes in the ceramic sector, raw material costs can also be reduced. When the studies on the recycling of wastes to be used in the ceramic industry are examined, it is seen that positive results have been obtained [17-18]. In addition, natural industrial wastes are used in ceramic industry recipes, especially marbel wastes, boren wastes etc. [19].

The concept of colour, which we express as a physical perception, is a chemical process. Different quality colours are obtained by mixing ceramic paints and pigments produced as a result of the chemical process. Obtaining the desired colour in the ceramic industry is a very important and difficult process. The use of ceramic colours both industrially and artistically depends on the content of the raw materials used first. Secondly, the production process is an effective parameter [20-21]. Colouring salts, oxides and compounds or pigments containing them are used in ceramics. Although colourants have their own unique colours, different colours can be obtained by controlling parameters such as production process, firing conditions, grain size and application thickness. The effects of different oxides and oxides in the form of pigments on ceramic glazes differ.

The aim of this study is to examine the properties of steel slag, which is iron and steel factory waste, as a colouring agent in ceramic glazes, which is an important component of ceramic products. Within the scope of the study, the effects of 45 recipes formed as a triple phase diagram of steel slag with CoO and Cr<sub>2</sub>O<sub>3</sub> on the glaze composition selected as low temperature glaze were investigated. L\*a\*b color and gloss values of the compositions were measured after firing under laboratory conditions at 950 °C. Microstructural colour effects of black, green and blue tone colours on low temperature glaze, the effect of waste, CoO and Cr<sub>2</sub>O<sub>3</sub> on colour performance were evaluated by SEM and EDX analyzes in the 3-phase diagram recipes, which are considered as paint application, in the recipes containing the most appropriate slag ratio affecting the colour density. In this study, the usability of steel slags in high silica bodies and leaded low temperature glazes as iron-based colouring oxide was investigated. Compositions formed with steel slag, CoO and Cr<sub>2</sub>O<sub>3</sub> were used as colourants at low temperatures.

## 2. MATERIALS AND METHODS

Within the scope of this study, the chemical analysis of the steel mill waste obtained from Kardemir Karabük Iron and Steel Industry is given in Table 1. Pigment mixture compositions were prepared based on the triple phase diagram given in Figure 1, consisting of steel slag, CoO and Cr<sub>2</sub>O<sub>3</sub> components. In Figure 2, recipe compositions are given.

45 pigment-dye recipes prepared in the form of a triple phase diagram were weighed separately as shown in Table 2 and ground as aqueous for 30 minutes. After the drying process, the pigment recipes were prepared as glaze compositions by adding 3% to the low temperature (950°C) glaze recipe and then grinding for 15 minutes separately. The prepared pigment-containing glaze recipes were applied on the high silica bodies produced within the scope of the T.C.

Strategy and Budget Directorate project, by the pouring method. High silica bodies contain % 91.54 SiO<sub>2</sub>, % 5.42 Na<sub>2</sub>O, % 1.01 Al<sub>2</sub>O<sub>3</sub>, % 1.21 CaO, % 0.42 Fe<sub>2</sub>O<sub>3</sub>, % 0.13 K<sub>2</sub>O, % 0.18 MgO, %0.04 TiO<sub>2</sub>. In the XRD analysis of the body given in Figure 1, high quartz and low cristobalite phases were detected.

The tiles were glazed with colored glazes and fired in a Protherm brand HLF60 model oven at 950°C for 30 minutes in a laboratory environment. According to the results of the triple-phase diagram, the colour scale obtained visually is given in Figure 3.

L\*a\*b\* colour values of glazed coloured bodies were measured with a PCE CSM-2 brand model device. The effect of waste on the colour distribution of the recipes selected from high silica bodies was examined with the Nova NanoSEM 650 brand model SEM EDX device and the results are given in Figures 4 and 5 and Tables 2,3,4 and 5.



Figure 1 Triple Phase Diagram.

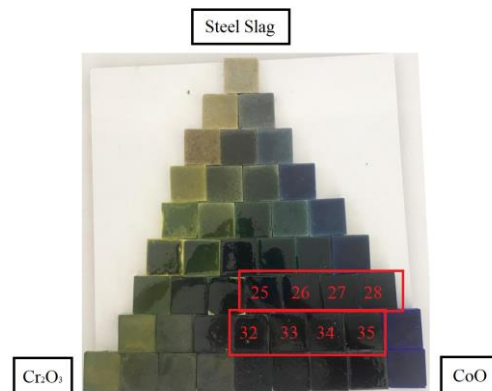


Figure 2 Colour values obtained in the triple phase diagram

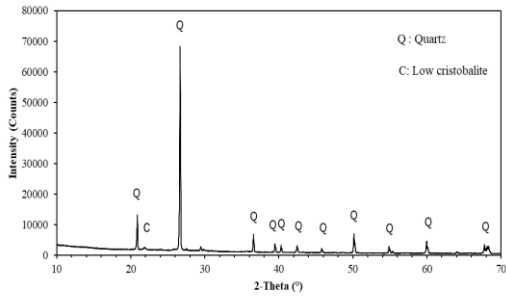


Figure 3 Phase analysis of high silica body.

Table 1 Chemical analysis results of steel slag

Oxides	Steel slag (%)	Glaze (%)
PbO	-	55.88
CaO	48.02	0.85
Fe <sub>2</sub> O <sub>3</sub>	21.09	0.10
Na <sub>2</sub> O	0.1	5.42
SiO <sub>2</sub>	12.34	34.14
MgO	3.86	0.30
Al <sub>2</sub> O <sub>3</sub>	2.92	3.17
MnO	5.11	0.05
SO <sub>3</sub>	1.08	-
P <sub>2</sub> O <sub>5</sub>	0.76	-
TiO <sub>2</sub>	0.48	0.01
Cr <sub>2</sub> O <sub>3</sub>	0.24	-
LIO	4.10	-

LIO: Loss on igniton

### 3. RESULT AND DISCUSSION

The gloss values of glazed samples are given in Table 2. Gloss can be defined as an optical property that indicates how well a completely impermeable surface reflects light in a specular (mirroring) direction. Another definition; It can be expressed as the ratio of the light intensity reflected from the surface of an object to the light intensity incident on the surface. In gloss meter measurements, the illumination from the light source in the gloss meter reflects from the surface at a certain angle (such as 20°, 60° and 85°) and reaches the sensors on the other side of the gloss meter. In the meantime, the ratio of the amount of light reflected on the surface and the amount of light coming from the device source is measured.

The resulting numerical value is expressed by converting to Gloss Unit (G.U.), a unit of gloss [22]. It is important to choose the correct

angle to measure the gloss, and to choose the surface gloss angle. This method is used on smooth, refined or unrefined surfaces such as polished stone, wood, laminate, flooring and ceramics. With the gloss meter, it can be determined whether the material analyzed is a high gloss, semi-gloss and matte. Gloss is measured by directing a constant-intensity light beam at a fixed angle to the test surface and then watching the light reflect off from the same angle. This visual reflection is measured using a gauge. Different surfaces have different reflection angles. The gloss measurement is based on the amount of light reflected on the surface relative to the polished glass reference standard measured in luminous units (G.U.).

By examining the color, surface quality and composition characteristics of the samples in the triple phase diagram, 8 samples with a visually black effect were selected for further examination. The recipe compositions of the selected samples are given in Table 3.

Table 2 Recipe and L\*a\*b\* and gloss values obtained according to the triple phase diagram.

Samples	L*	a*	b*	Images	Gloss (GU)
25	6.17	-1.10	3.85	Semi glossy	32.00
26	2.84	0.55	-0.11	Mat	10.90
27	30.40	0.83	-0.01	Mat	9.60
28	3.36	0.80	-1,39	Glossy	95.60
32	8.96	-2.52	-0.14	Glossy	94.00
33	8.21	-1.89	-0.52	Glossy	24.90
34	12.27	-2.29	-0.10	Glossy	46.60
35	4.75	0.53	-0.16	Semi glossy	53.70

Although various colour systems have been developed to characterize glaze colours in ceramics, CIE (Commission Internationale de l'Eclairage) systems are most commonly used today. In the CIE system, the colour detection phenomenon is based on experimental observations. In colour measurement, the light source, the observer and the surface are parameters that should always be considered. Colour measurements are needed for the estimation of the new colours that will be formed as a result of the determination of the

colour according to the reference values, its continuity and mixing with different colours. Colour is also a basic parameter that determines the glaze surface's visuality.

Colours are expressed with a three-dimensional coordinate system and this system is called colour space. Colour parameters were determined by measuring the colour distribution of the dye-added glaze trials, the recipe of which was determined according to the triple diagram, which was visually checked after firing (Table 2). The colour values of the glaze surfaces are determined by making  $L^*a^*b^*$  measurements of the 3 main colours for each glaze recipe. By comparing the data obtained as a result of this test, it was examined how the changes in waste, CoO and  $Cr_2O_3$  additives affected the changes in colors. The result obtained is green if it has a negative sign, and red if it has a positive sign. The b value is the yellow-blue value. The result obtained is blue if it has a negative sign, and yellow if it has a positive sign [23-24].

Table 3 Recipe compositions of glazed tiles.

Samples	Steel Slag (%)	CoO (%)	Cr <sub>2</sub> O <sub>3</sub> (%)
25	25	37.5	37.5
26	25	25	50
27	25	12.5	62.5
28	25	0	75
32	12.5	50	37.5
33	12.5	37.5	50
34	12.5	25	62.5
35	12.5	12.5	75

While there is fixed iron ore waste in the selected 25, 26, 27 and 28 recipes, it is seen that the CoO ratio decreases and the  $Cr_2O_3$  ratio increases in the recipe. In recipe no. 25, a semi-matt 32° gloss value was obtained. While the presence of waste CoO and  $Cr_2O_3$  created matte and semi-gloss in the recipe, the presence of waste and  $Cr_2O_3$  resulted in high gloss and low  $L^*a^*b^*$  colour values. When recipe 26 and recipe 28 were compared, the darkening rate of the colour was the highest. The presence of CoO in the glaze recipe created a matt effect on the surface.

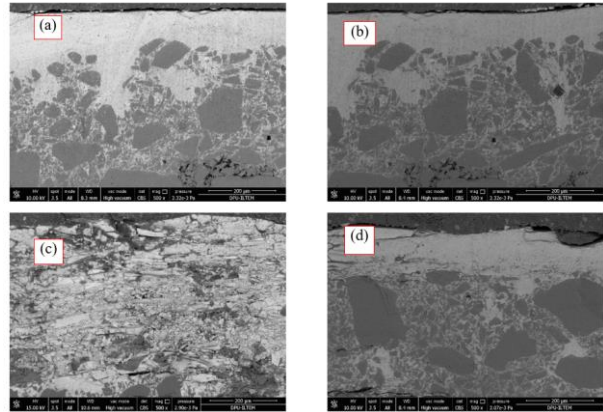


Figure 4 Microstructure images of coloured glazed samples; a) 25, b) 26, c) 27, d) 28.

In the SEM images of approximately 200-micron magnification given in Figure 4, it was determined that the oxides in the recipe compositions used as colouring dye in the glaze recipe were homogeneously distributed. As a result of the oxide-based EDX analyses given in Table 4; The presence of oxides varies proportionally in the direction of increase and decrease in the point analyzes at constant increasing CoO and decreasing  $Cr_2O_3$  ratios.

Table 4 EDX analyzes of the samples (recipes 25,26,27 and 28)

Oxides	Samples			
	25	26	27	28
Fe <sub>2</sub> O <sub>3</sub>	0.20	0.00	1.43	0.00
CoO	0.12	0.00	3.66	0.00
Na <sub>2</sub> O	4.42	7.67	5.80	2.94
MgO	1.04	0.00	0.05	0.98
Al <sub>2</sub> O <sub>3</sub>	1.58	0.36	0.58	2.50
SiO <sub>2</sub>	41.02	79.57	46.24	79.64
PbO <sub>2</sub>	43.17	11.31	38.84	11.91
K <sub>2</sub> O	0.84	0.01	-	0.26
CaO	2.13	0.41	1.70	1.21
Cr <sub>2</sub> O <sub>3</sub>	-	0.66	1.70	0.56

When the SEM images in Figure 5 were examined, it was determined that there was a homogeneous microstructure in the colored glazed samples. However, it was determined that the glazes were damaged during the polishing process. While there is fixed iron ore waste in these recipes, it is seen that the CoO ratio decreases and the  $Cr_2O_3$  ratio



increases in the recipe. In recipe 32, the high gloss value was 94 degrees. While the presence of waste, CoO and Cr<sub>2</sub>O<sub>3</sub> created matte and semi-gloss in the recipe, the presence of waste and Cr<sub>2</sub>O<sub>3</sub> brought high gloss and low L\*a\*b\* values. When recipe 33 and recipe 28 were compared, the darkening rate of the colour was the highest. The presence of CoO caused some opacity on the surface.

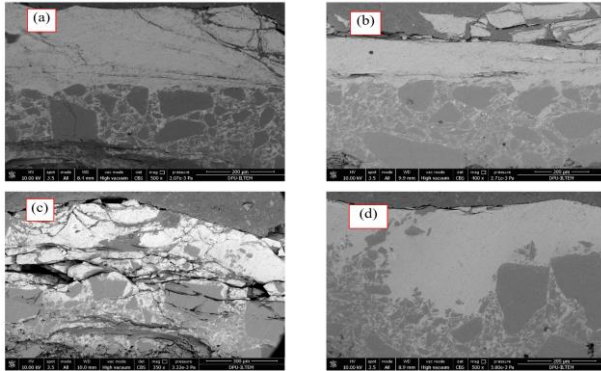


Figure 5 Microstructure images of coloured glazed samples; a) 32, b) 33, c) 34, d) 35

Table 5 EDX analysis of the samples (recipes 32,33,34 and 35)

Oxides	Samples			
	32	33	34	35
Fe <sub>2</sub> O <sub>3</sub>	-	-	0.01	-
CoO	-	-	-	0.34
Na O	3.08	4.14	3.47	2.71
MgO	0.18	-	-	0.24
Al <sub>2</sub> O <sub>3</sub>	0.60	-	0.70	0.80
SiO <sub>2</sub>	39.09	43.08	52.50	40.28
PbO <sub>2</sub>	48.44	48.49	39.00	49.51
CaO	2.01	-	1.74	3.00
Cr <sub>2</sub> O <sub>3</sub>	6.59	3.30	2.58	3.12

When the EDX analysis results and gloss values of the colour-glazed recipes 32, 33, 34 and 35 are examined, the presence of PbO<sub>2</sub> shows the gloss value in the recipes (Table 5). Among the samples examined, prescriptions 32 and 33 showed high gloss, while recipes 34 and 35 showed semi-gloss properties. It can be said that the presence of alkali and alkaline earth oxides causes the semi-gloss feature [25].

In Figure 6, the use of some of the compositions in which coloured glaze experiments were carried out, are given. While a much more colourful image was obtained in glazes, it was determined that the colours remained lighter in dyeing studies. It is thought that this situation causes the colour to be darker due to a thicker application in paint works. It has been seen that the real image of the colour is obtained in the painting studies.

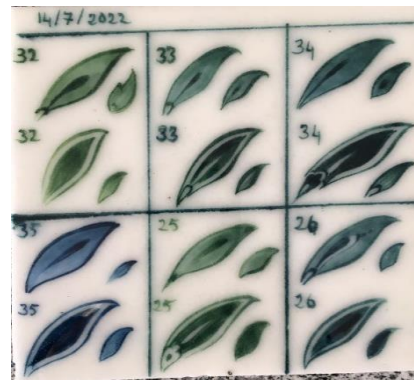


Figure 6 The image of dyeing studies of some compositions as colourant.

#### 4. CONCLUSIONS

In the study, the usability of waste steel slag as paint was examined by making recipe development studies over the triple phase diagram. The use of waste in glaze recipe has been evaluated by using it in low temperature glazes on high silica bodies. Glaze surfaces varied in the range of high gloss, semi-gloss and matte. With the change of oxides in the prescriptions, the change in L\*a\*b\* values and the rate of change in gloss values show differences. In the SEM-EDX examinations of the samples with high dark colour ratio, the effect of fixed waste ratio and varying oxide ratios on gloss, L\*a\*b\* was tried to be explained. Pigment application examples in underglaze pattern design are very diverse. Among the pigment recipes as 33, 34, 35, 25 and 26 the pattern design applications in Figure 6 are presented, and they show that they can be used as under-glaze paint applications and can be used as an alternative to under-glaze paint applications, especially

for low-temperature glazes. It has been seen that a wide colour scale can be obtained when this study is carried out in more.

### ***Acknowledgements***

This study was supported by the Republic of Turkey Strategy and Budget Presidency (Project No. 2018H040460). In addition, we would like to thank Kardemir Karabük Iron and Steel Industry for the waste raw material support they provided in the realization of this study, to Hüseyin Kızıl, Marwah Dawood, and İbrahim Dirbes for their contributions to the pre-tests, to Mehmet Akkaş from Dumlupınar University and Advanced Technologies Center (İLTEM), and to tile artist N. Nur AVLUPINAR for his help for the dyeing studies.

### ***Funding***

The author received no financial support for the research, authorship, and/or publication of this paper.

### ***The Declaration of Conflict of Interest/ Common Interest***

No conflict of interest or common interest has been declared by the author.

### ***The Declaration of Ethics Committee Approval***

The author declares that this document does not require ethics committee approval or any special permission.

### ***The Declaration of Research and Publication Ethics***

The author of the paper declares that he complies with the scientific, ethical, and quotation rules of SAUJS in all processes of the paper and that he does not make any falsification on the data collected. In addition, he declares that Sakarya University Journal of Science and its editorial board have no responsibility for any ethical violations that may be encountered and that this study has not been evaluated in any academic publication environment other than Sakarya University Journal of Science.

## **REFERENCES**

- [1] Z. Bayer Öztürk, K. Pekkan, E. Taşçı, S. Yılmaz, “The effect of granulated lead–zinc slag on aesthetic and microstructural properties of single-fired wall tile glazes”, Journal of the Australian Ceramic Society, vol. 56, no. 2, pp. 609-617, 2020.
- [2] Z. Bayer Öztürk, B. Atay, M. Çakı, N. Ay, “An investigation of color development by means of the factorial design in wall tile glazes with ferrochromium fly ash”, Indian Journal of Engineering and Materials Sciences, vol. 22, pp. 215–224, 2015.
- [3] L.Koroğlu, C. Pekşen, “The Replacement of Seashells with Calcite in White Ceramic Glaze Preparation”, Sakarya University Journal of Science, vol. 24, pp. 956-964, 2020.
- [4] M.Topal, E. Işıl Arslan Topal, S. Aslan, M. Kılıç, “Termik santral Uçucu külü, curufu ve arıtma çamurundan ağır metallerin liçlenebilirliği”, Sakarya University Journal of Science, vol. 15-2, pp. 97-104, 2011.
- [5] A. Kartal, Sır ve Sırlama Tekniği, Çizgi Matbaacılık, Banaz, 1998.
- [6] H. Yıldızay, E. Taşçı, “Lateritik nikel cevherinden elde edilen nikel-kobalt oksit kompozitinin stoneware sıradaki renk etkileri”, Afyon Kocatepe Üniversitesi Fen ve Mühendislik Bilimleri Dergisi vol. 19, pp. 204-211, 2019.
- [7] S. Yesilay, M. Cakı, R. Ceylantekin, “Recycling of AfyonIscehisar marble waste in transparent stoneware glaze recipes”, Journal Australian Ceramic Society, vol. 53, pp. 475–484, 2017.
- [8] N. Kılınc Mirdalı, “Inorganic wastes in glaze recipes and their effects on

- microstructure”, *Journal Australian Ceramic Society*, vol. 53, pp. 713–718, 2017.
- [9] B. Karasu, G. Kaya, A. Çakir, “Characterization of diopside-based glass-ceramic porcelain tile glazes containing borax solid wastes”, *Journal of Ceramic Processing Research*, vol. 12, pp. 135–139, 2011.
- [10] H. Cengizler, “Effect of calcination temperature on use of high-boron-content waste for low-temperature wall tile production”, *Ceramic International* vol. 48, pp. 6024-6036, 2022.
- [11] Z. Bayer Ozturk, E. Eren Gultekin, “Preparation of ceramic wall tiling derived from blast furnace slag”, *Ceramic International* vol. 41, pp. 12020–12026, 2015.
- [12] G. Binal, N. Ay, “The usage of magnesite production wastes in ceramic tile bodies”, *Journal of Ceramic Processing Research* vol. 15, pp. 107–111, 2014.
- [13] F. Andreola, L. Barbieri, F. Bondioli, “Agricultural waste in the synthesis of coral ceramic pigment”, *Dyes Pigments* vol. 94, pp. 207–211, 2012.
- [14] J.A. Labrincha, W. Hajjaji, M. P. Seabra, “Evaluation of metal-ions containing sludges in the preparation of black inorganic pigments”, *Journal of Hazardous Materials* vol. 185, pp. 619–625, 2011.
- [15] S. M. Toffoli, M. A. Abreu, “Characterization of a chromium-rich tannery waste and its potential use in ceramics”, *Ceramic International* vol. 35, pp. 2225–2234, 2009.
- [16] M. Batayneh, I. Marie, I. Asi, “Use of selected waste materials in concrete mixes”, *Waste Management* vol. 27, pp.1870–1876, 2007.
- [17] W. Jiang, X. Xiayi, T. Chen, L. Jianmin, X. Zhang, “Preparation and chromatic properties of  $\text{CoZrSiO}_4$  inclusion pigment via nonhydrolytic sol-gel method” *Dyes Pigments*, vol. 114, pp. 55–59, 2015.
- [18] K. Pekkan, Y. Gün, K. Kaymak, E. Taşçı, B. Karasu, “Farklı renk veren fosfor ışıl pigmentler açısından düşük sıcaklık sır bileşimlerinin belirlenip çini bünyelerde uygulanması” *Şişecam Teknik Bülten*, vol. 46-3, no. 232, pp.20-27, 2017.
- [19] M. Erdemoğlu, M. Göktaş, “Mermer artıklarından katma değeri yüksek ileri seramik tozların üretimi”, *Mermer Madenciliğinde Çevresel Yaklaşımlar Muğla Büyükşehir Belediyesi yayınevi*, Basım sayısı:1, Sayfa Sayısı 235-252.
- [20] H. Yıldızay, E. Taşçı, *Mühendislik Alanında Teori ve Araştırmalar*, Bölüm adı: “Ni-Co kompozit atığının borlu sırlarda etkilerinin incelenmesi” *Serüven Yayınevi*, Basım sayısı:1, Sayfa Sayısı 105, 2022.
- [21] H. Yıldızay, E. Taşçı, *Mühendislik Alanında Akademik Araştırma ve Değerlendirmeler*, Bölüm adı: “Ni-Co kompozitinin borlu sırlarda etkilerinin incelenmesi” *Serüven Yayınevi*, Basım sayısı:1, Sayfa Sayısı 136, 2021.
- [22] Tunçgenç, M., “Genel Boya Bilgileri”, *Teknik Bülten*, Akzo Nobel Kemipol A.Ş., 2004.
- [23] B.N Altay, “Dijital Baskı Sisteminde Kullanılan Baskı altı Malzemelerinin Renk Evrenine Etkisinin Tespiti”, *Yüksek Lisans Tezi*, Marmara Üniversitesi,13- 26, 2010.

- [24] Kodak, Introduction to Color and Printing, Internal Self-Study Guide. ABD, 2008.
- [25] Z. Bayer Öztürk, A. Can, D. Yarımçam, “Toprak Alkali Kaynağı Hammaddelerin Vitrikiye Sırlarında Ergimeye Olan Etkisinin İncelenmesi”, El-Cezerî Fen ve Mühendislik Dergisi vol. 8-1, pp. 195-201, 2021).



SAKARYA ÜNİVERSİTESİ

# FEN BİLİMLERİ ENSTİTÜSÜ DERGİSİ

Sakarya University Journal of Science  
SAUJS

ISSN 1301-4048 | e-ISSN 2147-835X | Period Bimonthly | Founded: 1997 | Publisher Sakarya University |  
<http://www.saujs.sakarya.edu.tr/>

Title: Common Solutions to Stein Inequalities

Authors: Şerife YILMAZ, Birgül AKSOY

Received: 2023-03-05 00:00:00

Accepted: 2023-07-25 00:00:00

Article Type: Research Article

Volume: 27

Issue: 5

Month: October

Year: 2023

Pages: 1097-1103

How to cite

Şerife YILMAZ, Birgül AKSOY; (2023), Common Solutions to Stein Inequalities.

Sakarya University Journal of Science, 27(5), 1097-1103, DOI:

10.16984/saufenbilder.1260438

Access link

<https://dergipark.org.tr/tr/journal/1115/issue/80257/1260438>

New submission to SAUJS

<http://dergipark.gov.tr/journal/1115/submission/start>

## Common Solutions to Stein Inequalities

Şerife YILMAZ<sup>\*1</sup> , Birgül AKSOY<sup>2</sup> 

### Abstract

In this paper for linear discrete time switched systems, the problem of existence of a common solution to Stein inequalities is considered. A sufficient condition for robust Schur stability of a matrix polyope by using Schur complement lemma and a necessary and sufficient condition for the existence of a common solution of Stein equation are given. As in the case of continuous time systems, the problem of existence of a common solution is reduced to a convex optimization one. An efficient solution algorithm which requires solving a linear minimax problem at each step is suggested. The algorithm is supported with a number of examples from the literature and observed that the method desired results fastly.

**Keywords:** Discrete-time system, Schur stability, Stein equation, common quadratic Lyapunov function, Schur complement

### 1. INTRODUCTION

Consider discrete-time system

$$x(k+1) = Ax(k), \quad (k = 1, 2, 3, \dots) \quad (1)$$

where  $x(k) \in \mathbb{R}^n$  and  $A \in \mathbb{R}^{n \times n}$ , where  $\mathbb{R}^{n \times n}$  is the set of  $n \times n$  dimensional real matrices. If all eigenvalues of  $A$  lie in the open unit disc of the complex plane then  $A$  is called Schur (stable) matrix. The Schur stability of  $A$  guarantees asymptotical stability of the system (1). An equivalent condition for the asymptotical stability of (1) is the existence of a positive definite matrix  $P > 0$  such that

$$A^T P A - P < 0, \quad (2)$$

where “ $< 0$ ” means the negative definiteness. The matrix inequality (2) is called the Stein inequality and for  $Q > 0$  the matrix equation  $A^T P A - P = -Q$  is called the Stein equation for (1). In this case the function  $V(x) = x^T P x$  is a discrete time Lyapunov function for system (1).

Consider discrete-time switched system

$$x(k+1) = A_i x(k) \quad (3)$$

where  $A_i, (i = 1, 2, \dots, N)$  are Schur matrices. If the following system of matrix inequalities

$$A_i^T P A_i - P < 0, \quad (i = 1, 2, \dots, N) \quad (4)$$

\* Corresponding author: serifeyilmaz@mehmetakif.edu.tr (Ş. YILMAZ)

<sup>1</sup> Mehmet Akif Ersoy University, Burdur, Türkiye

<sup>2</sup> Eskişehir Technical University, Eskişehir, Türkiye

E-mail: b\_aksoy@anadolu.edu.tr

ORCID: <https://orcid.org/0000-0002-7561-3288>, <https://orcid.org/0000-0002-9502-3648>



is satisfied for a  $P > 0$  then the positive definite matrix  $P$  is called a common solution and the function  $V(x) = x^T P x$  is called common Lyapunov function of system (3). In this paper we consider the problem of existence and evaluation of a common Lyapunov function for (3).

Stein equations and inequalities have been investigated in many works (see [1-3]).

In [1], necessary and sufficient conditions for the existence of a common quadratic Lyapunov function (CQLF) are given for two second-order discrete-time systems. In [2], the existence of parameter-dependent quadratic Lyapunov functions for finite set of Hurwitz stable matrices is considered via LMI method. In [3], the relationship between Lyapunov and Stein equations is given by using the Cayley transformation. Common solutions to matrix inequalities corresponding to continuous-time switched systems have been investigated in [4-11]. In [4], it is shown that provided the CQLF for pairwise commutative matrices by solving a sequence of Stein equations. In [5], LMI method is given for the common solution of matrix inequalities. In [6], it is shown that a CQLF exists if the Lie-algebra generated by the matrices is solvable. In [7], necessary and sufficient conditions for the existence a CQLF for a pair of second-order linear continuous-time systems are derived, and a constructive procedure is described for finding a CQLF when it exists.

In this paper we investigate system of matrix inequalities (4) and give a necessary and sufficient condition for the existence of a common solution  $P > 0$ . Our approach is based on the results obtained in [8].

## 2. COMMON SOLUTIONS

Consider the following matrix polytope

$$\mathcal{A} = \{A(\alpha) = \alpha_1 A_1 + \alpha_2 A_2 + \dots + \alpha_N A_N : \alpha_1 + \alpha_2 + \dots + \alpha_N = 1, 0 \leq \alpha_i \leq 1, i = 1, 2, \dots, N\} \quad (5)$$

with the  $A_i, (i = 1, 2, \dots, N)$ . Here the matrices  $A_i$  are called extreme (generator) matrices of the matrix polytope  $\mathcal{A}$ . Firstly we show that if  $P > 0$  is a common solution to (4) then it is a common solution to all polytope  $\mathcal{A}$ , that is for all  $A \in \mathcal{A}$  the matrix inequality

$$A^T P A - P < 0 \quad (6)$$

is satisfied.

In the Hurwitz case the proof of this statement is straightforward due to linearity of the Lyapunov inequality  $A_i^T P + P A_i < 0$  with respect to  $A_i$ . In the Schur case we will use the following proposition named the Schur complement lemma.

**Lemma 1 ([2]):** Let a matrix  $M \in \mathbb{R}^{(n+m) \times (n+m)}$  be partitioned as

$$M = \begin{bmatrix} M_1 & M_2 \\ M_2^T & M_3 \end{bmatrix},$$

where  $M_1 \in \mathbb{R}^{n \times n}$ ,  $M_2 \in \mathbb{R}^{n \times m}$ ,  $M_3 \in \mathbb{R}^{m \times m}$ ,  $M_1$  and  $M_3$  are symmetric and  $M_3$  is invertible. Then  $M > 0 \Leftrightarrow M_3 > 0$  and  $M_1 - M_2 M_3^{-1} M_2^T > 0$ .

**Theorem 1:** Let the polytope  $\mathcal{A}$  (5) be given and  $P > 0$  satisfies (4). Then for all  $A \in \mathcal{A}$  the inequality (6) is satisfied and consequently the family  $\mathcal{A}$  is robustly Schur stable.

**Proof:** Take  $M_1 = M_3 = P > 0$ ,  $M_2 = A_i^T P$ . Then

$$M_1 - M_2 M_3^{-1} M_2^T = P - A_i^T P P^{-1} (A_i^T P)^T = P - A_i^T P A_i > 0,$$

since  $P$  satisfies (4). By Lemma 1

$$\begin{bmatrix} P & A_i^T P \\ P A_i & P \end{bmatrix} > 0. \quad (7)$$

Multiplication both sides of (7) by  $\alpha_i$  and summation from  $i = 1$  to  $i = N$  gives

$$\begin{bmatrix} P & A^T(\alpha)P \\ PA(\alpha) & P \end{bmatrix} > 0 \quad (8)$$

(note that due to  $\alpha_1 + \alpha_2 + \dots + \alpha_N = 1$  there exists  $i$  such that  $\alpha_i > 0$ ). Applying Lemma 1 in the reverse direction we obtain

$$A^T(\alpha)PA(\alpha) - P < 0$$

which proves that for all  $A \in \mathcal{A}$  the inequality (6) is satisfied.

For a given matrix  $A$  the transformation

$$A \rightarrow \tilde{A} = (A + I)^{-1}(A - I)$$

is called the Cayley transformation, where  $I$  is the identity matrix.

If all eigenvalues of  $A \in \mathbb{R}^{n \times n}$  lie in the open left half plane then  $A$  is called Hurwitz (stable) matrix.

**Theorem 2 ([3]):**

- 1) If  $A$  is Schur matrix then  $\tilde{A}$  is Hurwitz matrix.
- 2) If  $P > 0$  satisfies Lyapunov inequality  $\tilde{A}^T P + P \tilde{A} < 0$  then the same  $P$  satisfies Stein inequality  $A^T P A - P < 0$ .

Due to Theorem 2 we have the following

**Theorem 3:** Assume that the matrices  $A_i$ , ( $i = 1, 2, \dots, N$ ) are given and  $\tilde{A}_i = (A_i + I)^{-1}(A_i - I)$ . Then  $P$  satisfies (4) if and only if

$$\tilde{A}_i^T P + P \tilde{A}_i < 0 \quad (i = 1, 2, \dots, N). \quad (9)$$

Now consider the existence and evaluation problem of  $P > 0$  satisfying (4). By Theorem 3, we can construct a new family  $\{\tilde{A}_1, \dots, \tilde{A}_N\}$  which is Hurwitz and use algorithm from [8]. On the other hand, by definition, at this approach at each  $i$  the inverse of  $(A_i + I)$  should be calculated and if an eigenvalue of  $A_i$  is near  $-1$  then  $\tilde{A}_i$  may have infinitely

large entries which is an undesirable situation. An example of this situation is given below.

**Example 1:** Consider the matrix

$$A = \begin{bmatrix} -20.8043 & 21.8113 & 3.9371 \\ -17.8239 & 18.5309 & 2.8413 \\ 1.9749 & -2.0749 & -0.6846 \end{bmatrix}.$$

Its eigenvalues are

$$-0.999363, -0.984077, -0.974559$$

and

$$(A + I)^{-1}(A - I) = \begin{bmatrix} -9.34 \times 10^7 & 1.16 \times 10^8 & 1.15 \times 10^8 \\ -8.7 \times 10^7 & 1.08 \times 10^8 & 1.07 \times 10^8 \\ 1.23 \times 10^7 & -1.53 \times 10^7 & -1.52 \times 10^7 \end{bmatrix}.$$

**Theorem 4:** Let the matrix  $A \in \mathbb{R}^{n \times n}$  be Schur matrix and there exists a symmetric matrix  $P_* \in \mathbb{R}^{n \times n}$  such that  $A^T P_* A - P_* < 0$ . Then  $P_* > 0$ .

**Proof:** Denote  $Q = P_* - A^T P_* A > 0$ . Then  $A^T P_* A - P_* = -Q$ . This equality can be written as

$$[(A^T - I)P_*(A + I) + (A^T + I)P_*(A - I)] = -2Q$$

Left multiplication by  $(A^T + I)^{-1}$ , right multiplication by  $(A + I)^{-1}$  gives (the inverses exist, since  $A$  is Schur matrix)

$$(A^T + I)^{-1}(A^T - I)P_* + P_*(A - I)(A + I)^{-1} = -2(A^T + I)^{-1}Q(A + I)^{-1}. \quad (10)$$

Since the matrix  $C = (A + I)^{-1}$  is nonsingular,

$$(A^T + I)^{-1}Q(A + I)^{-1} = [(A + I)^{-1}]^T Q(A + I)^{-1} = C^T Q C > 0.$$

Since  $(A - I)(A + I)^{-1} = (A + I)^{-1}(A - I)$ , from (10) it follows that

$$\tilde{A}^T P_* + P_* \tilde{A} < 0. \quad (11)$$



By Theorem 1  $\tilde{A}$  is Hurwitz matrix and by Lyapunov theorem  $P_* > 0$ .

### 3. THE EXISTENCE THEOREM

In this section we give number of propositions and the existence theorem without proofs. The proofs of these results are similar to the proofs in the Hurwitz case which have been carried out in [8], therefore are omitted.

Define  $d = \frac{n(n+1)}{2}$ ,  $X = [-1,1]^d$ , variable symmetric matrix

$$S(x) = \begin{bmatrix} x_1 & x_2 & \cdots & x_n \\ x_2 & x_{n+1} & \cdots & x_{2n-1} \\ \vdots & \vdots & \ddots & \vdots \\ x_n & x_{2n-1} & \cdots & x_d \end{bmatrix}$$

and convex positive homogeneous function

$$\begin{aligned} \varphi(x) &= \max_i \lambda_{\max}(A_i^T S(x) A_i - S(x)) \\ &= \max_i \max_{\|v\|=1} v^T [A_i^T S(x) A_i - S(x)] v \\ &= \max_{i, \|v\|=1} f(x, i, v), \end{aligned} \tag{12}$$

where  $f(x, i, v) = v^T [A_i^T S(x) A_i - S(x)] v$ .

**Proposition 1 ([8]):** Take any point  $\hat{x} \in X$ . Let the pair  $(\hat{i}, \hat{v})$  be a maximizing pair in (12) and  $\hat{g}$  be the gradient vector of the linear map  $x \mapsto f(x, \hat{i}, \hat{v})$ . Then  $\varphi(\hat{x}) = \langle \hat{x}, \hat{g} \rangle$  and  $\varphi(x) \geq \langle x, \hat{g} \rangle$  for all  $x \in X$ .

**Proposition 2:**  $\|\hat{g}\| \leq \sqrt{2}(M^2 + 1)$ , where  $M = \max_{1 \leq i \leq N} \|A_i\|$ , and  $\|A_i\|$  is the Frobenius norm of  $A_i$ .

**Proof:** The norm  $\|f\|$  of the linear functional  $f(x, \hat{i}, \hat{v}) = \langle x, \hat{g} \rangle$  equals  $\|\hat{g}\|$  and therefore ([9], p. 188)

$$\begin{aligned} \|\hat{g}\| &= \|f\| \\ &= \max_{\|x\| \leq 1} |f(x, \hat{i}, \hat{v})| \\ &= \max_{\|x\| \leq 1} |\hat{v}^T [A_i^T S(x) A_i - S(x)] \hat{v}| \\ &\leq \max_{\|x\| \leq 1} (|\hat{v}^T A_i^T S(x) A_i \hat{v}| + |\hat{v}^T S(x) \hat{v}|) \\ &\leq \max_{\|x\| \leq 1} (\|A_i^T S(x) A_i\| + \|S(x)\|) \\ &\leq (M^2 + 1) \max_{\|x\| \leq 1} \|S(x)\|. \end{aligned}$$

Since  $\|S(x)\|^2 \leq 2(x_1^2 + x_2^2 + \cdots + x_d^2) \leq 2$  for  $\|x\| \leq 1$ ,  $\|\hat{g}\| \leq \sqrt{2}(M^2 + 1)$ .

Let  $x^1$  be any nonzero vector from  $X$ , and  $g^1$  is calculated as in Proposition 1,  $s_1 = \min_{x \in X} \langle x, g^1 \rangle$  and  $x^2$  be a minimizer, that is  $s_1 = \langle x^2, g^1 \rangle$ . Having chosen  $x_1, x_2, \dots, x_k$ , let  $x^{k+1}$  be a minimizer in

$$s_k = \min_{x \in X} \max_{1 \leq i \leq k} \langle x, g^i \rangle. \tag{13}$$

**Proposition 3:** Assume that  $x^1 \in X$ ,  $x^1 \neq 0$ . There exists a common solution  $P > 0$  to (4) if and only if  $\varphi(x^{k_*}) < 0$  for some  $k_* \in \{1, 2, 3, \dots\}$ . If  $\lim_{k \rightarrow \infty} s_k = 0$  then common solution does not exist.

Solution of the linear minimax problem (13) can be obtained from the solution of the following linear programming (LP) problem.

**Proposition 4:** Let  $(x^*, t^*)$  be a solution of the following LP problem

$$\begin{aligned} t &\rightarrow \min \\ -1 &\leq x_i \leq 1, \quad j = 1, 2, \dots, d \\ -\sigma &\leq t \leq \sigma, \quad \sigma = \sqrt{2d}(M^2 + 1) \\ \langle x, g^i \rangle &\leq t \quad i = 1, 2, \dots, k. \end{aligned}$$

Then  $s_k = t^*$  and  $x^*$  is minimizer in (12).

The proofs of Propositions 3 and 4 follows the same scheme as the proofs of Theorem 5 and Proposition 6 in [8].

The following examples are taken from [1] and there it has been analytically shown the existence of a common solution for Example

2 and the nonexistence of a common solution for Example 3.

**Example 2 ([1]):** Consider the following Schur stable matrices

$$A_1 = \begin{bmatrix} 0.8 & 0 \\ 0 & 0.8 \end{bmatrix}, \quad A_2 = \begin{bmatrix} 0.35 & -0.25 \\ 0.50 & 0.85 \end{bmatrix}.$$

Let  $x^1 = (1,0,0)^T \in X = [-1,1]^3$ . Maximization of  $\lambda_{\max}(A_m^T S(x^1) A_m - S(x^1))$  with respect to  $m$  gives  $m = 2$  and

$$\lambda_{\max}(A_2^T S(x^1) A_2 - S(x^1)) = 0.0705.$$

The unit eigenvector of  $A_2^T S(x^1) A_2 - S(x^1)$  is

$$v^1 = (-0.091901, 0.995768)^T.$$

Since  $\varphi(x^1) = 0.0705$ , this process is continued for a new point  $x^2$ . The gradient vector is

$$g^1 = (0.0705, -0.2670, -0.3508)^T,$$

$$s_1 = \min_{x \in X} \langle x, g^1 \rangle = -0.688$$

and the minimizer is  $x^2 = (-1, 1, 1)^T$ . Repeating the procedure according (13) we obtain the following.

$$\begin{aligned} k = 2, \quad m = 2, \\ \varphi(x^2) = 1.520, s_2 = -0.419, \\ k = 3, \quad m = 1, \\ \varphi(x^3) = -0.172 < 0, \end{aligned}$$

where  $x^3 = (1, 0.521365, 1)^T$ . Consequently by Proposition 3 the matrix

$$S(x^3) = \begin{bmatrix} 1 & 0.521365 \\ 0.521365 & 1 \end{bmatrix}$$

is a common solution to Stein equation for the matrices  $\{A_1, A_2\}$ .

**Example 3 ([1]):** Consider the Schur stable matrices

$$A_1 = \begin{bmatrix} 0.8 & 0 \\ -1 & -0.8 \end{bmatrix}, \quad A_2 = \begin{bmatrix} 0.8 & 0 \\ 1 & -0.8 \end{bmatrix},$$

$$A_3 = \begin{bmatrix} 0.95 & -0.08 \\ 0.1 & 0.95 \end{bmatrix}.$$

It is known that these matrices have no CQLF [1]. Starting from  $x^1 = (1,0,0)^T \in X = [-1,1]^3$  and carrying out calculations as in Example 2 we obtain  $s_k = 0$  for  $k \geq 4$ . Therefore there is no CQLF for  $\{A_1, A_2, A_3\}$  by Proposition 3.

**Example 4:** Given Schur stable matrices

$$A_1 = \begin{bmatrix} 0.27 & 0.78 & -0.36 \\ 0 & -0.77 & 0.1 \\ -0.3 & -0.2 & -0.81 \end{bmatrix},$$

$$A_2 = \begin{bmatrix} -0.85 & 0.13 & -0.15 \\ 0.07 & -0.92 & 0 \\ 0.15 & 0 & -0.97 \end{bmatrix},$$

$$A_3 = \begin{bmatrix} 0.2 & 0.97 & 0.21 \\ -0.4 & -1.2 & 0.1 \\ 0.81 & 0.5 & -0.6 \end{bmatrix}.$$

Let  $x^1 = (1,0,0,0,0)^T \in X = [-1,1]^6$ . Maximization of  $\lambda_{\max}(A_m^T S(x^1) A_m - S(x^1))$  with respect to  $m$  gives  $m = 3$  and  $\varphi(x^1) = \lambda_{\max}(A_3^T S(x^1) A_3 - S(x^1)) = 1.005$ .

The unit eigenvector of  $A_3^T S(x^1) A_3 - S(x^1)$  is

$$v^1 = (0.100500, 0.972409, 0.210521)^T.$$

Since  $\varphi(x^1) > 0$ , this process is continued for a new point  $x^2$ . The gradient vector is

$$g^1 = (1.005, -2.585, 0.846, 0.461, -1.456, 0.15)^T,$$

$s_1 = -6.505$  and the minimizer is  $x^2 = (-1, 1, -1, -1, 1, -1)^T$ . The calculations give the following values:

$$\begin{aligned}
 k = 2, \quad m = 3, \\
 \varphi(x^2) = 2.746 > 0, s_2 = -1.077, \\
 k = 3, \quad m = 1, \\
 \varphi(x^3) = 0.928 > 0, s_3 = -0.558, \\
 \vdots \\
 k = 14, \quad m = 2, \\
 \varphi(x^{14}) = 0.020 > 0, s_{14} = -0.010, \\
 k = 15, \quad m = 3, \\
 \varphi(x^{15}) = -0.001647 < 0,
 \end{aligned}$$

where  
 $x^{15} = (0.684, 0.533, -0.170, 1, -0.204, 0.254)^T$

and the matrix

$$S(x^{15}) = \begin{bmatrix} 0.684 & 0.533 & -0.170 \\ 0.533 & 1 & -0.204 \\ -0.170 & -0.204 & 0.254 \end{bmatrix}$$

is a common solution for the Schur stable matrices  $\{A_1, A_2, A_3\}$ .

#### 4. CONCLUSION

In this paper, we considered the problem of existence and evaluation of a common solution to Stein equation for a finite number of real Schur stable matrices. We gave a sufficient condition for robust Schur stability of a matrix polyope by using Schur complement lemma and a necessary and sufficient condition for the existence of a common solution of Stein equation. In addition we gave a procedure that finds one of these solutions effectively in case a common solution of the Stein equation exists. We supported the method with a number of examples from the literature and observed that the method desired results fastly.

#### *Funding*

The authors have no received any financial support for the research, authorship or publication of this study.

#### *Authors' Contribution*

The authors contributed equally to the study.

#### *The Declaration of Conflict of Interest/ Common Interest*

No conflict of interest or common interest has been declared by the authors.

#### *The Declaration of Ethics Committee Approval*

This study does not require ethics committee permission or any special permission.

#### *The Declaration of Research and Publication Ethics*

The authors of the paper declare that they comply with the scientific, ethical and quotation rules of SAUJS in all processes of the paper and that they do not make any falsification on the data collected. In addition, they declare that Sakarya University Journal of Science and its editorial board have no responsibility for any ethical violations that may be encountered, and that this study has not been evaluated in any academic publication environment other than Sakarya University Journal of Science.

#### REFERENCES

- [1] M. Akar, K. S. Narendra, "On the existence of common quadratic Lyapunov functions for second-order linear time-invariant discrete-time systems," *International Journal of Adaptive Control and Signal Processing*, vol. 16, pp. 729-751, 2002.
- [2] J. C. Geromel, M. C. de Oliveira, L. Hsu, "LMI characterization of structural and robust stability," *Linear Algebra and its Applications*, vol. 285, pp. 69-80, 1998.
- [3] O. Taussky, "Matrices C with  $C^n \rightarrow 0$ ," *Journal of Algebra*, vol. 1, pp. 5-10, 1964.
- [4] K. S. Narendra, J. A. Balakrishnan, "Common Lyapunov function for stable LTI systems with commuting A-matrices," *IEEE Transactions on*

- Automatic Control, vol. 39(12), pp. 2469-2471, 1994.
- [5] S. P. Boyd, L. El Ghaoui, E. Feron, V. Balakrishnan, “Some standard problems involving LMIs” in Linear Matrix Inequalities in System and Control Theory, Philadelphia, PA, USA: SIAM, 1994, ch. 2, pp. 7-35.
- [6] D. Liberzon, J. P. Hespanha, A. S. Morse, “Stability of switched systems: a Lie-algebraic condition,” Systems & Control Letters, vol. 37, pp. 117–122, 1999.
- [7] R. N. Shorten, K. S. Narendra, “Necessary and sufficient conditions for the existence of a common quadratic Lyapunov function for M stable second order linear time-invariant systems,” in Proceedings of the American Control Conference, Chicago, IL, USA, 2000, pp. 359–363.
- [8] V. Dzhafarov, T. Büyükköroğlu, “On one inner point algorithm for common Lyapunov functions,” Systems & Control Letters, vol. 167, pp. 1-4, 2022.
- [9] E. Kreyszig, Introductory Functional Analysis with Applications, John Wiley & Sons, 1978.
- [10] Ş. Yılmaz, “Hurwitz Stability of Matrix Segment and The Common Solution Set of 2 and 3-Dimensional Lyapunov Equations,” Sakarya University Journal of Science, vol. 24, no. 2, pp. 357-364, 2020.
- [11] Ş. Yılmaz, “Common quadratic Lyapunov functions for two stable matrices,” Eskişehir Technical University Journal of Science and Technology B - Theoretical Sciences, vol. 10, no.1, pp. 18-26, 2022.



SAKARYA ÜNİVERSİTESİ

# FEN BİLİMLERİ ENSTİTÜSÜ DERGİSİ

Sakarya University Journal of Science  
SAUJS

ISSN 1301-4048 | e-ISSN 2147-835X | Period Bimonthly | Founded: 1997 | Publisher Sakarya University |  
<http://www.saujs.sakarya.edu.tr/>

Title: One-step and Cost-effective Conversion of Polyimide to Graphene by Utilizing a Desktop Laser

Authors: Nihan AYDEMİR

Received: 2022-11-09 00:00:00

Accepted: 2023-07-30 00:00:00

Article Type: Research Article

Volume: 27

Issue: 5

Month: October

Year: 2023

Pages: 1104-1110

How to cite

Nihan AYDEMİR; (2023), One-step and Cost-effective Conversion of Polyimide to Graphene by Utilizing a Desktop Laser. Sakarya University Journal of Science, 27(5), 1104-1110, DOI: 10.16984/saufenbilder.1201851

Access link

<https://dergipark.org.tr/tr/journal/1115/issue/80257/1201851>

New submission to SAUJS

<http://dergipark.gov.tr/journal/1115/submission/start>

# One-step and Cost-effective Conversion of Polyimide to Graphene by Utilizing a Desktop Laser

Nihan AYDEMİR<sup>1\*</sup> 

## Abstract

Herein a one-step, cost-effective, chemical-free, and versatile graphene fabrication by employing a CO<sub>2</sub> laser is presented. A cost-effective desktop laser, compared to expensive and bulky lasers reported in the literature, is utilized for the conversion of polyimide films to graphene. Optimization of the fabrication is enabled by the examination of laser parameters such as laser power and scanning speed. Also, various 2D pattern drawings and in-situ fabrication were realized by the Laser Draw software. Furthermore, characterization experiments such as Scanning Electron Microscopy (SEM), X-Ray Diffraction (XRD), Raman Spectroscopy, and X-Ray Photon Spectroscopy (XPS) were performed to prove the successive graphene fabrication.

**Keywords:** Graphene, laser scribed graphene, CO<sub>2</sub> laser

## 1. INTRODUCTION

Graphene has gained a considerable amount of attention in the last decade due to its high conductivity, super capacitive nature, enhanced mechanical properties as well as high thermal conductivity [1-3]. Hence, it has been utilized in various applications such as supercapacitors[4, 5], biosensors[6, 7], Li-ion batteries[8, 9], solar cells[10], field effect transistors [11, 12] etc. Due to the high demand for such applications, researchers investigated and developed different fabrication methods for graphene[2, 3]. The top-down approaches included mechanical exfoliation [13], chemical exfoliation[14], electrochemical exfoliation [14], and chemical synthesis [15] whereas bottom-up approaches were pyrolysis[16], epitaxial

growth [17], chemical vapor deposition (CVD) [18]etc.

The first method was suggested based on the mechanical exfoliation of graphene layers from graphite by using an adhesive scotch tape [13]. The consecutive stick and pull moves on subsequent surfaces led to the deposition of a few layers of graphene which was enough to investigate the properties of the material. Even though this study was awarded by Nobel Prize in 2010, clearly a more robust, repeatable, and scalable methodology is needed for further studies. One notable strategy is the Hummers' method where graphite is chemically exfoliated to form graphene oxide in the presence of strong oxidants such as H<sub>2</sub>SO<sub>4</sub>, KMnO<sub>4</sub>, and NaNO<sub>3</sub> and then obtained graphene oxide is treated by reducing agents such as hydrazine and

\* Corresponding author: naydemir@gtu.edu.tr (N. AYDEMİR)

<sup>1</sup> Gebze Technical University, Kocaeli, Türkiye

ORCID: <https://orcid.org/0000-0002-4345-186X>



NaBH<sub>4</sub> to form reduced graphene oxide (RGO) [14, 15].

In the case of electrochemical exfoliation, the graphite rod is connected as the working electrode (WE) and a platinum rod as the counter electrode (CE) [19]. Both electrodes are inserted into an electrolyte solution containing (NH<sub>4</sub>)<sub>2</sub>SO<sub>4</sub> and a direct potential of 10V is applied for 3-5 minutes yielding dispersed graphene flakes on the top of the solution [19]. Both Hummers' and electrochemical exfoliation produces graphene in powder form whereby further steps and additives are required for film fabrication.

Chemical Vapour Deposition (CVD) allows the production of either single or a few layers of graphene films. Either nickel (Ni) or copper (Cu) films are used as substrate [18]. The CVD chamber is purged with CH<sub>4</sub>/H<sub>2</sub> mixture and at high temperatures CH<sub>4</sub> decomposes leading C atoms to dissolve in the Ni or Cu substrate [18]. When the chamber is cooled, the C atoms diffuse out and join on the substrate surface to form hexagonal graphene structures [18]. Studies indicate that, in the case of Ni substrate, multiple layers of graphene are obtained whereas a single layer of graphene can be grown on Cu substrate. Despite yielding graphene films with high quality, high conductivity, and controllable thickness, CVD method requires expensive instrumentation and extensive labor which diminishes its applications in the short term.

Addressing the need of scalable and less labor-driven fabrication, Laser Scribed Graphene (LSG) or Laser Induced Graphene (LIG) was introduced whereby various organic materials can be utilized to produce graphene films via different types of lasers [20-23]. As the lasers are computer controlled, the films can be obtained in any shape, design, or pattern as desired. Hence, device fabrication can be proceeded in situ with the graphene film production. The laser reduction mechanism is based on 1)

absorption of the laser light by the material and 2) breaking down of functional groups due to the high and localized energy leaving carbon atoms behind, and 3) re-coordination of C atoms to form hexagonal graphene sheets [23].

First example of LSG was presented by El-Kady and Kaner whereby the graphene oxide (GO) solution was spin coated on PET substrates and consecutively reduced by a DVD writer laser with a wavelength of 405nm [20]. The laser absorption is crucial as the necessary energy for the graphene conversion is dependent on this step. One should note that each material might absorb laser at a distinctive wavelength range of value. Hence, lasers with different wavelengths have been utilized for various materials. For instance, the graphene conversion from polyimide (PI) films were realized with the CO<sub>2</sub> laser which has 10.6 μm wavelength [21]. The resulting film consisted of graphene flakes packed in a highly porous film with around 30 μm thickness and was applied in supercapacitor applications. CO<sub>2</sub> laser was also utilized for treating lignin films to produce graphene films which were used as electrochemical biosensors for the detection of glucose, lactate, and alcohol [24]. Despite the ease of fabrication, the major drawback for LIG production is the cost of the laser which usually starts from 20.000 USD. However, there are more cost-effective versions of this laser that can be bought from Asia.

Herein, the represented study employs a desktop K40 CO<sub>2</sub> laser that is worth only 500 USD. To the best of our knowledge, this is the first study utilizing K40 laser for the fabrication of LIG. The fabrication parameters were investigated and as well as detailed characterization such as Scanning Electron Microscopy (SEM), X-Ray Photon Spectroscopy (XPS), X-Ray Diffraction (XRD) and Fourier-transform infrared spectroscopy (FTIR) were performed.

## 2. MATERIALS AND METHODS

The desktop K40 CO<sub>2</sub> laser engraver was purchased from Peixu Tool Store in the Aliexpress e-commerce platform. Following the acquisition, the 40W default laser was changed with a 50W CO<sub>2</sub> laser tube to expand its potential to cut and engrave a wider range of materials. However, one should note that the default 40W laser is also sufficient for the graphene fabrication and the instrument can be used as acquired. Adhesive free Polyimide (PI) films with 100 μm thickness was obtained from Yatiz Electrics (Istanbul/Turkey) and they were used as acquired with no additional cleaning process. The characterization experiments were performed by using; Rigaku D-max RINT 220 for XRD measurements, Phillips XL 30 SFEG for SEM measurements, SPECS XRC 1000 for XPS measurements, Renishaw inVia Reflex Raman Microscope and Spectrometer for RAMAN measurements.

## 3. RESULTS AND DISCUSSIONS

### 3.1. Graphene Fabrication

The K40 Laser engraver/cutter utilized in this study can be seen in figure 1A. The system consists of a 50W CO<sub>2</sub> laser, optics to transfer and focus the laser beam on the substrate, a sample stage, a laptop computer, and a software (Figure 1a-1b). These types of lasers work in two distinctive modes namely cut or engrave. For the graphene fabrication the engrave mode is utilized. The Laser DRW 3 software was utilized for the laser control and pattern design. The main parameters effecting the graphene are laser power and scan speed which can be adjusted through the software. A range of power between 10-25 % of 50W was tested and found that power with %18 (±2) was best for repeatable graphene fabrication. The laser speed was adjusted to 375 mm/s with 1000 dpi setting.

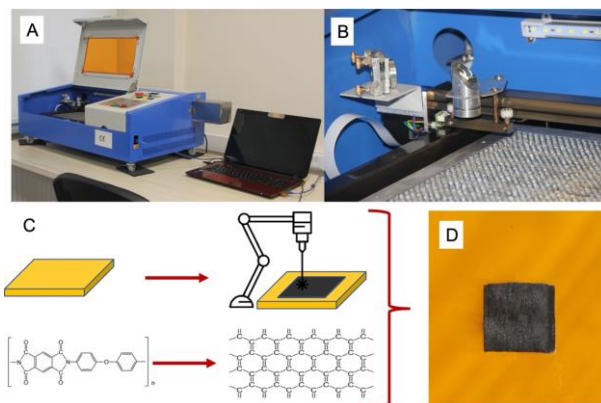


Figure 1 a) The K40 CO<sub>2</sub> laser system, b) Close up to optics, laser head, and sample stage c) Schematic representation of the working mechanism, d) Graphene film directly written on the PI surface.

The working mechanism of LIG is based on the absorbance of the laser light and the molecular conversions such as bond breakage due to the absorbed energy as well as the removal of certain molecules as gaseous side products and then re-arrangement of the remaining atoms [20,21]. When the laser beam reaches the surface, the energy is absorbed by the PI film and the bonds of functional groups are broken. Then, the remaining carbons come together in graphene form (Figure 1c). Indeed, the natural color of the PI is amber, whereas areas engraved with laser turn to black (Figure 1d). It is usually not possible to remove all the groups, hence a negligible amount of oxygen and hydrogen may remain as defects.

### 3.2. Characterization Results

Following the fabrication, obtained films were first characterized by SEM for visual inspection. Figure 2a represents the morphological difference between PI and graphene. Indeed, the PI film has a very smooth and flat surface, whereas graphene films are in foam form, extremely porous and consist of flakes with a few nanometers thickness (Figure 2c and figure 2d). These nanoflakes are packed in a foam type film which has a thickness of 30 μm (± 2μm) as it can be seen in Figure 2b. The nature of the graphene foam obtained by LIG method is proven itself to be a porous film consist of



connected nanoflakes similar to the observed in the literature [21].

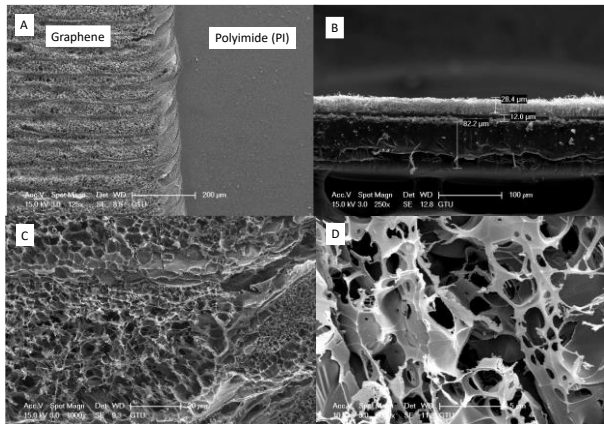


Figure 2 SEM micrographs of graphene films with magnifications of a) 125x, b) 1000x and c) 5000x, c) the cross-sectional image revealing the thickness of the graphene film

The crystallinity of the LIG was investigated by XRD (Figure 3) and also elemental analysis experiments were carried out through XRD and RAMAN studies (Figure 4 and Figure 5). The XRD pattern exhibits an intense peak centered at  $26.10$  ( $2\theta$ ) indicating a high degree of graphenization with multiple layers and a small peak at  $43.1$  ( $2\theta$ ) corresponds to in-plane structure (Figure 3) [21]. The spacing between planes of the graphene was calculated to be  $3.42 \text{ \AA}$ .

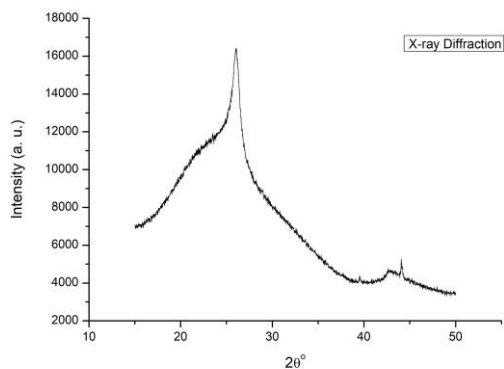


Figure 3 XRD analysis of Laser Scribed Graphene.

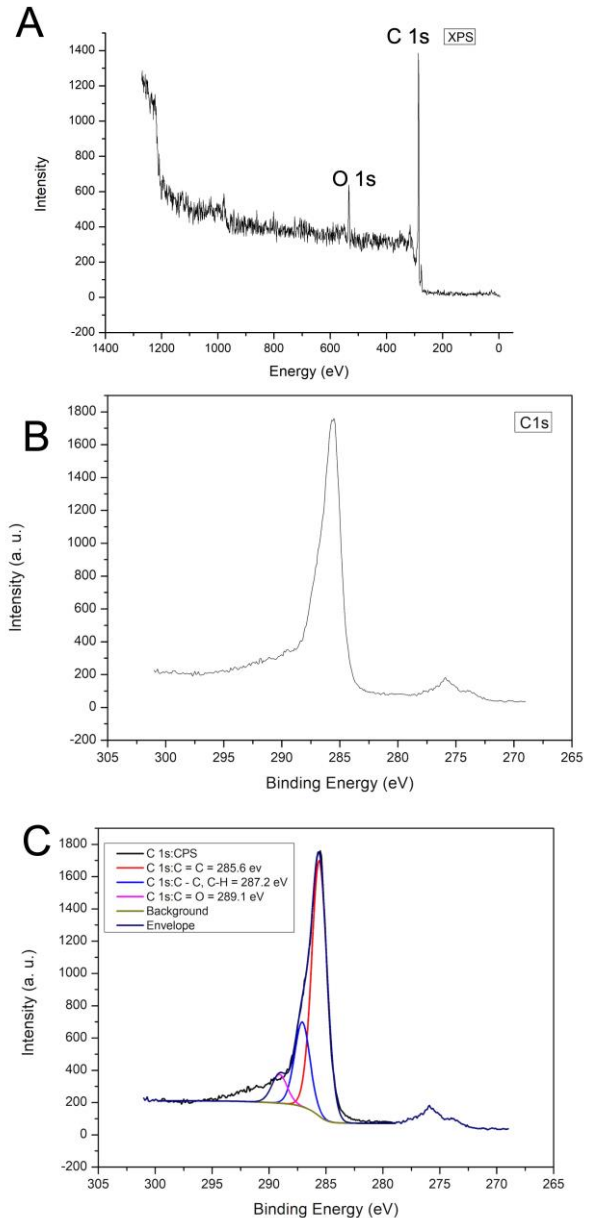


Figure 4 a) XPS Survey, b) XPS detailed C1s and c) fitted C1s analysis of the laser scribed graphene samples.

XPS survey spectrum reveals that obtained film contains mainly carbon presented at  $286 \text{ eV}$  and corresponds to  $sp^2$  carbons ( $C1s$ ) and a few amounts of oxygen presented at  $534 \text{ eV}$  and corresponds to  $O1s$  (Figure 4a) in agreement with the literature values [21]. There was no peak corresponding to Nitrogen which indicates the breakage of the N-C bonds and removal of the nitrogen as a gaseous side product. The further detailed analysis on the  $C1s$  (Figure 4b and 4c) revealed that a  $C=C$  bond at  $285.6 \text{ eV}$ ,  $C-C$

and C-H bonds at 287.2 eV and C=O bonds at 289 eV corresponds the existence of graphene with defects [25]. These defects make graphene more hydrophilic and hence they are desirable in the case of applications such as biosensors, liquid phase supercapacitors that performed in aqueous media [26]. The oxygen amount was found to be %17.14 and the carbon amount was %82.86 by calculating the area under each peak.

Raman spectrum of the LIG predominantly consists of three peaks which are referred to as D, G, and 2D bands (Figure5). The presence of the D band at the absence of D' band corresponds to the edges with high density due to the foamy nature of the LIG. D band is also a representation of the defects within the graphene structure which is in agreement with the XPS survey results that represents a few amount of oxygen in the LIG. The G band represents the stretching vibration of the sp<sup>2</sup> carbon lattice. The 2D band is the secondary D band which arises from the stacking of graphene sheets. The I<sub>D</sub>/I<sub>G</sub> ratio has been calculated as 0.52 which also represents the high-density edges of the foamy structure.

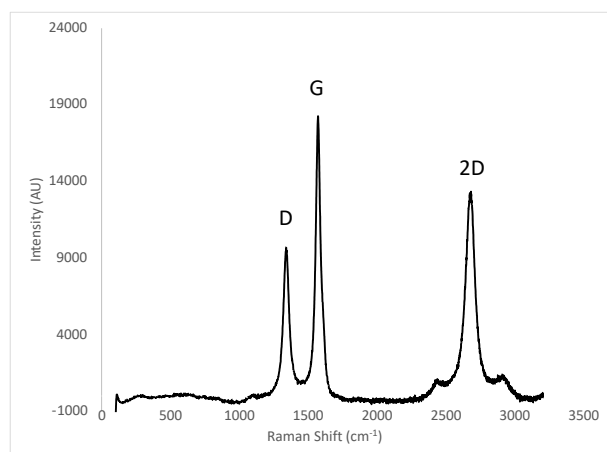


Figure 5 Raman spectrum of the LIG.

#### 4. CONCLUSIONS

Graphene films consisting of nanoflakes were fabricated utilizing a cost-effective desktop laser. The main parameters for the successive fabrication are the applied laser power and scanning speed. Obtained films are mainly

dominated by the sp<sup>2</sup> Carbons with a few amount of oxygen corresponding to the defects on the planar structure. The proposed CO<sub>2</sub> laser, despite costing only 500 USD, fabricated high-quality graphene from polymer films. The proposed system can be utilized to fabricate electronic devices such as supercapacitors, biosensors, solar cells, batteries etc.

#### *Acknowledgments*

The author would like to thank Gebze Technical University for funding.

#### *Funding*

The author would like to thank Gebze Technical University for funding.

#### *The Declaration of Conflict of Interest/ Common Interest*

No conflict of interest or common interest has been declared by the authors.

#### *The Declaration of Ethics Committee Approval*

This study does not require ethics committee permission or any special permission.

#### *The Declaration of Research and Publication Ethics*

The authors of the paper declare that they comply with the scientific, ethical and quotation rules of SAUJS in all processes of the paper and that they do not make any falsification on the data collected. In addition, they declare that Sakarya University Journal of Science and its editorial board have no responsibility for any ethical violations that may be encountered, and that this study has not been evaluated in any academic publication environment other than Sakarya University Journal of Science.

#### REFERENCES

- [1] A.K. Geim, K.S. Novoselov, The rise of graphene. Nature materials. vol. 6, no. 3, pp.183-91, 2007

- [2] J. Du, H. M. Cheng, "The fabrication, properties, and uses of graphene/polymer composites" *Macromolecular Chemistry and Physics*, vol. 213, no (10-11), pp.1060-1077, 2012
- [3] X. Jia, J. Campos-Delgado, M. Terrones, V. Meunier, M. S Dresselhaus, "Graphene edges: a review of their fabrication and characterization" *Nanoscale*, vol. 3, no. 1, pp. 86-95, 2011
- [4] A. Velasco, Y.K. Ryu, A. Boscá, A. Ladrón-de-Guevara, E. Hunt, J. Zuo, J. Pedrós, F. Calle, J. Martinez, "Recent trends in graphene supercapacitors: from large area to microsupercapacitors" *Sustainable Energy & Fuels*. vol. 5, no. 5, pp.1235-54.,2021
- [5] İ. I. Gurten, "Scalable activated carbon/graphene-based supercapacitors with improved capacitanceretention at high current densities" *Turkish Journal of Chemistry*, vol. 45, no. 3, pp.927-41, 2021.
- [6] I. Prattis, E. Hui, P. Gubeljak, G. S. Schierle, A. Lombardo, L. G. Occhipinti, "Graphene for biosensing applications in point-of-care testing" *Trends in Biotechnology*, vol. 39, no. 10, pp. 1065-1077, 2021
- [7] H. Tian, Y. Shu, Y. L. Cui, W. T. Mi, Y. Yang, D. Xie, T. L. Ren, "Scalable fabrication of high-performance and flexible graphene strain sensors" *Nanoscale*, vol. 6, no. 2, pp.699-705, 2014
- [8] H. Aghamohammadi, N. Hassanzadeh, R. Eslami-Farsani, "A review study on the recent advances in developing the heteroatom-doped graphene and porous graphene as superior anode materials for Li-ion batteries" *Ceramics International*, vol. 47, no.16, pp. 22269-22301, 2021
- [9] H. Kose, Ş. Dombaycioglu, H. Akbulut, A. O. Aydin, "Reduced graphene oxide supported tin oxide-boron oxide flexible paper anodes for Li-ion batteries" *Turkish Journal of Chemistry*, vol. 43, no. 5, pp. 1244-1257, 2019
- [10] P. Mandal, J. Debbarma, M. Saha, "A review on the emergence of graphene in photovoltaics industry" *Biointerface Research in Applied Chemistry*, vol. 11, no.6, 15009-15036, 2021.
- [11] B. Jmai, V. Silva, P. M. Mendes, "2D electronics based on graphene field effect transistors: Tutorial for modelling and simulation" *Micromachines*, vol.12, no.8, pp. 979-997, 2021
- [12] F. Pasadas, P. C. Feijoo, N. Mavredakis, A. Pacheco-Sanchez, F. A. Chaves, D. Jiménez, "Compact modeling technology for the simulation of integrated circuits based on graphene field-effect transistors" *Advanced Materials*, vol. 34, no.48 :2201691-2201691, 2022
- [13] K. S. Novoselov, A. K. Geim, S. V. Morozov, D.-e. Jiang, Y. Zhang, S. V. Dubonos, I. V. Grigorieva, A. A. Firsov, "Electric field effect in atomically thin carbon films" *Science*, vol. 306, no. 5696, pp. 666-669, 2004.
- [14] C. K. Chua, M. Pumera, "Chemical reduction of graphene oxide: a synthetic chemistry viewpoint" *Chemical Society Reviews*, vol. 43. no. 1. pp. 291-312, 2014
- [15] K. K. De Silva, H. H. Huang, R. K. Joshi, M. Yoshimura, "Chemical reduction of graphene oxide using green reductants" *Carbon*, vol. 119, pp. 190-199, 2017.

- [16] M. Eluyemi, M. Eleruja, A. Adedeji, B. Olofinjana, O. Fasakin, O. Akinwunmi, O. Ilori, A. Famojuro, S. Ayinde, E. Ajayi, "Synthesis and characterization of graphene oxide and reduced graphene oxide thin films deposited by spray pyrolysis method" *Graphene*, vol. 5, no. 3, pp.143-54, 2016
- [17] X. Xu, Z. Zhang, J. Dong, D. Yi, J. Niu, M. Wu, L. Lin, R. Yin, M. Li, J. Zhou, S. Wang, "Ultrafast epitaxial growth of metre-sized single-crystal graphene on industrial Cu foil" *Science bulletin*, vol. 62, no. 15, pp.1074-1080, 2017.
- [18] L. G. De Arco, Y. Zhang, A. Kumar, C. Zhou, "Synthesis, transfer, and devices of single-and few-layer graphene by chemical vapor deposition" *IEEE Transactions on Nanotechnology*, vol. 8, no. 2, pp.135-138, 2009
- [19] C. Y. Su, A. Y. Lu, Y. Xu, F. R. Chen, A. N. Khlobystov, L. J. Li, "High-quality thin graphene films from fast electrochemical exfoliation" *ACS Nano*, vol.5, no.3, pp.2332-2339, 2011
- [20] M. F. El-Kady, R. B. Kaner, "Scalable fabrication of high-power graphene micro-supercapacitors for flexible and on-chip energy storage" *Nature communications*, vol. 4, no.1, pp. 1-9, 2013.
- [21] J. Lin, Z. Peng, Y. Liu, F. Ruiz-Zepeda, R. Ye, E. L. Samuel, M. J. Yacaman, B. I. Yakobson, J. M. Tour, "Laser-induced porous graphene films from commercial polymers" *Nature communications*. vol. 5, no.1, pp.1-8, 2014
- [22] V. Strong, S. Dubin, M. F. El-Kady, A. Lech, Y. Wang, B. H. Weiller, R. B. Kaner, "Patterning and electronic tuning of laser scribed graphene for flexible all-carbon devices" *ACS Nano*, vol. 6, no.2, pp. 1395-1403, 2012.
- [23] N. Kurra, Q. Jiang, P. Nayak, H. N. Alshareef, "Laser-derived graphene: A three-dimensional printed graphene electrode and its emerging applications" *Nano Today*, vol. 24, pp.81-102, 2019.
- [24] Y. Lei, A. H. Alshareef, W. Zhao, S. Inal, "Laser-scribed graphene electrodes derived from lignin for biochemical sensing" *ACS Applied Nano Materials*, vol. 3, no. 2, pp.1166-1174, 2019.
- [25] W. Tian, W. Li, W. Yu, X. Liu, "A review on lattice defects in graphene: types, generation, effects and regulation" *Micromachines*, vol. 8, no. 5, pp. 163-178, 2017.
- [26] G. Yang, L. Li, W. B. Lee, M. C. Ng, "Structure of graphene and its disorders: a review" *Science and technology of advanced materials*, vol. 19, no. 1, pp. 613-48, 2018



SAKARYA ÜNİVERSİTESİ

# FEN BİLİMLERİ ENSTİTÜSÜ DERGİSİ

Sakarya University Journal of Science  
SAUJS

ISSN 1301-4048 | e-ISSN 2147-835X | Period Bimonthly | Founded: 1997 | Publisher Sakarya University |  
<http://www.saujs.sakarya.edu.tr/>

Title: Short-Term Electrical Load Forecasting in Power Systems Using Deep Learning Techniques

Authors: Nihat PAMUK

Received: 2023-02-26 00:00:00

Accepted: 2023-08-03 00:00:00

Article Type: Research Article

Volume: 27

Issue: 5

Month: October

Year: 2023

Pages: 1111-1121

How to cite

Nihat PAMUK; (2023), Short-Term Electrical Load Forecasting in Power Systems Using Deep Learning Techniques. Sakarya University Journal of Science, 27(5), 1111-1121, DOI: 10.16984/saufenbilder.1256743

Access link

<https://dergipark.org.tr/tr/journal/1115/issue/80257/1256743>

New submission to SAUJS

<http://dergipark.gov.tr/journal/1115/submission/start>

## Short-Term Electrical Load Forecasting in Power Systems Using Deep Learning Techniques

Nihat PAMUK\*<sup>1</sup> 

### Abstract

The use of big data in deep neural networks has recently surpassed traditional machine learning techniques in many application areas. The main reasons for the use of deep neural networks are the increase in computational power made possible by graphics processing units and tensor processing units, and the new algorithms created by recurrent neural networks and CNNs. In addition to traditional machine learning methods, deep neural networks have applications in anticipating electricity load. Using a real dataset for one-step forecasting, this article compares three deep learning algorithms for short-term power load forecasting: LSTM, GRUs, and CNN. The statistics come from the Turkish city of Zonguldak and include hourly electricity usage loads and temperatures over a period of three years, commencing in 2019 and ending in 2021. The mean absolute percentage error is used to compare the performances of the techniques. Forecasts are made for twelve representative months from each season. The main reason for the significant deviations in the forecasts for January, May, September, and December is the presence of religious and national holidays in these months. This was solved by adding the information obtained from religious and national holidays to the modeling. This is not to say that CNNs are not good at capturing long-term dependencies and modeling sequential data. In all experiments, LSTM, GRUs and encoder-decoder LSTM outperformed simple CNN designs. In the future, these new architectural methods can be applied to long- or short-term electric charge predictions and their results can be compared to LSTM, GRUs and their variations.

**Keywords:** Short-term forecasting, electricity load, graphical process units, tensor process units

### 1. INTRODUCTION

One of the key issues that capture the interest of both scholars and electricity supplier companies is the forecasting of electricity load. Electricity load forecasting affects provider companies' operations in operational, tactical, and strategic ways. Overestimating or underestimating loads can result in unstable energy distributions, poor

quality supply for distribution systems, excessive resource deployment for the entire supply system, and additional costs like penalty fees and profit losses [1]. Poor forecasting may have long-term negative effects on changes in electricity pricing, competitiveness, and market share of the companies [2]. On the other hand, various forecasting techniques, including statistical, parametric, and non-parametric ones, as well

\* Corresponding author: nihampamuk@beun.edu.tr (N. PAMUK)

<sup>1</sup> Zonguldak Bulent Ecevit University, Zonguldak, Türkiye

ORCID: <https://orcid.org/0000-0001-8980-6913>



as machine learning techniques, have been created and applied to forecasting issues from the perspective of scholars.

Very short-term load forecasting, short-term load forecasting, mid-term load forecasting, and long-term load forecasting are the four categories into which forecasting horizons are divided into forecasting issues [3, 4]. Very short-term load forecasting horizon spans a minute up to half-hour. The short-term load forecasting horizon spans one hour up to one week. Mid-term load forecasting and long-term load forecasting horizons span from one week up to several weeks, and several months to several years, respectively.

In this study, real case data for Zonguldak in Turkey are used to anticipate short-term load. Three years' worth of hourly temperature data and Zonguldak's electricity load consumption are included in the data. One step ahead electricity load forecasting is done by contrasting the data with deep learning techniques like the Gated Recurrent Unit (GRU), Long-Short-Term Memory (LSTM), and Convolutional Neural Network (CNN). Although several traditional machine learning methods are used in the literature for short-term load forecasting, such as in [5-9], deep learning methods are now being used and taking the place of these traditional methods.

In the literature for short-term load forecasting, simple Long-Short-Term Memory (LSTM), and GRUs, as well as simple and encoder-decoder bidirectional LSTM and GRU, are primarily employed techniques as deep learning tools. GCNNs and GRU are utilized in [10-12], while bidirectional LSTM and an attention mechanism are used in [13]. CNN and recurrent neural networks with parallel structures were employed by the authors [14]. In [15], CNN and LSTM are combined, while in [16], GRUs and LSTM are employed to conduct a comparative analysis. In addition to these studies, deep learning approaches may be used with other techniques to improve forecasting, such as empirical mode

decomposition, wavelet transform, and Kalman filter. Details on the methodology and applications are provided in the following sections. Conclusions are made, and suggestions for further research are discussed.

The objective of the study is to obtain information about the near future behavior of electric energy consumption in the study region by short-term electrical load forecasting. These forecasts are of great importance in applications such as management of power grids, balancing electricity supply and demand, planning power generation and distribution, integration of renewable energy and efficient and safe operation of power systems. For all these reasons, short-term electrical load forecasting involves the use of different disciplines, data analysis and statistical methods in the electric power sector. These forecasts are beneficial for society and the environment by improving the efficiency of the power sector, ensuring the sustainable use of energy resources, and increasing the security of power systems.

## 2. LOAD ESTIMATION METHODOLOGY

The selection of the estimation technique to be used is very important in determining the forward load demands. Depending on the nature of the load changes, one method may show advantages or disadvantages over the other. Before choosing a particular method, it is necessary to study the behavior of the load. By choosing the behavior of the load, it can be determined whether it is more accurate to choose an appropriate curve or a stochastic model for the system. Since electrical networks show different characteristics, it is very necessary to examine the structure of the existing system.

Choosing the most suitable method for the examined system is realized by knowing the advantages and disadvantages of different methods. There are basically two estimation methods: extrapolation and correlation analysis. The extrapolation method is an

estimation method in which assumptions are made for the future by examining past data and the power values affecting these data [17]. There are many extrapolation methods in which mathematical growth curves are interpreted. Another variation of the extrapolation method is to use the growth averages of the past years for future years.

Correlation is an estimation method performed by associating the condition of the loads with other factors such as weather conditions or economic conditions [18]. In the correlation method, the relationship between weather conditions and the electrical load is digitized. The most important advantage of correlation is that it can evaluate the factors affecting growth according to their importance. The correlation method is also used to determine the cause in case of deviation between the estimated values and the actual values. The economic approach methods used for short, medium, and long-term load estimation, among the estimation methods whose development has accelerated in recent years, are the model structures that are closest to general use. In short-term load forecasting, generally; a similar day approach, various regression models, time series, surface load estimation models Artificial Neural Networks (ANN), and fuzzy logic are used.

Graphical Processing Units (GPUs) are tools of great importance in short-term load forecasting, especially because they have high parallel processing capacity. GPUs are specialized processors optimized for scientific computing and data-intensive operations and are often used to accelerate graphics processing. Electricity consumption data often form large and complex data sets and need to be processed quickly.

For this reason, GPUs are frequently used in short-term load forecasting. Thanks to its parallel processing capability, it significantly reduces processing time by executing repetitive calculations in parallel. It performs large matrix operations, vector operations,

transformations, and similar operations quickly. In deep learning studies, it is used to accelerate the training and prediction phases in memory management by minimizing data transfer times. As a result, GPU-based computing approaches contribute to faster and more efficient predictions on large datasets. It also provides advantages such as energy efficiency and time savings.

## 2.1. Time Series Analysis

From the time series analysis, electricity consumption is estimated using extrapolation techniques. While performing the extrapolation process, the most appropriate function is tried to be obtained by arranging the historical data to reflect the growth trend [19]. Time series are data sets formed by the chronological order of numerical data that occur in certain periods of time-related to a variable. Considering that the data obtained from the past will show similar characteristics in the future, predictions are made on numerical models.

Data on time series are stochastic. The trend of a series can be linear or curvilinear. However, an important feature of the trend is that it is stable in both cases. The factors that affect the trend are called intrinsic factors [20]. Cyclical variations consist of long-term fluctuations around a trend line. While calculating trends, cyclical changes, and seasonal changes with Time series analysis SA, random changes cannot be calculated in any way. Box-Jenkins technique is used as an analysis and estimation method in time series [21]. This technique is based on discrete, linear stochastic processes. In addition, auto-regressive, moving average, auto-regressive-moving average, and combined auto-regressive-moving average estimation models are also used.

## 2.2. Last User Model Approaches

The econometric model approaches and their combinations are widely used methods for medium and long-term load estimation.



Detailed data such as the identification of the devices used by customers, the width of the houses, the lifetime of the devices, changes in technology, customer habits, and population dynamics are often included in the simulation and statistical models in last-user approaches [22]. Economic factors such as per capita income, working levels, working hours, and electricity prices are added to the econometric models. These models are used in combination with last-user approaches.

### **2.3. Average Percentage of Increase Estimation Method**

In this method, future estimates are made by finding the averages of the annual increase rates in the energy consumed in the past years. It works on the assumption that the average energy increase in the past years will be the same in the future. With this simple method, generally accurate results are obtained. However, different data sources should be evaluated while making future projections of a concept such as energy, which is closely related to every aspect of daily life and economic life, and therefore constantly changing according to time.

### **2.4. Econometric Methods**

Econometric methods combine economic data and statistical techniques for electrical energy demand forecasting. A mathematical function is obtained by establishing a connection between the variables. With this approach, the relationship between energy consumption and economic data is calculated. Regression analysis works by making connections between dependent and independent variables [23]. The demand for electrical energy is not only a function of time but is also affected by economic and social changes, technological developments, innovations in the industry, and environmental conditions. Regression analysis is used to explain the relationship between the mentioned variables and energy demand.

### **2.5. Regression Analysis**

The effect and direction of the independent variables on the dependent variables are indicated by statistical equations. It is decided whether a connection can be established between the two variables by drawing the scatter diagram between the dependent and independent variables. If the connection is established, how the function structure will be determined? The function structure can be in the form of one or more free variables, linear, curvilinear, additive, or non-additive. Graphic drawings are used to determine the functional structure. With regression analysis, different situations that a variable represents with one or more variables are specified as a continuous function. In this way, the existence, direction, form, and standard error of the relationship that is thought to exist between the examined variables are calculated.

## **3. SUGGESTED SYSTEM MODEL AND APPLICATIONS**

This part will provide a brief explanation of data pretreatment and preparation through exams and inspections of the data, along with the methodologies that were used. This section also includes experiment results and analyses.

### **3.1. Preparing and Processing Data Sets**

According to preliminary analyses of the relationship between temperature and load, there is a correlation between temperature and loads of the five-type that is prevalent in electricity load forecasting issues, indicating that temperature will be utilized as a feature in models. Additionally, load pattern is significantly impacted by periodicity. As a result, periodicity is found by inspecting the autocorrelation function plot. The autocorrelation function plot indicates that a weekly cycle exists, hence time lag 186 will be used in my studies. Figure 1 and Figure 2 show the temperature-load pattern and the autocorrelation function, respectively.

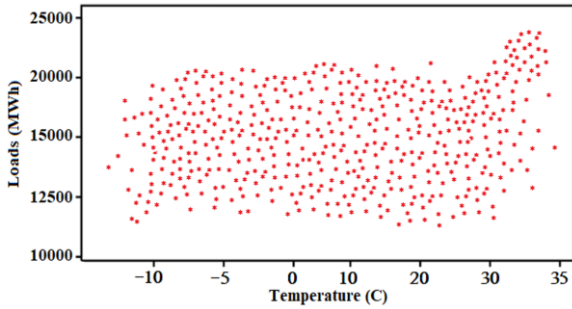


Figure 1 Load temperature correlation

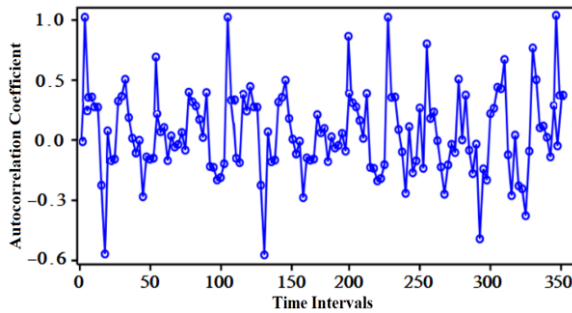


Figure 2 Autocorrelation function plot

In short-term load estimation, the autocorrelation function measures the relationship between previous time intervals. The graph of the function in Figure 2 shows the time intervals on the x-axis and the autocorrelation coefficient on the y-axis. The autocorrelation coefficient on the y-axis measures the relationship between previous time intervals and the current time interval. Dummy variables are employed to represent the effects of these aspects because the dataset also contains information about the seasonal and daily effects on load patterns in addition to the main periodicity. Experimental characteristics are listed in Table 1.

Table 1 Experimental characteristics

<i>Characteristics</i>	<i>Analysis</i>
Seasons	4 categorical factors
Days	7 categorical factors
Load	Hourly load values
Temperature	Hourly temperature values

### 3.2. Application of Deep Learning Techniques

One category of sequential data is time series. In this study, forecasting is carried out using two exceptional recurrent neural network

subtypes, GRU, and LSTM, which are deep neural network variants. GRUs and LSTM are good at capturing long-term dependencies in data by applying gating techniques. These approaches' specifications and formulas can be found in [24, 25].

GRUs and LSTM applications are taken into consideration for the challenge because the data displays autoregressive features with weekly regularity. Moreover, one-dimensional CNNs have become popular in modeling sequential data such as speech recognition, text classification, and sentiment classification. This emergence is considered, and a CNN is added to the experiments along with GRUs and LSTM. [26] contains the technical specifications and CNN formulas.

### 3.3. Application and Tools

In this study, the deep learning methods are applied with some architectural changes. While the CNN is employed with dilations and causal padding as investigated in [26], simple GRUs, LSTM, and encoder-decoder LSTM are also used. After looking at the validation data, the ideal parameters for the experiments are identified. In a CNN, the RMSProp optimizer is employed with values of 0.008 learning rate, 0.96 rho, and 0.001 decay rate. In this technique, different dilation rates are used in successive layers with 150 and 300 filter sizes in subsequent convolutional layers.

The RMSProp optimizer is employed in simple GRUs and LSTM with the following settings: 0.002 learning rate, 0.96 rho, and 0.001 decay rate. Both GRUs and LSTM employ 250, 225, and one filter sizes. Moreover, the RMSProp optimizer is employed in the encoder-decoder LSTM approach with values of 0.0008 learning rate, 0.96 rho, and 0.0006 decay rate. The CNN with a 1200 filter size is initially presented as a previous feature extractor with 1x1 convolution in the encoder component of this LSTM, followed using the 300 and 275 filter sizes in the LSTM. The encoded states are

then repeated 15 times using a repeat vector, followed by the usage of successive max-pooling layers within each decoder layer and 225, 200, and 175 filter sizes in the decoding portion.

The top layers of all approaches use dense layers with linear activation functions and rectified linear unit activation functions. All models employ the mean squared error metric as their loss function since it may quadratic penalize weights, is a frequent loss function in regression-type situations, and easily guides a model to local minima during optimization. Mean absolute percentage error, a frequently used performance statistic in time series, is used to compare one model to the others. Mean absolute percentage error and mean squared error formulas are given in equation 1.

$$MAPE = \frac{1}{n} \sum_{i=1}^n \frac{|A_i - F_i|}{A_i} \quad (1)$$

$$MSE = \frac{1}{n} \sum_{i=1}^n (A_i - F_i)^2$$

In equation 1,  $A_i$  is the actual value,  $F_i$  is the forecast value and  $n$  is the total number of observations. Tensors built from experiment inputs have a batch size x time step x feature dimension of (24x168x13), where the batch size is 24, the time step is 168, and the feature is 13 for all models.

The experiments have been performed using the Python 3.4 environment and Keras 2.2.2 with Tensor flow 1.10.0 as the backend. Intel® Core™ i7-13700K desktop with 16 CPUs and an NVIDIA GeForce RTX6600, 8 GB central process unit has carried out computations. It has taken between 25 and 30 minutes, and the models have been run through 20, 30, and 35 epochs. While examining the validation processes, it has been found that different epochs are suitable for different models and that consequently, a different number of epochs is used with different models.

### 3.4. Results and Discussions

Three months for each season made up the entire duration of the experiment, which lasted a full year. All test data for each training are for 2021, and 0.18 of the training datasets is split for validation. Mean absolute percentage error comparisons of one-week one-step forward estimates are given in Table 2. As demonstrated in Table 2, all models performed poorly in January compared to other months, notably on Friday, Saturday, and Sunday. This fact might be explained by the fact that it's the first week of the year this week. After the Christmas holiday at the end of December, this week comes. The model that performed the best in January was GRUs, with just minor variations compared to LSTM, and encoder-decoder LSTM. Also, the first day of the year may not have the same electricity consumption as other similar days of the week. These facts, when considered, might be said to have had a negative impact on our autoregressive models. LSTM and encoder-decoder LSTM perform best in March and April, followed by GRUs.

In contrast to the estimates for January, there are little discrepancies between the forecasts for the days. While LSTM and GRUs show the best performance in June, July, and August, they are followed by encoder-decoder LSTM with slight differences. The low differences between the forecasts of the days are also seen in these months.

In September, October, and November, LSTM and encoder-decoder LSTM perform best, followed by GRUs with slight margins. The low differences in the forecasts of the days are seen again in these months. In every trial, the CNN has been clearly outperformed by LSTM, GRUs, and encoder-decoder LSTM in this task. Simple LSTM and GRUs have been seen to perform at least as well as encoder-decoder LSTM in this forecasting test. To compete with LSTM and GRU approaches in these types of tasks, the CNN may pass several architectural modifications.

Table 2 Mean absolute percent error comparison of electricity demand forecast values for each month

	Days	Methods			
		Convolutional Neural Network	Long-Short Term Memory	Encoder Decoder Long-Short Term Memory	Gated Recurrent Units
Months	January 02, 2021	0.0139	0.0114	0.0101	0.0103
	January 03, 2021	0.0143	0.0097	0.0087	0.0065
	January 04, 2021	0.0139	0.0081	0.0083	0.0069
	January 05, 2021	0.0127	0.0073	0.0062	0.0187
	January 06, 2021	0.0199	0.0115	0.0148	0.0251
	January 07, 2021	0.0273	0.0286	0.0313	0.0233
	January 08, 2021	0.0301	0.0184	0.0156	0.0109
	February 04, 2021	0.0135	0.0127	0.0109	0.0106
Months	February 05, 2021	0.0139	0.0093	0.0077	0.0084
	February 06, 2021	0.0148	0.0072	0.0070	0.0071
	February 07, 2021	0.0121	0.0069	0.0061	0.0089
	February 08, 2021	0.0184	0.0154	0.0198	0.0137
	February 09, 2021	0.0286	0.0201	0.0217	0.0310
	February 10, 2021	0.0310	0.0179	0.0103	0.0189
	March 01, 2021	0.0081	0.0072	0.0094	0.0077
Months	March 02, 2021	0.0077	0.0105	0.0107	0.0131
	March 03, 2021	0.0107	0.0051	0.0090	0.0304
	March 04, 2021	0.0073	0.0059	0.0109	0.0194
	March 05, 2021	0.0092	0.0071	0.0302	0.0083
	March 06, 2021	0.0144	0.0067	0.0181	0.0096
	March 07, 2021	0.0212	0.0132	0.0103	0.0083
	April 05, 2021	0.0084	0.0089	0.0062	0.0076
Months	April 06, 2021	0.0063	0.0078	0.0060	0.0061
	April 07, 2021	0.0074	0.0043	0.0049	0.0063
	April 08, 2021	0.0091	0.0054	0.0055	0.0078
	April 09, 2021	0.0081	0.0057	0.0372	0.0081
	April 10, 2021	0.0095	0.0069	0.0213	0.0069
	April 11, 2021	0.0102	0.0062	0.0099	0.0093
	May 08, 2021	0.0091	0.0055	0.0083	0.0113
Months	May 09, 2021	0.0121	0.0085	0.0091	0.0118
	May 10, 2021	0.0096	0.0216	0.0107	0.0136
	May 11, 2021	0.0186	0.0162	0.0219	0.0131
	May 12, 2021	0.0104	0.0108	0.0241	0.0094
	May 13, 2021	0.0083	0.0193	0.0164	0.0208
	May 14, 2021	0.0088	0.0138	0.0203	0.0221
	June 03, 2021	0.0098	0.0135	0.0095	0.0132
Months	June 04, 2021	0.0103	0.0101	0.0084	0.0114
	June 05, 2021	0.0094	0.0073	0.0081	0.0097
	June 06, 2021	0.0128	0.0059	0.0066	0.0075
	June 07, 2021	0.0107	0.0064	0.0062	0.0217
	June 08, 2021	0.0088	0.0070	0.0074	0.0312
	June 09, 2021	0.0083	0.0081	0.0093	0.0093
	July 05, 2021	0.0098	0.0123	0.0096	0.0057
Months	July 06, 2021	0.0083	0.0098	0.0082	0.0077
	July 07, 2021	0.0120	0.0066	0.0071	0.0089
	July 08, 2021	0.0149	0.0074	0.0176	0.0096
	July 09, 2021	0.0203	0.0173	0.0098	0.0106
	July 10, 2021	0.0242	0.0139	0.0080	0.0068
	July 11, 2021	0.0093	0.0081	0.0097	0.0172

Table 2 Mean absolute percent error comparison of electricity demand forecast values for each month (Continue)

	Days	Methods			
		Convolutional Neural Network	Long-Short Term Memory	Encoder Decoder Long-Short Term Memory	Gated Recurrent Units
Months	August 04, 2021	0.0086	0.0138	0.0094	0.0078
	August 05, 2021	0.0103	0.0101	0.0083	0.0109
	August 06, 2021	0.0099	0.0060	0.0080	0.0203
	August 07, 2021	0.0116	0.0058	0.0062	0.0402
	August 08, 2021	0.0103	0.0064	0.0065	0.0071
	August 09, 2021	0.0091	0.0069	0.0087	0.0216
	August 10, 2021	0.0098	0.0073	0.0076	0.0222
Months	September 02, 2021	0.0117	0.0042	0.0037	0.0203
	September 03, 2021	0.0186	0.0061	0.0053	0.0097
	September 04, 2021	0.0093	0.0054	0.0051	0.0187
	September 05, 2021	0.0204	0.0081	0.0066	0.0194
	September 06, 2021	0.0185	0.0101	0.0094	0.0211
	September 07, 2021	0.0126	0.0077	0.0069	0.0304
	September 08, 2021	0.0198	0.0049	0.0089	0.0176
Months	October 07, 2021	0.0086	0.0054	0.0063	0.0108
	October 08, 2021	0.0091	0.0069	0.0059	0.0102
	October 09, 2021	0.0137	0.0098	0.0083	0.0084
	October 10, 2021	0.0081	0.0059	0.0061	0.0171
	October 11, 2021	0.0088	0.0063	0.0055	0.0128
	October 12, 2021	0.0114	0.0057	0.0067	0.0135
	October 13, 2021	0.0208	0.0102	0.0084	0.0193
Months	November 04, 2021	0.0103	0.0066	0.0055	0.0082
	November 05, 2021	0.0180	0.0051	0.0063	0.0098
	November 06, 2021	0.0091	0.0088	0.0069	0.0149
	November 07, 2021	0.0206	0.0104	0.0091	0.0183
	November 08, 2021	0.0174	0.0093	0.0070	0.0126
	November 09, 2021	0.0139	0.0080	0.0081	0.0205
	November 10, 2021	0.0141	0.0072	0.0103	0.0133
Months	December 09, 2021	0.0162	0.0117	0.0099	0.0142
	December 10, 2021	0.0145	0.0063	0.0078	0.0111
	December 11, 2021	0.0111	0.0098	0.0075	0.0189
	December 12, 2021	0.0176	0.0069	0.0054	0.0077
	December 13, 2021	0.0193	0.0073	0.0063	0.0083
	December 14, 2021	0.0214	0.0059	0.0066	0.0098
	December 15, 2021	0.0283	0.0087	0.0087	0.0094

#### 4. CONCLUSIONS

Forecasts for January, May, September, and December have seen some significant departures from forecasts for other months within the days reviewed. This forecasting issue might be resolved by inspecting these special days along with other religious and national holidays and adding the information that is extracted after the inspections to the models. However, this does not mean that

convolutional neural networks are not good at capturing long-term dependencies and modeling sequential data. In all trials, long-short-term memory, gated recurrent units, and encoder-decoder long-short-term memory saliently outperform simple convolutional neural network designs. In the literature, new designs for sequential data modeling using one-dimensional convolutional networks have been proposed.

Future studies may focus on applying these new architectures to issues with electrical load forecasting and comparing the results with long short-term memory, gated recurrent units, and their variations. As an alternative to one-step ahead forecasting, multi-step ahead forecasting, such as next-24-hour recasting with used models and their modifications, may be produced and compared as a new area of research. Finally, combining several signal processing methods, such as empirical mode decomposition, wavelet transform, and Fourier transform, with deep learning algorithms may be another potential research area.

#### ***Acknowledgments***

The author would like to thank “Enerjisa Baskent Electricity Distribution Corporation” employees for their contributions.

#### ***Funding***

The author has no received any financial support for the research, authorship or publication of this study.

#### ***The Declaration of Conflict of Interest/ Common Interest***

No conflict of interest or common interest has been declared by the author.

#### ***The Declaration of Ethics Committee Approval***

This study does not require ethics committee permission or any special permission.

#### ***The Declaration of Research and Publication Ethics***

The author of the paper declares that they comply with the scientific, ethical, and quotation rules of SAUJS in all processes of the paper and that they do not make any falsification on the data collected. In addition, they declare that Sakarya University Journal of Science and its editorial board have no responsibility for any ethical violations that may be encountered and that this study has not been evaluated in any academic publication environment other than Sakarya University Journal of Science.

## **REFERENCES**

- [1] S. Fan, R. J. Hyndman, “Short-Term Load Forecasting based on a Semi-Parametric Additive Model,” *IEEE Transactions on Power Systems*, vol. 27, no. 1, pp. 134-141, 2011.
- [2] N. Pamuk, “Empirical Analysis of Causal Relationship between Electricity Production and Consumption Demand in Turkey Using Cobb-Douglas Model,” *Journal of Polytechnic*, vol. 19, no. 4, pp. 415-420, 2016.
- [3] K. Kaysal, E. Akarslan, F. O. Hocaoglu, “Comparison of Machine Learning Methods in Turkey’s Short-Term Electricity Load Demand Estimation,” *Bilecik Seyh Edebali University Journal of Science*, vol. 9, no. 2, pp. 693-702, 2022.
- [4] A. Allee, N. J. Williams, A. Davis, P. Jaramillo, “Predicting Initial Electricity Demand in off-grid Tanzanian Communities Using Customer Survey Data and Machine Learning Models,” *Energy for Sustainable Development*, vol. 62, pp. 56-66, 2021.
- [5] J. Huo, T. Shi, J. Chang, “Comparison of Random Forest and SVM for Electrical Short-Term Load Forecast with Different Data Sources,” *7th IEEE International Conference on Software Engineering and Service Science (ICSESS)*, 26-28 August, Beijing, China, 2016, pp. 1077-1080.
- [6] G. Mitchell, S. Bahadoorsingh, N. Ramsamooj, C. Sharma, “A Comparison of Artificial Neural Networks and Support Vector Machines for Short-Term Load Forecasting Using Various Load Types,” *IEEE Manchester PowerTech*, 18-22 June, Manchester, UK, 2017, 17044934.

- [7] S. H. Rafi, S. R. Deeba, E. Hossain, "A Short-Term Load Forecasting Method Using Integrated CNN and LSTM Network," *IEEE Access*, vol. 9, pp. 32436-32448, 2021.
- [8] P. Singh, P. Dwivedi, V. Kant, "A Hybrid Method Based on Neural Network and Improved Environmental Adaptation Method Using Controlled Gaussian Mutation with Real Parameter for Short-Term Load Forecasting," *Energy*, vol. 174, pp. 460-477, 2019.
- [9] J. Lin, J. Ma, J. Zhu, Y. Cui, "Short-Term Load Forecasting Based on LSTM Networks Considering Attention Mechanism," *International Journal of Electrical Power & Energy Systems*, vol. 137, 107818, 2022.
- [10] C. Yang, Z. An, H. Zhu, X. Hu, K. Zhang, K. Xu, Y. Xu, "Gated Convolutional Networks with Hybrid Connectivity for Image Classification," In *Proceedings of the AAI Conference on Artificial Intelligence*, vol. 34, no. 07, pp. 12581-12588, 2020.
- [11] Y. Mo, Q. Wu, X. Li, B. Huang, "Remaining Useful Life Estimation via Transformer Encoder Enhanced by A Gated Convolutional Unit," *Journal of Intelligent Manufacturing*, vol. 32, pp. 1997-2006, 2021.
- [12] Y. Wang, M. Liu, Z. Bao, S. Zhang, "Short-Term Load Forecasting with Multi-Source Data Using Gated Recurrent Unit Neural Networks," *Energies*, vol. 11, no. 5, 1138, 2018.
- [13] Z. Ferdoush, B. N. Mahmud, A. Chakrabarty, J. Uddin, "A Short-Term Hybrid Forecasting Model for Time Series Electrical-Load Data Using Random Forest and Bidirectional Long Short-Term Memory," *International Journal of Electrical and Computer Engineering*, vol. 11, no. 1, pp. 763-771, 2021.
- [14] R. Wan, S. Mei, J. Wang, M. Liu, F. Yang, "Multivariate Temporal Convolutional Network: A Deep Neural Networks Approach for Multivariate Time Series Forecasting," *Electronics*, vol. 8, no. 8, 876, 2019.
- [15] J. C. Nunez, R. Cabido, J. J. Pantrigo, A. S. Montemayor, J. F. Velez, "Convolutional Neural Networks and Long Short-Term Memory for Skeleton-Based Human Activity and Hand Gesture Recognition," *Pattern Recognition*, vol. 76, pp. 80-94, 2018.
- [16] C. Tian, J. Ma, C. Zhang, P. Zhan, "A Deep Neural Network Model for Short-Term Load Forecast Based on Long Short-Term Memory Network and Convolutional Neural Network," *Energies*, vol. 11, no. 12, 3493, 2018.
- [17] P. W. Khan, Y. C. Byun, A. J. Lee, D. H. Kang, J. Y. Kang, H. S. Park, "Machine Learning-Based Approach to Predict Energy Consumption of Renewable and Nonrenewable Power Sources," *Energies*, vol. 13, no. 18, 4870, 2020.
- [18] H. M. Al-Hamadi, S. A. Soliman, "Long-Term/Mid-Term Electric Load Forecasting Based on Short-Term Correlation and Annual Growth," *Electric Power Systems Research*, vol. 74, no. 3, pp. 353-361, 2005.
- [19] N. Edison, A. C. Aranha, J. Coelho, "Probabilistic Methodology for Technical and Non-Technical Losses Estimation in Distribution System," *Electric Power Systems Research*, vol. 97, no. 11, pp. 93-99, 2013.
- [20] N. Pamuk, "Determination of Chaotic Time Series in Dynamic Systems," *Journal of Balikesir University Institute*

- of Science and Technology, vol. 15, no. 1, pp. 78-92, 2013.
- [21] A. Singh, G. C. Mishra, "Application of Box-Jenkins Method and Artificial Neural Network Procedure for Time Series Forecasting of Prices," *Statistics in Transition new series*, vol. 16, no. 1, pp. 83-96, 2015.
- [22] N. Srivastava, G. Hinton, A. Krizhevsky, I. Sutskever, R. Salakhutdinov, "Dropout: A Simply Way to Prevent Neural Networks From Overfitting," *The Journal of Machine Learning Research*, vol. 15, no. 1, pp. 1929-1958, 2014.
- [23] N. Yampikulsakul, E. Byon, S. Huang, S. Sheng, M. You, "Condition Monitoring of Wind Power System with Nonparametric Regression Analysis," *IEEE Transactions on Energy Conversion*, vol. 29, no. 2, pp. 288-299, 2014.
- [24] S. Li, Y. Han, X. Yao, S. Yingchen, J. Wang, Q. Zhao, "Electricity Theft Detection in Power Grids with Deep Learning and Random Forests," *Journal of Electrical and Computer Engineering*, vol. 2019, 4136874, pp. 1-12, 2019.
- [25] Z. Zheng, Y. Yang, X. Niu, H. N. Dai, Y. Zhou, "Wide and Deep Convolutional Neural Networks for Electricity-Theft Detection to Secure Smart Grids," *IEEE Transactions on Industrial Informatics*, vol. 14, no. 4, pp. 1606-1615, 2018.
- [26] A. H. Nizar, Z. Y. Dong, Y. Wang, A. N. Souza, "Power Utility Nontechnical Loss Analysis with Extreme Learning Machine Method," *IEEE Transactions on Power Systems*, vol. 23, no. 3, pp. 946-955, 2008.





SAKARYA ÜNİVERSİTESİ

# FEN BİLİMLERİ ENSTİTÜSÜ DERGİSİ

Sakarya University Journal of Science  
SAUJS

ISSN 1301-4048 | e-ISSN 2147-835X | Period Bimonthly | Founded: 1997 | Publisher Sakarya University |  
<http://www.saujs.sakarya.edu.tr/>

Title: Mulatu Numbers Which Are Concatenation of Two Fibonacci Numbers

Authors: Fatih ERDUVAN, Merve GÜNEY DUMAN

Received: 2023-01-16 00:00:00

Accepted: 08.06.2023

Article Type: Research Article

Volume: 27

Issue: 5

Month: October

Year: 2023

Pages: 1122-1127

How to cite

Fatih ERDUVAN, Merve GÜNEY DUMAN; (2023), Mulatu Numbers Which Are Concatenation of Two Fibonacci Numbers. Sakarya University Journal of Science, 27(5), 1122-1127, DOI: 10.16984/saufenbilder.1235571

Access link

<https://dergipark.org.tr/tr/journal/1115/issue/80257/1235571>

New submission to SAUJS

<http://dergipark.gov.tr/journal/1115/submission/start>

## Mulatu Numbers Which Are Concatenation of Two Fibonacci Numbers

Fatih ERDUVAN<sup>1</sup> , Merve GÜNEY DUMAN<sup>\*2</sup> 

### Abstract

Let  $(M_k)$  be the sequence of Mulatu numbers defined by  $M_0 = 4, M_1 = 1, M_k = M_{k-1} + M_{k-2}$  and  $(F_k)$  be the Fibonacci sequence given by the recurrence  $F_k = F_{k-1} + F_{k-2}$  with the initial conditions  $F_0 = 0, F_1 = 1$  for  $k \geq 2$ . In this paper, we showed that all Mulatu numbers, that are concatenations of two Fibonacci numbers are 11, 28. That is, we solved the equation  $M_k = 10^d F_m + F_n$ , where  $d$  indicates the number of digits of  $F_n$ . We found the solutions of this equation as  $(k, m, n, d) \in \{(4, 2, 2, 1), (6, 3, 6, 1)\}$ . Moreover the solutions of this equation displayed as  $M_4 = \overline{F_2 F_2} = 11$  and  $M_6 = \overline{F_3 F_6} = 28$ . Here the main tools are linear forms in logarithms and Baker Davenport basis reduction method.

**Keywords:** Mulatu and Fibonacci numbers, linear forms in logarithms, exponential Diophantine equations

### 1. INTRODUCTION

Let  $(M_k)$  be the sequence of Mulatu numbers defined by  $M_0 = 4, M_1 = 1, M_k = M_{k-1} + M_{k-2}$  for  $k \geq 2$ . The Mulatu numbers are introduced in [1]. Let  $(F_k)$  be the Fibonacci sequence given by the recurrence  $F_k = F_{k-1} + F_{k-2}$  with the initial conditions  $F_0 = 0, F_1 = 1$  for  $k \geq 2$ . Binet formulas of these numbers are

$$M_k = \left(\frac{10-\sqrt{5}}{5}\right) \alpha^k + \left(\frac{10+\sqrt{5}}{5}\right) \beta^k,$$

$$F_k = \frac{\alpha^k - \beta^k}{\sqrt{5}}$$

where  $\alpha = \frac{1+\sqrt{5}}{2}$  and  $\beta = \frac{1-\sqrt{5}}{2}$ .  $\alpha$  and  $\beta$  are the roots of  $1 + x - x^2 = 0$ . The relation between  $M_k$  and  $F_k$  with  $\alpha$  is given by

$$\alpha^{k-1} \leq M_k \leq 4\alpha^k \quad \text{for all } k \geq 0 \quad (1)$$

$$\alpha^{k-2} \leq F_k \leq \alpha^{k-1} \quad \text{for all } k \geq 1. \quad (2)$$

By induction, the inequalities (1) and (2) can be proved. In [2], let  $d$  be the number of digits of  $F_n$ , authors gave solutions of the equation

$$F_k = 10^d F_m + F_n$$

as

$$(k, m, n, d) = (7, 1, 4, 1), (7, 2, 4, 1),$$

$$(8, 3, 1, 1), (8, 3, 2, 1), (10, 5, 5, 1).$$

\* Corresponding author: merveduman@subu.edu.tr (M. GÜNEY DUMAN)

<sup>1</sup> Ministry of National Education (MEB)

<sup>2</sup> Sakarya University of Applied Sciences

E-mail: erduvanmat@hotmail.com

ORCID: <https://orcid.org/0000-0001-7254-2296> <https://orcid.org/0000-0002-6340-4817>



In [3], Alan determined that Fibonacci numbers which are concatenations of two Lucas numbers and also Lucas numbers which are concatenations of two Fibonacci numbers. Inspired of these works, we solved the Diophantine equation

$$M_k = 10^d F_m + F_n, \tag{3}$$

where  $d$  indicates the number of digits of  $F_n$ . If  $m = 0$ , then we have

$$M_k = F_n$$

from the equality (3). Moreover, the equality

$$M_k = F_{k-3} + F_{k-1} + F_{k+2}$$

can be found in [4]. When we consider the above two equalities together, we get Fibonacci numbers that are sums of the three Fibonacci numbers. But this problem is also solved in [5]. Moreover, we will take  $m \geq 2$  since  $F_1$  and  $F_2$  values are the same.

## 2. PRELIMINARIES

Let  $\gamma$  be an algebraic number of degrees  $d$  over  $\mathbb{Q}$  with minimal primitive polynomial

$$c_0 x^d + c_1 x^{d-1} + \dots + c_d = c_0 \sum_{i=1}^d (x - \gamma^{(i)}) \in \mathbb{Z}[x],$$

with  $\gamma^{(i)}$ 's are conjugates of  $\gamma$  and  $c_0 > 0$ . Then logarithmic height of  $\gamma$  is given

$$h(\gamma) = \frac{1}{d} (\log c_0 + \sum_{i=1}^d \log(\max\{|\gamma^{(i)}|, 1\})).$$

The following properties are given in [6].

$$h(\gamma_1 \mp \gamma_2) \leq \log 2 + h(\gamma_1) + h(\gamma_2) \tag{4}$$

$$h(\gamma_1 \gamma_2^{\pm 1}) \leq h(\gamma_1) + h(\gamma_2) \tag{5}$$

$$h(\gamma_1^r) = |r| h(\gamma_1). \tag{6}$$

The following lemma can be found in [7].

**Lemma 1.** Let  $\gamma_1, \gamma_2, \dots, \gamma_n$  be positive real algebraic numbers and let  $b_1, b_2, \dots, b_n$  be nonzero integers. Let  $D$  be the degree of the number field  $\mathbb{Q}(\gamma_1, \gamma_2, \dots, \gamma_n)$  over  $\mathbb{Q}$ . Let  $B \geq \max\{|b_1|, |b_2|, \dots, |b_n|\}$ ,  $A_i \geq \max\{D \cdot h(\gamma_i), |\log \gamma_i|, (0.16)\}$

for all  $i = 1, 2, \dots, n$ . If

$$\Gamma := \gamma_1^{b_1} \cdot \gamma_2^{b_2} \dots \gamma_n^{b_n} - 1 \neq 0$$

then

$$|\Gamma| > \exp(-1.4 \cdot 30^{n+3} \cdot n^{4.5} \cdot D^2 \cdot (1 + \log D) \cdot (1 + \log B) \cdot A_1 \cdot A_2 \dots A_n).$$

In [8], the authors put forward a different version of conclusion of Dujella and Pethő's Lemma in [9]. This lemma is given below.

**Lemma 2.** Let  $\tau$  be irrational number,  $M$  be a positive integer and  $\frac{p}{q}$  be a convergent of the continued fraction of  $\tau$  such that  $q > 6M$ , and let  $A, B, \mu$  be some real numbers with  $A > 0$  and  $B > 1$ . Put

$$\varepsilon := \|\mu q\| - M \|\tau q\|,$$

where  $\|\cdot\|$  denotes the distance from the nearest integer. If  $\varepsilon > 0$ , then there is no positive integer solution  $(r, s, t)$  to the inequality

$$0 < |r\tau - s + \mu| < A \cdot B^{-t}$$

subject to the restrictions that

$$r \leq M \text{ and } t \geq \frac{\log(Aq/\varepsilon)}{\log B}.$$

The following lemma are given in [10].

**Lemma 3.** Let  $\rho, \Gamma \in \mathbb{R}$ . If  $0 < \rho < 1$  and  $|\Gamma| < \rho$ , then

$$|\log(1 + \Gamma)| < \frac{\log(1-\rho)}{-\rho} \cdot |\Gamma|$$

and

$$|\Gamma| < \frac{-\rho}{e^{-\rho}-1} \cdot |e^\Gamma - 1|.$$

The following lemma is also useful. We will use it to prove our theorem.

**Lemma 4.** Suppose that  $M_k = 10^d F_m + F_n$ , where  $d$  indicates the number of digits of  $F_n$ . Then we have the following inequalities.

- a)  $d < \frac{n+3}{4}$
- b)  $F_n < 10^d < 10F_n$
- c)  $n + m - 7 < k < n + m + 4$
- d)  $k - m > 1$
- e)  $k - n \geq -1$

**Proof. a)** Since  $d$  is the number of digits of  $F_n$ , we can write  $d = \lfloor \log_{10} F_n \rfloor + 1$ . From here, we find

$$\frac{n-2}{5} < \log_{10} \alpha^{n-2} \leq \log_{10} F_n < \lfloor \log_{10} F_n \rfloor + 1 = d.$$

Thus, we obtain  $d < \frac{n+3}{4}$ .

**b)** Since  $d = \lfloor \log_{10} F_n \rfloor + 1$ , we find

$$F_n = 10^{\log_{10} F_n} < 10^d \leq 10^{\log_{10} F_n + 1} < 10F_n.$$

**c)** By using Lemma 4(b), the inequalities (1) and (2) we obtain

$$\begin{aligned} \alpha^{k-1} &\leq M_k = 10^d F_m + F_n \\ &< 10F_n F_m + F_n F_m \\ &= 11F_n F_m < \alpha^{n+m+3} \end{aligned}$$

and

$$\begin{aligned} \alpha^{k+3} &> 4\alpha^k \geq M_k = 10^d F_m + F_n \\ &> F_n F_m > \alpha^{n+m-4}. \end{aligned}$$

Thus, we get  $n + m - 7 < k < n + m + 4$ .

**d)** Let consider the inequality

$$M_k = 10^d F_m + F_n \geq 10F_m$$

and the equality

$$M_k = 4F_{k+1} - 3F_k$$

given in [1]. If  $k \leq m + 1$  then we have  $10F_m \leq M_k = 4F_{k+1} - 3F_k = 3F_{k-1} + F_{k+1} \leq 3F_m + F_{m+2} \leq 6F_m$ ,

which is a contradiction. Thus,  $k - m > 1$ .

**e)** Considering the inequality

$$M_k = 10^d F_m + F_n > F_n F_m + F_n \geq 2F_n,$$

it can be seen that  $k - n \geq -1$  similar to the proof of Lemma 4(d).

### 3. MAIN THEOREM

**Theorem 5.** Let  $d$  be the number of digits of  $F_n$ ,  $d \geq 1$ ,  $m \geq 2$  and  $n, k \geq 0$ . If  $M_k = 10^d F_m + F_n$  then

$$(k, F_m, F_n, M_k) \in \{(4,1,1,11), (6,2,8,28)\}.$$

**Proof.** Assume that the equation (3) is satisfied. If  $0 \leq k \leq 109$ , we find  $(k, M_k, F_m, F_n) \in \{(4,11,1,1), (6,28,2,8)\}$ . So suppose that  $k \geq 110$ . We arrange the equation (3) as

$$\begin{aligned} \left(\frac{10-\sqrt{5}}{5}\right) \alpha^k - 10^d \cdot \frac{\alpha^m}{\sqrt{5}} = \\ - \left(\frac{10+\sqrt{5}}{5}\right) \beta^k - 10^d \frac{\beta^m}{\sqrt{5}} + F_n. \end{aligned}$$

If we multiply both sides of the above equality by  $\frac{\sqrt{5}}{10^d \cdot \alpha^m}$  and taking absolute values of this equality, we obtain

$$\begin{aligned} \left| \frac{(2\sqrt{5}-1) \cdot \alpha^{k-m}}{10^d} - 1 \right| \leq \\ \frac{2\sqrt{5}+1}{10^d \cdot \alpha^{k+m}} + \frac{1}{\alpha^{2m}} + \frac{\sqrt{5} \cdot F_n}{10^d \cdot \alpha^m} \leq \\ \frac{1}{\alpha^m} \left( \frac{2\sqrt{5}+1}{10^d \cdot \alpha^k} + \frac{1}{\alpha^m} + \sqrt{5} \right), \end{aligned}$$

i.e.,

$$\left| \frac{(2\sqrt{5}-1) \cdot \alpha^{k-m}}{10^d} - 1 \right| \leq \frac{2.62}{\alpha^m}, \tag{7}$$

where we use that  $k \geq 110$ ,  $m \geq 2$  and  $d \geq 1$ . Now, we are ready to apply Lemma 1 with  $\gamma_1 := \alpha$ ,  $\gamma_2 := 10$ ,  $\gamma_3 := 2\sqrt{5} - 1$  and  $b_1 := k - m$ ,  $b_2 := -d$ ,  $b_3 := 1$ . Furthermore,  $D = 2$ . Put

$$\Gamma_1 := \frac{(2\sqrt{5}-1) \cdot \alpha^{k-m}}{10^d} - 1.$$

Suppose that  $\Gamma_1 = 0$ . Then, we get  $\alpha^{k-m} = \frac{(1+2\sqrt{5})10^d}{19}$ . If we conjugate in  $\mathbb{Q}(\sqrt{5})$ , then we obtain  $\beta^{k-m} = \frac{(1-2\sqrt{5})10^d}{19}$ . From this, it can be seen that  $F_{k-m} = \frac{4 \cdot 10^d}{19}$ . This is not possible. Moreover  $h(\gamma_1) = \frac{\log \alpha}{2}$ ,  $h(\gamma_2) = \log 10$  and

$$h(\gamma_3) = h(2\sqrt{5} - 1) \leq \frac{\log 80}{2}.$$

Hereby, we can choose  $A_1 := \log \alpha$ ,  $A_2 := \log 100$ ,  $A_3 := \log 80$ . Considering Lemma 4(a), (c), we can write

$$d < \frac{n+3}{4} < k - m + 3 < k + 3. \tag{8}$$

From here, we can say  $B := k + 3$ . Let  $A = (-1.4) \cdot 30^6 \cdot 3^{4.5} \cdot 2^2$ . By using Lemma 1 and the inequality (7), we have

$$2.62 \times \alpha^{-m} > |\Gamma_1| > \exp((1 + \log 2) \cdot A \cdot (1 + \log(k + 3))) \cdot \log 100 \cdot \log \alpha \cdot \log 80$$

i.e.,

$$m \log \alpha - \log 2.62 < 9.42 \times 10^{12} \cdot (1 + \log(k + 3)). \tag{9}$$

Now, from (3), we write

$$\alpha^k \left( \frac{10-\sqrt{5}}{5} - \frac{\alpha^{n-k}}{\sqrt{5}} \right) - F_m \cdot 10^d = - \left( \frac{10+\sqrt{5}}{5} \right) \beta^k - \frac{\beta^n}{\sqrt{5}},$$

i.e.,

$$\alpha^k \left( (2\sqrt{5} - 1) - \alpha^{n-k} \right) - 10^d \cdot \sqrt{5} \cdot F_m$$

$$= -(2\sqrt{5} + 1)\beta^k - \beta^n. \tag{10}$$

After making necessary calculations, we get

$$\left| 1 - \frac{10^d \cdot F_m \cdot \sqrt{5}}{\alpha^k \left( (2\sqrt{5}-1) - \alpha^{n-k} \right)} \right| \leq \frac{1}{\alpha^k} \left| \frac{1}{(2\sqrt{5}-1) - \alpha^{n-k}} \right| \left( \frac{2\sqrt{5}+1}{\alpha^k} + \frac{1}{\alpha^n} \right),$$

i.e.,

$$\left| 1 - \frac{10^d \cdot \sqrt{5} \cdot F_m}{\alpha^k \left( (2\sqrt{5}-1) - \alpha^{n-k} \right)} \right| \leq \frac{0.55}{\alpha^k}, \tag{11}$$

where we kept in view that  $n \geq 0$ ,  $k \geq 110$  and  $k - n \geq -1$ . Put  $\gamma_1 := \alpha$ ,  $\gamma_2 := 10$ ,  $\gamma_3 := \frac{\sqrt{5} \cdot F_m}{(2\sqrt{5}-1) - \alpha^{n-k}}$ ,  $b_1 := -k$ ,  $b_2 := d$  and  $b_3 := 1$ . Moreover,  $D = 2$ . Let

$$\Gamma_2 := 1 - \frac{10^d \cdot \sqrt{5} \cdot F_m}{\alpha^k \left( (2\sqrt{5}-1) - \alpha^{n-k} \right)}.$$

If  $\Gamma_2 = 0$ , then we can write

$$10^d F_m = \left( 2 - \frac{\sqrt{5}}{5} \right) \alpha^k - \frac{\sqrt{5}}{5} \alpha^n. \tag{12}$$

Conjugating in  $\mathbb{Q}(\sqrt{5})$ , we get

$$10^d F_m = \left( 2 + \frac{\sqrt{5}}{5} \right) \beta^k + \frac{\sqrt{5}}{5} \beta^n. \tag{13}$$

Thus, from the equalities (12) and (13), we obtain  $2 \cdot 10^d \cdot F_m = M_k - F_n$ . This is impossible since  $M_k = 10^d F_m + F_n$ . As

$$\begin{aligned} h(\gamma_3) &\leq h(F_m) + h(\sqrt{5}) + h(2\sqrt{5} - 1) \\ &\quad + (k - n)h(\alpha) + \log 2 \\ &\leq (2m + 3) \frac{\log \alpha}{2} + \log 10 + 2 \log 2 \\ &= \frac{2 \log 40 + 3 \log \alpha}{2} + m \log \alpha, \end{aligned}$$

we can choose  $A_1 := \log \alpha$ ,  $A_2 := \log 100$ ,  $A_3 := 8.83 + 2m \log \alpha$ . By using (8), we obtain  $B := k + 1$ . By using the inequality (11) and Lemma 1, we can say

$$0.55 \times \alpha^{-k} > |\Gamma_2| >$$

$$\exp((1 + \log 2) \cdot A \cdot (1 + \log(k + 1)) \cdot \log \alpha \cdot \log 100 \cdot (8.83 + 2m \log \alpha)),$$

i.e.,

$$k \log \alpha - \log(0.55) < 2.15 \times 10^{12} \cdot (1 + \log(k + 1)) \cdot (8.83 + 2m \log \alpha). \quad (14)$$

Combining the inequalities (9) and (14), we get  $k < 4.03 \times 10^{29}$ . Now, let us reduce this bound. Let

$$z_1 := (k - m) \log \alpha - d \log 10 + \log(2\sqrt{5} - 1)$$

and so  $\Gamma_1 := e^{z_1} - 1$ . From (7), we have

$$|\Gamma_1| := |e^{z_1} - 1| < \frac{2.62}{\alpha^m} < 0.62.$$

Taking  $\rho := 0.62$ , we obtain the inequality

$$|z_1| < -\frac{\log 0.38}{0.62} \cdot \frac{2.62}{\alpha^m} < 4.09 \times \alpha^{-m}$$

by Lemma 3. Therefore, we can write

$$0 < |(k - m) \log \alpha - d \log 10 + \log(2\sqrt{5} - 1)| < 4.09 \times \alpha^{-m}$$

i.e.,

$$0 < \left| (k - m) \frac{\log \alpha}{\log 10} - d + \frac{\log(2\sqrt{5} - 1)}{\log 10} \right| < 1.78 \times \alpha^{-m}. \quad (15)$$

Put  $\tau := \frac{\log \alpha}{\log 10} \notin \mathbb{Q}$ ,  $\mu := \left( \frac{\log(2\sqrt{5} - 1)}{\log 10} \right)$ ,  $A := 1.78$ ,  $B := \alpha$ ,  $t := m$  and  $M := 4.03 \times 10^{29}$ . We have  $k - m > 1$  from Lemma 4(d). Moreover, we found  $q_{61} > 6M$  and then

$$\varepsilon := \|\mu q_{61}\| - M \|\tau q_{61}\| < 0.47.$$

According to Lemma 2, if (15) has a solution, then

$$m \leq \frac{\log\left(\frac{Aq_{61}}{\varepsilon}\right)}{\log B} \leq 151.55.$$

Thus,  $m \leq 151$ . By using (14), we have  $k < 2.68 \times 10^{16}$ . Put

$$z_2 :=$$

$$d \log 10 - k \log \alpha + \log\left(\frac{\sqrt{5} \cdot F_m}{(2\sqrt{5} - 1) - \alpha^{n-k}}\right)$$

and so  $\Gamma_2 := 1 - e^{z_2}$ . Since  $k \geq 110$ , it is clear that

$$|\Gamma_2| := |1 - e^{z_2}| < 0.55 \cdot \alpha^{-k} < 0.01$$

by the inequality (11). So, choosing  $\rho := 0.01$  in Lemma 3, we get

$$\left| d \log 10 - k \log \alpha + \log\left(\frac{\sqrt{5} \cdot F_m}{(2\sqrt{5} - 1) - \alpha^{n-k}}\right) \right| < \frac{\log\left(\frac{100}{99}\right)}{0.01} \cdot \frac{0.55}{\alpha^k} < 0.56 \times \alpha^{-k}$$

i.e.,

$$0 < \left| d \frac{\log 10}{\log \alpha} - k + \frac{\log\left(\frac{\sqrt{5} \cdot F_m}{(2\sqrt{5} - 1) - \alpha^{n-k}}\right)}{\log \alpha} \right| < 1.17 \times \alpha^{-k}, \quad (16)$$

where  $\tau := \frac{\log 10}{\log \alpha}$  and  $\mu := \frac{\log\left(\frac{\sqrt{5} \cdot F_m}{(2\sqrt{5} - 1) - \alpha^{n-k}}\right)}{\log \alpha}$ .

By using (8), we can take  $M := 2.68 \times 10^{16}$ . Here we found  $q_{40} \geq 6M$ . Thus, we can say

$$\varepsilon := \|\mu q_{40}\| - M \|\tau q_{40}\| < 0.498$$

for  $-1 \leq k - n \leq m + 4$  and  $3 \leq m \leq 151$ . In Lemma 2, let  $A := 1.17$ ,  $B := \alpha$ ,  $t := k$ . Hence, if (16) has a solution, then from Lemma 2, we get

$$k \leq \frac{\log\left(\frac{Aq_{40}}{\varepsilon}\right)}{\log B} \leq 104.5.$$

Thus  $k \leq 104$  contradicts our presumption that  $k \geq 110$ . When we take into account the case  $m = 2$  for  $k \geq 110$  it can be seen that  $k \leq 91$ . This is a contradiction. Thus, the proof of our theorem is finished.

**Funding**

The author (s) has no received any financial support for the research, authorship or publication of this study.

**Authors' Contribution**

The authors contributed equally to the study.

**The Declaration of Conflict of Interest/ Common Interest**

No conflict of interest or common interest has been declared by the authors.

**The Declaration of Ethics Committee Approval**

This study does not require ethics committee permission or any special permission.

**The Declaration of Research and Publication Ethics**

The authors of the paper declare that they comply with the scientific, ethical and quotation rules of SAUJS in all processes of the paper and that they do not make any falsification on the data collected. In addition, they declare that Sakarya University Journal of Science and its editorial board have no responsibility for any ethical violations that may be encountered, and that this study has not been evaluated in any academic publication environment other than Sakarya University Journal of Science.

**REFERENCES**

- [1] M. Lemma, "The Mulatu Numbers" *Advances and Applications in Mathematical Sciences*, vol. 10, no. 4, pp. 431-440, 2011.
- [2] W.D. Banks, F. Luca, "Concatenations with binary recurrent sequences" *Journal of Integer Sequences*, vol. 8, no. 5, pp. 1-3, 2005.
- [3] M. Alan, "On Concatenations of Fibonacci and Lucas Numbers" *Bulletin of the Iranian Mathematical Society*, vol. 48, no. 5, pp. 2725-2741, 2022.
- [4] M. Lemma, J. Lambrigt, "Some Fascinating theorems of Mulatu Numbers", *Hawai University International Conference*, 2016.
- [5] N. Irmak, Z. Siar, R. Keskin, "On the sum of three arbitrary Fibonacci and Lucas numbers" *Notes on Number Theory and Discrete Mathematics*, vol. 25, no. 4, pp. 96-101, 2019.
- [6] Y. Bugeaud, "Linear Forms in Logarithms and Applications" *IRMA Lectures in Mathematics and Theoretical Physics* 28, Zurich, European Mathematical Society, 1-176, 2018.
- [7] Y. Bugeaud, M. Mignotte S. Siksek, "Classical and modular approaches to exponential Diophantine equations I. Fibonacci and Lucas perfect powers" *Annals of Mathematics*, vol. 163, no. 3, pp. 969-1018, 2006.
- [8] J.J. Bravo, C.A. Gomez, F. Luca, "Powers of two as sums of two k-Fibonacci numbers" *Miskolc Mathematical Notes*, vol. 17, no. 1, pp. 85-100, 2016.
- [9] A. Dujella, A. Pethò, "A generalization of a theorem of Baker and Davenport" *Quarterly Journal of Mathematics Oxford series (2)*, vol. 49, no. 3, pp. 291-306, 1998.
- [10] B. M. M. de Weger, "Algorithms for Diophantine Equations" *CWI Tracts* 65, Stichting Mathematisch Centrum, Amsterdam, 1-69, 1989.



SAKARYA ÜNİVERSİTESİ

# FEN BİLİMLERİ ENSTİTÜSÜ DERGİSİ

Sakarya University Journal of Science  
SAUJS

ISSN 1301-4048 | e-ISSN 2147-835X | Period Bimonthly | Founded: 1997 | Publisher Sakarya University |  
<http://www.saujs.sakarya.edu.tr/>

Title: Enhancing Brain Tumor Detection on MRI Images Using an Innovative VGG-19 Model-Based Approach

Authors: Abdullah ŞENER, Burhan ERGEN

Received: 2023-05-25 00:00:00

Accepted: 2023-09-18 00:00:00

Article Type: Research Article

Volume: 27

Issue: 5

Month: October

Year: 2023

Pages: 1128-1140

How to cite

Abdullah ŞENER, Burhan ERGEN; (2023), Enhancing Brain Tumor Detection on MRI Images Using an Innovative VGG-19 Model-Based Approach. Sakarya University Journal of Science, 27(5), 1128-1140, DOI: 10.16984/saufenbilder.1302803

Access link

<https://dergipark.org.tr/tr/journal/1115/issue/80257/1302803>

New submission to SAUJS

<http://dergipark.gov.tr/journal/1115/submission/start>



## Enhancing Brain Tumor Detection on MRI Images Using an Innovative VGG-19 Model-Based Approach

Abdullah ŞENER\*<sup>1</sup>, Burhan ERGEN<sup>1</sup>

### Abstract

Early detection and diagnosis of brain tumors have a critical impact on the treatment of brain tumor patients. This is because initiating interventions early directly impacts the patient's chances of continuing their life. In the field of medical research, various methods are employed for the detection of brain tumors. Among these methods, magnetic resonance imaging (MRI) is the most popular due to its superior image quality. By leveraging technological advancements, the utilization of deep learning techniques in the identification of brain tumors ensures both high accuracy and simplification of the process. In a conducted study, a new model was developed by utilizing the VGG-19 architecture, a popular convolutional neural network model, to achieve high accuracy in brain tumor detection. In the study, precision, F1 score, accuracy, specificity, Matthews correlation coefficient, and recall metrics were used to evaluate the performance of the developed model. The deep learning model developed for brain tumor detection was trained and evaluated on an open-source dataset consisting of MRI images of gliomas, meningiomas, pituitary tumors, and healthy brains. The results obtained from the study demonstrate the promising potential of using the developed model in clinical applications for brain tumor detection. The high accuracy achieved by the developed model emphasizes its potential as an auxiliary resource for healthcare professionals in brain tumor detection. This research aims to evaluate the model as a valuable tool that can assist physicians in making informed treatment decisions regarding brain tumor diagnosis.

**Keywords:** Brain tumor detection, image classification, VGG-19 architecture, deep learning, support vector machines.

### 1. INTRODUCTION

The brain, situated within the cranium, represents the most intricate and vital component of the central nervous system. It governs crucial functions such as the regulation of consciousness, emotions, movement, and other cognitive processes [1]. It processes sensory signals received from the

body and serves as a central hub for generating appropriate responses to these signals [2]. Through intricate mechanisms of signal processing, the brain controls fundamental functions such as movement, emotion, and response [3]. Cancer, characterized by the uncontrolled and unrestrained proliferation of cells arising from genetic abnormalities, can manifest in

\* Corresponding author: asener@bingol.edu.tr (A. ŞENER)

<sup>1</sup> Bingöl University, Bingöl, Türkiye

E-mail: bergen@firat.edu.tr

ORCID: <https://orcid.org/0000-0002-8927-5638>, <https://orcid.org/0000-0003-3244-2615>



any region of the human body. When such cellular abnormalities occur in the brain, it is referred to as a brain tumor. This medical condition involves the rapid, uncontrolled, and irregular proliferation of cells in the brain. Brain tumors can be classified broadly into benign and malignant forms. Benign brain tumors are generally less harmful and exhibit slower growth compared to malignant tumors. Conversely, malignant tumors grow rapidly, irregularly, and uncontrollably. Malignant brain tumors lack well-defined boundaries and have a tendency to infiltrate surrounding tissues and even distant areas of the body. As malignant brain tumors grow, they exert increased pressure on the skull, leading to structural abnormalities. Early diagnosis of this condition is crucial in preventing its progression to critical stages.

In recent years, there has been a significant increase in mortality rates associated with brain tumors, positioning them as one of the leading causes of death among both males and females. The timely detection of brain tumors holds utmost significance in enhancing the survival rates of patients. A wide array of diagnostic tests and medical imaging modalities are utilized in the identification and localization of brain tumors. The latest technology used in brain tumor diagnosis is augmented reality applications, which have been developed in recent years. Considering the researches on their use and the research results in education thanks to the successes achieved with augmented reality technology, it is normal that it is one of the popular study topics [4]. Another method used in the diagnosis of brain tumors is biopsy. Biopsy, which involves the surgical sampling of cells, fluids, or tissues from areas suspected of disease, is commonly used for cancer diagnosis. However, biopsies carry inherent risks and require prolonged decision-making processes [5]. Magnetic Resonance Imaging (MRI), X-ray imaging and Computed Tomography (CT) are among the commonly employed diagnostic modalities for the visualization and characterization of brain tumors. Another critical diagnostic approach

for brain tumors involves the evaluation of magnetic resonance images (MRI) by specialists and radiologists. MRI imaging plays a pivotal role in detecting and classifying tumors as either benign or malignant. The accuracy of brain tumor detection from MRI images is greatly influenced by the proficiency and expertise of the reviewing physician, emphasizing the critical role of their knowledge in the diagnostic process. Brain tumors can be broadly classified into two main categories: benign tumors and malignant tumors. Glioma tumors, categorized as malignant, arise from the abnormal proliferation of glioma cells in the brain or spinal cord. Pituitary tumors, on the other hand, originate within the pituitary gland and are typically benign, arising from the excessive growth of pituitary cells. Meningioma tumors, predominantly benign, develop in the meninges, which are the membranes that cover the brain and spinal cord.

Artificial intelligence (AI) has gained significant popularity in various research domains, particularly in the field of medicine. In recent years, the use of AI techniques in brain tumor detection has been increasing [6]. Thank you to artificial intelligence and deep learning techniques, it is not only possible to detect brain tumors, but also to calculate the area covered by the brain tumor [7]. AI-based methods have demonstrated the ability to identify crucial details that may be overlooked during manual examinations by experts. As a result, numerous applications employing AI algorithms for the analysis of brain MRI images have emerged. The outcomes achieved through these applications have facilitated the development of novel methodologies, thereby improving the success rates in brain tumor detection. These AI-based applications leverage the inherent capabilities of deep learning and machine learning algorithms to effectively analyze and interpret brain MRI images. The algorithms are trained on large datasets containing diverse MRI images, enabling them to learn intricate patterns and features associated with

different types of brain tumors. By utilizing the acquired knowledge, these AI systems can accurately detect the presence of tumors, classify them as benign or malignant, and provide valuable insights for clinical decision-making. The integration of AI techniques in brain tumor detection has demonstrated remarkable potential in complementing and enhancing the capabilities of healthcare professionals. By assisting in the detection of brain tumors, AI applications contribute to early diagnosis, thereby facilitating timely interventions and improving patient outcomes. The continuous advancements in AI algorithms and technologies hold promise for further refining and expanding the scope of brain tumor detection and classification, ultimately contributing to the advancement of medical practice.

The rapid advancement of technology has positively influenced the development of computer-based systems for brain tumor detection. These developed systems hold great importance in the diagnoses of medical professionals. Previously, brain tumor diagnosis by experts was a time-consuming method. However, computer-based systems utilizing artificial intelligence provide a more efficient, fast, and accurate approach to brain tumor detection. Deep learning techniques, a subset of machine learning, offer seamless and automated results in the diagnostic process of brain tumors for medical experts. In recent years, the application of machine learning and deep learning methodologies has demonstrated remarkable advancements in the field of brain tumor detection and classification. [5]. In the present study, a publicly accessible dataset comprising MRI images of three distinct tumor types along with healthy brain samples was employed for the purpose of deep learning-based brain tumor detection. A custom model utilizing the VGG-19 architecture, a prominent deep learning model, was devised to accurately detect and classify brain tumors. Remarkably, the developed model exhibited an impressive 95% accuracy in the identification of brain

tumors. The outcomes derived from this investigation offer substantial support and represent a valuable asset for healthcare practitioners engaged in the realm of brain tumor detection.

Reviewing the rest of the paper; Section II includes recent work on brain tumor detection in MRI images using various deep learning models. Section III presents the research framework including brain MRI image enhancement and data augmentation, image preprocessing, CNN models and a detailed description of the classifier used for this research. The developed model is tested with the dataset and the corresponding results and complexity matrix are compared with other works in Section IV. Section V contains the conclusion.

## 2. METHODOLOGY

### 2.1. Data Set

To evaluate the performance of the classification model developed in this study, an open-source dataset consisting of MRI images of 4 classes was used [8]. The dataset consists of MRI images of pituitary, meningioma, glioma and healthy brain. Some of the images that make up the dataset are shown in Figure 1. Pituitary tumor is caused by abnormal growth of pituitary cells. Pituitary tumor is one of the benign tumors. Patients diagnosed with pituitary tumors remain asymptomatic and harmless throughout their lives. However, since the function of the pituitary gland is very important in the human body, it can cause serious health problems as the tumor grows and secretes hormones that the body does not need [9]. Meningioma tumors are among the most common primary brain tumors. It is a type of tumor that occurs in the meninges and is not dangerous. However, during the growth of these tumors, pressure on the brain or spinal cord can cause some problems [10]. Glioma tumors, classified as malignant neoplasms, are characterized by the aberrant proliferation of glioma cells within the central

nervous system, specifically the brain or spinal cord. Glioma tumors can occur at any age. It tends to occur in older adults [11].

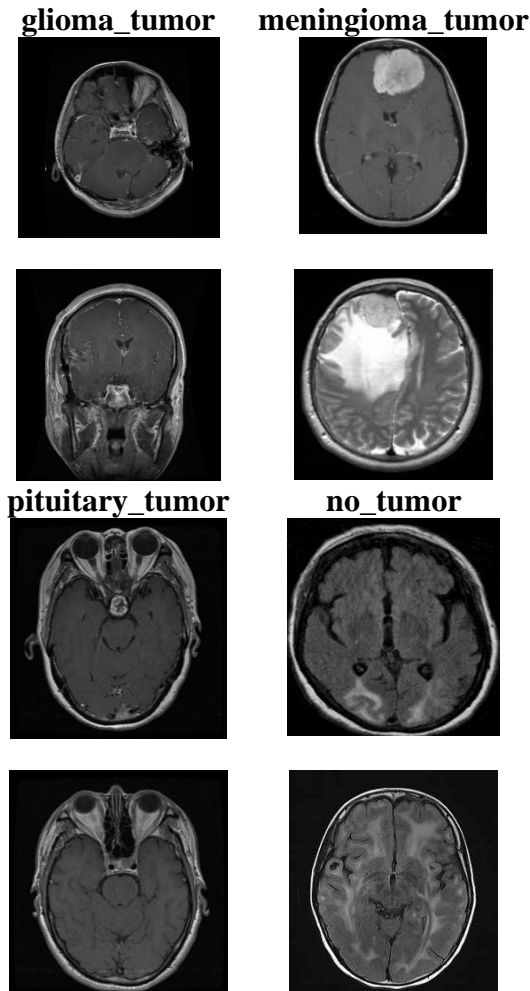


Figure 1 Sample images from the dataset used for the study [8]

The dataset utilized in this study comprises a total of 7,678 grayscale images with varying resolutions. These images encompass 1,796 glioma, 1,784 meningioma, 2,162 healthy, and 1,936 pituitary tumor MRI images. The dataset was divided into three subsets, with 74% of the images allocated for training, 17% for testing, and 9% for validation purposes.

## 2.2. Data Augmentation

One of the primary obstacles encountered in machine learning and deep learning investigations pertains to the limited availability of training data to effectively train the network. Insufficient data can lead to

overfitting issues, where the network memorizes the training samples and struggles to generalize to unseen data. To tackle this issue, researchers commonly adopt two prevalent strategies: augmenting the training data through various techniques and expanding the size of the available dataset. Increasing the training data involves acquiring additional samples to enrich the dataset. This can be done by collecting more data through various means, such as conducting additional experiments or collaborating with other institutions. By expanding the dataset, the network can learn from a more diverse range of examples and improve its ability to recognize and classify new instances. Data augmentation, on the other hand, is a technique used to artificially generate more training samples by applying various operations to the existing images. This approach helps to overcome the limitation of insufficient data by creating augmented versions of the original images. Common transformations employed in data augmentation include horizontal flipping, 90-degree rotation, adjusting brightness and contrast randomly, blurring, optical distortion, scaling the image with rotation, transposing, and grid distortion. Figure 2 illustrates some examples of data augmentation methods.

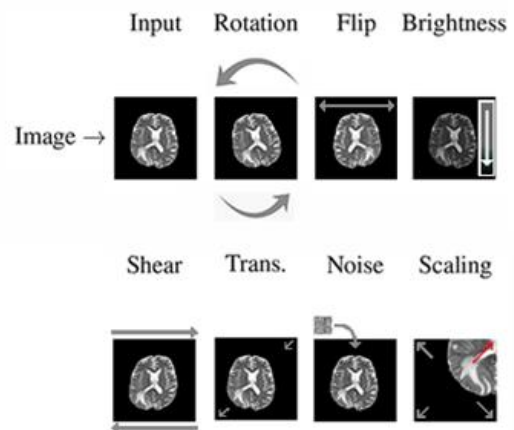


Figure 2 Some examples of data augmentation methods [12]

## 2.3. Deep Learning

Deep learning encompasses a class of artificial neural networks that consist of one

or more concealed layers, along with machine learning methodologies that exhibit similar characteristics to these network architectures. [13]. The fundamental aim of deep learning is to extract novel insights and knowledge by leveraging artificial neural networks. Deep learning techniques can be classified into supervised, semi-supervised, and unsupervised learning paradigms, each tailored to specific learning objectives and data availability [14]. Artificial neural networks were initially developed to model information processing and infer new knowledge from data, drawing inspiration from the functioning of the human brain. Although artificial neural networks and the human brain share the common objective of performing tasks, they exhibit distinct disparities in their characteristics and functionalities. Neural networks tend to be static and symbolic, whereas the brain operates dynamically and in an analog fashion [13-16].

Convolutional Neural Networks (CNNs) have emerged as a prominent deep learning methodology, garnering substantial attention and widespread recognition within the research community [17-19]. The architecture of CNNs is specifically engineered to emulate the intricate operations of the visual cortex, effectively integrating comparable features to facilitate object recognition within image data [20, 21]. The CNN architecture comprises several layers, each performing distinct operations. The building blocks of CNNs consist of several essential layers, encompassing the convolution layer, nonlinearity layer, pooling layer, smoothing layer, and fully connected layers [19]. In the CNN architecture, the convolution layer plays a crucial role as it involves extensive mathematical operations. The convolution layer, serving as the cornerstone of the CNN architecture, assumes the crucial role of detecting features at various levels, employing filters to process input images.

The nonlinear layer plays a pivotal role in identifying nonlinearities inherent in the system. Additionally, the pooling layer is responsible for downsampling feature maps, effectively reducing the network's parameter and weight count. This reduction is typically achieved through operations such as maximum pooling (dividing the image into  $n \times n$  matrices and selecting the highest value within each matrix) or average pooling (dividing the image into  $n \times n$  matrices and calculating the average of the values within each matrix). The smoothing layer plays a crucial role in the CNN architecture by preparing the data for the ultimate component, referred to as the fully connected layer. This layer integrates and processes the features extracted from previous layers to generate the final output. This is often accomplished by transforming the incoming data into a one-dimensional matrix. The fully connected layer establishes correlations between the input and output layers [22, 23].

## 2.4. VGG-19

VGG-19 is a convolutional neural network renowned for its depth, comprising a total of 24 layers. These layers encompass 16 convolutional layers, 5 pooling layers, and 3 fully connected layers, collectively contributing to the network's intricate architecture [24]. It is pre-trained on more than one million images from the ImageNet database. The VGG-19 network has an image input of 224 x 224 pixels. The VGG-19 architecture consists of approximately 138 million parameters [25]. To effectively minimize the parameter count within the VGG-19 architecture, the convolutional layer is designed to employ 3x3 pixel-sized filters. This strategic choice optimizes the network's efficiency while preserving its ability to capture and extract meaningful features from input data.

## 2.5. Support Vector Machines

In the realm of classification tasks, the Support Vector Machine (SVM) stands out as

a prominent supervised learning technique widely employed for its efficacy and versatility. SVM aims to separate data points belonging to different classes by drawing a line on a plane. The key objective is to position the line in such a way that it maximizes the distance from the points of the two separated classes. This method is particularly effective for small to medium-sized datasets with complex structures [26]. An example of SVM classification is illustrated in Figure 4, where two distinct classes, black and white, are depicted. The primary goal in classification tasks is to determine the class to which a new shape will be assigned. To achieve class separation, a line is drawn, and the green region shown in Figure 3, called the Margin, represents the area between  $\pm 1$  of this line. The wider the margin, the better the classification performance.

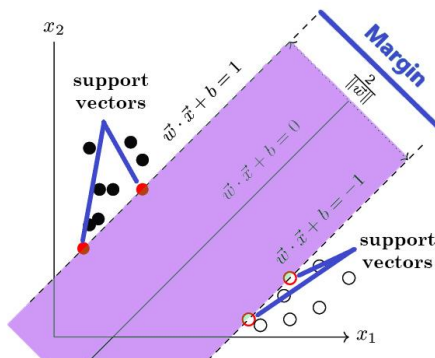


Figure 3 Support Vector Machines classification example

In Support Vector Machines (SVM), as depicted in Figure 3, the weight vector is denoted by  $w$ , the input vector by  $x$ , and the deviation by  $b$ . In the example of SVM classification, if the computed value is less than 0, the new instance will be classified as being closer to the white dots shown in Figure 4. Conversely, if the computed value is equal to or greater than 0, the new instance will be considered closer to the black dots depicted in Figure 3. The calculation formula employed in Support Vector Machines is presented in Equation 1

$$y = \begin{cases} 0 & \text{eğer } w^T \cdot x + b < 0, \\ 1 & \text{eğer } w^T \cdot x + b \geq 0 \end{cases} \quad (1)$$

## 2.6. Recommended Approach

This study introduces a pioneering approach in brain tumor detection, presenting a novel model built upon the VGG-19 architecture. The performance assessment of the proposed model is carried out utilizing a publicly available dataset consisting of brain MRI images, enhancing the credibility and applicability of the findings. To ensure balanced representation of image classes within the dataset, efforts were made to address any class imbalance issues. To expand the dataset and enhance training efficacy, diverse data augmentation techniques were implemented, resulting in a larger pool of images for model training. The augmented dataset was partitioned into distinct subsets, with 74% allocated for training purposes, 17% for testing, and 9% reserved for validation, ensuring robust evaluation and effective model generalization. In the subsequent stage of the investigation, a preprocessing step was implemented to standardize the sizes and resolutions of images, ensuring consistency and compatibility for further analysis. The images were resized to a uniform dimension of 224x224 pixels, serving as the standardized input size for the proposed model. This standardization process facilitates seamless integration and enables accurate and efficient processing within the model framework. Resizing the input images to a fixed size is performed to accelerate the classification process and manage computational memory usage effectively. It is crucial to strike a balance when resizing the images, avoiding excessive reduction that could hinder the extraction of essential information required for accurate classification. Once the images are resized, the classification is performed on images with a consistent size and resolution. The overall framework of the proposed approach is presented in Figure 4.

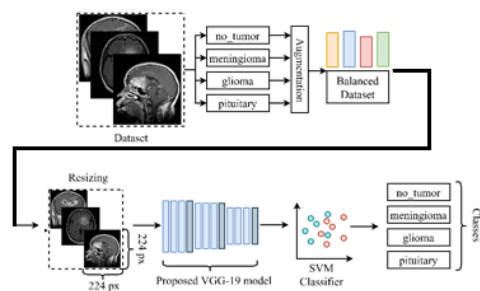


Figure 4 Overall design of the proposed approach

The model shown in Figure 4 consists of 25 layers in total. The model consists of 16 Convolution, 5 Maximum Pooling, 1 Smoothing, 2 Fully Connected Kaman and 1 dense layer. The developed model consists of 139,586,628 parameters.

When the proposed model is examined, 16 convolution and 5 pooling (maximum) layers are applied to the brain MRI input image in gray format. After the convolution and pooling layers are completed, smoothing and full connectivity layers are applied. Full connectivity-1 (FC1) layer and bulk normalization-1 layers are applied after the smoothing process. After these layers, the forgetting process is performed with a dropout rate between 0.3 and 0.5. In the developed model, the forgetting layer is used to prevent the network from memorizing. Then the full connectivity-2 layer and aggregate normalization-2 layers are used. In the next stage, forgetting is performed again with a dropout rate between 0.3 and 0.5. In the last part of the model, the Softmax optimization algorithm is used to obtain an output with 4 classes. In addition, ReLU activation function is used in the convolution layers of the model.

All training and testing of the network models was performed on a workstation with hardware features such as Intel(R) Xeon(R) CPU @ 2.30GHz, 24 GB RAM, and Tesla T4-16GB graphics card. Frameworks such as Python, Tensorflow and Keras were also used for software coding for the proposed model.

### 3. RESULTS AND DISCUSSION

The conducted research involved partitioning a brain MRI dataset comprising a total of 7678 images into distinct subsets to facilitate the training, testing, and validation stages. Specifically, approximately 74% of the images, corresponding to 5682 images, were allocated for training purposes. This strategic data allocation ensures a sufficient volume of samples for the model to learn from, thereby promoting robust learning and generalization capabilities. Around 17% of the images (1311 images) were allocated for testing, and the remaining 9% (685 images) were used for validation. Figure 5 provides a graphical representation of the accuracy rate and loss values achieved during the training phase of the developed model. The graphs demonstrate the rapid learning of the network, as observed from the fluctuations in the curves from the 10th iteration to the 150th iteration. Upon completion of the training process, the developed model achieved an accuracy rate of 95%.

The results of this study demonstrate that brain MRI images can be effectively analyzed and accurately classified using machine learning methods. The developed model attained a high accuracy rate due to being trained on an adequate number of samples. This can contribute to the development of deep learning models to be used in the diagnosis of brain diseases or treatment planning in future similar studies.

The evaluation of the developed classification model's performance often involves the utilization of a confusion matrix, which is widely used in classification tasks. The confusion matrix incorporates the terms True Positive (TP), False Positive (FP), True Negative (TN), and False Negative (FN) to provide a comprehensive assessment. Using these terms, the model's Precision, Sensitivity, Accuracy, F1-Score and Matthews correlation coefficient (MM) [27] values can also be calculated. Accuracy is the ratio of correct predictions to all predictions

in classification problems. Sensitivity is the effectiveness of the model in predicting the positive class label of the target variable, i.e., the ratio of correctly classified positive samples to the total number of positive samples.

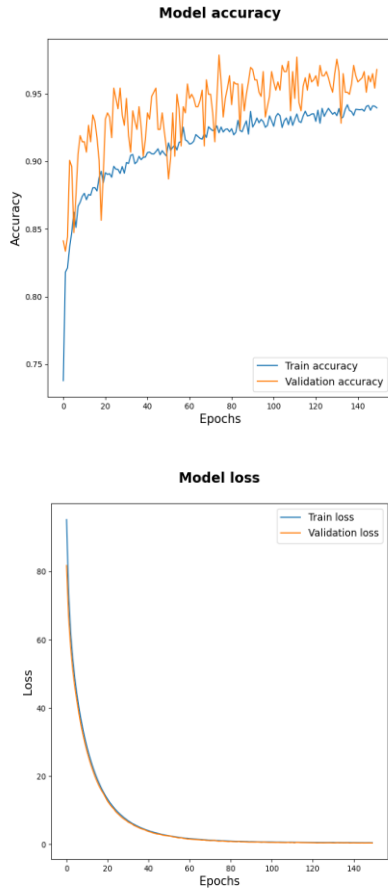


Figure 5 Accuracy and loss graph of the developed model

Precision is the ratio of correctly classified positive samples to the total number of positive predicted samples. The F1 score is the harmonic mean of the precision and sensitivity performance evaluation criteria and provides the ability to consider both criteria together. Matthews (MCC) measures the correlation of classification results with precision in the basic categories TP, TN, FP, FN. These four categories are used to evaluate the performance of the model by comparing the classification results with the actual values. The mathematical operations given in equations 2, 3, 4, 5 and 6 are used to calculate these values.

$$Precision = \frac{TP}{TP+FP} \tag{2}$$

$$Sensitivity = \frac{TP}{TP+FN} \tag{3}$$

$$Accuracy = \frac{TP+TN}{TP+TN+FP+FN} \tag{4}$$

$$F1 - Score = \frac{2*Precision*Sensitivity}{Precision+Sensitivity} \tag{5}$$

$$MM = \frac{(FP*FN-TP*TN)}{\sqrt{((TN+FP)*(TN+FN)*(TP+FN)*(TP+FP))}} \tag{6}$$

The results of the analysis of the classification processes obtained using the test data of the proposed model are shown in Table 1.

Table 1 Analysis results of classification processes

<i>Classes</i>	<i>Support</i>	<i>Sensitivity</i>	<i>Precision</i>
Glioma	300	97%	83%
Meningioma	306	83%	97%
Healthy	405	100%	99%
Pituitary	300	100%	97%
	<i>F1-Score</i>	<i>Matthews</i>	<i>Accuracy</i>
Glioma	89%	87%	95.5%
Meningioma	90%	86%	94.74%
Healthy	99%	99%	99.62%
Pituitary	98%	98%	99.31%

Figure 6 displays the confusion matrix formed based on the results obtained from the classification process of the developed model.

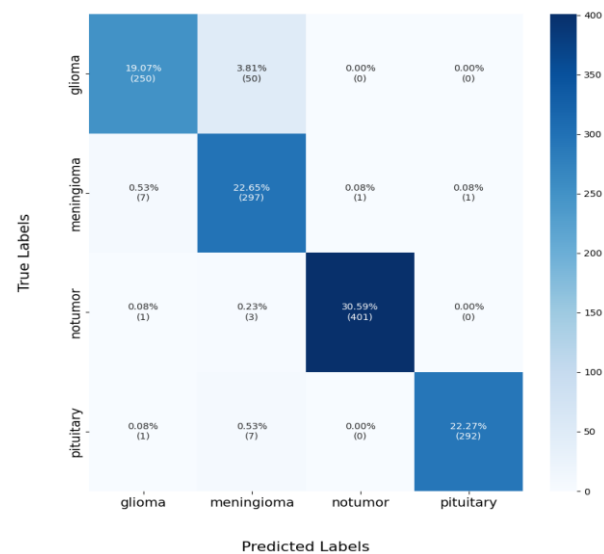


Figure 6 Confusion matrix of the model



Table 2 showcases a comparative analysis between the outcomes achieved by the proposed model and the results obtained from other models focusing on brain tumor detection. This evaluation encompasses not only the dataset utilized in this study but also analogous datasets documented in the existing literature.

Table 2 Comparison of studies with similar datasets

<i>Ref.</i>	<i>Architecture/Method</i>	<i>Results (%)</i>
[28]	EWS ResNet50 and ResNet50	90 - 92
[29]	CNN	91.43
[30]	CNN	94.58
[31]	LSTM Network	78.33
[32]	AlexNet CNN	91
[33]	CNN	84.19
[34]	SVM and kNN	91.28
[35]	Capsnet	90.89
[36]	Random Forest Classifier	86
[37]	BrainMRNe	96.05
[38]	Transfer Learning	92.34
[39]	Markov Random Field Alg.	87
Prop. App.	VGG-19	95

The studies conducted for brain tumor detection are presented in Table 2 in the literature. The results obtained from these studies demonstrate the popularity and significance of the topic. Sharma et al. [28] developed a modified ResNet50 model based on the watershed segmentation (EWS) algorithm. They achieved an accuracy rate of 90% with their modified ResNet50 model and 92% with the ResNet50 model. Paul et al. [29] obtained results with an accuracy rate of 91.43% using their modified CNN model. Sajad et al. [30] achieved a 94.58% accuracy rate in classifying brain tumor images using their CNN-based approach. Kumar et al. [31] demonstrated a classification accuracy of 78.33% by utilizing an LSTM network for brain tumor image classification.

Khwaldeh et al. [32] achieved a classification accuracy of 91% using the widely adopted CNN model, AlexNet. Abiwinanda et al. [33] reported a classification accuracy of 84.19% by employing a pre-trained sequential CNN model. Cheng et al. [34] achieved a

classification accuracy of 91.28% through the utilization of kNN and SVM classifiers for brain tumor image classification. Afshar et al. [35] developed a Capsnet CNN model that yielded an accuracy rate of 90.89%. Soltaninejad et al. [36] achieved a classification accuracy of 86% by employing a random forest classifier on brain MRI datasets. Togacar et al. [37] proposed a novel convolutional neural network model, achieving an impressive classification accuracy of 96.05%. Anaya-Isaza and Mera-Jiménez [38] utilized transfer learning techniques and achieved an accuracy of 92.34% for brain tumor image classification. Faruk et al. [39] compared and analyzed the performance of image segmentation methods in brain tumor detection. In the study, Markov Random Field Algorithm gave better results than other methods in the study with an accuracy rate of 87%.

#### 4. CONCLUSION

A brain tumor is a pathological condition characterized by the uncontrolled proliferation of cells within the cranial cavity. It can be broadly categorized into two distinct classes: benign and malignant brain tumors. Benign tumors are non-cancerous in nature and generally exhibit a slow growth pattern. Conversely, malignant tumors are characterized by their cancerous properties, manifesting as rapid and uncontrolled cell growth. The timely detection of brain tumors holds immense significance in improving patient prognosis, as it enables prompt intervention and management before the disease advances to an irreversible stage.

The primary objective of this research is to design and evaluate a deep learning model capable of accurately and efficiently detecting and classifying brain tumors from brain MRI images. The model architecture employed in this study is based on the widely recognized VGG-19 convolutional neural network (CNN) model. To train and evaluate the model, a publicly available dataset containing a diverse range of brain MRI images,

including three distinct tumor classes and healthy brain images, is utilized. The model is trained and assessed using grayscale images with standardized dimensions of 224x224 pixels. Furthermore, the performance of the developed model is compared with other state-of-the-art models used in previous studies employing the same dataset. The comparative analysis reveals that the proposed model surpasses its counterparts in terms of classification accuracy, achieving an impressive success rate of 95%.

In future investigations, the aim is to make adjustments to the developed deep learning model to increase its accuracy percentage and evaluate its applicability in various domains beyond brain tumor detection.

#### ***Funding***

The author (s) has no received any financial support for the research, authorship or publication of this study.

#### ***The Declaration of Conflict of Interest/ Common Interest***

No conflict of interest or common interest has been declared by the authors.

#### ***Authors' Contribution***

The authors contributed equally to the study.

#### ***The Declaration of Conflict of Interest/ Common Interest***

No conflict of interest or common interest has been declared by the authors.

#### ***The Declaration of Ethics Committee Approval***

This study does not require ethics committee permission or any special permission.

#### ***The Declaration of Research and Publication Ethics***

The authors of the paper declare that they comply with the scientific, ethical and quotation rules of SAUJS in all processes of the paper and that they do not make any falsification on the data collected. In addition, they declare that Sakarya University Journal

of Science and its editorial board have no responsibility for any ethical violations that may be encountered, and that this study has not been evaluated in any academic publication environment other than Sakarya University Journal of Science.

## **REFERENCES**

- [1] M. Tanveer, M.A. Ganaie, I. Beheshti, T. Goel, N. Ahmad, K. T. Lai, C. T. Lin. "Deep learning for brain age estimation: A systematic review". Information Fusion, 2023.
- [2] S. Solanki, U. P. Singh, S. S. Chouhan, S. Jain. "Brain Tumor Detection and Classification using Intelligence Techniques: An Overview". IEEE Access, 2023.
- [3] S. Asif, W. Yi, Q. U. Ain, J. Hou, T. Yi, J. Si. "Improving Effectiveness of Different Deep Transfer Learning-Based Models for Detecting Brain Tumors From MR Images". IEEE Access, vol. 10, pp. 34716-34730, 2022.
- [4] H. N. Kiliç, Y. Uzun. "Beyin Cerrahisi İçin Artırılmış Gerçeklik Uygulaması Gerçekleştirmek". Avrupa Bilim ve Teknoloji Dergisi, vol. 33, pp. 290-296, 2022.
- [5] R. K. Gupta, S. Bharti, N. Kunhare, Y. Sahu, N. Pathik. "Brain Tumor Detection and Classification Using Cycle Generative Adversarial Networks". Interdisciplinary Sciences: Computational Life Sciences, pp. 1-18, 2022.
- [6] Z. Zhou, Z. He, Y. Jia. "AFPNet: A 3D fully convolutional neural network with atrous-convolution feature pyramid for brain tumor segmentation via MRI images". Neurocomputing, vol. 402, pp. 235-244, 2020.

- [7] B. Kapusiz, Y. Uzun, S. Koçer, Ö. Dündar. "Brain Tumor Detection and Brain Tumor Area Calculation with Matlab". *Journal of Scientific Reports-A*, vol. 052, pp. 352-364, 2023.
- [8] Dataset: <https://www.kaggle.com/datasets/sartajbhuvaji/brain-tumor-classification-mri> Access Date: 05.07.2022.
- [9] A Tiwari., S. Srivastava, M. Pant. "Brain tumor segmentation and classification from magnetic resonance images: Review of selected methods from 2014 to 2019. *Pattern Recognition Letters*, vol. 131, pp. 244-260, 2020.
- [10] K. Dağlı, O. Eroğul. "Classification of Brain Tumors via Deep Learning Models". In *2020 Medical Technologies Congress (TIPTEKNO)* (pp. 1-4). IEEE, 2020.
- [11] G. Mohan, M. M. Subashini. "MRI based medical image analysis: Survey on brain tumor grade classification". *Biomedical Signal Processing and Control*, vol. 39, 139-161, 2018.
- [12] M. Cossio. "Augmenting Medical Imaging: A Comprehensive Catalogue of 65 Techniques for Enhanced Data Analysis". *arXiv preprint arXiv:2303.01178*, 2023.
- [13] X. Liu, Z. Deng, Y. Yang. "Recent progress in semantic image segmentation". *Artificial Intelligence Review*, vol. 52, pp. 1089-1106, 2019
- [14] K. Sharifani, M. Amini. "Machine Learning and Deep Learning: A Review of Methods and Applications". *World Information Technology and Engineering Journal*, vol. 10, no. 07, pp. 3897-3904, 2023.
- [15] N. Kanwisher, M. Khosla, K. Dobs. "Using artificial neural networks to ask 'why' questions of minds and brains". *Trends in Neurosciences*, vol. 46, no. 3, pp. 240-254, 2023.
- [16] A. H. Marblestone, G. Wayne, K. P. Kording. "Toward an integration of deep learning and neuroscience". *Frontiers in computational neuroscience*, 94, 2016.
- [17] S. Cong, Y. Zhou. "A review of convolutional neural network architectures and their optimizations". *Artificial Intelligence Review*, vol. 56, no. 3, pp. 1905-1969, 2023.
- [18] J. Gu, Z. Wang, J. Kuen, L. Ma, A. Shahroudy, B. Shuai, T. Chen. "Recent advances in convolutional neural networks". *Pattern recognition*, vol. 77, pp. 354-377, 2018.
- [19] S. Min, B. Lee, S. Yoon. "Deep learning in bioinformatics". *Briefings in bioinformatics*, vol. 18, no. 5, pp. 851-869, 2017.
- [20] M. Mirbabaie, S. Stieglitz, N. R. J. Frick. "Artificial intelligence in disease diagnostics: A critical review and classification on the current state of research guiding future direction". *Health Technology (Berl)* vol. 11, no. 4, pp. 693-731, 2021.
- [21] K. Hanbay. "Hyperspectral image classification using convolutional neural network and two-dimensional complex Gabor transform". *Journal of the Faculty of Engineering and Architecture of Gazi University*, vol. 35, no. 1, 443-456, 2020.
- [22] M. Niepert. M. Ahmed, K. Kutzkov. "Learning convolutional neural networks for graphs". In *International conference on machine learning*, . Germany, vol. 2016. pp. 2014-2023, 2014.

- [23] F. Kurt. "Investigation of the Effect of Hyper Parameters in Neural Networks". Ankara:Hacettepe University, 2018. Computational Science, vol. 30, pp. pp. 174-182, 2019.
- [24] M. Toğaçar, B. Ergen, F. Özyurt. "Classification of Flower Images Using Feature Selection Methods in Convolutional Neural Network Models". *Firat University Journal of Engineering Sciences*, vol. 32, no. 1, pp. 47-56, 2020.
- [25] M. Mateen, J. Wen, S. Song, Z. Huang. "Fundus image classification using VGG-19 architecture with PCA and SVD". *Symmetry*, vol. 11, no. 1, 1, 2018.
- [26] S. Huang, N. Cai, P. P. Pacheco, S. Narrandes, Y. Wang, W. Xu. "Applications of support vector machine (SVM) learning in cancer genomics". *Cancer genomics & proteomics*, vol. 15, no. 1, pp. 41-51, 2018.
- [27] F. Bulut. "Sınıflandırıcı topluluklarının dengesiz veri kümeleri üzerindeki performans analizleri". *Bilişim Teknolojileri Dergisi*, 9(2), 153, 2016.
- [28] A. K. Sharma, A. Nandal, A. Dhaka, D. Koundal, D. C. Bogatinoska, H. Alyami. "Enhanced watershed segmentation algorithm-based modified ResNet50 model for brain tumor detection". *BioMed Research International*, 2022.
- [29] J. S. Paul, A. J. Plassard, B. A. Landman, D. Fabbri. "Deep learning for brain tumor classification" *Proc. SPIE*, vol. 10137, Art. no. 1013710, 2017.
- [30] M. Sajjad, S. Khan, K. Muhammad, W. Wu, A. Ullah, S. W. Baik. "Multi-grade brain tumor classification using deep CNN with extensive data augmentation" *Journal of*
- [31] S. Kumar, A. Sharma, T. Tsunoda. "Brain wave classification using long short-term memory network based Optical predictor" *Scientific Reports*, vol. 9, no. 1, pp. 1-13, 2019.
- [32] S. Khawaldeh, U. Pervaiz, A. Rafiq, R. Alkhawaldeh. "Noninvasive grading of glioma tumor using magnetic resonance imaging with convolutional neural networks" *Applied Science*, vol. 8, no. 1, p. 27, 2017.
- [33] N. Abiwinanda, M. Hanif, S. T. Hesaputra, A. Handayani, T. R. Mengko. "Brain tumor classification using convolutional neural network" in *Proc. World Congress on Medical Physics and Biomedical Engineering Singapore: Springer*, pp. 183-189, 2018.
- [34] J. Cheng, W. Huang, S. Cao, R. Yang, W. Yang, Z. Yun, Z. Wang, Q. Feng. "Enhanced performance of brain tumor classification via tumor region augmentation and partition" *PLoS ONE*, vol. 10, no. 10, Art. no. e0140381, 2015.
- [35] P. Afshar, K. N. Plataniotis, A. Mohammadi. "Capsule networks for brain tumor classification based on MRI images and coarse tumor boundaries" in *Proceedings IEEE International Conference of Acoustic, Speech and Signal Processing (ICASSP)*, pp. 1368-1372, 2019.
- [36] M. Soltaninejad, G. Yang, T. Lambrou, N. Allinson, T. L. Jones, T. R. Barrick, F. A. Howe, X. Ye. "Supervised learning based multimodal MRI brain tumor segmentation using texture features from supervoxels" *Computer Methods Programs in Biomedicine*, vol. 157, pp. 69-84, 2018.

- [37] M. Toğaçar, B. Ergen, Z. Cömert. “BrainMRNet: Brain tumor detection using magnetic resonance images with a novel convolutional neural network model”. *Medical hypotheses*, 134, 109531, 2020.
- [38] A. Anaya-Isaza, L. Mera-Jiménez. “Data Augmentation and Transfer Learning for Brain Tumor Detection in Magnetic Resonance Imaging”. *IEEE Access*, vol. 10, pp. 23217-23233, 2022.
- [39] F. Bulut, İ. Kılıç, İ.F. İnce. “Comparison And Performance Analysis Of Image Segmentation Algorithms On Brain Tumor Detection”. *Dokuz Eylül University Faculty of Engineering Science and Engineering Journal*, 20(58), pp.173-186, 2018.



SAKARYA ÜNİVERSİTESİ

# FEN BİLİMLERİ ENSTİTÜSÜ DERGİSİ

Sakarya University Journal of Science  
SAUJS

ISSN 1301-4048 | e-ISSN 2147-835X | Period Bimonthly | Founded: 1997 | Publisher Sakarya University |  
<http://www.saujs.sakarya.edu.tr/>

Title: Fractal Approach to Dielectric Properties of Single Walled Carbon Nanotubes Reinforced Polymer Composites

Authors: Aykut ILGAZ, Mehmet BAYIRLI

Received: 2023-02-14 00:00:00

Accepted: 2023-10-03 00:00:00

Article Type: Research Article

Volume: 27

Issue: 5

Month: October

Year: 2023

Pages: 1141-1149

How to cite

Aykut ILGAZ, Mehmet BAYIRLI; (2023), Fractal Approach to Dielectric Properties of Single Walled Carbon Nanotubes Reinforced Polymer Composites. Sakarya University Journal of Science, 27(5), 1141-1149, DOI: 10.16984/saufenbilder.1250945

Access link

<https://dergipark.org.tr/tr/journal/1115/issue/80257/1250945>

New submission to SAUJS

<http://dergipark.gov.tr/journal/1115/submission/start>

## Fractal Approach to Dielectric Properties of Single Walled Carbon Nanotubes Reinforced Polymer Composites

Aykut ILGAZ<sup>\*1</sup>, Mehmet BAYIRLI<sup>1</sup>

### Abstract

In this paper, the internal structure and dielectric properties of unsaturated polyester resin-based neat and single-walled carbon nanotube reinforced composites were comprehensively evaluated with the fractal analysis using the Fast Fourier Transform (FFT). The greyscale images, bitmap (BMP) images and 3D tomographic images were obtained by converting the scanning electron microscope images of the materials. It was observed that the distributions of components in the resin for both materials are irregular and their surfaces exhibit anisotropic behaviors. The surface coating rate (SCR) and fractal dimensionality (FD) of the materials were also calculated using the power spectrum. It has been observed that the fractal dimensionality of the composites can be changed by the doping process and the fractalization of the nanotube doped sample increases compared to the pure material due to nanotube agglomeration, spatial distribution and the orientation. The increase in fractalization as a result of this agglomeration and orientation in carbon nanotubes explains the high dielectric constant values observed at low frequencies by increasing the number and size of carbon nanotubes clusters that act as micro capacitors in certain regions of the matrix. It has been reported that the calculations for the surface coverage ratios for both samples also support these results.

**Keywords:** Fast Fourier Transform, fractal analysis, power spectrum, dielectric properties, carbon nanotubes

### 1. INTRODUCTION

In recent years, studies on the doping of nanomaterials with various ratios in order to improve the performance of polymer composites in charge storage capacitor applications have led to the production of composite materials with high dielectric constants [1-4]. Single-walled carbon nanotubes are nanomaterials with superior mechanical properties as well as unique

dielectric properties. Ultra-high dielectric constant values can be obtained in nanotube-doped polymer composites due to polarizations occurring at the interfaces as a result of the combination of carbon nanotubes with conductive nature and insulating composites [5]. Samir et al. estimated dielectric permittivity for different concentrations of nanotubes. It was stated that adding 0.5 wt. % nanotubes to the neat sample increased the dielectric constant about 30

\* Corresponding author: aykut17ilgaz@gmail.com

<sup>1</sup> Balıkesir University, Balıkesir, Türkiye

E-mail: drbayirli@gmail.com

ORCID: <https://orcid.org/0000-0002-9632-0281>, <https://orcid.org/0000-0002-7775-0251>



times [6]. Belhimria et al. studied effect of CNT and graphite reinforcements on dielectric behaviours of polyester based neat composite. It has been reported that nanotubes and graphite additives significantly increase the dielectric constant of the material, even at small concentrations [7].

In addition to experimental efforts, the properties of doped composites and solids can also be explained with a theoretical model that includes the fractal characteristics, morphological and topographic properties. For this purpose, studies have been carried out to analyze the correlation between properties and morphological characteristics of materials in recent years [8-12]. The relationship between the fractal dimension and dielectric relaxation mechanism of the carbon nanotube doped epoxy-based polymer composites using small angle neutron scattering (SANS) and impedance spectroscopy (IS) methods has been studied [9].

Pander et al. investigated CNT forest structure by fractal dimension and lacunarity analysis using a box-counting method [13]. It is determined that the fractalization decreased with the increasing thickness during the fractality analysis of the catalyst particles. Zhang et al. reported a simple method to determine the amount of the interface's surface area and uniformity using fractal dimension calculation based on SEM images [14]. They studied on rubber and plastic composites to directly correlate the fractal dimension of the CNT interfacial surface area with the composite properties. They found that with increasing fractal dimension of the CNT interface surface area, the electrical conductivity of the composites increased exponentially and the tensile strength linearly increased. Hopkins et al. have demonstrated that the fractal dimension is related to the dielectric relaxation process [15].

So far, most of the researches on the dielectric behavior of nanotube-doped polymer composites have used multi-walled carbon

nanotubes. We thought that the effect of single-walled carbon nanotubes, which have different mechanical, thermal and electrical properties from multi-walled carbon nanotubes, on the dielectric properties of composite materials should be investigated. Additionally, there are not enough studies in the literature to fully reveal the relation between the capacitor behaviors of the single-walled carbon nanotube doped material and its morphological structure.

This motivated us to consider a detailed and systematic study to understand the correlation between them. Therefore, the main purpose of this study is to reveal the degree of correlation between the experimentally determined dielectric performance of pure and nanotube loaded composites and fractal analysis parameters.

## 2. MATERIAL AND METHOD

### 2.1. Material

Pure and nanotube-filled polymer composites were manufactured using Sheet Moulding Compound (SMC) method that involves a mixture of glass fiber, thermosetting resin, additives, calcium carbonate, fillers such as carbon nanotube, carbon fiber. In this study, FWR6 glass fiber was (16  $\mu\text{m}$  filament diameter, 2200 roving tex count (g/1000 m)) purchased from Sisecam Turkey. Polipol 3401 orthophthalic-based unsaturated polyester obtained from Poliya was used as resin which has styrene monomer content 37-41% with viscosity value of 350 cps. The 3-methacryloxypropyltrimethoxy silane was employed as a coupling agent that enhances adhesion ratio between resin and glass fibers and improves quality of electrical properties. Single walled carbon nanotubes (Tuball Matrix, OCSiAl, Germany Laboratories) with the average diameter of 20 nm and the length in the range of  $\sim 22 \mu\text{m}$  were used, in which the purity is higher than 93 wt. %.

The materials produced also include methyl ethyl ketone peroxide, calcium carbonate,



thickener mixture, zinc sulphide. The above-mentioned components and unsaturated polyester resin were added into the single-walled carbon nanotube suspension, which was subjected to an ultrasonic bath for 1 hour at room temperature. The dough, which became paste-like, was transferred to the conveyor system by mixing with the help of a mechanical stirrer. The dough, on which glass fiber was clipped and pressed again in order to ensure homogeneity, was put into molds until it had the appropriate viscosity and sent to the oven. After the optimum conditions were satisfied, the material removed from the mold was pressed on test plates.

## 2.2. Method and Morphology

Surface images were obtained using scanning electron microscopy (SEM) and transferred to digital media using Gwyddion free software in order to investigate the surface morphology of the pure and carbon nanotube loaded samples [16]. Five different images with 200 x 200 pixel mesh were selected from the SEM microphotographs to determine the regional fractal morphology features.

Firstly, the particle density  $\rho(x_i, y_j)$  according to the location of the particles on the sample surfaces, black cells as one (1), white cells as zero (0) were determined to calculate the surface coating rate (SCR). SCR can be defined as

$$\sigma(N, L) = L^{-d} \sum_{i=1, j=1}^{i=L, j=L} \rho(x_i, y_j) \quad (1)$$

where  $\sum_{i=1, j=1}^{i=L, j=L} \rho(x_i, y_j)$  is total number of particles,  $L$  is the side of the square mesh in BMP image format and  $d = 2$  Euclidean dimension.

Secondly, surface height density can be obtained using following equation:

$$\bar{h}(h, L) = (L^{-d}) \sum_{j=1}^L \sum_{i=1}^L h_{i,j} \quad (2)$$

where  $\sum_{j=1}^L \sum_{i=1}^L h_{i,j}$  is the total value of image density on the total grayscale of the

surface. The  $h_{i,j}$  value is the number of data points and the height value at each data point on the surface of the composite material displayed in 3 dimensions. In the matrix array representing the composite surface, the height value for each pixel in the image is defined as follows:

$$h_{i,j} = \begin{cases} 0 & \text{black pixels} \\ \text{from 0 to 255} & \text{grey pixels} \end{cases} \quad (3)$$

In this model, the height value of each pixel on the surface of the composite is an integer and takes values between 0 and 255 on the grayscale.

The power spectrum is one of the useful methods for fractal dimension calculation of the material and is based on the power spectrum dependence of the irregular Brownian motion [17-19]. To find the fractal dimension of an image, the intensity distribution in a particular aspect of the image converted to gray scale is determined using appropriate image processing software. The Fast Fourier Transform (FFT) of the obtained data is extracted. The square of the amplitude of the Fourier transform is the power spectrum  $w(f)$  which is defined as proportional to  $\beta$

$$w(f) \sim k^{-\beta} \quad (4)$$

where  $f$  is the frequency and  $k = 1.37 \times 10^{-23}$  J/K is the Boltzmann constant. The calculated  $\beta = 7 - 2d_f$  value is related to the fractal dimension  $d_f$ . Integrating Eq. (4), we have

$$\log w(f) = -\beta \log k + c \quad (5)$$

where  $c$  is the integration constant. However the calculated fractal dimension values have a relative measurement uncertainty which can be expressed as

$$\frac{\Delta d_f}{\bar{d}_f} = \frac{d_f - \bar{d}_f}{\bar{d}_f} \quad (6)$$

where  $\bar{d}_f$  is the average of the regional fractal dimension values of the composite.

### 3. IMPEDANCE SPECTROSCOPY

The frequency dependent impedance measurements were carried out at room temperature in the frequency range from  $10^{-2}$  Hz to 1 MHz. The samples in the form of 3 mm thick square plates with 20 mm side length were placed between two parallel plate electrodes. The results extracted from these measurements are used to determine complex impedance ( $Z^*$ ) of the specimens. The real part ( $Z'$ ) of the represents the resistance of the material, while the imaginary part ( $Z''$ ) defines the loss factor [20]. Using the impedance data, the real ( $\epsilon'$ ) and imaginary parts ( $\epsilon''$ ) of the complex dielectric permittivity ( $\epsilon^*$ ) of the polymer material are obtained with the following formulas [7].

$$\begin{aligned}\epsilon'(\omega) &= Z''/2\pi fC_0Z^2 \\ \epsilon''(\omega) &= Z'/2\pi fC_0Z^2\end{aligned}\quad (7)$$

where  $C_0$  is the capacitance of sample.

### 4. RESULTS

The surfaces of neat and nanotube-doped samples are given in Fig. 1 as typical greyscale images and bitmap (BMP) images. When the surface morphology of the neat sample is examined, it is reported that a systematic and symmetrical distribution is not observed and the structure is irregular. The cylindrical fiber structures are randomly distributed along the upper and lower lateral edges of the lattice and the sizes of the particles that form the matrix appear to be different from each other.

On the other hand, the components were distributed relatively more homogeneously in the resin and the carbon nanotubes exhibited a different structure by adhering randomly to the materials forming the matrix in the carbon nanotube doped sample. In addition, agglomerations of carbon nanotubes clusters were observed in certain regions in the matrix.

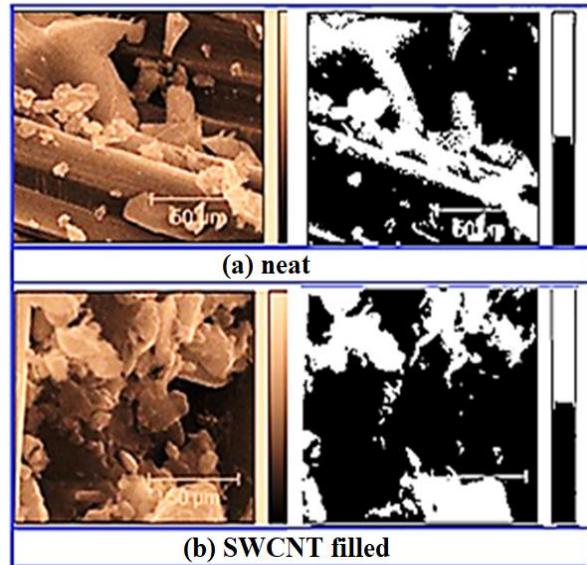


Figure 1 The greyscale and BMP images of the neat and SWCNT filled materials

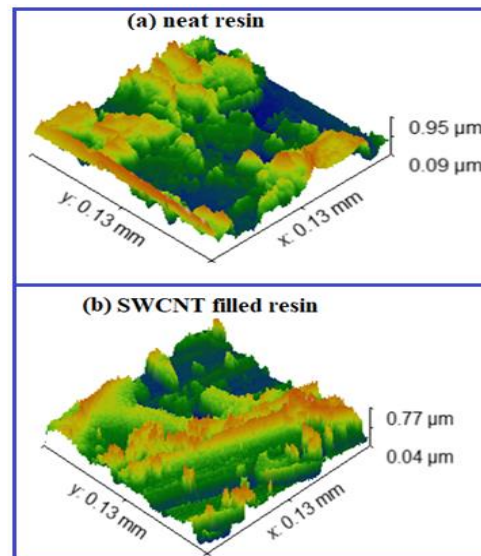


Figure 2 The tomographic images of the neat and SWCNT filled materials

The surface coating rate (SCR) value calculated from BMP image format for the pure material varies between 36.82% and 58.29%, with an average value of 45.08%. The SCR value for the carbon nanotube composite varies between 42.48% and 52.32%, and the average value was calculated as 47.51%. This situation was attributed to the balanced distribution of carbon nanotubes in the matrices and interfaces.

The morphologies of the surface formations of the specimens were examined by 3D tomographic images as given in Figure 2. It

was revealed from images that internal structures of the polymer composites were heterogeneous and irregular.

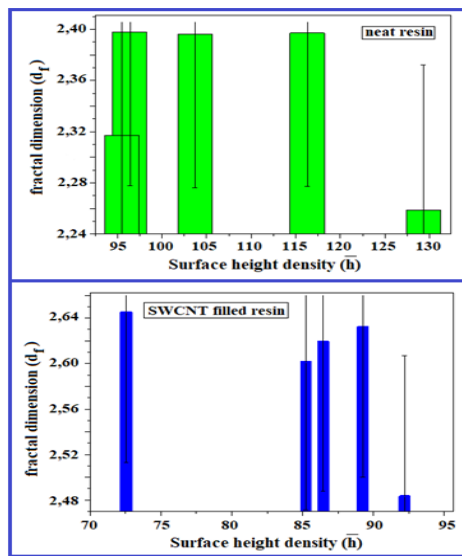


Figure 3 Surface height density versus fractal dimension graph of the neat and SWCNT filled materials

Fig. 3 shows the relation between surface height density and fractal dimension for both samples.  $(\bar{h})$  varies between 95.518 and 129.296 with an average value of 108.246 neat composites. Surface height density  $(\bar{h})$  value is between 85.139 and 92.22 for nanotube added polymer and its average value was calculated as 87.247. Error lines have been added on the bar chart. The regional surface densities were found to be different from each other due to the fact that the carbon nanotubes added to the polyester-based composite were not homogeneously dispersed into the polymer composite.

The fractal dimension parameter ( $d_f$ ) are obtained by  $\beta$  value from the slope of  $\log w$  ( $f$ )- $\log k$  graph as illustrated in Fig. 4 of the power spectrum [19]. It was revealed that the fractal dimension values of the pure sample obtained by the Fourier spectral analysis method ranged from 2.259 to 2.398 and the average value was 2.353. The fractal dimension value of the carbon nanotube added sample increased from 2.483 and 2.632 and the average value was calculated as 2.636.

The measurement uncertainty for the pure and doped sample was calculated as 0.022 and 0.027, respectively. The  $d_f$  value of the carbon nanotube added samples was found to be higher than the undoped samples. This situation can be attributed to the possible existence of high fractalization and surface anisotropy in the doped material. Experimental data reported that while the value found by spectroscopy is between 2.02 and 2.21, the value found by SANS technique is between 2.29 and 2.31 [9]. It should be noted that the obtained dimensionality parameters take values closer to 3 rather than 2. That is, they are higher than the surface size but smaller than the volume dimension. The reason for this can be interpreted as that not only carbon nanotubes and other components shape the agglomeration, but also the chemical surface properties have an active role in this case [21].

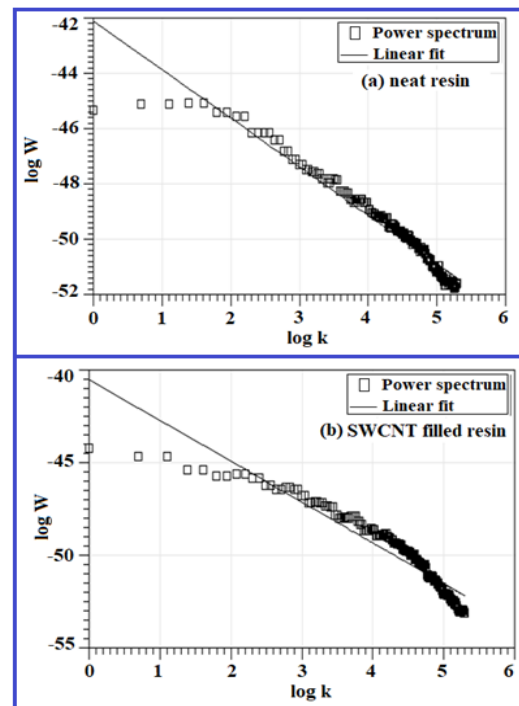


Figure 4  $\log w$  ( $f$ )- $\log k$  graph of the neat and SWCNT filled materials

Fig. 5 (a) and (b) provides plots of the dielectric constant dielectric loss factor of neat and SWCNT filled resin. It is seen that the dielectric constant values found for the neat resin are almost independent of frequency. However, the nanotube doped

sample has high dielectric constants at low frequencies.

This can be attributed to the fact that the electric field generated in the material prevents charge accumulation at the interface between the matrix and the single-walled carbon nanotubes. Another reason can be considered as polarization and Maxwell-Wagner-Sillars interaction effects in the low frequency region [22].

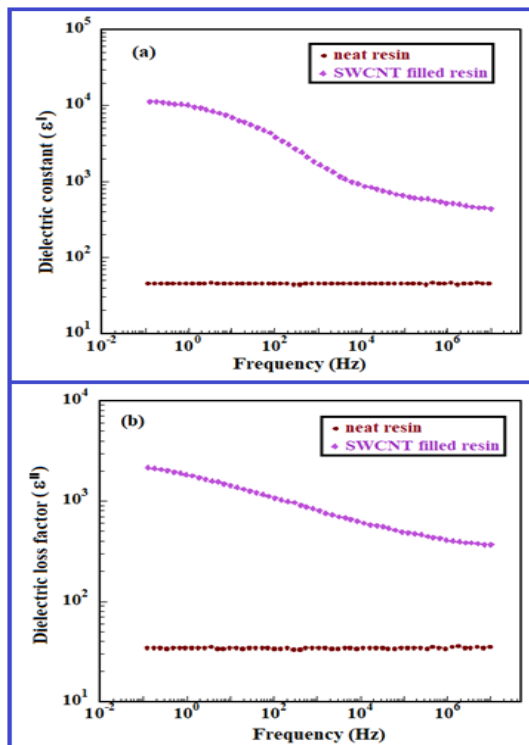


Figure 5 (a) Dielectric constant and (b) dielectric loss factor of neat and SWCNT filled resin.

The fact that carbon nanotubes act as capacitors in the matrix as a result of aggregation which is presented by fractal analysis is also one of the factors that increase the dielectric constant. At high frequencies, the dielectric constant decreases as the polarization effects weaken and carbon nanotubes act as conductive sources. As can be seen from the graphs, no loss peaks were observed within our frequency limits measured in the loss spectrum. The loss factor, which is high at low frequencies, gradually decreases with increasing frequency due to the interfacial polarization

and direct current conductivity contributing to the dielectric relaxation process.

## 5. CONCLUSIONS AND DISCUSSION

The polymer-based composites are known to be ideal candidates for designing materials with high dielectric permeability over a wide frequency range. However, in the last two decades, it has been revealed that adding carbon nanotubes to polymer-based composites improves the dielectric properties of the material. At the same time, there are studies in which this effect is related to the morphological structure and fractal behavior of the material. In this study, pure and single-walled carbon nanotube doped materials were manufactured to test this correlation between dielectric properties and morphological structure. Firstly, the real (dielectric constant) and imaginary (dielectric loss factor) components of complex permittivity for materials were obtained using the impedance spectrum data.

It has been observed that the pure sample has a dielectric value that is almost unaffected by the frequency, however, the dielectric properties of the carbon nanotube added material show frequency-dependent behaviors. Doping has been found to increase fractalization due to the agglomeration and orientation of carbon nanotubes. It has been interpreted that increasing nanotube clusters also act as a microcapacitor at low frequencies and increase the dielectric constant. At high frequencies, due to their conductive nature, they become conductive and the dielectric constant begins to decrease as Belhimria et al. stated in literature [9]. Similar interpretations can be made for the dielectric loss factor in parallel with the values found by Samir et al [6].

Since it is known from that the polarization effects and dielectric performance of the composite material affect by the homogeneity of structure and material morphology, a theoretical model that includes fractal geometry has been used to evaluate different

parameters such as fractal dimension, surface height density, and surface coating rate. The gray scale, BMP and 3-dimensional fractal graphics are observed to better define the surfaces of materials. The fractal dimension ( $d_f$ ) of the carbon nanotube added samples was found to be higher than the undoped samples as expected. The average fractal dimension extracted from Fourier spectral analysis method was 2.3 for neat and 2.5 for nanotube filled matrix. The fractal dimensions found in the literature are between 2.02 and 2.21 by impedance spectroscopy and between 2.29 and 2.31 by the SANS method [9].

As a result of, dielectric properties have been studied in detail both experimentally with impedance results and theoretically with fractal approach. The results show that the fractalization method can be used as a useful tool to evaluate the additive dispersion character in the polymer composite mixture and to predict effect of filler on the properties of the material. In other studies, the contribution of the area-perimeter relationship of the components on the surface to the AC conductivity can be discussed.

#### ***Acknowledgments***

The authors would like to thank Literatür Kimya for contributions.

#### ***Funding***

The author (s) has no received any financial support for the research, authorship or publication of this study.

#### ***Authors' Contribution***

The authors contributed equally to the study.

#### ***The Declaration of Conflict of Interest/ Common Interest***

No conflict of interest or common interest has been declared by the authors.

#### ***The Declaration of Ethics Committee Approval***

This study does not require ethics committee permission or any special permission.

#### ***The Declaration of Research and Publication Ethics***

The authors of the paper declare that they comply with the scientific, ethical and quotation rules of SAUJS in all processes of the paper and that they do not make any falsification on the data collected. In addition, they declare that Sakarya University Journal of Science and its editorial board have no responsibility for any ethical violations that may be encountered, and that this study has not been evaluated in any academic publication environment other than Sakarya University Journal of Science.

#### **REFERENCES**

- [1] M. F. Frechette, M. L. Trudeau, H. D. Alamdari, S. Boily, "Introductory remarks on nanodielectrics," IEEE Transactions on Dielectrics and Electrical Insulation, vol. 11, pp. 808–818, 2004.
- [2] Y. Yan, Q. Cheng, G. Wang, C. Li, "Growth of polyaniline nanowhiskers on mesoporous carbon for supercapacitor application," Power Sources vol. 196 pp. 7835–7840, 2011.
- [3] J. Zhu, H. Gu, Z. Luo, N. Haldolaarachige, D. P. Young, S. Wei, Z. Guo, "Carbon nanostructure-derived polyaniline metacomposites: Electrical, Dielectric, and Giant Magnetoresistive Properties," Langmuir, vol. 28, pp. 10246–10255, 2012.
- [4] V. P. Anju, P. R. Jithesh, S. K. Narayanankutty, "A novel humidity and ammonia sensor based on nanofibers/polyaniline/polyvinylalcohol," Sensors and Actuators A, vol. 285, pp. 35–44, 2019.
- [5] C. R. Bowen, S. Buschhorn and V. Adamaki, "Manufacture and characterization of conductor-insulator composites based on carbon nanotubes and thermally reduced graphene oxide",

- Pure Applied Chemistry, vol. 86, no.5, pp. 765–774, 2014.
- [6] Z. Samir, Y El Merabet, M. P. F. Graca, S. S. Teixeira, M. E. Achour and L. C. Costa, “Dielectric behaviour of carbon nanotubes particles-filled polyester polymer composites,” *Journal of Composite Materials*, vol. 51, no. 13, pp. 1831–1837, 2017.
- [7] R. Belhimria, Z. Samir, S. Boukheir, S. S. Teixeira, M. E. Achour, A. Anson-Casaos, J. M. Gonzalez-Dominguez, L. C. Costa and M. El Hasnaoui, “Thermal and dielectric properties of carbon nanotubes/graphite/polyester ternary composites,” *Journal of Composite Materials*, Vol. 55, no. 25, pp. 3741–3750, 2021.
- [8] D. Risovic, S. M. Poljacek, K. Furic, and M. Gojo, “Inferring fractal dimension of rough/porous surfaces—A comparison of SEM image analysis and electrochemical impedance spectroscopy methods,” *Applied Surface Science*, vol. 255, no. 5, pp. 3063-3070, 2008.
- [9] R. Belhimria, S. Boukheir, Z. Samir, A. Len, M. E. Achour, N. Eber, L. C. Costa, A. Oueriagli, “Fractal Approach to Alternating Current Impedance Spectroscopy Studies of Carbon Nanotubes/Epoxy Polymer Composites,” *Applied Microscopy*, vol. 47, no. 3, pp. 126-130, 2017.
- [10] J. Lira-Olivares, D. Marcano, C. Lavelle, and F. G. Sánchez, “Determination of porosity by dielectric permittivity measurements in porous ceramics,” *Revista Latinoamericana de Metalurgia y Materiales*, vol. 20, no. 2, pp. 68-79, 2000.
- [11] S. Boukheir, A. Len, J. Füzi, V. Kenderesi, M. E. Achour, N. Éber, L. C. Costa, A. Oueriagli and A. Outzourhit, “Structural characterization and electrical properties of carbon nanotubes/epoxy polymer composites,” *Journal of Applied Polymer Science*, vol. 134, no. 8, pp. 44514, 2016.
- [12] K. Yaman, “Fractal characterization of electrical conductivity and mechanical properties of copper particulate polyester matrix composites using image processing,” *Polymer Bulletin*, vol. 79, no. 5, pp.3309–3332, 2022.
- [13] A. Pander, T. Onishi, A. Hatta, H. Furuta, “Study of self-organized structure in carbon nanotube forest by fractal dimension and lacunarity analysis,” *Materials Characterization*, vol. 160, pp. 110086, 2020.
- [14] M. Zhang, W. Zhang, N. Jiang, D. N. Futaba, M. Xu, “A general strategy for optimizing composite properties by evaluating the interfacial surface area of dispersed carbon nanotubes by fractal dimension” *Carbon*, vol. 154, pp. 457-465, 2019.
- [15] A. R. Hopkins, S. J. Tomczak, V. Vij, and A. J. Jackson, “Small Angle Neutron Scattering (SANS) characterization of electrically conducting polyaniline nanofiber/polyimide nanocomposites,” *Thin Solid Films*, vol. 520, no. 5, pp. 1617-1620, 2011.
- [16] Necas, David & Klapetek, Petr. (2011). Gwyddion: An open-source software for SPM data analysis. *Central European Journal of Physics*
- [17] D. S. Bychanok, M. A. Kanygin, A. V. Okotrub, M. V. Shuba, A. G. Paddubskaya, A. O. Pliushch, P. P. Kuzhir, S. A. Maksimenko, “Anisotropy of the electromagnetic properties of polymer composites based on multiwall carbon nanotubes in the gigahertz frequency range,” *Journal of*

Experimental and Theoretical Physics Letters, vol. 93, no. 10, pp. 607–611, 2011.

- [18] K. Kempa, J. Rybczynski, Z. Huang, K. Gregorczyk, A. Vidan, B. Kimball, J. Carlson, G. Benham, Y. Wang, A. Herczynski, Z. F. Ren, “Carbon Nanotubes as Optical Antennae,” *Advanced Materials*, vol. 19, no. 3, pp. 421–426, 2007.
- [19] P. Avouris, M. Freitag, V. Perebeinos, “Carbon-nanotube photonics and optoelectronics,” *Nature Photonics*, vol. 2 no. 6, pp. 341–350, 2008.
- [20] J. Jyoti, A. Kumar, S. R. Dhakate, B. P. Singh, “Dielectric and impedance properties of three dimension graphene oxide-carbon nanotube acrylonitrile butadiene styrene hybrid composites,” *Polymer Testing*, vol. 68, pp. 456–466, 2018.
- [21] L. Salome and F. Carmona, “Fractal structure study of carbon blacks used as conducting polymer fillers,” *Carbon*, vol. 29, no. 4-5, pp. 599-604, 1991.
- [22] Z. M. Dang, J. K. Yuan, J. W. Zha, T. Zhou, S. T. Li, G. H. Hu, “Fundamentals, processes and applications of high-permittivity polymer–matrix composites,” *Progress in Materials Science*, vol. 57, no. 4, 660–723, 2012.

Sakarya University Journal of Science  
SAUJS

e-ISSN 2147-835X Period Bimonthly Founded 1997 Publisher Sakarya University  
<http://www.saujs.sakarya.edu.tr/>

Title: Metabolism Determination by Soft Computing Methods From Breath Molecules

Authors: Sedat METLEK, Hatice AKMAN, Ismail BAYRAKLI

Received: 2021-04-12 00:00:00

Accepted: 2022-04-08 00:00:00

Article Type: Research Article

Volume: 26

Issue: 2

Month: April

Year: 2022

Pages: 429-437

How to cite

Sedat METLEK, Hatice AKMAN, Ismail BAYRAKLI; (2022), Metabolism Determination by Soft Computing Methods From Breath Molecules. Sakarya University Journal of Science, 26(2), 429-437, DOI: 10.16984/saufenbilder.911990

Access link

<https://dergipark.org.tr/tr/journal/1115/issue/69580/911990>

New submission to SAUJS

<http://dergipark.gov.tr/journal/1115/submission/start>



## Metabolism Determination by Soft Computing Methods From Breath Molecules

Sedat METLEK<sup>1</sup>, Hatice AKMAN\*<sup>2</sup>, Ismail BAYRAKLI<sup>3</sup>

### Abstract

The breath analysis is a non-invasive risk-free and painless method used to diagnose specific diseases. Since the breath analysis method is a new study field than the other methods, there are many unsettled standards and unknown parameters. Numerous complex metabolisms are constantly working in the human body. Therefore, there are numerous unknown molecular relationships. ANN can produce solutions in these unexplained situations.

In our pilot study, breath of 19 healthy people has been analyzed. The TD / GC-MS method, which is an analytical method of breath analysis, has been used to detect molecules in the breaths. Using soft computing methods to the results of the 19 breath samples, the relation between fermentation and carbon hydrate metabolism has been associated with breath analysis technique. The results indicated that, there can be a relationship between these metabolisms. There must be done more studies for the exact results.

**Keywords:** Breath Analysis, Artificial Neural Network, acetone, hexanal, butanol.

### 1. INTRODUCTION

Breath analysis method gains importance day by day in the diagnosis of diseases and in monitoring the health status of the patient. Breath molecules are exhaled by the different and unknown metabolisms. The present study has been done to understand the relationship between molecules from lipid metabolism and lipid peroxidation metabolism. Acetone and butanol molecules are

the products of lipid metabolism and hexanal is known as the product of the lipid peroxidation metabolism.

Acetone is an organic compound that is one of three ketone bodies together with acetoacetate and 3- $\beta$ -hydroxybutyrate. These bodies are produced in the liver (Figure 1). Acetone is produced in two ways: by acetoacetate decarboxylation and by isopropanol dehydration. Acetone is produced by the spontaneous decarboxylation of acetoacetate

\* Corresponding author: haticeakman@isparta.edu.tr

<sup>1</sup> Burdur Mehmet Akif Ersoy University, Vocational School of Technical Sciences  
E-mail: sedatmetlek@mehmetakif.edu.tr

ORCID: <https://orcid.org/0000-0002-0393-9908>

<sup>2</sup> Isparta University of Applied Sciences, Faculty of Technology, Department of Biomedical Engineering  
ORCID: <https://orcid.org/0000-0002-8906-2122>

<sup>3</sup> Aksaray University, Faculty of Engineering, Department of Electrical-Electronics Engineering  
E-mail: ismailbayrakli@aksaray.edu.tr  
ORCID: <https://orcid.org/0000-0002-4512-8783>

[1]. Acetone cannot be converted into acetyl-CoA [2] again and is therefore excreted with urine and breath. In the literature, acetone sources and formation ways are summarised in detail [3]. The brain usually uses glucose necessarily as an energy source. However, when carbohydrates are limited with starvation, the brain cannot use glucose anymore. With the change of metabolism, the brain obtains ketone bodies from fats instead of carbohydrates, which are the main energy source. The fats taken generally dissolve into acetyl-CoA molecules by  $\beta$ -oxidation in the liver, then, produce energy through adenosine triphosphate (ATP) production by entering the cycle of the tricarboxylic acid (TCA). Acetyl-CoA, which is required for the biosynthesis of ketone bodies, is an important intermediate product in the energy metabolism. In the case of fasting, the tissues increase the fatty acid oxidation to meet the energy requirement, and as a result of this, a part of the excess acetyl-CoA is incorporated into the ketone body biosynthesis. The liver lacks the necessary enzymes to degrade ketone bodies.  $\beta$ -hydroxybutyrate and acetoacetate participate in the circulation through tissues such as the brain and muscle. Thus, the brain is able to utilise ketones, which are the main oxidative substrates for cerebral metabolism, through fasting or high fat/low carbohydrate uptake. Due to fasting, the ketones pass through the blood-brain barrier with an easy diffusion with the monocarboxylate transporter. With fasting, the brain monocarboxylate transporter levels get better. Neurons and glial cells separate  $\beta$ -hydroxybutyrate and acetoacetate into the acetyl-CoA fragment. ( $\beta$ -hydroxybutyrate dehydrogenase and 3-oxoacid CoA-transferase) Acetyl-CoA molecules can be considered to enter the Krebs Cycle and produce energy [4, 5]. In the brain, ketone bodies are an essential source of energy during fasting or strenuous exercise. In the brain, ketone bodies are an essential source of energy during fasting or strenuous exercise. The studies indicated that breath acetone can be used for the ketogenic state during fasting [6-9].

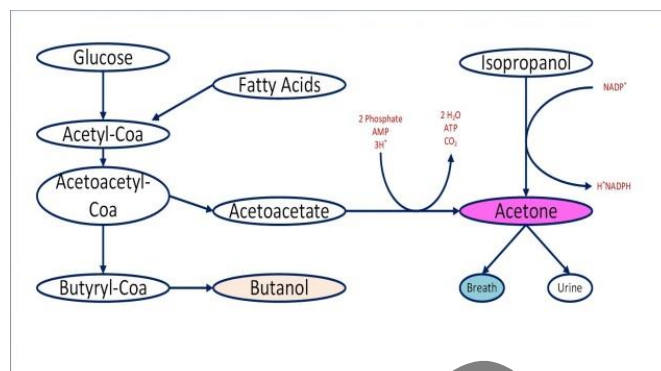


Figure 1 Biochemical pathways of acetone and butanol [10, 11]

Butanol can be produced from the microbial fermentation of carbohydrates such as glucose, for example, *Clostridium acetobutylicum* [10]. This process has been metabolised to produce acetone and butanol from carbohydrates for various applications by means of acetone-butanol fermentation. Butyryl-CoA produced from acetoacetyl-CoA is converted to butanol in this process. Butanol was detected in human breath samples [12]. Filipiak et al. [13], analysed VOCs released by *Streptococcus pneumoniae* and *Haemophilus influenzae* cultures using the GC-MS method and found butanol at slightly high concentrations in both bacterial cultures. Kushch et al. [14], compared the breaths of smokers with those of non-smokers and found that the butanol molecule was not a significant biomarker for smokers. However, the butanol molecule was found at a significantly higher concentration in the breaths of lung cancer patients compared to the healthy control group.

There is not enough information about how the butanol molecule is formed and its effects on the cellular system. Some studies have shown the effects of acetone and butanol as anti-inflammatory agents [15, 16].

During lipid peroxidation, along with the increase in the formation of reactive oxygen species (ROS) that cause the increase in oxidative stress and neurotoxicity in the brain, an increase in lipid peroxidation markers as hexanal [17]. Lipid peroxidation metabolism is shown in Figure 2. Hexanal lipid peroxidation during lipid peroxidation is the molecule that occurs in the breath as a biomarker [18-22].

At the first stage of lipid peroxidation, lipid radical is formed by removing an H atom containing an electron from conjugated double bonds in fatty acids. The lipid radical forms the lipid peroxide radical (LOOH) by reacting with oxygen. LOOH degradation occurs with the ion catalysis of the transition metals. The cell membrane and organelle lipid peroxidation can be stimulated by free radicals and increases in the presence of transition metals. The formation of the hydroxyl radical ( $\text{OH}\cdot$ ) from hydrogen peroxide ( $\text{H}_2\text{O}_2$ ) can initiate a chain reaction. As a result of these reactions, aldehydes (e.g. hexanal) emerge as end products [23]. The lipid peroxidation metabolism progressing without enzymes is a very harmful chain reaction. In these reactions, the membrane structure is directly damaged and the produced reactive aldehydes indirectly damage other cell components. This can cause many diseases [24], [25].

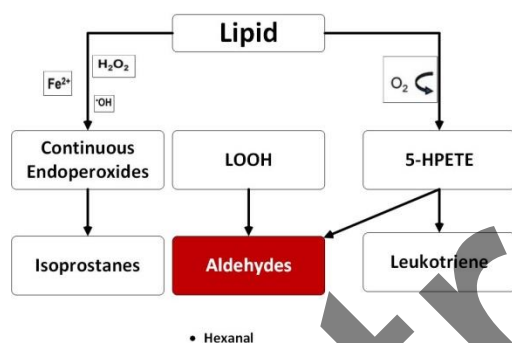


Figure 2 Lipid peroxidation metabolism [26]

## 2. MATERIAL METHOD

### 2.1. Breath Collection

Breath of 19 healthy people has been collected via tubes from marks and translated to TENAX-TA 200 cartridge stored at the  $4\text{C}^0$  to preserve VOCs (Figure 3). The information of the people breath collected from are shown at the Table 1.



Figure 3 Breath collection tube and cartage

Table 1 Breath Samples Collected Group

Gender (male/female)	10/9
Age (years)	Between 21 and 43 years Average: 28,8 years Standard Deviation (SD): 7,3
BMI ( $\text{kg m}^{-2}$ )	Between 21 and 25,2 Average :23,2 SD: 1,5

### 2.2. GC-MS/TD Method

In conjunction with MS, GC is commonly used for breath analysis. In this study, TD - GCMS was used for analysis of breath acetone hexanal and butanol levels (Agilent Technologies 7890A 5975C). VOCs are thermally decomposed by thermal decomposers injected into GC / MS. Conditions for thermal decomposer are shown in Table 2.

The undifferentiated (non-split) mode has been applied to the TD system. GC / MS injector temperature was set to  $250\text{ }^\circ\text{C}$  and the flow rate was set to 20 psi. The column oven temperature was raised to  $180\text{ }^\circ\text{C}$  by keeping it at  $60\text{ }^\circ\text{C}$  for 4 minutes and then increasing it by  $20\text{ }^\circ\text{C}$  per minute. After holding at  $180\text{ }^\circ\text{C}$  for 15 minutes, the temperature was raised again to  $215\text{ }^\circ\text{C}$  at a rate of  $4\text{ }^\circ\text{C} / \text{min}$ . It was held at this temperature for 20 minutes. In addition, the column oven was heated up to  $240\text{ }^\circ\text{C}$  at  $4\text{ }^\circ\text{C}$  per minute. It was held at this temperature for 35 minutes. Analytes were then injected into a DB-5 non-polar capillary column of 30 m length and 0.25 mm inner diameter. Selective ion tracking / imaging (SIM) mode was used to obtain lower detection limits. SIM mode allows us to get much more effective results in full scan mode. Helium gas (99.999%)

was used as a carrier in the analytical column with a flow of about 20 psi. Ionization of individual compounds was accomplished by electron impact ionization at 70 eV.

Table 2 Thermal desorption unit settings

<b>Pre-desorption settings</b>	
Split on in standby	
Flow path temperature	200°C
Minimum transporter pressure	5 psi
Pre-purification time	1 min
<b>Tube / sample desorption settings</b>	
Tube desorption time	5 min
Tube desorption temperature	250°C
<b>Trap Settings</b>	
Pre-trap fire purge	Minimum 1 min of trap flow
Trap low	-10°C
Trap heating rate	Maximum
Trap fixation / minute	3 min
Split	Open
Trap maximum	300°C

### 2.3. ANN

Artificial neural networks (ANN) are computer programs that are developed on the basis of the human brain, which are mainly connected to each other and which perform parallel and distributed information processing, each of which performs its own processing [27]

Examples related to the operations to be made to artificial neural networks are given. Thus, ANN can collect relevant information, make generalizations, and then decide on those samples using information learned in comparison with samples that have never been seen. Due to these learning and generalization features, artificial neural networks now find wide application in many scientific fields and demonstrate their ability to solve complex problems successfully [28].

ANN can be applied to many fields such as control and system identification, image and voice recognition, prediction and estimation, failure analysis, medicine, communication, traffic, production management [29].

There are also many different types of ANN developed for linear and non-linear systems such as perceptron neural networks, multi-layered artificial neural networks (MLF-ANN), and ADALINE / MADALINE. Since the nonlinear data are used in the study, the MLF-ANN structure of ANN is preferred.

#### 2.3.1. Multi-layered Artificial Neural

##### Networks (MLF-ANN)

It is a structure developed for systems without linear solution. The MLF-ANN is a model in which the inputs are entered during the training phase and outputs are expected to be generated for these inputs.

Generated output based on network input [30]. The Multilayer Network structure is shown in Figure 4. The layer that the incoming information is transmitted to the hidden layer is the input layer. The hidden can be one or more. Here, the information received at the input layer is processed. On the output layer, the output values are calculated for each input against the information received from the hidden layer.

#### 2.3.2. Feedback

Feedback in Artificial Neural Networks is done when the output of at least one neuron enters itself or other neurons and obtain error is usually made.

The feedback can be between neurons in a layer as well as between neurons in a layer. With this structure, feedback-driven ANN shows a non-linear dynamic behavior. Therefore, the feedbacks with different structures and behavior can be obtained according to the shape of the artificial neural networks.

Figure 4. below shows an ANN structure with three layers and feedback to the input layer.

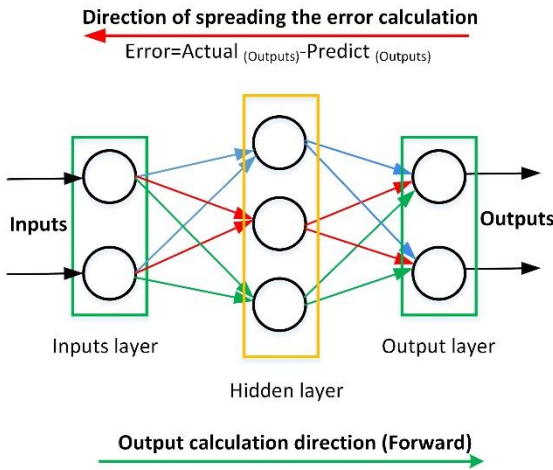


Figure 4 Feedback Neural Network

### 2.3.3. Back Propagation Algorithms

The backpropagation algorithm finds the error signal between the inputs and outputs, and the weights are updated with this error signal. The error  $e(t)$  is the difference between the actual output  $t(t)$  and the output of the neural network  $y(t)$  [31].

$$e(t) = t(t) - y(t); \quad t = 1, \dots, m \quad (1)$$

The backpropagation algorithm spreads the effects of the  $e(t)$  function on all weights on the network. Thus, the total error value is the lowest.

$$TH = \frac{1}{2} \sum_m E^2 \quad (2)$$

In Equation 2, TH represents the Total Error value.  $m$  is the output layer  $m$ . it is the element. Equation 2 shows that if the TH value is reduced in any experiment, the system error will decrease.

Methods that re-update the weight values on the network based on the decrease in system error and to support this decrease are used. The training process is based entirely on this update process.

With this algorithm  $x_i$ . For input, the  $w_{ji}(t)$  change in weights between the  $i$  and  $j$  times processing elements is calculated. This expression is given in Equation 3.

$$\Delta w_{ji}(t) = \eta \delta_j x_i + \alpha \Delta w_{ji}(t - 1) \quad (3)$$

In Equation 3,  $\eta$  is the learning coefficient,  $\alpha$  is the momentum coefficient, and  $\delta_j$  is a factor of any  $j$ -neuron at the intermediate or output level. For the output stage, this factor is given as follows.

$$\delta_j = \frac{\partial f}{\partial net_j} (y_j^{(t)} - y_j) \quad (4)$$

Where  $y_j^{(t)}$  is the target output of the  $j$  processor element. For the Process Elements (PE) in the hidden layers (Process Elements - Neurons), this factor is expressed as in Equation 5.

$$\delta_j = \left( \frac{\partial f}{\partial net_j} \right) \sum w_{qi} \delta_q \quad (5)$$

Since there is no target output for neurons in hidden layers, Equation 5 is used instead of Equation 4. Depending on this situation, starting at the output layer,  $\delta_j$  factor is calculated for neurons in all layers. The weights are then updated for all links based on the form in Equation 3. The activation function to be used in the backpropagation algorithm should have several important properties.

The activation function must be a continuous, derivative-derived function that does not degrade in a uniform manner. The reason for this preference is that the derivation of this function is easy. In general, the function is expected to lie between the minimum and maximum asymptotes [32].

In our study, the breathing of 19 healthy persons was examined. The TD / GC-MS method, which is an analytical method of breath analysis, has been used to detect molecules in the breaths. Breath samples taken from 19 individuals are shown in Table 3 and structure of prepared MLF-ANN Model is created.

Table 3 Inputs and outputs used in Feedback Multilayer Artificial Neural Network

	Inputs		Outputs
	Hexanal (ppb)	Acetone (ppb)	Butanol
1	0,62	92	0,18
2	2,02	97	0,57
3	1,13	97	0,25

4	2,23	114	0,63
5	8,22	119	0,67
6	5,55	148	1,26
7	1,11	148	1,12
8	5,69	199	0,25
9	0,98	210	0,89
10	2,56	216	0,36
11	6,56	219	0,36
12	0,85	243	1,25
13	1,62	267	0,44
14	0,82	305	0,3
15	2,5	305	0,56
16	1,99	307	1,51
17	1,25	309	0,75
18	1,92	317	0,56
19	5,05	772	0,28

MATLAB 2017a version was used to process the data. The structure of the prepared model is shown in Figure 5. In this structure Hexanal and Aceton were taken as input and Butanol was taken as output. Thirteen of the data in the Table 1 are used for training (70%), 3 data (15%) for testing, and 3 data (15%) for validation.

Levenberg-Marquart, Bayesian Regularization and Scaled Conjugate Gradient functions were tested for training. The results obtained are shown in Table 4. Mean squared error values are used to evaluate the performance of the system.

When Table 4 and Figures 5,6,7 examined, it is seen that the Bayesian Regularization method gives better results in training and test results in two-input, 10 hidden-layer and one output system than the other two methods.

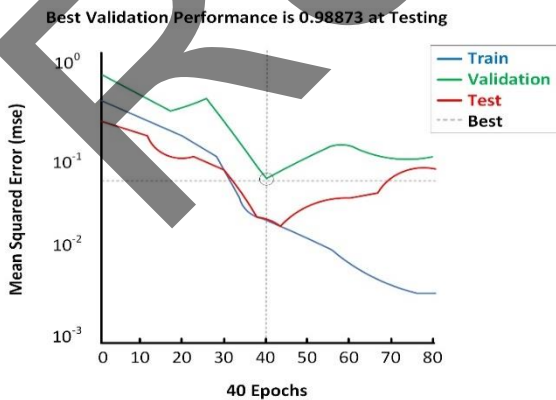


Figure 5 Levenberg-Marquart

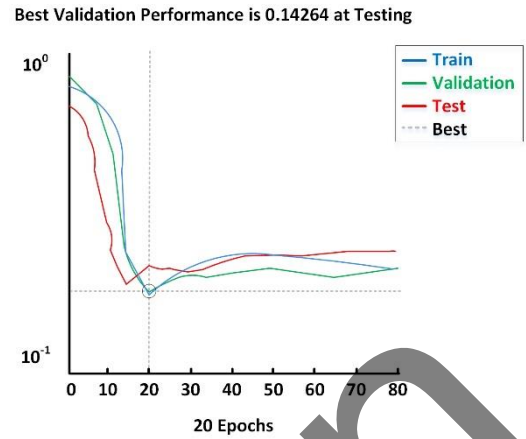


Figure 6 Bayesian Regularization

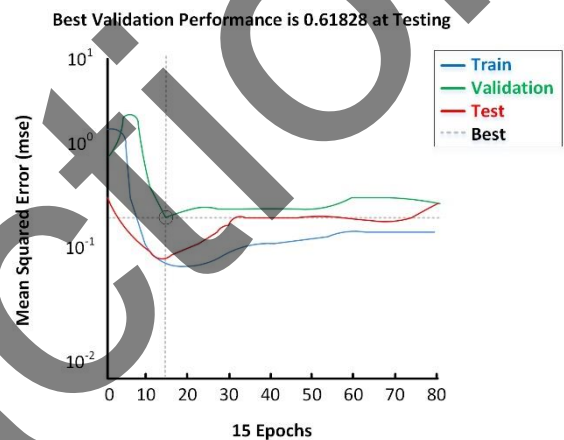


Figure 7 Scaled Conjugate Gradient

Table 4 Results Obtained from Feedback Model Neural Network Model

		Samples	Number of neurons in hidden layer	Iterations	Mean Squared Error (MSE)
Levenberg-Marquart	Training	13	10	40	0,80314
	Validation	3	10	40	0,64211
	Testing	3	10	40	0,98873
Bayesian Regularization	Training	13	10	20	0,12345
	Validation	3	10	20	0,13708
	Testing	3	10	20	0,14294
Scaled Conjugate Gradient	Training	13	10	15	0,73701
	Validation	3	10	15	0,70095
	Testing	3	10	15	0,61828

Despite the small number of data used in the study, high accuracy was obtained in the training and testing processes as the data completely covered the research subject.

### 3. CONCLUSIONS

Hexanal and acetone is the end product of the carbon hydrate metabolism and can be detected from breath. Butanol is the end product of the carbon hydrate fermentation. Many complex metabolisms occur in the body and there are lots of undefined metabolisms. This pilot study is done to understand the indeterminate metabolisms' products. This is a preliminary study to discover metabolism, and can be a method to diagnose diseases but more data is needed. Hexanal and Acetone are defined as input and Butanol as a output at the model which is prepared by using feedback artificial neural network method which is a flexible calculation method. The prepared ANN model is also an example of human metabolism. According to this pilot study there can be a relationship between fermentation and carbon hydrate metabolism.

An association is established between these non-linear data. It is a preliminary study of what chemicals will enter the human metabolism in the future and which components will result in a reaction. If there are more and more data from human metabolism, they can be explained more clearly in relation to each other. As a result, the personalized ANN model can be obtained. Thus, according to certain chemical results to be taken from the person, the anomalies of the person's body can be determined much more quickly and accurately.

#### *The Declaration of Research and Publication Ethics*

In the writing process of this study, international scientific, ethical and citation rules were followed, and no falsification was made on the collected data. Sakarya University Journal of Science and its editorial board have no responsibility for all ethical violations. All responsibility belongs to the responsible author and this study has not been evaluated in any academic publication

environment other than Sakarya University Journal of Science.

#### *The Declaration of Ethics Committee Approval*

The authors declare that this document does not require an ethics committee approval or any special permission. B

#### *The Declaration of Conflict of Interest/ Common Interest*

No conflict of interest or common interest has been declared by the authors.

#### *Authors' Contribution*

*Sedat Metlek:* Artificial Neural Network Design, Writing

*Hatice Akman:* Breath Analysis, Writing

*İsmail Bayraklı:* Breath Analysis

### REFERENCES

- [1] A. Prabhakar, A. Quach, D. Wang, H. Zhang, M. Terrera, and D. Jackemeyer "Breath acetone as biomarker for lipid oxidation and early ketone detection," *Glob. J. Obesity, Diabetes Metab. Syndr.*, vol. 1, no. 1, pp. 12–19, 2014.
- [2] W. Li, Y. Liu, X. Lu, Y. Huang, Y. Liu., and S. Cheng, "A cross-sectional study of breath acetone based on diabetic metabolic disorders," *J. Breath Res.*, vol. 9, no. 1, p. 16005, 2015.
- [3] Z. Wang and C. Wang, "Is breath acetone a biomarker of diabetes? A historical review on breath acetone measurements," *J. Breath Res.*, vol. 7, no. 3, p. 37109, 2013.
- [4] S. A. Masino and J. M. Rho, "Mechanisms of ketogenic diet action," *Epilepsia*, vol. 51, no. 5, p. 85, 2010.
- [5] J. W. Wheless, "History of the ketogenic diet," in *Epilepsia*, 2008, vol. 49, no. SUPPL. 8, pp. 3–5.

- [6] C. N. Tassopoulos, D. Barnett, and T. R. Fraser, "Breath-acetone and blood-sugar measurements in diabetes," *Lancet*, vol. 293, no. 7609, pp. 1282–1286, 1969.
- [7] O. E. Owen, V. E. Trapp, C. L. Skutches, M. A. Mozzoli, R. D. Hoeldtke, G. Boden, and G. A. Reichard, "Acetone metabolism during diabetic ketoacidosis," *Diabetes*, vol. 31, no. 3, pp. 242–248, 1982.
- [8] D. Smith, P. Spanel, and S. Davies, "Trace gases in breath of healthy volunteers when fasting and after a protein-calorie meal: a preliminary study," *J. Appl. Physiol.*, vol. 87, no. 5, pp. 1584–1588, 1999.
- [9] M. Righettoni, A. Schmid, A. Amann, and S. E. Pratsinis, "Correlations between blood glucose and breath components from portable gas sensors and PTR-TOF-MS," *J. Breath Res.*, vol. 7, no. 3, p. 37110, 2013.
- [10] D. T. Jones and D. R. Woods, "Acetone-butanol fermentation revisited," *Microbiol. Rev.*, vol. 50, no. 4, p. 484, 1986.
- [11] C. C. Pamela, A. H. Richard, and R. F. Denise, "Lippincotts illustrated reviews biochemistry." Lippincott Williams and Wilkins, Philadelphia, 2005.
- [12] M. Libardoni, P. Stevens, J. H. Waite, and R. Sacks, "Analysis of human breath samples with a multi-bed sorption trap and comprehensive two-dimensional gas chromatography (GC $\times$  GC)," *J. Chromatogr. B*, vol. 842, no. 1, pp. 13–21, 2006.
- [13] W. Filipiak, A. Sponring, M. Baur, C. Ager, A. Filipiak, H. Wiesenhofer, M. Nagl, J. Troppmair, and A. Amann, "Characterization of volatile metabolites taken up by or released from *Streptococcus pneumoniae* and *Haemophilus influenzae* by using GC-MS," *Microbiology*, vol. 158, no. 12, pp. 3044–3053, 2012.
- [14] I. Kushch K. Schwarz, L. Schwentner, B. Baumann, A. Dzien, and Smith D., "Compounds enhanced in a mass spectrometric profile of smokers' exhaled breath versus non-smokers as determined in a pilot study using PTR-MS," *J. Breath Res.*, vol. 2, no. 2, p. 26002, 2008.
- [15] J.-E. Huh B.-K. Seo, Y.-H. Baek, S. Lee, J.-D. Lee, D.-Y. Choi, D.-S. Park, "Standardized butanol fraction of WIN-34B suppresses cartilage destruction via inhibited production of matrix metalloproteinase and inflammatory mediator in osteoarthritis human cartilage explants culture and chondrocytes," *BMC Complement. Altern. Med.*, vol. 12, no. 1, p. 1, 2012.
- [16] M. Gupta, S. Sasmal, and A. Mukherjee, "Therapeutic effects of acetone extract of *saraca asoca* seeds on rats with adjuvant-induced arthritis via attenuating inflammatory responses," *ISRN Rheumatol.*, vol. 2014, 2014.
- [17] R. Paul, A. Choudhury, and A. Borah, "Cholesterol - A putative endogenous contributor towards Parkinson's disease," *Neurochemistry International*, vol. 90, pp. 125–133, 2015.
- [18] C. J. Dillard and A. L. Tappel, "Lipid peroxidation products in biological tissues," *Free Radic. Biol. Med.*, vol. 7, no. 2, pp. 193–196, 1989.
- [19] H. Orhan, "Analyses of representative biomarkers of exposure and effect by chromatographic, mass spectrometric, and nuclear magnetic resonance techniques: method development and application in life sciences," *J. Sep. Sci.*, vol. 30, no. 2, pp. 149–174, 2007.
- [20] H. Esterbauer, R. J. Schaur, and H. Zollner, "Chemistry and biochemistry of 4-hydroxynonenal, malondialdehyde, and related aldehydes," *Free Radic. Biol. Med.*, vol. 11, no. 1, pp. 81–128, 1991.
- [21] W. A. Pryor, B. Das, and D. F. Church, "The ozonation of unsaturated fatty acids: aldehydes and hydrogen peroxide as



- products and possible mediators of ozone toxicity.," *Chem. Res. Toxicol.*, vol. 4, no. 3, pp. 341–348, 1991.
- [22] M. Kinter, "Analytical technologies for lipid oxidation products analysis," *J. Chromatogr. B Biomed. Sci. Appl.*, vol. 671, no. 1, pp. 223–236, 1995.
- [23] S. Demirci, S. Kutluhan, M. Naziroğlu, and A. C. Uğuz, V. A. Yürekli, and K. Demirci, "Effects of selenium and topiramate on cytosolic Ca<sup>2+</sup> influx and oxidative stress in neuronal PC12 cells," *Neurochem. Res.*, vol. 38, no. 1, pp. 90–97, 2013.
- [24] D. E. Stanley, "Tietz Textbook of Clinical Chemistry," *JAMA J. Am. Med. Assoc.*, vol. 282, no. 3, pp. 283–283, 1999.
- [25] İ. Akkuş, "Serbest radikaller ve fizyopatolojik etkileri". Mimoza yayınları, 1995.
- [26] A. Higdon, A. R. Diers, J. Y. Oh, A. Landar, and V. M. Darley-Usmar, "Cell signalling by reactive lipid species: new concepts and molecular mechanisms.," *Biochem. J.*, vol. 442, no. 3, pp. 453–64, 2012.
- [27] Ç. Elmas, "Yapay Sinir Ağları" Kuram, Mimari, Eğitim, Uygulama, Seçkin Yayıncılık, Ankara, 2003.
- [28] H. Ergezer, M. Dikmen and E. Özdemir, "Yapay Sinir Ağları ve Tanıma Sistemleri" - PiVOLKA, vol 2, no. 6, pp. 14-17, 2003.
- [29] H. Pirim, "Yapay Zeka". Journal of Yaşar University, pp. 81-93, 2006.
- [30] İ. Gör, "Çok Katmanlı Algılayıcı Yapay Sinir Ağı ile Lineer Diferansiyel Denklemler Sisteminin Çözümü". 18. Akademik Bilişim Konferansı, 30 Ocak-5 Şubat 2016, Adnan Menderes Üniversitesi, Aydın, 2016.
- [31] K. Görgülü,, E. Arpaz, and Ö. Uysal,. Investigation of the effects of blasting design parameters and rock properties on blast-induced ground vibrations. *Arab J Geosci.*, vol. 8, no. 4269, 2015.
- [32] A.G. Yüksek, H. Bircan, M. Zontul, O. Kaynar, "Sivas İlinde Yapay Sinir Ağları İle Hava Kalitesi Modelinin Oluşturulması Üzerine Bir Uygulama", *C.Ü. İktisadi ve İdari Bilimler Dergisi*, vol. 8, no. 7, 2007.